More free publications from Archimer

Ecole Centrale de Nantes

ÉCOLE DOCTORALE

Sciences pour l'Ingénieur, Géosciences, Architecture

Année 2009-2010 N° B.U. :

Thèse de DOCTORAT

Spécialité : DYNAMIQUE DES FLUIDES ET TRANSFERTS

Présentée et soutenue publiquement par :

JEAN-BAPTISTE - SAULNIER

le 4 décembre 2009
à l'Ecole Centrale de Nantes

TITRE

REFINED WAVE CLIMATOLOGY AS A CONTRIBUTION TO THE DESIGN OF WAVE ENERGY CONVERSION SYSTEMS

JURY

Président :	Jérôme BROSSARD, Professeur, Laboratoire des Ondes et Milieux Complexes, Université du Havre
Rapporteurs :	Michel BENOIT, Docteur HDR, Laboratoire National d'Hydraulique et Environnement, EDF R&D, Chatou António Carlos MENDES, Professeur agrégé, Dep^{to} de Eng^{a} Electromecânica, Universidade da Beira Interior, Covilhã
Examinateur :	Fernando VELOSO GOMES, Professeur, Faculdade de Engenharia, Universidade do Porto
Membres invités:	Teresa PONTES, Docteur, Laboratório Nacional de Energia e Geologia, Lisbonne Marc PREVOSTO, Docteur, Service Hydrodynamique et Océano-Météo, IFREMER, Brest

Directeurs de thèse : Alain H. CLEMENT (France) / António F. de O. FALCAO (Portugal)
Laboratoires : L.M.F. de l'E.C.N. (Nantes)/ I.D.M.E.C. de l'I.S.T. (Lisbonne)
Co-encadrants : Marc PREVOSTO / Teresa PONTES
Laboratoires : I.F.R.E.M.E.R. (Brest) / I.N.E.T.I.-L.N.E.G. (Lisbonne) N° ED : 498-80

Ecole Centrale de Nantes

ÉCOLE DOCTORALE

Sciences pour l'Ingénieur, Géosciences, Architecture

Année 2009-2010 N° B.U. :

Thèse de DOCTORAT

Spécialité : DYNAMIQUE DES FLUIDES ET TRANSFERTS

Présentée et soutenue publiquement par :

JEAN-BAPTISTE - SAULNIER

le 4 décembre 2009
à l'Ecole Centrale de Nantes

TITRE

REFINED WAVE CLIMATOLOGY AS A CONTRIBUTION TO THE DESIGN OF WAVE ENERGY CONVERSION SYSTEMS

JURY

Président :	Jérôme BROSSARD, Professeur, Laboratoire des Ondes et Milieux Complexes, Université du Havre
Rapporteurs :	Michel BENOIT, Docteur HDR, Laboratoire National d'Hydraulique et Environnement, EDF R&D, Chatou António Carlos MENDES, Professeur agrégé, Dep^{to} de Eng^{a} Electromecânica, Universidade da Beira Interior, Covilhã
Examinateur :	Fernando VELOSO GOMES, Professeur, Faculdade de Engenharia, Universidade do Porto
Membres invités:	Teresa PONTES, Docteur, Laboratório Nacional de Energia e Geologia, Lisbonne Marc PREVOSTO, Docteur, Service Hydrodynamique et Océano-Météo, IFREMER, Brest

Directeurs de thèse : Alain H. CLEMENT (France) / António F. de O. FALCAO (Portugal)
Laboratoires : L.M.F. de l'E.C.N. (Nantes)/ I.D.M.E.C. de l'I.S.T. (Lisbonne)
Co-encadrants : Marc PREVOSTO / Teresa PONTES
Laboratoires : I.F.R.E.M.E.R. (Brest) / I.N.E.T.I.-L.N.E.G. (Lisbonne) N° ED : 498-80

Abstract (french)

Ces travaux portent sur la caractérisation spectrale des états de mer dans le cadre du développement de systèmes récupérateurs de l'énergie des vagues (SREVs). Jusqu'alors, cette caractérisation s'est limitée à des paramètres globaux basiques tels que la hauteur significative et la période moyenne des vagues. Les présents travaux soulignent notamment, à l'aide de modèles simplifiés, que cette description est insuffisante car un SREV montre encore une grande variabilité en termes de production moyenne, ces deux paramètres étant fixés par ailleurs. On s'intéresse donc à raffiner cette description en considérant des caractéristiques de vagues nouvelles, comme le groupement de vagues, lui-même lié à la largeur de bande de l'état de mer. Les approches classiques – spectrales – sur l'étude descriptive des groupes de vagues et la littérature permettent de dégager un certain nombre de paramètres spectraux (ν, κ, Q_p, ε_0, B_w …). On observe ensuite la sensibilité de modèles de SREVs offshore simplifiés (modèles fréquentiels linéaires) à ces paramètres de largeur globale. La question de l'estimation déterministe de performance moyenne (dans le cas de convertisseurs non-linéaires) est également abordée, étant elle-même liée à cette caractéristique.

Un état de mer étant constitué de plusieurs systèmes de vagues (houles, mer de vent), il est encore possible de raffiner sa description grâce à une approche multi-système. Celle-ci permet en outre de suivre ces systèmes indépendamment dans le temps et l'espace. Un algorithme d'analyse spatio-temporelle est proposé et illustré à cet égard.

Enfin, l'influence de ces raffinements est observée en différents sites (Portugal, Mer du Nord, Californie) sur des cas de SREVs divers (systèmes axi-symétriques linéaires, SEAREV 3D d'hydrodynamique non-linéaire), et montre que dans tous les cas, le raffinement apporté permet de mieux caractériser la production à court et long terme de ces dispositifs.

Mots-clés : énergie des vagues, systèmes houlomoteurs, groupement de vagues, largeur spectrale, état de mer, densité spectrale, système de vagues, cohérence spatio-temporelle, simulations numériques, processus gaussiens, modèles stochastiques.

Title and abstract (english)

Refined wave climatology as a contribution to the design of wave energy conversion systems

This work focuses on the refinement of sea-states spectral characterisation in the frame of the development of wave energy converters (WECs). Until now, this characterisation has been limited to the consideration of basic global parameters such as the significant wave height and mean wave period. The present work namely underlines – thanks to simplified numerical models – that such a description is not sufficient to account for the performance of WECs, for they still exhibit a large variability in terms of mean production while wave energy and period are fixed. It is therefore needed to refine this description by introducing new wave characteristics, such as the wave groupiness, which is itself related to the sea-state's spectral bandwidth. The classical – spectral – approaches, allowing a statistical analysis of wave groups along with other works in the literature, permit to draw a set of relevant spectral parameters (ν, κ, Q_p, ε_0, B_w…). The sensitivity of simplified offshore WEC models (linear in the frequency domain) to these parameters is then observed. The question of deterministic mean power estimation – namely in the case of non-linear models – is also raised, for it is also related somehow to the bandwidth of the wave field.

A sea-state is actually made of a superimposition of various wave systems (as swells and wind-sea). It is then possible to refine even more its description, namely through the multi-system approach. This latter enables indeed to track the wave systems in both time and space independently of each other. An algorithm for the automatic spatiotemporal analysis is proposed and illustrated to this end.

Lastly, the influence of such description refinements (wave groupiness and multi-system approach) is observed at several locations (Portugal, North Sea, California) by considering various WEC models (linear axi-symmetric heaving devices, 3D SEAREV with non-linear hydrodynamics): in all cases, it is shown that both extended descriptions allow for a better characterisation of the mean WEC performance at both short and long term.

Key-words : wave energy, WECs, wave groupiness, spectral bandwidth, sea-state, spectral density, wave system, spatiotemporal coherence, numerical simulations, Gaussian processes, stochastic models.

Acknowledgements

As this PhD thesis was carried out in two countries (Portugal and France), and involved several academic and research institutions (namely ECN, IST, IFREMER and INETI), it is my duty to acknowledge all those who helped me realise and achieve the work presented hereafter.

First of all, I sincerely thank the Portuguese members of the PhD jury, starting with emeritus Pr António Falcão from IST, Lisbon, for his continuous availability and support, especially in remotely administrative purposes. I also thank Pr António Carlos Mendes from Universidade da Beira Interior, Covilhã, who kindly accepted to revise this document, and Pr Fernando Veloso Gomes from Universidade do Porto. Finally, I am very grateful to my Portuguese co-supervisor, Dr Teresa Pontes, from INETI/LNEG, Lisbon, with whom I have learnt a lot about wave energy and research during the three years I spent in Portugal. I am all the more grateful to her as without her, and without her will of exploring wave groupiness in wave-energy, I would certainly never have started this PhD.

Then, I would like to warmly thank the French part of the jury, and first of all my supervisor, Dr Alain H. Clément, from ECN, Nantes, for its support all along these years in spite of the distances, when based in Lisbon and Brest. I also thank Pr Jérôme Brossard, from Université du Havre, as well as Dr Michel Benoit, from EDF, Châtou, who kindly accepted to revise the thesis. Lastly, I want to thank my French co-supervisor, Dr Marc Prevosto, from IFREMER, Brest, for his natural welcome and the numerous and fruitful discussions we had throughout the last two years.

Then, I want to acknowledge all the people involved in the institutions I have patronized.

From INETI (now LNEG), Lisbon, I sincerely thank:

Dr Paulo Justino, who early passed me on the "famous" paper of Tucker *et al.*;

Dr João Campos Henriques and Paulo Costa, for their endless patience and help in computer sciences;

José Cândido, Miguel Bruck and André Candelária, for their friendship and support in the wave-energy research unit, and for the numerous discussions we had on that topic;

All the staff of the Renewable Energies Department of INETI, from the director to the last *bolseiro* (grantee), who introduced a lot of humanity in my professional and personal lives (I cannot list them, there is too many of them).

From IST, Lisbon, I warmly thank:

Pierpaolo Ricci, who helped me lead some crucial parts of this work – which resulted in publications in international conferences –, with whom every night out in Lisbon was usually giving rise to new work ideas;

All the students of the first floor of the Mechanical Engineering building (Miguel Lopes, among others, and a very deep thought to Afonso Tiago, who died in Berlin in early 2009).

More generally, from Portugal, I want to acknowledge:

Dr José de Bettencourt, from Ecosphere, Lisbon, who helped me a lot about wave groupiness, and the Hilbert-Huang Empirical Modal Decomposition in particular;

Dr Rui Capitão, from LNEC, Lisbon, for his warm welcome and availability when I was making up my bibliographic review on wave groups;

All the staff of the Wave Energy Centre, Lisbon (Pr António Sarmento, Frank Neumann, Dr Ana Brito e Melo, Janete Gonçalves, Sofia Patrício and Marco Alves, among others), for their constant happiness and the visits to the Pico plant in the Azores;

Dr Henrique Oliveira Pires, for his kind interest in my works and advices;

Drs João Cruz, from Garrad-Hassan, Lisbon, and Miguel Prado, Teamwork Technology, Zijdewind, for the numerous and rewarding discussions we had, as fellows of the E.U. WAVETRAIN Research Training Network.

From ECN, Nantes, I notably thank:

Dr Aurélien Babarit, for his legendary availability and patience about numerical WEC modelling and hydrodynamics Fortran codes in general (SHEBWEC, "ABHIL3D", Aquatimes, SEAREV3D…), and also for his growing interest in my thesis work and advices;

All the staff of the Fluid Mechanics Laboratory of ECN working in the wave-energy field, and also the administrative one, for their help and availability.

From IFREMER Brest Centre – and to a larger extent, from Brest –, I namely thank:

Dr Christophe Maisondieu, for the numerous and stirring talks we had on waves and oceanography, as well as for his nice interest in my PhD;

Dr Marie-Aurélie Kerbiriou, former post-doc at Ifremer, for her explanations and clarifications about the SPOP's algorithm;

Michel Olagnon, for his numerous advices and references about wave statistics and wave simulations;

Tina Odaka, from the Computer Sciences Department, for her very efficient involvement in the implementation of the SEAREV three-dimensional simulation code in the time domain (from ECN) on the Caparmor computational server;

Dr Fabrice Ardhuin, from SHOM, for the large amount of WaveWatch III spectral data he made available to us, from which I could benefit a lot;

Nicolas Raillard, from UBO, for his precious geostatistician viewpoints;

All the colleagues – staff, post-docs, PhD students and trainees – of the "service HO", who welcomed me very early, in spite of my unusual introduction.

Now, more generally and more internationally, I also want to acknowledge: Pr George H. Smith, from Exeter university, for his kind attention and support when meeting at international conferences; Dr Jeffrey L. Hanson, from USACE-ERDC, who nicely sent me some of his publications about wave systems partitioning; Pr Lars Berdahl, from Chalmers university, Göteborg, for his active participation in WAVETRAIN deliverables; Pr José Carlos Nieto-Borge, from Alcalá university, and Pr Harald E. Krogstad, from NTNU, Trondheim, for some very captivating discussions we had.

I want to thank also the Dutch Rijkswaterstaat, for the free use of buoy spectral data in the North Sea; the Dutch company ARGOSS, for the free use of WaveWatch III spectral data in the Bay of Biscay; and, finally, the E.U. WAVETRAIN Research Training Network (Marie Curie Action), which funded the first part of this PhD, and allowed many students – among which, myself – to acquire an invaluable experience in the wave-energy field, notably through the participation to a number of short-courses, seminars and pilot days.

Lastly, I cannot close these acknowledgements pages without addressing my deepest gratitude to all – family, colleagues and friends – who, to different extents, supported me throughout the realisation of this PhD, in crests and troughs, in the best moments as well as in the worst ones, in happiness and pain, and particularly physical pain, which fortunately has not prevented myself from going ahead and achieving this work.

«Eloï, Eloï, lama sabacthani ?»

(Mk, 15,34)

Contents

1 INTRODUCTION **1**

I Identification of groupiness characteristics for the performance study of WECs **7**

2 Descriptive analysis of the wave groupiness phenomenon **8**
2.1 Introduction 8
2.2 Energy spectral density and spectral moments 10
2.3 Theory of runs for independent wave heights 12
2.4 Markov chain theory for successive wave heights 14
2.4.1 Kimura's method 14
2.4.2 Kimura's spectral method 15
2.5 Envelope methods 16
2.5.1 Hilbert envelope 16
2.5.2 List envelope 19
2.6 S.I.W.E.H. 20
2.7 Envelope spectra for Gaussian signals 22
2.8 Hilbert-Huang decomposition and Hilbert spectrum 24
2.9 Groupiness parameters at Nazaré (Portugal) 30
2.10 Conclusion on the wave groupiness spectral characterisation 44

3 Global spectral shape and mean power extraction of WECs **45**
3.1 Introduction 45
3.2 Modelling of a 1-DOF linear WEC 46
3.3 Sensitivity of a 2-DOF heaving linear point absorber to spectral shape 53
3.4 Groupiness statistics for a linear WEC 65
3.5 Influence of spectral bandwidth in wave numerical simulations 69
3.5.1 Estimation error on the variance of a simulated Gaussian centred signal 69
3.5.2 Application to the numerical estimation of H_{m0}^2 and $\overline{P_{PTO}}$ (linear system) 72

3.5.3 Application to the numerical estimation of $\overline{P_{PTO}}$ (non-linear system) . . . 79
3.6 Inertial WEC modelling and groupiness characterisation . . . 85
3.6.1 Instantaneous power filtering by inertial flywheel . . . 86
3.6.2 Short-term energy storage reservoir with nominal output power . 91
3.7 Conclusion about the global spectral shape of sea-states and its influence upon the mean power extracted by WECs . . . 99

II Refined sea-state description and wave systems space and time tracking 101

4 Uni- and multimodal sea-state representations 102
4.1 Unimodal representation . . . 102
4.2 Sensitivity to unimodal sea-state modelling of a directional linear WEC . 105
4.3 Multimodal representation . . . 109
4.4 Conclusion about the uni- and multimodal sea-state representations . . . 111

5 Wave systems extraction, time tracking and identification 112
5.1 Wave systems extraction . . . 112
5.1.1 Partitioning of directional spectra $E(f, \theta)$ . . . 113
5.1.2 Partitioning of omnidirectional spectra $E(f)$ . . . 115
5.2 Wave systems evolution and time tracking . . . 116
5.2.1 Wind-sea and swell systems dynamics . . . 116
5.2.2 Partitions grouping, parameterisation and time tracking . . . 121
5.3 Conclusion about the extraction, time tracking and identification of wave systems . . . 126

6 Wave systems coherence and spatiotemporal tracking 127
6.1 Geostatistics and variographic analysis . . . 127
6.1.1 semi-variogram and covariogram . . . 127
6.1.2 Specificity of the sea-state spatial coherence study . . . 133
6.2 Space and time tracking of extracted wave systems . . . 133
6.2.1 Spatiotemporal cross-assignment of wave systems at small scale (local) . . . 133
6.2.2 Cross-assignment by homogeneous structures tracking at meta-scale (global) . . . 135
6.2.3 Spatiotemporal wave systems tracking algorithm . . . 136
6.2.4 Applications . . . 142
6.3 Conclusion about the spatiotemporal coherence and tracking of wave systems . . . 159

III Effect of sea-state description refinements on WEC performance estimations 160

7 Estimation of long-term production operated by linear systems 161
7.1 Estimation of long-term production operated by axi-symmetrical WECs in shape-variable unimodal sea-states 161
7.2 Comparison of uni- and multimodal sea-states representations for the long-term performance estimation of a linear directional WEC 164
7.3 Conclusion about the estimation of long-term production operated by linear systems 164

8 Performance study of a non-linear directional WEC in a Californian site 166
8.1 Objectives and context 166
8.2 Numerical WEC simulation code and hypothesis 168
8.3 Californian wave climate 174
8.4 Simulation results 184
8.4.1 Simulation results in relation to the global spectrum 186
8.4.2 Simulation results in relation to the active wave system 191
8.4.3 Dispersion of the numerical power estimators 192
8.5 Conclusion about the performance study of a non-linear WEC 193

9 CONCLUSIONS 195

IV Appendices 199

A Spectral bandwidth parameters 200
A.1 The spectral bandwidth of literature 200
A.2 Influence of spectral density smoothing on the numerical value of spectral parameters 205
A.3 Influence of high-frequency cut-off on the numerical value of spectral parameters 208

B Note on the Fourier series decomposition of the water elevation signal 213
B.1 Fourier series of the water elevation signal 213
B.2 Gaussian signal simulation from spectral data 215

C Note on the Q_p-spectra 217
C.1 The unimodal Q_p-spectrum 217
C.2 Generalisation to n systems: multimodal formulation 220
C.3 Bimodal formulation 222

D Stochastic modelling of a 1-DOF linear heaving WEC 225

E Matrix determination of indirect associations **227**

List of Figures

1.1 Pico Island (Azores) wave-energy plant (a), articulated attenuator (wave profiler) *Pelamis* recently deployed in Portugal (b), and O.P.T. heaving *PowerBuoy* installed in the New-Jersey (c). 2
1.2 Wave-energy statistical data provided by the European atlas WERATLAS. 4

2.1 Wave group in a time series of the free surface elevation (successive zero up-crossing wave heights exceeding 2m) 9
2.2 *Run* (or *high run*) and *total run* of high waves in a signal 12
2.3 Elevation signal and related Hilbert envelope. 17
2.4 Splitting effect on the elevation signal's Hilbert envelope: a group of two successive waves (red portion of signal) is cut into two sub-groups according to the envelope. 18
2.5 Id. Fig. 2.3 with List envelopes (List, 1991). 19
2.6 Id. Fig. 2.3 with SIWEH (Funke and Mansard, 1980) and squared envelope function $\Pi(t)$ (Medina and Hudspeth, 1990) 21
2.7 Estimated spectral densities of two wave records ((a)&(c)) and the estimated and fitted spectra of the related Hilbert envelopes ((b)&(d)) at Nazaré (Portugal). 23
2.8 Instantaneous frequency (top) and amplitude (bottom) of an IMF. 25
2.9 Empirical Mode Decomposition: processed input signal (top) decomposed into eight successive IMF and a residue (from top to bottom). 26
2.10 Hilbert spectrum: IMFs' instantaneous amplitude (m) against time (X-axis) and instantaneous frequency (Y-axis). 28
2.11 Elevation signal (light blue line) and instantaneous energy density level (green line). 29
2.12 Mean duration (a) and mean group energy (b) against non-dimensional energy threshold level $IE^*/\overline{IE(t)}$. 29
2.13 Geographical localisation of the Waverider buoy (Nazaré, Portugal). . . . 30
2.14 T_{02} against T_z at Nazaré (March 2004). 32
2.15 Time evolution of parameters H_s, T_p, T_{-10}, Q_p, and P_w at Nazaré (March 2004). 33
2.16 Time evolution of wave periods T_p, T_z, T_{02} and T_{-10} at Nazaré (March 2004). 34
2.17 Time evolution of spectral parameters ε_0, ε_1, ε_2 and κ at Nazaré (March 2004). 35

2.18 Parameters ε_0, ε_1, and ε_2 against κ at Nazaré (March 2004). 36
2.19 Time evolution of groupiness parameters B_w, β, C, GF_{Hilb}, GF_{Π}, GF_{SIWEH} and GF_{IE} at Nazaré (March 2004). 37
2.20 Signals $\eta(t)$, $SIWEH(t)$, $\Pi(t)$, and $IE(t)$ obtained at Nazaré on the $1^{st}$of March, midnight). 38
2.21 Signals $\eta(t)$, $SIWEH(t)$, $\Pi(t)$, and $IE(t)$ obtained at Nazaré on the $3^{rd}$of March, 9AM). 39
2.22 Factor β against B_w at Nazaré (March 2004). 40
2.23 Factor GF_{IE} against groupiness factor GF_{SIWEH} at Nazaré (March 2004). 41
2.24 Spectral parameters ε_0 (a), κ (b), Q_p (c) and B_w (d) against groupiness factor GF_{SIWEH} at Nazaré (March 2004). 42
2.25 Spectral parameters ε_0 (a), κ (b), Q_p (c) and B_w (d) against groupiness factor GF_{IE} at Nazaré (March 2004). 43

3.1 Mechanical scheme of a simple 1-DOF linear point absorber in heave. . . 46
3.2 Target (Bretschneider, dark blue line) and simulated (light blue line) energy spectra of water elevation η (a), squared modulus of heave velocity impedance (b), and target (dark purple line) and simulated (light pruple line) energy spectra of the buoy's heave velocity. 49
3.3 Scheme of IPS heaving buoy. 53
3.4 IPS buoy configurations (IPS1, 2, 3 et 4): power transfer functions (PTF). 54
3.5 Buoy measurements locations: FF (Figueira da Foz, Portugal) and K13 station (North Sea, Netherlands). 55
3.6 χ_P distribution for configurations IPS1 and IPS2 at FF (left) and K13 (right): mean value, 5th and 95th percentiles, and results obtained with standard Bretschneider sea-state as wave input. 57
3.7 χ_P distribution for configurations IPS3 and IPS4 at FF (left) and K13 (right): mean value, 5th and 95th percentiles, and results obtained with standard Bretschneider sea-state as wave input. 58
3.8 Capture width χ_P against ε_0 at FF for $T_{10} = 7s$ and WEC configuration IPS1; quadratic trend fitting and determination coefficient R^2. 59
3.9 Coefficient R^2 of χ_P-distribution fitted with a quadratic law against T_{-10} for each spectral parameter and configuration IPS1 at FF (a) and K13 (b); sub-sample mean extracted power (kW) (red spots). 61
3.10 Id. Fig. 3.9 for configuration IPS2. 62
3.11 Id. Fig. 3.9 for configuration IPS3. 63
3.12 Id. Fig. 3.9 for configuration IPS4. 64
3.13 Statistics on groups of successive wave heights (top) and power peaks (bottom) for $\eta(t)$ and $P_{PTO}(t)$ simulated over 3600s (Bretschneider target sea-state); the mean lengths of high runs (a) and total runs (b) are given against the dimensionless height $2\rho^*/H_s$; the mean lengths of high peaks runs (c) and total runs (d) are given against the dimensionless power $P^*_{PTO}/\overline{P_{PTO}}$; the theoretical curves obtained from equations (2.33), (3.35)&(3.36) are plotted in blue. 67

3.14 Numerical simulation of an axi-symmetric heaving buoy: instantaneous extracted power (kW) and multiples (gray levels) of mean extracted power $\overline{P_{PTO}(t)}$ (red level). 68
3.15 H_{m0}^2 estimator distributions obtained in 300 wave simulation samples of duration $T = 100, 300, 600, 1200, 1800$ and $3600s$ (a-f); mean value (μ) and standard deviation (σ) of the distributions (m^2). 74
3.16 Theoretical (plain line) and sample (markers) mean values (left Y-axis) and standard deviations (right Y-axis) related to wave parameter H_{m0}^2; results in absolute $[m^2]$ (a) and relative (b) value (non-dimensionalised by the theoretical mean value); Bretschneider target sea-state ($H_{m0} = 2m$ et $T_p = 10s$, *method a*). 75
3.17 Theoretical (dotted line) and sample (circles) mean values (left Y-axis) and standard deviations (right Y-axis) related to mean power $\overline{P_{PTO}}$ in a Bretschneider target sea-state ($H_{m0} = 2m$ and $T_e = 7s$, *method a*) after transient regime of the linear WEC buoy modelled in the time domain; results obtained with *method b* are plotted with stars. 77
3.18 $\overline{P_{PTO}}$ estimator distributions obtained in 300 wave simulation samples of duration $T = 100, 300, 600, 1200$ and $3600s$ (a-e) after transient regime of the linear WEC buoy modelled in the time domain; mean value (μ) and standard deviation (σ) of the distributions (kW), and Gaussian-law fitting. 78
3.19 Heaving buoy WEC equipped with a hydraulic PTO device (low- and high-pressure gas accumulators coupled to a hydraulic motor, as described in Ricci et al., 2008; Saulnier et al., 2009). 79
3.20 Sample (circles) mean values (left Y-axis) and standard deviations (right Y-axis) related to mean power $\overline{P_{PTO}}$ in a Bretschneider target sea-state ($H_{m0} = 2m$ and $T_e = 7s$, *method a*) after transient regime of the non-linear WEC buoy modelled in the time domain; results obtained with *method b* are plotted with stars. 80
3.21 Sea-state spectral densities estimated by buoy measurements off Figueira da Foz (Portugal): $26^{th}$of October 1983, 12AM (a), $7^{th}$of December 1989, 0AM (c) and $24^{th}$of April 1994, 9AM (e) (Saulnier and Pontes, 2006); id. Fig. 3.20 for the corresponding estimated spectra (a,c,e). 82
3.22 Spectral bandwidth parameter related to the heave velocity of an equivalent linear system against T (Eq. (3.49)) obtained from simulations of the target spectra: Bretschneider ($H_{m0} = 2m$ et $T_e = 7s$)(a) and Figueira da Foz sea-states (FF198310261200, FF198912070000, and FF199404240900 resp.)(b,c,d). 83
3.23 Wave spectral bandwidth parameters $\Lambda(Hz)$, ε_0 and κ against mean velocity spectral bandwidth of the linear equivalent system $\overline{\Lambda_v}(Hz)$ (Eq (3.49)) for the four sea-states Bretschneider ($H_{m0} = 2m$ and $T_e = 7s$), FF198310261200, FF198912070000, and FF199404240900. 84

3.24 Simulation of a heaving axi-symmetric WEC equipped with a flywheel of inertia: $\mu = 0$ (no inertia), $\mu = 5s$ (low inertia), $\mu = 25s$ (mean inertia), and $\mu = 100s$ (high inertia) in a Bretschneider sea-state ($H_s = 2m$, $T_p = 8s$). 87
3.25 Id. Fig. 3.24 in a mixed sea-state (swell: $H_s = 1m$, $T_p = 11s$, $Q_p = 5$; wind-sea: $H_s = 1m$, $T_p = 5s$, $Q_p = 2$). 88
3.26 Target spectra of the simulated sea-states in figures 3.24 & 3.25: swell (black line) and mixed sea swell/wind-sea (red line). 89
3.27 Inter-correlation function of the (centred and normalised) electrical power signals $P_{e1}(t)$, $P_{e2}(t)$ $P_{e3}(t)$ output from the flywheel with (centred and normalised) instantaneous wave energy signals $SIWEH(t)$(a) and $IE(t)$(b). 90
3.28 Simulation of an axi-symmetrical heaving buoy coupled to a short-term energy reservoir (without upper limit) in a Bretschneider sea-state ($H_s = 2m$, $T_p = 8s$, *method a*). 92
3.29 Expectation (left axis, blue line) ans standard deviation (right axis, green line) of the estimation of quality factor Φ_q obtained in 300-simulations samples of the heaving buoy with both methods a(circles) and b(stars) against simulation-length T. 93
3.30 Expectation of quality factor $\Phi_q(600s)$ (right axis, purple line) in Bretschneider target sea-states with increasing Q_p (1 to 7) estimated from 300-simulations samples of the heaving buoy; corresponding narrowness parameters ε_2 and $\varepsilon_{\dot{z},2}$ (left axis, lue and red dashed lines). 94
3.31 Groupiness statistics on power output from the reservoir against dimensionless nominal power $P_s^* = P_{nom}/\overline{P_{PTO}}$: expectation of $\Phi_{q,P_{nom}}(1200s)$(a), mean discharge lengths (log. scale)(b), and mean discharged energy (log. scale)(c). 95
3.32 Simulation of an axi-symmetrical heaving buoy coupled to a short-term energy reservoir (with $1000kJ$ energy-storage limit) in a Bretschneider sea-state ($H_s = 2m$, $T_p = 8s$, *method a*). 96
3.33 Expectation of quality factor $\Phi_q(1200s)$ against energy-storage limit $E_{max}(kJ)$ in the reservoir from 300-simulations samples in a Bretschneider target sea-state ($H_s = 2m$, $T_p = 8s$) simulated with both methods a and b. . . . 96
3.34 Estimator of quality factor $\Phi_q(1200s)$ against groupiness parameter GF_{SIWEH} of the water elevation signal in a 500-simulations sample and in a Bretschneider target sea-state ($H_s = 2m$, $T_p = 8s$) simulated with *method b*. 98

4.1 cos^{2s} distribution for $s = 1 \ldots 6$. 103
4.2 Synthetic directional wave spectrum $[m^2.s/rad]$ as the product of a Bretschneider spectrum with cos^{2s} directional distribution function for $s = 2$. 104
4.3 Power directional transfer function $[kW.m^{-2}]$ of a linearised SEAREV WEC (polar plot: frequency increases with radius); the bow is here aligned with the geographical North (0 °). 106

4.4 WWIII wave spectra (left) and unimodal model (right) near Yeu Island at two dates : 1st of January, midnight (a) and 3rd of January 2008, 12AM (b); the unimodal shapes are synthesized from Bretschneider ($Q_p = 2$) and cos^{2s} ($s = 40$) shapes. 107
4.5 Exact (blue curve) and estimated (unimodal sea-state prepresentation, red curve) mean production (kW) operated by the linear directional WEC over the two-months WWIII dataset at Yeu Island (top); relative error (%) between both figures (bottom). 108
4.6 Example of sea-state decomposition into individual wave systems, operated by SPOP (Kerbiriou et al., 2007). 110

5.1 Wave systems partitioning by steepest ascent path (or *catchment area*) algorithm*[from Hanson and Phillips (2001)]*. 114
5.2 Time evolution of peak frequency ($rad.s^{-1}$) of waves generated by a $30kn$-wind (a) and significant wave height for three wind velocities and fixed fetch (b) *[from Price and Bishop, 1974]*. 117
5.3 Swell generation zones estimated from western Europe wave data *[from Kerbiriou (2007)]*. 119
5.4 Typical peak frequency time evolution of swell ("H") and wind-sea ("M") with separation frequency ("f_s"). 120
5.5 Wave spectrum partitioning with catchment area technique (*watershed*) operated by SPOP: for a multimodal sea-state before (a) and after (b) partitions grouping; here, a swell and a wind-sea partition – both of very low energy – have been grouped to the closest respective swell and wind-sea partitions of the sea-state. 121
5.6 Example of parametric shapes (against frequency – red curves) fitting wave partitions extracted from a given spectrum with (a) and without (b) mutual influences correction; the blue and green curves respectively refer to the original and reconstructed (superposition of the fitting parametric shapes) spectral densities *[from Kerbiriou, 2007]*. 123
5.7 Peak frequency time evolution (a) of wave systems extracted by SPOP in the Bay of Biscay in March 2005; linear regressions applied to the frequency evolution of identified swells with corresponding cut-off frequencies (b) (see Gjevik et al., 1988) [The colour system is not the same in both figures]. 124
5.8 Peak direction (a) and significant wave height (b) time evolutions of wave systems extracted by SPOP in the Bay of Biscay in March 2005. 125
5.9 Estimated generation zones corresponding to the swells identified in figure 5.7(b). 125

6.1 Estimated and modelled semi-variogram. 129
6.2 WWIII control points in South Brittany (France). 130
6.3 Distribution of (time) mean significant wave height H_{m0} in South Brittany from January to May 2008. 131

6.4 Distribution of significant wave height H_{m0} (time) standard deviation in South Brittany from January to May 2008. 131
6.5 Variograms of centred and normalised significant wave height H_{m0} estimated and Gaussian-fitted in South Brittany on the 1st of January, midnight (a), 13th of January, 9AM (b), and 10th of february, midnight (c); homogeneous scatter zones highlighted in gray (d). 132
6.6 Models of covariograms related to peak frequency parameter f_p: linear (Eq. (6.11)), Gaussian (Eq. (6.12)), exponential (Eq. (6.13)), spherical (Eq. (6.14)) and extrema (default, Eq. (6.2.3)). 139
6.7 Bay of Biscay zone (1.25 °x1 °): 9 points (ARGOSS data). 143
6.8 Grouping and spatiotemporal tracking of coherent wave systems: instantaneous structures grouping (a), structures time tracking (b), vector field representation (c) with bird's eye view (d - left) and multivariable covariogram of each structure (d - right) in the Bay of Biscay. 145
6.9 Wave systems tracking by spatiotemporal correlation in the Bay of Biscay (point n°1): peak frequency (a), peak direction (b), and significant wave height (c); wind data (separation frequency and mean direction are yellow-plotted (in Fig. (a) and (b) resp.). 146
6.10 Id. Fig 6.9 for point n°3. 147
6.11 Id. Fig 6.9 for point n°5. 148
6.12 Id. Fig 6.9 for point n°7. 149
6.13 Sequence of sea-states with time tracking of space-coherent wave systems in the Bay of Biscay by $3h$ time steps on the 1st of April 2005 from midnight (a) to 3PM (f). 151
6.14 Yeu Island: 4 points (SHOM data). 152
6.15 Grouping and spatiotemporal tracking of coherent wave systems: instantaneous structures grouping (a), structures time tracking (b), vector field representation (c) with bird's eye view (d - left) and multivariable covariogram of each structure (d - right) near Yeu Island. 154
6.16 Wave systems tracking by spatiotemporal correlation in the Bay of Biscay (point n°1): peak frequency (a), peak direction (b), and significant wave height (c); wind data (separation frequency and mean direction are yellow-plotted (in Fig. (a) and (b) resp.). 155
6.17 Id. Fig 6.16 for point n°2. 156
6.18 Id. Fig 6.16 for point n°3. 157
6.19 Id. Fig 6.16 for point n°4. 158

7.1 Capture width χ_P of WEC configuration IPS4 against parameter ε_1 computed for spectra with $T_{-10} \approx 7.5s$ estimated at Figueira da Foz and analytical shape-variable Q_p-spectra. 163

8.1 3D-view of hull *DES1129* of the SEAREV WEC (a) – incoming waves arising from negative x – and simplified technical sketch (lateral view xOz)(b). 168

8.2 Instantaneous extracted energy (kJ) by the SEAREV simulated in monochromatic waves with ($\beta = 30$, right hand figures) and without ($\beta = 0$, left hand figures) incoming wave incidence, for periods $T_{exc} = 8s$(a,b), $10s$(c,d), and $12s$(e,f), and crest-to-trough wave height $2m$. 170
8.3 Re-sampling of the raw WWIII directionl spectrum at the Californian location NDBC 46063, on the 20th of January 2007, 3AM. 171
8.4 Mean power (kW) extracted by the SEAREV in monochromatic waves against wave period (left hand figures) and wave frequency (right hand figures) for three wave incidence cases: $\beta = 0$(a,b), 15(c,d), and 30(e,f); the mean power value is calculated over the whole simulation signal ($500s$ from rest position, red line) as well as over the permanent regime only (400 last seconds of the simulations, blue line). 173
8.5 California zone: buoy locations NDBC 46063 and 46069, off Santa Barbara and Los Angeles (Califorina, U.S.A.). 175
8.6 Time tracking of peak frequency (a), peak direction (b), and significant wave height (c) of wave systems extracted in January 2007 at the NDBC 46063 location, derived from the spatiotemporal coherence analysis lead on two points with linear co-variogram model ([0.6,0.3,0.1]); yellow plots stand for local wind data (separation frequency – Eq. (5.6) – in (a) and mean direction in (b)). 176
8.7 Active partition as extracted from the wave spectrum on the 20th of January 2007 at Point Conception (to be related to Fig. 8.3), corresponding frequency spectral density and directional distribution (beware, in this latter directions do not match with the actual ones due to some definition vector changings operated in the SPOP algorithm). 177
8.8 Time tracking of parameters $f_{p,sa}$ and f_p (a), $H_{m0,sa}$ and H_{m0} (b), and $P_{w,sa}$ and P_w in log. scale (c) in the nine active partitions sequences during the month of January 2007 at sea point NDBC 46063. 179
8.9 Id. Fig. 8.8 for parameters $\varepsilon_{2,sa}$ and ε_2 (a), $\varepsilon_{0,sa}$ and ε_0 (b), and κ_{sa} and κ (c). 180
8.10 Id. Fig. 8.8 for parameters $Q_{p,sa}$ and Q_p (a), and $Q_{e,sa}$ and Q_e (b). 181
8.11 Id. Fig. 8.8 for parameters Λ_{sa} and Λ (a), and $B_{w,sa}$ and B_w (b). 182
8.12 Id. Fig. 8.8 for parameters $\sigma_{f,sa}$ and σ_f (a), and $\sigma_{T,sa}$ and σ_T (b). 183
8.13 Mean power extracted by the SEAREV WEC estimated in nine wave sequences during the month of january 2007 at Point Conception (NDBC 46063) in linear (a) and logarithmic scale (b); capture width related to the global spectrum (χ_P, Eq. (3.28)) and active partition ($\chi_{P,sa}$, Eq. (8.1)) in logarithmic scale (c). 185
8.14 Mean estimated power (kW) against global omnidirectional wave power P_w (kW/m) in linear (a) and logarithmic (b) scale in the nine sequences over January 2007 at sea point NDBC 46063. 186
8.15 Capture-width χ_P against parameters Λ(a) and B_w(b). 188
8.16 Id. Fig. 8.15 against parameters Q_p(a) and Q_e(b). 188
8.17 Id. Fig. 8.15 against parameters ε_2(a) and ε_0(b). 189

8.18 Id. Fig. 8.15 against parameters σ_f(a), σ_T(b) and κ(c). 190
8.19 Capture width $\chi_{P,sa}$ against parameters $Q_{e,sa}$(a) and Λ_{sa}(b). 191
8.20 Mean estimated power (kW) against active (partition) omnidirectional wave power $P_{w,sa}$ (kW/m) in linear (a) and logarithmic (b) scale in the nine sequences over January 2007 at sea point NDBC 46063. 192
8.21 Standard deviation against mean of power estimator $\hat{P}_{PTO}$ in the SEAREV 3D-simulation sample obtained at the Californian site, and linear regression. 193

A.1 Energy spectral density of water elevation (Bretschneider spectrum) against frequency (a) and period (b). 202
A.2 JONSWAP spectra used by Rye (1977). 209
A.3 Stability of parameters ε_4(a), ε_2(b), ε_1(c), ε_0(d) and κ(e) to cut-off high-frequency (non-dimensionalised by peak frequency, in logarithmic scale) calculated on the JONSWAP spectra depicted in figure A.2. 210
A.4 Id. Fig. A.3 for parameters Q_p(a), Q_e(b), B_w(c, in Hz) and Λ(d, in Hz). 211

C.1 Examples of Q_p-spectra ($Q_p = 1, 2, 3.145, 5$) and JONSWAP ($\gamma = 3.3$) spectrum, all with $H_{m0} = 2m$ and $T_{-10} = 10s$. 220
C.2 Example of multimodal spectrum resulting from the superposition of four Q_p-spectra ($H_{m0} = 2m$ and $T_p \approx 8s$). 221
C.3 Underlying directional spectrum (a&b) corresponding to frequency spectrum of figure C.2. 222
C.4 Example of bimodal spectra resulting from the superimposition of two Q_p-spectra such that $H_{m0} = 2m$, $T_{-10} = 10s$, $\eta = 0.6$, $Q_{p1} = 1, 1.5 \ldots 4$, $Q_{p2} = 2$ and $\tau = 1.5$(a) and $\varphi = 0.4$(b). 224

D.1 Panelized heaving buoy (hull). 225

List of Tables

2.1 Nazaré site measurements characteristics. 31

3.1 Spectral characteristics of three spectra estimated off Figueira da Foz, Portugal (Saulnier and Pontes, 2006). 81

4.1 Statistics on the sea-state composition (occurrences of swells "SW" and wind-seas "WS") observed in the Bay of Biscay for year 2005 from WaveWatch III spectral data (Kerbiriou, 2007). 105

7.1 Estimation error (%) on the annual converted energy of the four WEC IPS-configurations with respect to reference figure E_{ex} $(MWh/year)$ at Figueira da Foz for long-term production estimators E_{Bret}, E_{Eps0}, E_{Eps1} et E_{Bw}. 163

7.2 Id. Table 7.1 at station K13. 164

A.1 Characteristics of the JONSWAP spectra depicted in figure A.2. 212

Chapter 1

Introduction

Among the marine renewable energies that are rising at dawn of the 21^{st}century, the colossal and unexhaustible energy carried by ocean waves is certainly the most fascinating one. The design of tidal plants and current-turbines (submerged turbines actuated by marine streams), ocean thermal energy converters or even offshore wind-turbines, among others, is focussed on a few well-defined technologies. For wave-energy converters (WECs) however, a large variety of designs and devices may be envisioned, so that the prototypes list may be still increasing as long as the fertile imagination of inventors does not wear down.

Eventhough sea and waves seem familiar to everyone, many people still have doubt about the WECs' capacity of converting energy (both kinematic and potential) from waves into electricity, whereas several principles and onshore/offshore devices already have proved them. The wave-power plant in Pico Island (Azores, Portugal, Fig. 1.1(a)) based on the oscillating water column (OWC) principle, the *Pelamis*[1] machine (Fig. 1.1(b)) tested in the Orkney Islands and the portuguese *Aguçadoura* zone, or even the O.P.T. *PowerBuoy*[2] (Fig. 1.1(c)) commissioned in many parts of the Pacific Ocean among many others, illustrate the reality of this new energy-ressource as well as the outstanding diversity of WECs.

The main issue encountered in wave-energy harnessing lies in its random and irregular nature. Wave energy varies at different time scales, from wave to wave, sea-state to sea-state, day to day, month to month, and even year to year ... The planning and development of WECs must therefore include this variability in order to supply a significant and stabilised power level to the electrical grid whatever the sea-states. To this aim, any relevant study of WEC installation must start with a preliminary statistical knowledge of the wave ressouce, characterising the energy directly convertible by the device.

[1] `http://www.pelamiswave.com/`
[2] `http://www.oceanpowertechnologies.com/`

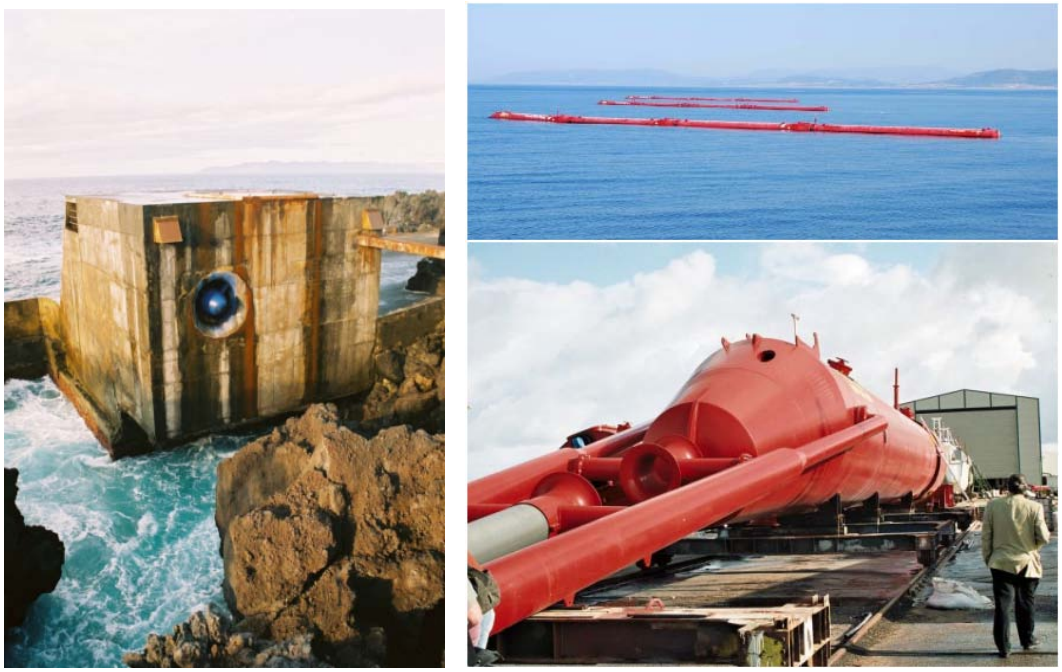

(a) (b)

(c)

Figure 1.1: Pico Island (Azores) wave-energy plant (a), articulated attenuator (wave profiler) *Pelamis* recently deployed in Portugal (b), and O.P.T. heaving *PowerBuoy* installed in the New-Jersey (c).

The thorough analysis of the oceanic wave climates undoubtedly goes back to the time when seamen started to estimate onboard the mean characteristics of the sea-state, as the significant wave height[3] – used to define the degree of sea severity – and the mean wave period of sea-states encountered on the shipping-route. Hogben and Lumb (1967) collected about a million of observations provided by several hundreds of voluntary ships and boats between 1953 and 1961. The H_s/T_m joint occurrences tables and histograms which resulted from these massive amount of data have been used for decades by navy and merchant marines.

In the frame of oil extraction offshore projects – more and more complex as oil rarefies – as well as in oceanographic research, the knowledge of the local wave-field variations had to improve continuously. In the 1960s, the first wave measurements by accelerometric buoys (see e.g. Cartwright and Smith, 1964) permitted to derive precise estimations of wave parameters through spectral analysis of the onboard recorded wave signals. Again, refined statistical tables and histograms were produced from the local (or *in situ*) measurements. Improvements on the spectro-directional description of the sea-states energy contents are continuously addressed by several authors up to the 1980s (Mitsuyasu et al., 1975; Long, 1980).

The first computers bring the first computation codes of wind-wave prediction models from wind-field data of 1st, $2^{nd}$and – above all – 3^{rd}generation, like the WAM-model (The WAMDI Group, 1988). Wave parameters are calculated by integration on the spectral contents and compared with in situ or remote-sensed estimations (buoys and satellite-altimeters, ...) in order to find out appropriate correction laws for each data source according to its degree of reliability. Since the 1990s, it is possible to accurately calculate the directional wave spectra of the sea-states almost anywhere through the oceans and seas provided that high-quality wind data are available[4] (see namely Komen et al., 1994; Ardhuin et al., 2008).

As far as the wave-energy field is concerned, the first investigations on the resource have been lead in the United Kingdom, namely by Mollison (Mollison, 1985). Then in the early 1990s, a E.U. research program (JOULE) funded by the European Commission drew recommendations and guidelines for wave-energy resource studies, and lead to the realisation of the first European wave-energy atlas *WERATLAS*[5] (Pontes et al., 1997; Pontes, 1998). This atlas is mainly based on WAM-model results validated against in situ buoy data, and provides extended annual and seasonal wave statistics in Atlantic waters along the western coast of Europe and in Mediterranean Sea (see Fig. 1.2). The statistical tables are built on global mean wave parameters such as wave height, period, direction and wave power by unit of crest length (proportional to mean energy period

[3] H_s, mean wave height (m) estimated by experienced observers, commonly related to the statistical wave height $H_{1/3}$ drawn from wave-by-wave analysis, which refers to the mean value of the highest one-third.

[4] ERA40 ocean data website: `http://www.ecmwf.int/products/data/archive/descriptions/e4/index.html`, and WaveWatch III model: `http://polar.ncep.noaa.gov/waves/wavewatch/`

[5] `http://www.ineti.pt/download.aspx?id=23D554A7272EB9BC553C12D3D78B845D`

T_e and H_s^2, in kW/m). However, eventhough this description already appear quite elaborate, it does not include more relevant wave parameters which may also influence the dynamic behaviour of WECs. To date, no existing wave-energy atlas provides such complementary wave parameters.

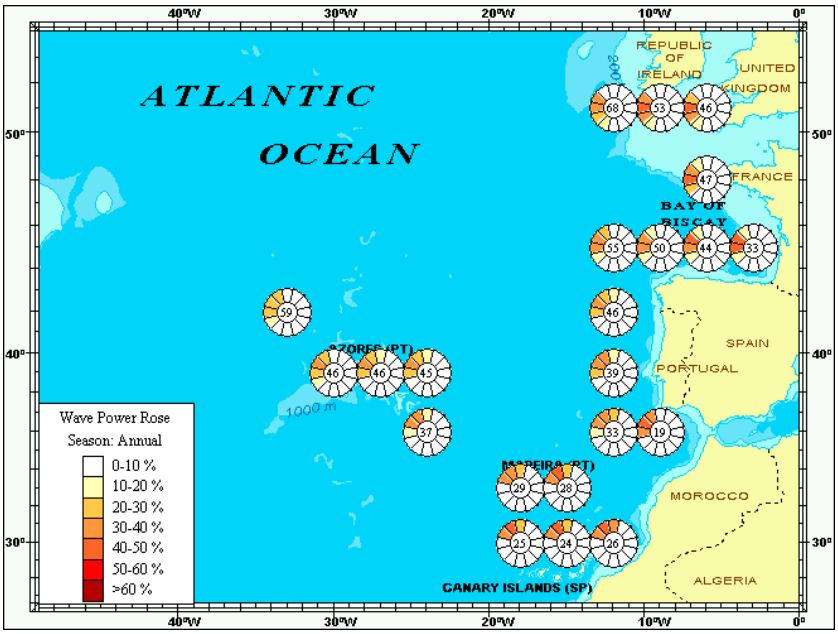

Figure 1.2: Wave-energy statistical data provided by the European atlas WERATLAS.

Though, WECs are sensitive to the groupiness of waves – as any offshore physical structure. This phenomenon is characterised by the visible succession of several waves which meet some particular energy criteria in a given wave-field. The common criterion is based on the crest-to-trough wave height, which is directly related to the energy of the wave. A sequence of high waves may cause important damages on the structures indeed, up to complete ruin sometimes – just as the Dutch Indiaman *Batavia*, which was entirely destroyed by waves after a few days, stucked in the shallows off the western coast of Australia. This is the case of offshore oil platforms, which regularly have to face rough sea-states. Historically, the concept of wave groupiness naturally appeared to improve the structures' survivability, with or without forward speed.

In the frame of WEC design, wave groupiness – beyond survivability issues – is seen in a very different way. Far from being a "harmful" aspect of the surrounding environment, it may condition the WEC's behaviour – and thus, the energy conversion – according to its capacity (*inertia*) of storing energy at short term through the power take-off (*PTO*) mechanism that is equipping the WEC (hydraulic circuit with gas accumulators, direct drive generators, air/water turbines, ...). It therefore deals with a crucial parameter for the dimensioning and design of such devices.

The behaviour of a WEC equipped with PTO mechanism(s) at an early stage of

development is generally assessed through numerical simulations and wave tank experimental models. In all cases, the characterisation of the sea-state is ensured by the knowledge of the water elevation's spectral density, as either directional ($E(f, \theta)$) or omnidirectional ($E(f)$). The spectrum describes the spatiotemporal wave process experienced by the WEC. As said hereabove, it permits to compute some global wave parameters, which are representative of the sea-state and relevant to account for the WEC's performance, such as the (integrated) significant wave height H_{m0} ($\equiv H_s$), mean energy period T_{-10} (commonly denoted by T_e) and possibly, the mean direction followed by the waves. Such a characterisation remains though incomplete for the sea-states may sometimes be composed of several superimposed wave systems (swells and wind-sea) which sometimes yield very complex spectral shapes: complementary parameters have thus to be found to account for these particularities.

Wave groupiness is a key characteristic, which permits to adequately complete the sea-state description for – as shown in next chapter – it is related to the spectral bandwidth (against frequency) of the process and, accordingly, to the sea-state's spectral shape. In the literature, several bandwidth and groupiness parameters have been introduced to this aim, with a descriptive viewpoint. The first part of this work investigates the sensitivity of WECs to these global parameters, namely in relation to their production. Several approaches are reviewed, which mostly link the groupiness phenomenon to some appropriate probabilistic or deterministic parameter (Chapter 2). Indeed, some of them apply for stationary narrow-banded wave processes (Hilbert envelope, Markov chain, ...) while others are intended for analysing non-stationary deterministic wave signals (SIWEH, Hilbert-Huang Empirical Mode Decomposition). In all cases, these methods can refer to a particular global spectral groupiness parameter or factor.

After the descriptive review on wave groupiness is completed, the work follows up by observing the relationships linking global bandwidth parameters to the mean performance of *offshore* oscillating WECs (Chapter 3). Simplified WECs are modelled (linear in the frequency domain, heaving and axi-symmetrical hulls, linear PTO model, ...) to provide a deeper understanding of the WEC performance sensitivity to the groupiness effect, or, in other words, the mean converted (or extracted) power in relation to the global spectral shape in a given sea-state. The modelled devices are assumed to be independent to wave directionality (axi-symmetrical bodies), which allows to focus on the spectral shape against frequency only. The influence of wave directionality more specifically is beyond the scope of this work. The groupiness' influence on WECs shall be assessed in both frequency and time domain, which implies the numerical estimation of deterministic mean power figures (mean power converted over the whole duration of a sea-state and quality factor in particular) to be compared or related to probabilistic values. This leads to question the wave simulation method itself, which is supposed to synthesize Gaussian random wave signals over a finite duration T: there again, spectral bandwidth has a significant role to play, as it will be shown in that chapter. Then, theoretical statistics on the instantaneous power peaks output from a linear WEC are formulated thanks to some wave groupiness method and validated against numerical

simulations. Downstream of the device, capacitive conveters (inertial PTO systems) are modelled and coupled to the linear system's output so that realistic PTO mechanisms may be easily simulated this way: instantaneous output power filtering by flywheel effect and short-term energy storage realised by a hydraulic circuit with gas accumulator and hydraulic motor. Throughout this first part, the spectral bandwidth of the water elevation is considered as global, that is, calculated on the whole frequency contents of the sea-state. However, as the mechanical structures are likely to be more sensitive to some specific frequency (and direction) intervals, a more refined sea-state description may be required in a second step.

The second part of this work is devoted to the multisystem description of sea-states, which are characterised by the superimposition of various coexisting wave systems of possibly independent origins. Accordingly, the resulting spectral densities happen to look multimodal, whose peaks denote isolated wave trains. The multisystem description therefore is much superior as it takes the physical composition of the sea-states into account, contrary to the unimodal description – widely used in naval architecture, offshore and coastal engineering –, which is nothing but a simplified representation of real sea-states observed at sea, as confirmed by in situ and remote-sensed measurements (Chapter 4). In addition, the multisystem analysis permits to better observe the sea-state time evolution in agreement with ocean physics, through the consideration of independent wave systems which may locally interact with each other (Chapter 5). Then, the wave systems tracking may be extended to spatiotemporal scale, which is implemented in this work and draws its inspiration from basic geostatistical tools (Chapter 6). Studying the sensitivity of WECs to the individual wave systems then becomes possible through the multisystem description.

The third and last part of this work focusses on the impact of the sea-state description refinements on the short- and long-term mean production of some particular WEC models. Their sensitivity to the spectral bandwidth of the most harnessable wave systems is then observed by representing sea-states: as unimodal shape-variable spectra for heaving and axi-symmetrical WECs in Portugal and North-Sea on the one hand, and as multimodal spectra for a 3D-model of the SEAREV WEC in a Californian location on the other hand.

In the end of this work, the most capital conclusions about the relevance of considering the global spectral bandwidth (wave groupiness) of sea-states as well as their possible multisystem description – through a spatiotemporal wave systems tracking approach – for the design of WECs are summarised and close the present thesis.

Part I

Identification of groupiness characteristics for the performance study of WECs

Chapter 2

Descriptive analysis of the wave groupiness phenomenon

2.1 Introduction

Groupiness is a crucial wave characteristic for the design of ships, offshore and nearshore structures. At a particular location, a train of successive high waves may have a large impact on the structures, either by exciting undesirable low-frequency resonant modes, or by continuously exerting hydrodynamic efforts that may deeply damage or even ruin them. It is the same for WECs, whose global design has to include such a characteristic as well as for the PTO systems equipping the devices. Of major interest also is the wave groupiness phenomenon in the design of WECs, not only for fatigue or survivability in extreme situations purposes, but also for the wave energy extraction optimisation in ordinary conditions, where the energy level of the sea-states is mean and the mean period close to resonance.

From previous works of Rice at the end of the Second World War (Rice, 1944, 1945), an increasing attention towards groupiness has been paid by offshore engineers and naval architects. The wave group characterisation is commonly dealt with by considering successive zero up- (*z.u.c.*) or down-crossing (*d.u.c.*) crest-to-trough wave heights exceeding a given threshold (Fig. 2.1). Such a definition is consistent for the energy of the wave is known to be directly proportional to the square of its height. In the following, it will be assumed that a "wave" in a free-surface elevation signal is defined as a portion contained within two successive zero up-crossings (i.e., z.u.c. wave heights).

The most immediate way of studying groups in wave records – when available – in view of obtaining statistics is by resorting to wave-by-wave analysis. Very often though, such records (measured by e.g. *in situ* accelerometric buoys) are not yet available. It is then necessary to draw the same information from the available related spectral contents, that is, the (omnidirectional) energy spectral density or wave spectrum $E(f)$, which is

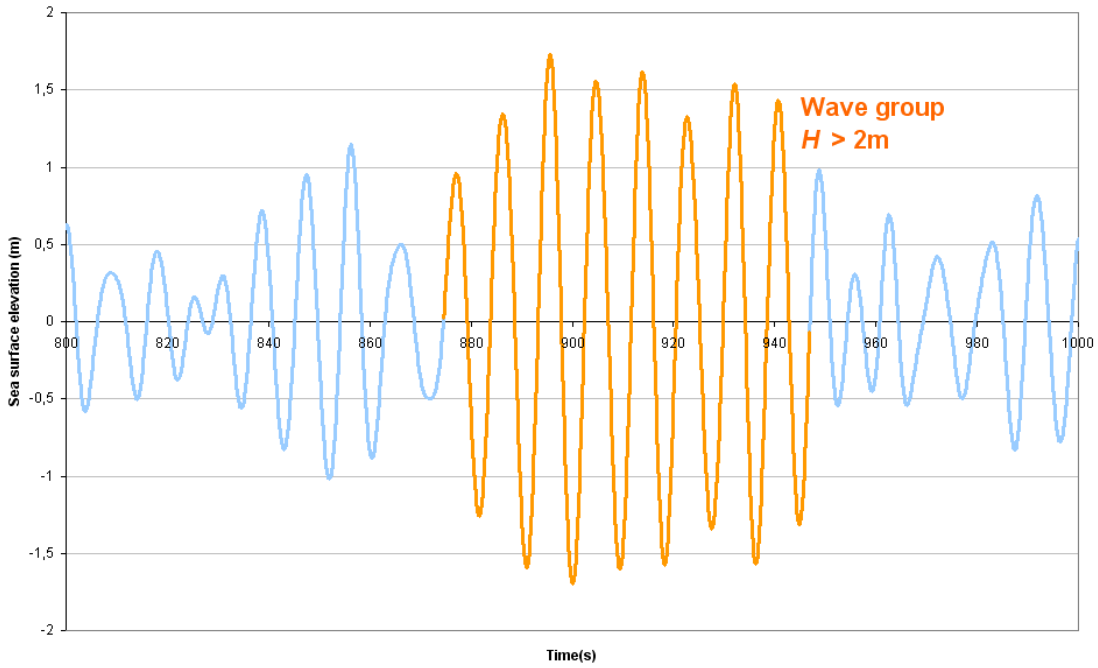

Figure 2.1: Wave group in a time series of the free surface elevation (successive zero up-crossing wave heights exceeding 2m)

usually computed onboard (Waverider/Wavec buoys equipped with Datawell softwares[1]) by spectral analysis after deletion of the time data. Assuming the wave elevation process is stationary in time, thirty or twenty minutes of recording are sufficient to estimate the spectrum as representative of the current sea-state, up to the next recording (one to three hours in general). The – quite short – raw wave data are only used to *estimate* the ongoing elevation process. It is therefore necessary to derive groupiness information from the spectrum, and this purpose has been worked on continuously from the 1970's on. Furthermore, it was shown (Tucker et al., 1984; Elgar et al., 1984) that the classical 1st order random (and Gaussian) wave model could perfectly reproduce the groupiness phenomenon observed at sea, so that the groupiness studies are not restricted to measured data only but can also be extended to numerical simulations from the estimated (or target) spectral contents.

From a certain number of investigations, which have pointed out that the groupiness of waves is more pronounced as the spectral bandwidth of the elevation process decreases (namely Goda, 1970), some spectral approaches were proposed in the litterature. The most famous of them are based on the envelope of the elevation process (Ewing, 1973; Longuet-Higgins, 1984) or start from the correlation modelling of successive wave heights (Goda, 1976; Kimura, 1980). In all cases, these theories are built upon a single spectral parameter, from which wave group statistics – like the mean group length – can be computed for the related sea-state. These were tested and validated in numerical

[1] `http://www.datawell.nl/`

simulations as well as in measured narrow-banded wave records.

Parallel to the wave height, the instantaneous wave energy has also be used as a criterion to describe groupiness. From the 1980's on, a large interest has been dedicated to the instantaneous wave energy histories, which are mostly related to the square of the elevation signal or its envelope (Hudspeth and Medina, 1988; Funke and Mansard, 1980; Thompson and Seelig, 1984). From these signals, new deterministic groupiness parameters (or factors) based on the energy variability can be obtained and compared to – probabilistic – spectral ones, under certain circumstances. Among the most recent techniques, let us cite the Wavelet method (see e.g. Liu, 2000) and the Hilbert-Huang decomposition (Huang et al., 1998; Schlurmann et al., 2002), which both can be applied on both non-linear and non-stationary processes.

This first part reviews different approaches for the description of the wave groupiness characteristics in a sea-state, among which those presented hereabove. As both the Hilbert-Huang decomposition and the Wavelet method have similar purposes, only the first one – more recent – is presented hereafter. A basic background about the computation of spectral data is given first as a preamble.

2.2 Energy spectral density and spectral moments

The ocean free surface elevation $\eta(t, x, y)$ is commonly assumed as a Gaussian, centred (i.e. zero-mean), stationary, homogeneous and ergodic random process in a space and time window ranging over a few hours and square kilometres. The autocorrelation function $R(\tau)$ of the signal $\eta(t)$ of length T defined within $[-\frac{T}{2}; \frac{T}{2}]$ at a given sea location $P(x, y)$ is calculated as

$$\begin{aligned} R(\tau) = R_{\eta\eta}(\tau) &= E[\eta(t)\eta(t+\tau)] = \overline{\eta(t)\eta(t+\tau)} \\ &= \lim_{T\to\infty} \frac{1}{T} \int_{-\frac{T}{2}}^{\frac{T}{2}} \eta(t)\eta(t+\tau)\,\mathrm{d}t \end{aligned} \tag{2.1}$$

where the bar equally denotes the time mean value and the ensemble mean $E[\cdot]$ here. This function is real and even, and so its Fourier transform $G(\omega)$ (divided by a factor 2π), which is expressed for component ω (in $rad.s^{-1}$) as

$$G(\omega) = \frac{1}{2\pi} \int_{-\infty}^{\infty} R(\tau) e^{-i\omega\tau}\,\mathrm{d}\tau = \frac{1}{2\pi} \mathcal{F}\{R(\tau)\}(\omega) \tag{2.2}$$

or, against frequency f in Hz,

$$G(f) = \int_{-\infty}^{\infty} R(\tau) e^{-2i\pi f\tau}\,\mathrm{d}\tau = \mathcal{F}\{R(\tau)\}(f) \tag{2.3}$$

as $\omega = 2\pi f$. Conversely (*Wiener-Khinchine's theorem*), we obtain

$$\begin{aligned} R(\tau) &= \int_{-\infty}^{\infty} G(\omega) e^{i\omega\tau} \, \mathrm{d}\omega \\ &= 2\pi \int_{-\infty}^{\infty} G(f) e^{2i\pi f\tau} \, \mathrm{d}f \end{aligned} \tag{2.4}$$

[Concerning the basics about definitions and operations related to Fourier transforms, convolution products, ... which are not necessarily reminded in this report, the reader can find them in any fundamental books on signal processing and applied probability, like Papoulis (1991) or Ochi (1988)].

The signal's one-sided energy (or "variance") spectral density $E(\omega)$ ($m^2.s.rad^{-1}$) is defined as

$$E(\omega) = E_\eta(\omega) = E_{\eta\eta}(\omega) = \begin{cases} 2G(\omega) & \text{if } \omega \geq 0 \\ 0 & \text{otherwise} \end{cases} \tag{2.5}$$

For the sake of commodity, symbols linked to the sea elevation signal $\eta(t)$ are not always given the indexes "$_\eta$" or "$_{\eta\eta}$", contrary to any other signal or crossed density (e.g. inter-correlation functions, ...) which are duly indexed in order to avoid confusion. Let us also stress that in this report, $E(\omega)$ refers to the estimated spectral density, whereas $S(\omega)$ is exclusively used for analytical spectral forms (like JONSWAP, Bretschneider/Pierson-Moskowitz ... presented later on). The default notation for spectra in formulae is $E(\omega)$ (or $E(f)$).

In offshore engineering, it is common to consider wave spectra against frequency in Hz (f) instead of circular frequency in $rad.s^{-1}$ (ω). The frequency spectrum – expressed in $m^2.Hz^{-1}$ or $m^2.s$ – is related to $E(\omega)$ by the relation

$$E(f) = \left| \frac{\mathrm{d}\omega}{\mathrm{d}f} \right| E(\omega) = 2\pi E(\omega) \tag{2.6}$$

The nth-order spectral moments of the spectrum (in ($m^2.s^{-n}$)) are defined as

$$m_n = (2\pi)^{-n} \int_0^{\infty} \omega^n E(\omega) \, \mathrm{d}\omega = \int_0^{\infty} f^n E(f) \, \mathrm{d}f \tag{2.7}$$

From equations (2.4) and (2.5), the variance of the elevation is easily derived as

$$R(0) = \overline{\eta^2(t)} = \int_0^{\infty} E(f) \, \mathrm{d}f = m_0 \tag{2.8}$$

The spectral moments are very precious figures, as shown in the following. They enable to formulate a large set of wave parameters quite simply, like the spectral significant wave height H_{m0} calculated as

$$H_{m0} = 4\sqrt{m_0} \tag{2.9}$$

2.3 Theory of runs for independent wave heights

Goda (Goda, 1976) established a set of statistics about the length (i.e. number of waves) of wave groups assuming the successive wave heights are statistically independent. Let p be the probability of a wave height exceeding a threshold h^* and q the probability of the same height being inferior or equal to that threshold. We then have the straightforward relation

$$p = 1 - q \tag{2.10}$$

where $q = P\left[h : h \leq h^*\right]$. Goda uses the classical Rayleigh distribution $f_{R1}(h)$ to model the wave height probability for narrow-banded processes, as

$$p = \int_{h^*}^{\infty} f_{R1}(h)\,\mathrm{d}h = \int_{h^*}^{\infty} \frac{h}{4m_0} e^{-h^2/8m_0}\,\mathrm{d}h = e^{-h^{*2}/8m_0} \tag{2.11}$$

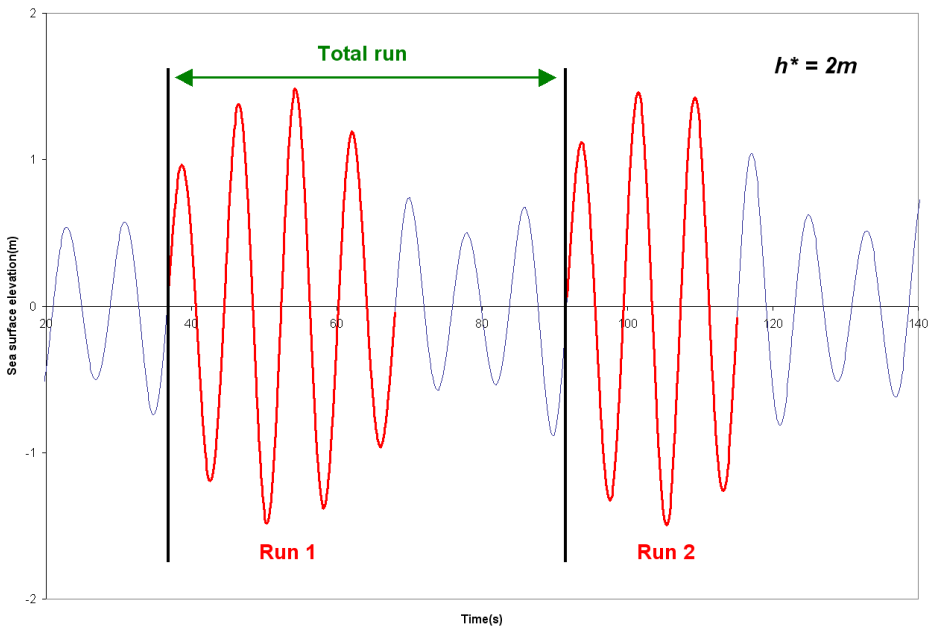

Figure 2.2: *Run* (or *high run*) and *total run* of high waves in a signal

It may be shown (see Longuet-Higgins, 1984) that the respective probabilities of a train of high waves H – *high run* – and a repetition train between two successive wave group starts G – *total run*, see Fig. 2.2) – containing j z.u.c. waves are

$$P_H(j) = p^{j-1}q \tag{2.12}$$

$$P_G(j) = \frac{pq}{p-q}(p^{j-1} - q^{j-1}) \tag{2.13}$$

The respective mean group lengths ($\overline{H}$ and $\overline{G}$) are therefore given by

$$\overline{H} = \sum_{j=1}^{\infty} jP_H(j) = \frac{1}{q} = \frac{1}{1-p} \tag{2.14}$$

$$\overline{G} = \sum_{j=1}^{\infty} jP_G(j) = \frac{1}{p} + \frac{1}{q} = \frac{1}{p(1-p)} \tag{2.15}$$

with standard deviations

$$\sigma_H = \sqrt{\overline{H^2} - \overline{H}^2} = \frac{\sqrt{p}}{q} = \frac{\sqrt{p}}{1-p} \tag{2.16}$$

$$\sigma_G = \sqrt{\frac{p}{q^2} + \frac{q}{p^2}} \tag{2.17}$$

Successive wave heights at sea actually are not absolutely independent. In addition, it was shown (Goda, 1976) that successive waves become more and more dependent as the width of the wave spectrum decreases. Goda characterises the spectral width of the sea-state with a peakedness factor Q_p expressed as

$$Q_p = \frac{2}{m_0^2} \int_0^{\infty} fE^2(f)\,\mathrm{d}f \tag{2.18}$$

which increases as the bandwidth decreases (the spectral peakedness is more pronounced).

It is widely admitted that the theory of runs for independent waves is correct asymptotically for broad-banded processes. This was namely confirmed by many authors like Elgar et al. (1984). These authors also highlight a theoretical paradox regarding the method, which models wave heights with a Rayleigh distribution under narrow-banded process assumptions whereas this latter should not be so. Numerous sea observations showed though that the Rayleigh distribution may be extended to broader processes, so that it is not physically inconsistent to use it.

2.4 Markov chain theory for successive wave heights

Sawnhey (1963) and Rye (1974) have proven the dependence of successive wave heights by analysing wave and pressure records. Rye characterises their correlation in a record with the deterministic coefficient

$$r_m = \frac{1}{\sigma_h^2(N-m)} \sum_{i=1}^{N-m} (h_i - \overline{h})(h_{i+m} - \overline{h}) \tag{2.19}$$

where N represents the total number of measured z.u.c. heights (or waves), m the number of waves (wave lag) between two considered waves, h_i the successive wave heights in the signal, $\overline{h}$ and σ_h the mean and standard deviation of the recorded heights respectively. These authors emphasize that the coefficient or correlation vanishes very rapidly as the wave lag m increases, which underlines the weak but real dependence between successive waves ($m = 1$).

2.4.1 Kimura's method

Kimura (1980) models the dependence ot two successive waves by means of a 1st-order Markov chain assuming two successive waves are correlated, but two waves separated by more than one wave are not. In other terms, $r_1 \neq 0$ and $r_i = 0$, $i > 1$ (Eq. (2.19)). The conditional probabilities of height-threshold exceedence are determined by joint Rayleigh distributions $f_{R2}(h_1, h_2)$ for two successive wave heights h_1 and h_2. Narrow-band process assumptions are made in order to consider that the heights are equal to twice the related wave amplitude (for more details, we namely refer to Longuet-Higgins, 1984).

$$p_+ = \frac{\int_{h^*}^{\infty}\int_{h^*}^{\infty} f_{R2}(h_1, h_2)\,\mathrm{d}h_1\,\mathrm{d}h_2}{\int_{h^*}^{\infty} f_{R1}(h)\,\mathrm{d}h} \qquad p_- = \frac{\int_{0}^{h^*}\int_{0}^{h^*} f_{R2}(h_1, h_2)\,\mathrm{d}h_1\,\mathrm{d}h_2}{\int_{0}^{h^*} f_{R1}(h)\,\mathrm{d}h} \tag{2.20}$$

with

$$f_{R2}(h_1, h_2) = \frac{h_1 h_2}{16 m_0^2 (1-\kappa^2)} I_0\Big(\frac{\kappa h_1 h_2}{4 m_0 (1-\kappa^2)}\Big) e^{-\frac{h_1^2 + h_2^2}{8 m_0 (1-\kappa^2)}} \tag{2.21}$$

where $I_0(\cdot)$ denotes the modified Bessel function of 1st-order defined in $\mathbb{R}_+$ as

$$I_0(z) = \frac{1}{2\pi}\int_0^{2\pi} e^z \cos\theta\,\mathrm{d}\theta \equiv 1 + \sum_{i=1}^{\infty} \frac{z^{2i}}{(2^i i!)^2} \tag{2.22}$$

and κ is a correlation parameter characterising the dependence between two successive wave heights. Such a formulation therefore includes the wave dependence. Let p_+ be the conditional probability of a wave height exceeding the threshold-level while the previous one does also. In the same way, let p_- be the conditional probability of a wave height not exceeding threshold-level while the previous one does not either. The Markov chain theory yields then the following mean group length statistics

$$\overline{H} = \frac{1}{1-p_+} \qquad \overline{G} = \frac{1}{1-p_+} + \frac{1}{1-p_-} = \overline{H} + \overline{L} \tag{2.23}$$

where L represents a train of low waves – *low run* –, that is, the number waves separating two groups (H+L=G). It is shown (Uhlenbeck, 1943; Middleton, 1960) that the correlation parameter κ is linked to coefficient r_1 by

$$r_1 = \frac{\mathrm{E}(\kappa) - \frac{1}{2}(1-\kappa^2)\mathrm{K}(\kappa) - \frac{\pi}{4}}{1-\frac{\pi}{4}} \tag{2.24}$$

where functions $\mathrm{E}(\kappa)$ and $\mathrm{K}(\kappa)$ denote the complete elliptic integrals of 1st- and 2nd-order respectively

$$K(\kappa) = \int_0^{\pi/2} (1-\kappa^2 \sin^2\theta)^{-\frac{1}{2}}\,\mathrm{d}\theta \qquad E(\kappa) = \int_0^{\pi/2} (1-\kappa^2 \sin^2\theta)^{\frac{1}{2}}\,\mathrm{d}\theta \tag{2.25}$$

2.4.2 Kimura's spectral method

The main issue one encounters when using Kimura's method for dealing with wave groups is the fact the parameter and coefficient of correlation κ and r_1 have to be estimated from the time-series. Then, a full probabilistic method is not possible anymore since wave-by-wave analysis must be resorted to. An alternative has to be found in order to work only with spectral data.

Battjes et Van Vledder (Battjes and van Vledder, 1984) proposed one such solution from previous works of Arhan et Ezraty (Arhan and Ezraty, 1978) for narrow-banded elevation processes: the deterministic correlation parameter κ can then be estimated from the spectral density $E(f)$. This spectral parameter is function of the time lag τ representing the mean time separation between two waves' starts, that is, a mean wave period such as $\overline{T} \equiv T_{01} = m_0/m_1$ or the mean z.u.c. period $T_z \equiv T_{02} = \sqrt{m_0/m_2}$. The parameter is computed as

$$\kappa = \kappa(\tau) = \frac{1}{m_0}\left|\int_0^\infty E(f)e^{2i\pi f\tau}\,\mathrm{d}f\right| \tag{2.26}$$
$$= \frac{1}{m_0}\sqrt{\Big(\int_0^\infty E(f)\cos(2\pi f\tau)\,\mathrm{d}f\Big)^2 + \Big(\int_0^\infty E(f)\sin(2\pi f\tau)\,\mathrm{d}f\Big)^2}$$

Accordingly, this new formulation was called *Kimura's spectral method* (voir Liu et al., 1993; Masson and Chandler, 1993). Elgar et al. (1984) point out yet that, since the dependence between successive waves is much likely to increase as the bandwidth decreases, the assumption of zero correlation between two waves sparated by more than one wave may not be valid anymore (i.e. $r_i > 0$, $i > 1$). Hence, the spectral Kimura's method may lack of relevance for very narrow-banded sea-states, whereas the spectral computation of $\kappa(\tau)$ (Eq. (2.26)) paradoxally yields the expected theoretical value, according to theory.

2.5 Envelope methods

2.5.1 Hilbert envelope

Instead of considering sequences of consecutive wave heights or waves, Rice (Rice, 1944, 1945), Longuet-Higgins (Longuet-Higgins, 1957) and Nolte and Hsu (Nolte and Hsu, 1972) among others, consider the envelope function of the elevation signal $\eta(t)$ as an alternative for calculating wave group statistics in a given sea-state, which is assumed – once again – to be narrow-banded. The elevation signal is classically modelled as the superposition of a large number of monochromatic and independent frequency components with random phases uniformly distributed within $[0; 2\pi]$, as

$$\eta(t) = \sum_j \eta_j \cos(\omega_j t + \varphi_j) = \Re\Big\{\sum_j \eta_j e^{i(\omega_j t + \varphi_j)}\Big\} \tag{2.27}$$

where amplitudes η_j are directly computed[2] from the (discrete) spectral density $E(f)$

$$\eta_j^2 = 2E(\omega_j)\Delta\omega_j = 2E(f_j)\Delta f_j \tag{2.28}$$

where $\omega_j = 2\pi f_j$ denotes the circular frequency corresponding to frequency f_j, and Δf_j ($\Delta\omega_j$) denotes the related frequency bin. The signal may be rewritten as

[2]Such a statement is abusive in reality, as stressed by Tucker et al (Tucker et al., 1984); amplitudes η_j actually also have to be randomly selected following a Rayleigh distribution of same variance as the spectrum's one for the considered frequency. Appendix B looks more closely at that issue in the frame of numerical simulations of the wave-field.

$$\eta(t) = \Re\{\underline{A}(t)e^{i\overline{\omega}t}\} \tag{2.29}$$

with

$$\overline{\omega} = \frac{2\pi}{\overline{T}} = \frac{2\pi}{T_{01}} = 2\pi f_{01} = 2\pi\frac{m_1}{m_0} \tag{2.30}$$

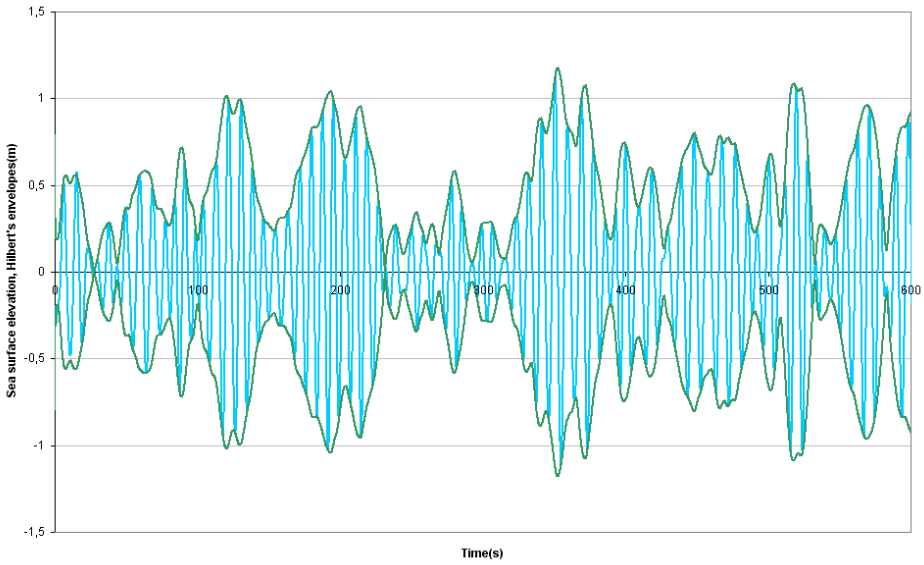

Figure 2.3: Elevation signal and related Hilbert envelope.

The Hilbert envelope function of the signal may be expressed as

$$\rho(t) = \sqrt{\eta^2(t) + \hat{\eta}^2(t)} \tag{2.31}$$

where $\hat{\eta}(t)$ is the Hilbert transform of $\eta(t)$, defined as

$$\hat{\eta}(t) = \frac{1}{\pi}P\Big[\int_{-\infty}^{\infty}\frac{\eta(s)}{t-s}\,\mathrm{d}s\Big] = \sum_j \eta_j \sin(\omega_j t + \varphi_j) \tag{2.32}$$

where $P[\cdot]$ stands for the Cauchy's principal value (see Bendat and Piersol, 1986). According to the linear formulation adopted to model $\eta(t)$ (Eq. (2.27)), such a transform boils down to introducing a $\pi/2$ phase delay in the cosine terms of the series, therefore changing cosine into sine. Figure 2.3 illustrates the Hilbert envelope $\rho(t)$ for a given narrow-banded signal, along with its symmetric for negative excursions.

As $\eta(t)$ is Gaussian (i.e. normally distributed), it is shown that the envelope function $\rho(t)$ as well as its first time derivative $\mathrm{d}\rho/\,\mathrm{d}t$ are Rayleigh and normally distributed respectively. Let ρ^* be the wave amplitude threshold level taken as half the wave height

one under narrow-banded process assumptions (i.e. $\rho^* = h^*/2$), the following expressions are obtained for the mean high run and total run lengths (voir Longuet-Higgins, 1984)

$$\overline{H} = \frac{1}{\sqrt{2\pi}}\left(\frac{\sqrt{1+\nu^2}}{\nu}\right)\frac{\sqrt{m_0}}{\rho^*} \qquad \overline{G} = \frac{1}{\sqrt{2\pi}}\left(\frac{\sqrt{1+\nu^2}}{\nu}\right)\frac{\sqrt{m_0}}{\rho^*}e^{\frac{\rho^{*2}}{2m_0}} \tag{2.33}$$

where ν is the narrowness parameter introduced by Longuet-Higgins, as

$$\nu = \sqrt{\frac{m_0 m_2}{m_1^2} - 1} \tag{2.34}$$

This author recommends that low- and high-frequency cut-off be set upon the wave spectrum – respectively at $0.5f_p$ and $1.5f_p$, with f_p as spectrum's peak frequency – when calculating that parameter, in order to limit the influence of low energetic low- and high-frequency components. In particular, the 2nd-order moments (Eq. (2.7)) makes the computation of parameter ν awfully sensitive to the high-frequency tail of the spectral density. In the following, both the filtered (ν) and non-filtered (denoted by ε_2) narrowness parameters shall be considered as two different parameters (see Appendix A). Then, if one multiplies equations (2.33) by any mean wave period characterising the sea-state (like T_{01}, T_{02}, ...), new statistics on wave groups duration (in s) may be drawn.

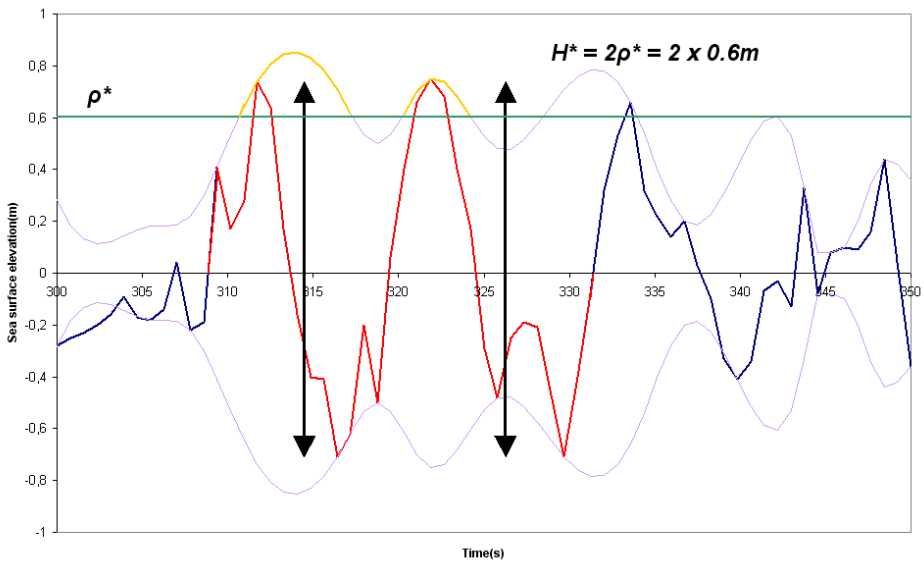

Figure 2.4: Splitting effect on the elevation signal's Hilbert envelope: a group of two successive waves (red portion of signal) is cut into two sub-groups according to the envelope.

In despite of its extreme simplicity, this method presents some important limits due to the narrow bandwidth assumption, which were pointed out by Masson and Chandler (Masson and Chandler, 1993), among others. They namely argue that, since the original wave record is not considered anymore so that the groups are tracked thanks to the envelope function, both have to be fairly correlated. Yet, practically, the wave

envelope happens sometimes to briefly exceed the amplitude threshold level ρ^* while the actual wave height does not exceed $h^* = 2\rho^*$. This may result in biased statistics on the mean group length, by adding spurious short groups and systematically over-estimating the deterministic value. Longuet-Higgins proposed a correction scheme in order to take this effect into account in the statistical analysis, which is also criticized by these authors. Besides, Masson and Chandler identify an opposite issue – not taken into account by the correction scheme – due to the fact the wave envelope sometimes happens to briefly be under the threshold while the actual wave group is still on, resulting in shorter groups than expected (splitting effect). However, they admit that the combination of both the correction scheme and the splitting effect yields satisfying results for mid-range group lengths. In the rest of the report, it will be assumed that the original version of the method is correct for most of narrow-banded processes.

2.5.2 List envelope

List (1991) proposes an alternative to the Hilbert envelope method, which is based on the filtering of the absolute value $|\eta(t)|$. Contrary to the Hilbert transform computation, this procedure permits to control the high-frequency noise of the envelope function (Fig. 2.5).

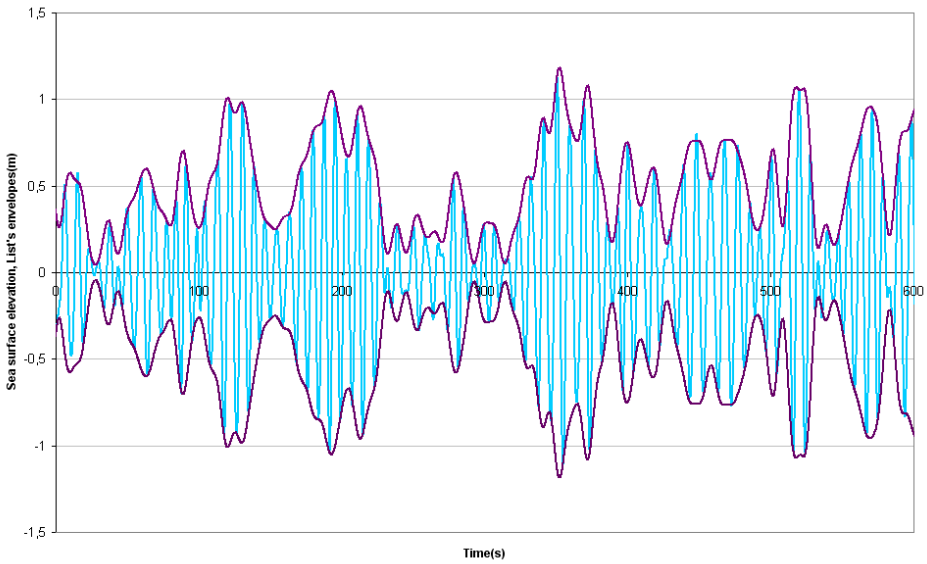

Figure 2.5: Id. Fig. 2.3 with List envelopes (List, 1991).

In addition, List introduces the groupiness factor GF_{List}, which is obtained as a variability coefficient of the envelope, and which may be somewhat similar to the SIWEH groupiness factor (see Section 2.6). It is defined as

$$GF_{List} = \frac{\sqrt{2}\sigma_{\rho_{List}}}{\overline{\rho_{List}(t)}} \tag{2.35}$$

where σ_{List} and $\overline{\rho_{List}(t)}$ respectively denote the standard deviation and mean value of the envelope function $\rho_{List}(t)$. This factor – as that of the SIWEH – takes value between 0 (sine signal) and 1, though it may be highly sensitive to filtering. For narrow-banded elevation signals, such a function becomes very close to the Hilbert's one $\rho(t)$, as figures 2.3 and 2.5 namely highlight. It can be shown (see Tayfun and Lo, 1989) that the List's groupiness factor (Eq. (2.35)) obtained for $\rho(t)$ theoretically is constant and equal to

$$\begin{aligned} GF_{Hilb} = \frac{\sqrt{2}\sigma_\rho}{\overline{\rho(t)}} &= \frac{\kappa(0)}{\sqrt{2}}\sqrt{1 + \frac{\kappa^2(0)}{16} + \frac{\kappa^4(0)}{24} + \dots} \\ &= \sqrt{2}\sqrt{\frac{4}{\pi} - 1} \\ &\approx 0.74 \end{aligned} \tag{2.36}$$

2.6 S.I.W.E.H.

In view of studying wave groups on elevation signals for wave generation in tank, a few authors like Funke and Mansard (Funke and Mansard, 1980) tried to work on instantaneous energy histories of the wave record instead of the envelope or the instantaneous wave height function defined as $H(t) = 2\rho(t)$ (see Medina and Hudspeth, 1987, 1990; Hudspeth and Medina, 1988). To this aim, they compute the S.I.W.E.H. (*Smoothed Instantaneous Wave Energy History*) as the squared elevation convoluted with a Bartlett window based on the peak period T_p, as

$$SIWEH(t) = \frac{1}{T_p}\int_{-\infty}^{\infty} \eta^2(t+\tau)Q(\tau)\,\mathrm{d}\tau \tag{2.37}$$

where $Q(\tau)$ is the Bartlett filter, defined as

$$Q(\tau) = \begin{cases} 1 - \frac{|\tau|}{T_p} & , |\tau| < T_p \\ 0 & , |\tau| \geq T_p \end{cases} \tag{2.38}$$

The groupiness factor GF_{SIWEH} is then expressed as

$$\begin{aligned} GF_{SIWEH} &= \frac{1}{\overline{SIWEH(t)}}\sqrt{\frac{1}{T}\int_0^T \left(SIWEH(t) - \overline{SIWEH(t)}\right)^2 \mathrm{d}t} \\ &= \frac{\sigma_{SIWEH}}{\overline{SIWEH(t)}} \end{aligned} \tag{2.39}$$

where T is the length of the signal and $\overline{SIWEH(t)}$ and σ_{SIWEH} the mean value and standard deviation of the SIWEH respectively. One can easily show that

$$\overline{SIWEH(t)} = \frac{1}{T}\int_0^T SIWEH(t)\,\mathrm{d}t = \sigma_\eta^2 \equiv m_0 \tag{2.40}$$

Funke and Mansard obtain GF_{SIWEH} values within [0.4;1] for a six months wave dataset in the Japan Sea. Besides, they also emphasize the fact far different groupiness regimes can be simulated from a same target spectrum $E(f)$. This is possible indeed by setting the groupiness factor to a fixed value and searching for the right phases (iterative algorithm), which are not uniformly distributed anymore. As the random Gaussian wave model requires the random selection of uniformly distributed phases within $[0; 2\pi]$, the resulting simulated process may slightly move away from Gaussian.

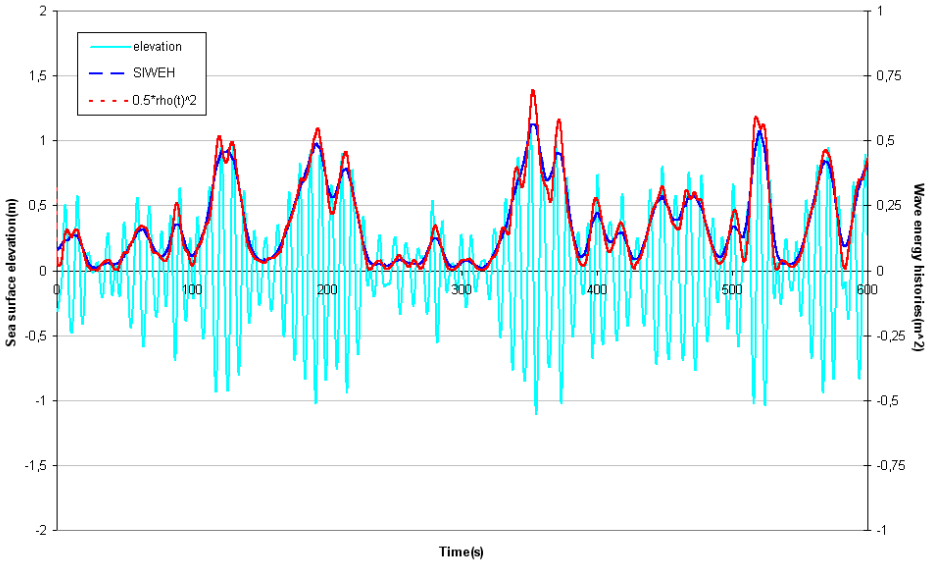

Figure 2.6: Id. Fig. 2.3 with SIWEH (Funke and Mansard, 1980) and squared envelope function $\Pi(t)$ (Medina and Hudspeth, 1990)

Hudspeth and Medina (1988) criticized however the GF_{SIWEH}'s ability to constitute a relevant groupiness factor, namely because of the filtering influence on broad-banded elevation signals. Along with List (1991), they argue that the default use of peak period T_p is not always consistent in some cases and should be reconsidered. As an example, using T_{02} ($\equiv T_z$) could be a good compromise.

Figure 2.6 depicts both the SIWEH and squared Hilbert enveloppe $\Pi(t)$ ($= \rho^2(t)/2 = H^2(t)/8$) obtained on the same elevation signal as in figures 2.3 and 2.5. Medina and

Hudspeth (Medina and Hudspeth, 1990) show that function $\Pi(t)$ exactly isolates the low-frequency components of $\eta^2(t)$, which accordingly may be compared to the SIWEH. In this figure, the plotted SIWEH is computed using T_z (wave-by-wave analysis) as reference period instead of T_p. For narrow-banded elevation processes as the one in figure 2.6, one can see that both energy signals are fairly correlated to each other.

2.7 Envelope spectra for Gaussian signals

Many authors have investigated the spectral density of (Hilbert) wave envelope for Gaussian signals, like Rice (1944, 1945), Nolte and Hsu (1972), Bendat and Piersol (1986) and Medina and Hudspeth (1990), among others. All of them were lead to analytical expressions involving the convolution term

$$\Psi(f) = \int_0^\infty E(\varphi)E(f+\varphi)\,\mathrm{d}\varphi \tag{2.41}$$

Tayfun and Lo (1989) have thoroughly reviewed the theoretical expression of even and odd powers of the envelope spectrum. In particular, they derive an exact formulation for the spectrum of $\rho^2(t)$, as

$$E_{\rho^2(t)}(f) = 8\Psi(f) \tag{2.42}$$

whereas an approached one is found only for the spectrum of $\rho(t)$, as

$$E_\rho(f) \approx \frac{4-\pi}{m_0}\Psi(f) \tag{2.43}$$

Assuming the elevation process is Gaussian – and namely modelled with random phases within $[0; 2\pi]$ – it is shown that these spectra are all monotonic and decreasing against frequency, so that their maximum value is theoretically observed at $f = 0$ (mean value). Tayfun and Lo also derive an exact expression for the SIWEH spectrum, which exhibits the same properties. Funke and Mansard (1980), however, notice a non-zero peak frequency on their own SIWEH spectra, yet while selecting phases as non-uniformly distributed.

Prevosto (1988) fits the envelope spectrum (Eq. (2.43)) with the simple exponential shape

$$S_\rho(f) = Ce^{-f/\beta} \tag{2.44}$$

where β is theoretically equal to the spectral bandwidth parameter (en Hz)

$$
\begin{aligned}
B_w &= \frac{4}{m_0^2}\int_0^\infty E^2(f)(f-\overline{f})^2\,\mathrm{d}f \\
&= \frac{4}{m_0^2}\int_0^\infty E^2(f)(f-\frac{m_1}{m_0})^2\,\mathrm{d}f
\end{aligned}
\tag{2.45}
$$

This kind of parameter is naturally suitable for monopeaked wave spectra $E(f)$, as Q_p. Both B_w and β, which is obtained by spectral fitting, represent interesting groupiness parameters for Gaussian signals.

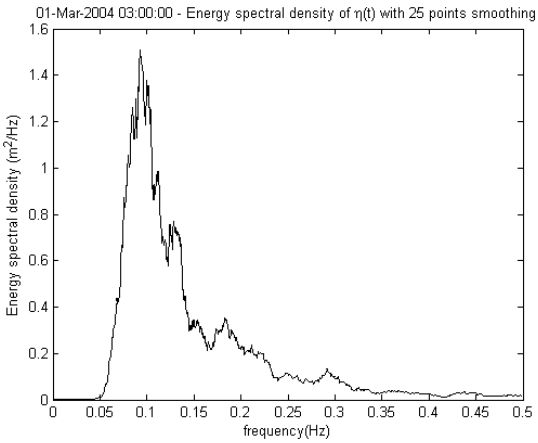

(a) $E_\eta(f)$ - 04/03/01, 3AM

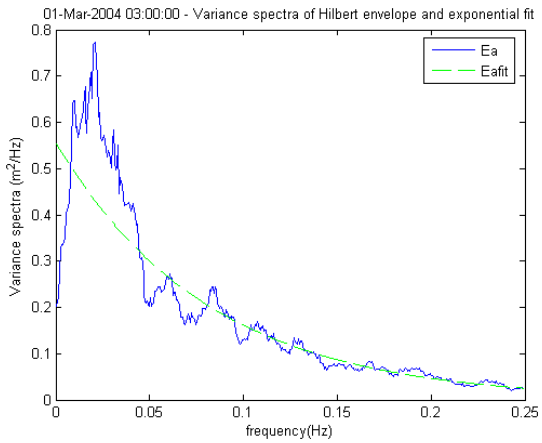

(b) $E_\rho(f)$ and $S_\rho(f)$, 04/03/01, 3AM (C=0.56 $m^2.s$, β=0.081 Hz)

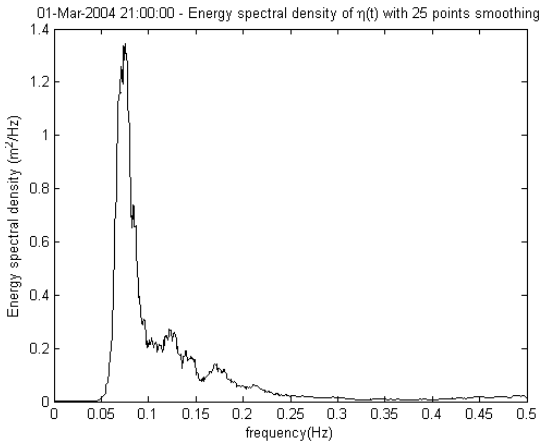

(c) $E_\eta(f)$ - 04/03/01, 9PM

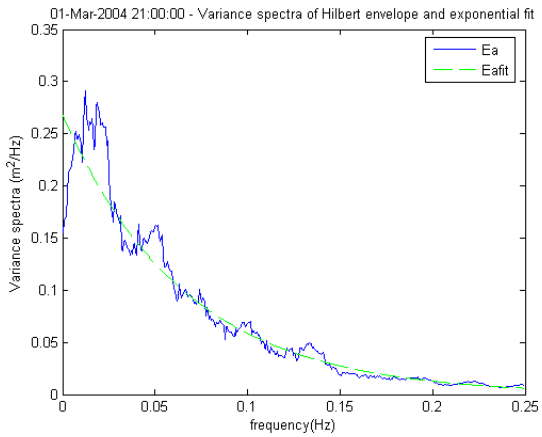

(d) $E_\rho(f)$ and $S_\rho(f)$, 04/03/01, 9PM (C=0.27 $m^2.s$, β=0.066 Hz)

Figure 2.7: Estimated spectral densities of two wave records ((a)&(c)) and the estimated and fitted spectra of the related Hilbert envelopes ((b)&(d)) at Nazaré (Portugal).

From equations (2.41) and (2.44), we have

$$C = \frac{4-\pi}{m_0}\Psi(0) = \frac{4-\pi}{m_0}\int_0^\infty E^2(f)\,\mathrm{d}f \tag{2.46}$$

This parameter (in $m^2.s$) appears to be highly correlated to the wave energy contents of the sea-state, as the integral of the squared wave spectrum divided by variance m_0. In addition, one may remark that its expression is very close to that of the equivalent spectral bandwidth Λ (see Appendix A). Parameters C and β are practically determined from the envelope's spectrum fitting (linear fit of the logarithmic spectrum) illustrated in figures 2.7(a-d), where both the wave (a&c) and Hilbert envelope's spectra (b&d) estimated for two recorded elevation signals at Nazaré (March 2004, buoy measurements) are depicted. From the envelope spectra fitting, C and β are respectively computed as the zero-frequency value and decrease exponent against frequency of spectrum $S_\rho(f)$, according to definition (2.44). The smaller β, the narrower the envelope spectrum.

2.8 Hilbert-Huang decomposition and Hilbert spectrum

Huang et al. (1998) present a new method using the Hilbert transform (Eq. (2.32)) for the spectral analysis of time series, which can be seen as a generalisation of the classical Fourier transform applicable to non-linear and non-stationary processes. According to these authors, the Fourier transform presents several drawbacks: first, it is computed for many harmonics that are not necessarily involved in the physical phenomenon under consideration, and therefore not relevant to describe it properly; second, it is valid only for signals assumed as linear and stationary. On the contrary, the Hilbert decomposition is built on the concept of instantaneous frequency, which is physically consistent as soon as the signal is narrow-banded. Any time record can therefore be decomposed into a finite sum of independent (an orthogonal) sub-signals that meet these assumptions: these sub-signals are called *Intrinsic Mode Functions* (IMF), which characterise various particular time scales of the process.

Unless Fourier harmonic components, the IMF are far of being monochromatic since they have time-varying amplitude and frequency (see Fig. 2.8). From that decomposition, Huang et al. compute the instantaneous energy distribution of the signal against frequency, which is called the *Hilbert spectrum*.

The Hilbert-Huang spectral analysis is structured in two steps. In the first step – called *Empirical Mode Decomposition* (EMD) –, the signal is decomposed into a finite number of IMF and a residue thanks to a *sifting process* based on empirical stopping criteria (the number of decompositions is infinite indeed). Any IMF must meet the following conditions:

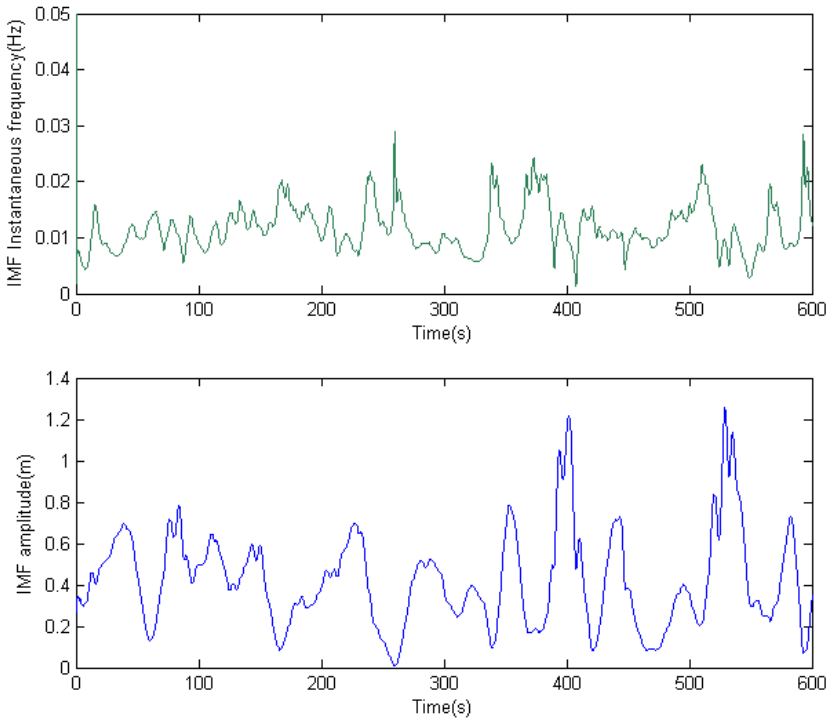

Figure 2.8: Instantaneous frequency (top) and amplitude (bottom) of an IMF.

1. in the entire signal, the number of local extrema and zero-crossings must be equal (± 1); the mean duration between two successive extrema characterises then a particular time-scale of the physical phenomenon;

2. at each instant, the sum of both the upper and lower envelopes (defined by cubic-spline fitting of the local maxima and minima) must be zero, so that both envelopes should look almost symmetric.

Any signal $\eta(t)$ is seldom likely to present all of the IMF's properties hereabove listed by itself, due to possible rapid curvature changes and high-frequency bumps. If one computes the corresponding Hilbert transform – i.e. the quadrature signal $\hat{\eta}(t)$ –, the graphical representation of its complex envelope $\eta(t) + i\hat{\eta}(t)$ will exhibit loops that do not contain the origin of the complex plane, resulting in negative instantaneous frequencies (see e.g. Stansell et al., 2004). The objective of processing an EMD is to separate the signal into various components which meet the IMF conditions (narrow-band) and whose instantaneous frequencies always are positive. Another advantage of decomposing a signal into many components is to enable a provide visualisation of the Hilbert spectrum, as shown in the following.

The *sifting process* (Huang et al., 1998; Veltcheva, 2002) is controlled by user-defined

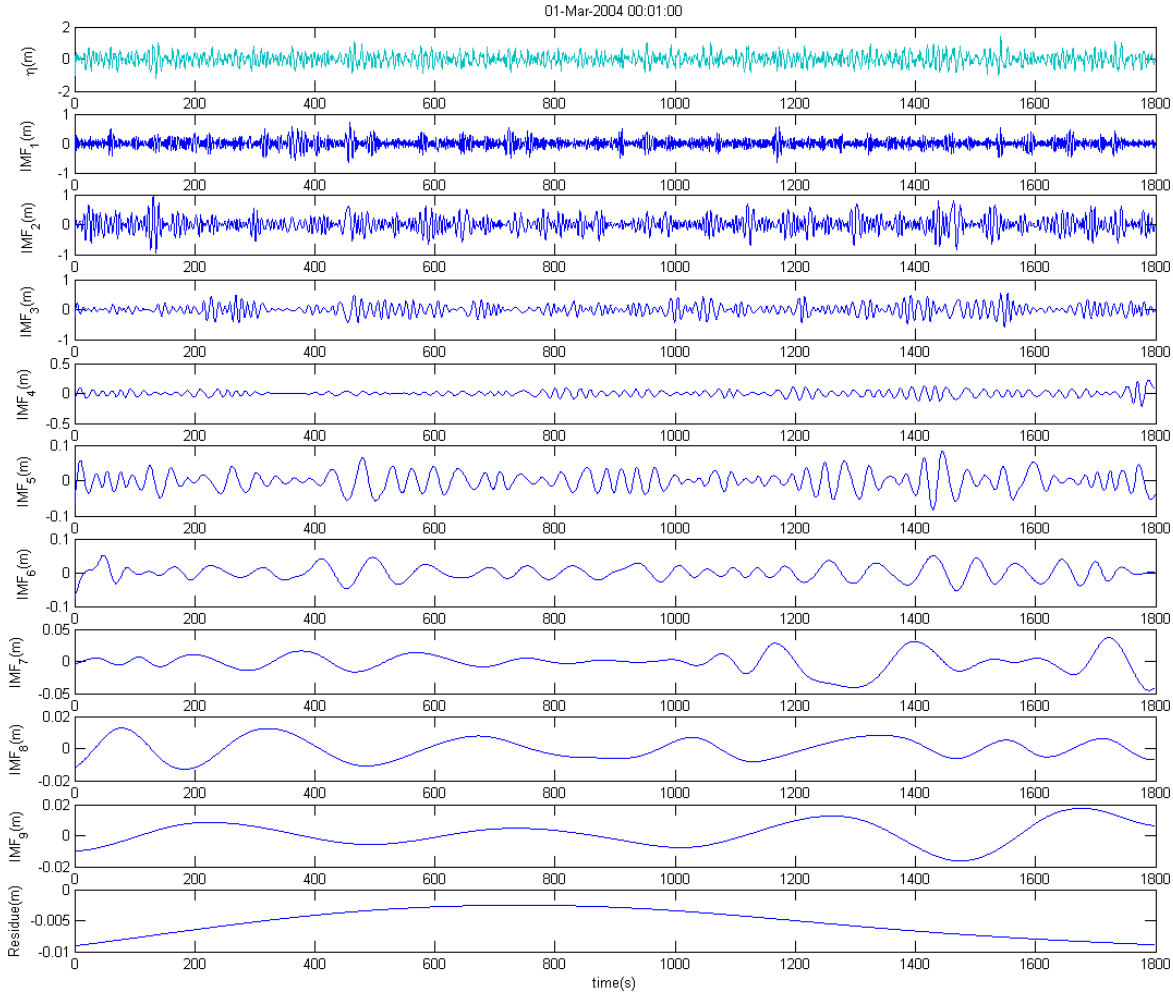

Figure 2.9: Empirical Mode Decomposition: processed input signal (top) decomposed into eight successive IMF and a residue (from top to bottom).

criteria that permit to stop the iterations as soon as the required precision is reached for each IMF, up to the residue. One such decomposition is depicted in Figure 2.9. In the end, the signal $\eta(t)$ is decomposed into n IMFs $c_j(t)$ plus a residue res and may be rewritten as

$$\eta(t) = \sum_{j=1}^{n} c_j(t) + res \tag{2.47}$$

The second step consists in calculating the Hilbert transform of each IMF $\hat{c}_j(t)$ as in equation (2.32)

$$\hat{c}_j(t) = \frac{1}{\pi} P\Big[\int_{-\infty}^{\infty} \frac{c_j(s)}{t-s}\,\mathrm{d}s\Big] \tag{2.48}$$

The complex envelope signal is then written as

$$\underline{z}_j(t) = c_j(t) + i\hat{c}_j(t) = \tilde{a}_j(t)e^{i\tilde{\varphi}_j(t)} \tag{2.49}$$

where instantaneous amplitude $\tilde{a}_j(t)$, phase $\tilde{\varphi}_j(t)$, and circular frequency $\tilde{\omega}_j(t)$ are defined as

$$\tilde{a}_j(t) = \big|\underline{z}_j(t)\big| = \sqrt{c_j^2(t) + \hat{c}_j^2(t)} \tag{2.50}$$

$$\tilde{\varphi}_j(t) = \arg\big(\underline{z}_j(t)\big) \equiv \arctan\Big(\frac{\hat{c}_j(t)}{c_j(t)}\Big) \tag{2.51}$$

$$\tilde{\omega}_j(t) = \frac{\mathrm{d}\tilde{\varphi}_j(t)}{\mathrm{d}t} \tag{2.52}$$

Hence, the original signal $\eta(t)$ may be reformulated as

$$\eta(t) = \sum_{j=1}^{n} \tilde{a}_j(t)e^{i\int_0^t \tilde{\omega}_j(s)\,\mathrm{d}s} \tag{2.53}$$

where the residue res was deliberately left out. It generally deals with high-period oscillations (and possibly highly energetic) compared to the signal's length, which are not part of the observed phenomenon. The formulation (2.53) better emphasizes the similarity with the Fourier decomposition, for which both harmonic amplitudes and frequencies are constant in time.

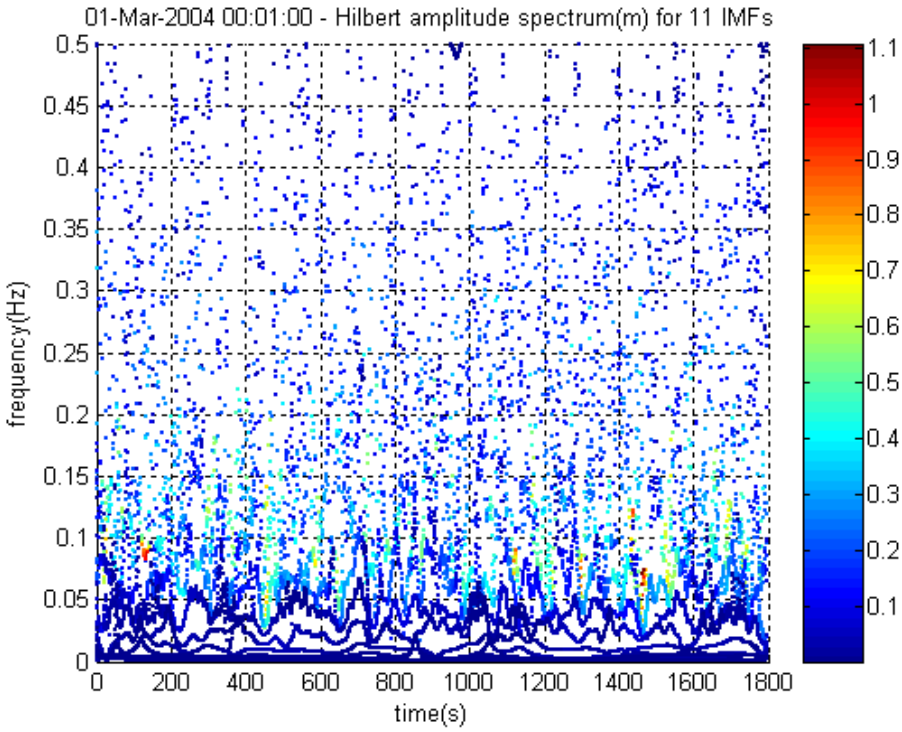

Figure 2.10: Hilbert spectrum: IMFs' instantaneous amplitude (m) against time (X-axis) and instantaneous frequency (Y-axis).

The Hilbert spectrum $\tilde{H}(\tilde{\omega}, t)$ (Fig. 2.10) represents the IMFs' instantaneous amplitude distribution against time and instantaneous frequency. Each ribbon plot refer to a particular IMF. Of course, the more the IMFs, the better the visualisation of the spectrum.

The signal's instantaneous energy density level $IE(t)$ is calculated as

$$IE(t) = \int_{\omega} \tilde{H}^2(\tilde{\omega}, t)\, \mathrm{d}\tilde{\omega} \tag{2.54}$$

This energy history permits to identify the energy variations of $\eta(t)$ in time and may therefore be compared to $SIWEH(t)$ or $\Pi(t)$ (Section 2.6). Figure 2.11 gives an illustration of wave record $\eta(t)$ and its instantaneous energy density level $IE(t)$ computed with EMD.

The marginal spectrum $\tilde{h}(\tilde{\omega})$

$$\tilde{h}(\tilde{\omega}) = \int_0^T \tilde{H}^2(\tilde{\omega}, t)\, \mathrm{d}t \tag{2.55}$$

may be compared to the wave spectrum $E(\omega)$ (based on Fourier transform) although frequencies do not have the same meaning in both representations.

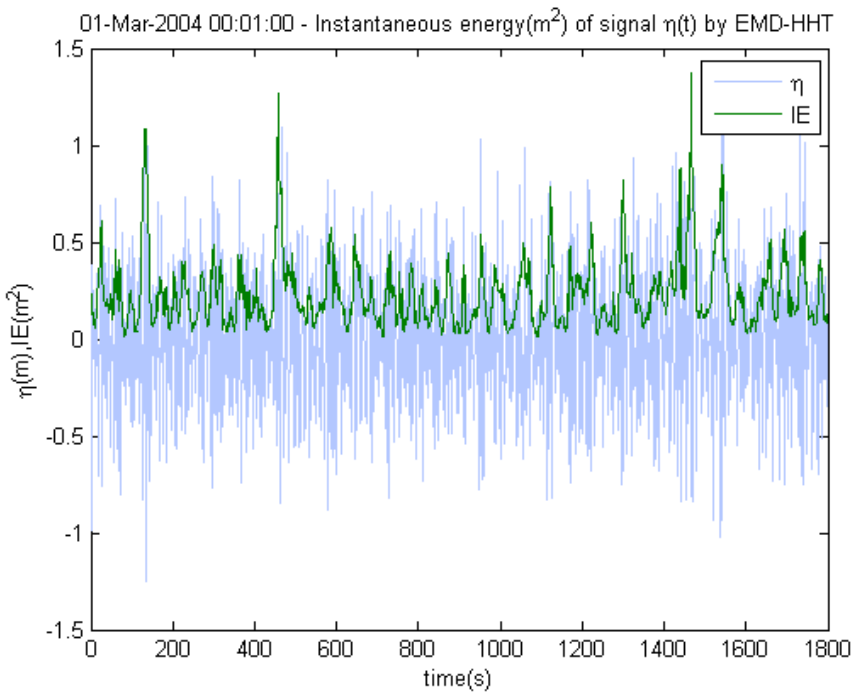

Figure 2.11: Elevation signal (light blue line) and instantaneous energy density level (green line).

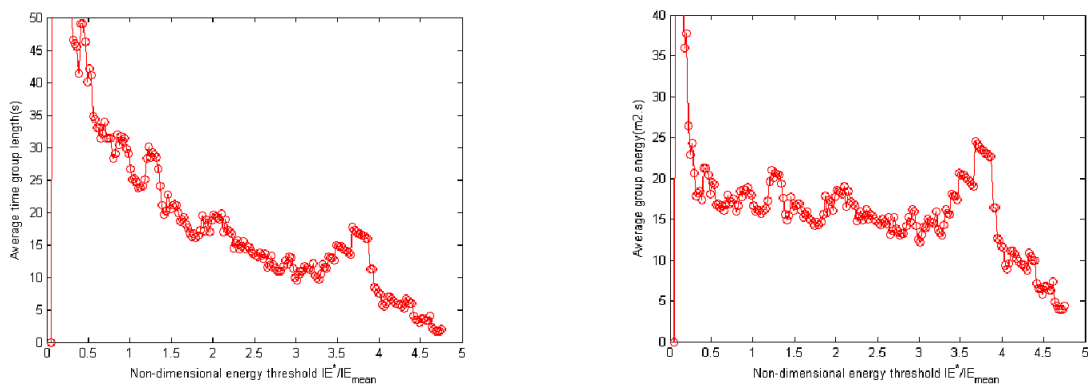

(a) (b)

Figure 2.12: Mean duration (a) and mean group energy (b) against non-dimensional energy threshold level $IE^*/\overline{IE(t)}$.

If one fixes an energy threshold level IE^* for $IE(t)$, it becomes then possible to identify portions of the wave-signal where instantaneous energy is significant (with respect to that level), which may be assimilated to wave energy groups (see e.g. Veltcheva, 2002). After, one can figure out the mean duration $\bar{t}_{gr}$ of each group as well as the energy E_{gr} contained in each group, as

$$E_{gr} = \int_{t_{gr}} IE(t)\,\mathrm{d}t = \int_{t_{gr}} \int_{\omega} \tilde{H}^2(\tilde{\omega}, t)\,\mathrm{d}\tilde{\omega}\,\mathrm{d}t \tag{2.56}$$

whose mean value $\overline{E}_{gr}$ over the signal constitutes another relevant wave group parameter along with $\bar{t}_{gr}$. This is depicted in figures 2.12(a&b) against non-dimensional energy threshold level $IE^*/\overline{IE(t)}$.

2.9 Groupiness parameters at Nazaré (Portugal)

Wave records from buoy data collected off the western coast of Portugal are processed by both spectral and temporal analysis in view of comparing the groupiness parameters drawn from both approaches.

Figure 2.13: Geographical localisation of the Waverider buoy (Nazaré, Portugal).

Table 2.1: Nazaré site measurements characteristics.

Buoy data	
Position	$[39\,°37'36'';09\,°09'13'']$
Local water depth	$\sim 50m$
Measuring system	Directional Waverider buoy
Measurements repetition	Every 3 h
Sample frequency	1.28 Hz
Recording duration	30 min
Recovery rate	99.6 % (247/248)

The Waverider buoy data consist in measurements of the local sea surface elevation by double integration of the float's acceleration. The buoy was deployed off Nazaré (Fig. 2.13) and records the water excursion every $3h$ during $30min$ at a approximately $50m$ water depth. The conditions at this site perfectly suit to an operational wave-energy farm or plant, since there is a nice compromise between wave energy level, water depth and distance to the coast (submarine cables installation, visual and noise impact...). March 2004 data inly are kept for our purpose here, whose characteristics are listed in table 2.1.

The recovery rate is quite high (> 99 %): this is why the month of March was retained here for it ensures a good observation continuity in time. At that location, the sea-states are mostly dominated by north-western swells; the estimated spectral densities therefore exhibit monopeaked looks most of the time.

For each $30min$ wave-record, the data are processed in both time and frequency domain as described herebelow:

- Wave-by-wave analysis: computation of parameters $H_s(= 4\sigma_\eta)$ (m) and T_z (s);
- Estimation of wave spectrum $E(f)$ and computation of spectral parameters (H_{m0}, T_{02}, T_{-10}, ...);
- SIWEH and related groupiness factor;
- Hilbert envelope and related groupiness factor;
- Hilbert-Huang spectral analysis.

with the following computational characteristics:

- The estimation of spectrum $E(f)$ is carried out by Fast Fourier Transform (FFT) of the elevation signal and convolution with a rectangular window (25-points moving average);

- The spectral parameters (see Appendix A for a comprehensive presentation of these parameters) are computed over the same frequency interval $[0.05Hz; 0.5Hz]$;
- Finite water-depth conditions are assumed for the calculation of wavenumbers and group celerity according to linear theory (see Eq. (2.61));
- Parameter κ is computed using mean period T_{02} as a reference for the mean correlation lag between successive waves;
- SIWEH is computed using peak period T_p as smoothing period for the Bartlett window, as originally suggested by Funke and Mansard (1980);
- The energy densities of the elevation signal's envelope ($\eta(t)$ being assumed a Gaussian and stationary) are estimated by FFT as described hereabove, and the fitting envelope spectrum $S_\rho(f)$ is calculated by linear regression of the estimated spectrum's logarithm (up to $0.25Hz$), from which parameters C and β are in turn derived.

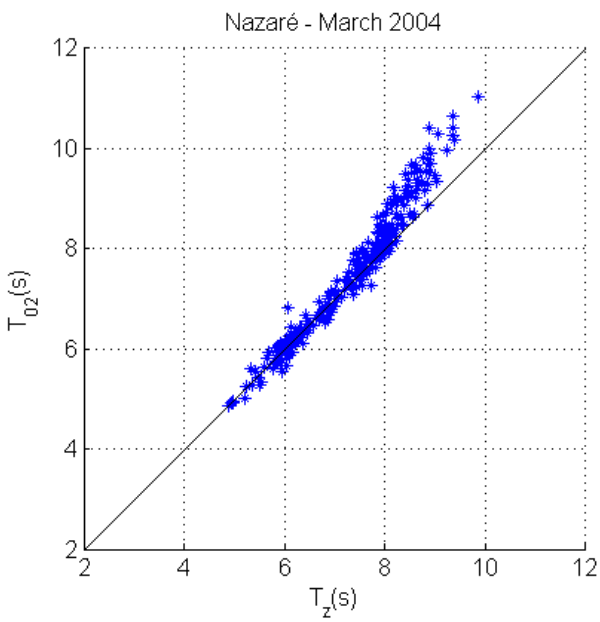

Figure 2.14: T_{02} against T_z at Nazaré (March 2004).

In figure 2.14, the period parameters T_z and T_{02} are compared to each other. T_z is estimated from wave-by-wave analysis while T_{02} is obtained from the 0th- and 2nd-order spectral moments of the smoothed spectrum. Both seem satisfactorily correlated up to a period of $\approx 8s$, from which the spectral parameter slightly overestimates the deterministic one (bias). This is possibly due to the fact T_{02} is notably sensitive to the cut-off high-frequency. If the parameter is calculated over the entire (broader) definition interval, T_{02} is found to decrease slightly, so that the bias appears for low periods where

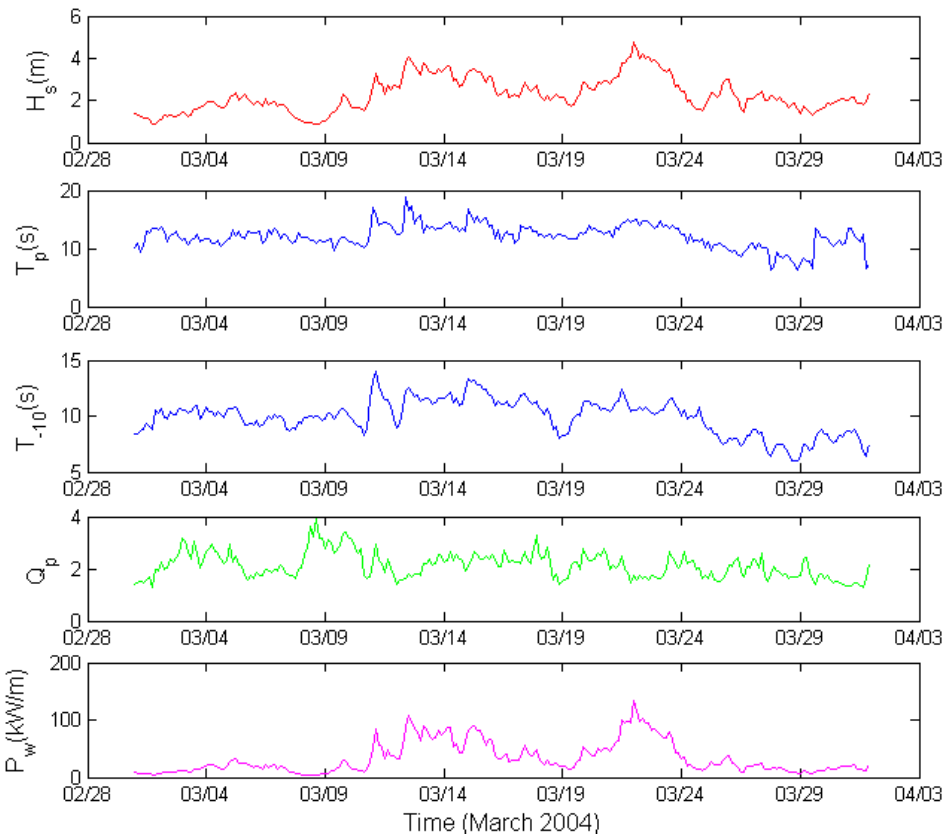

Figure 2.15: Time evolution of parameters H_s, T_p, T_{-10}, Q_p, and P_w at Nazaré (March 2004).

T_z overestimates T_{02}, while high periods are quite well correlated.

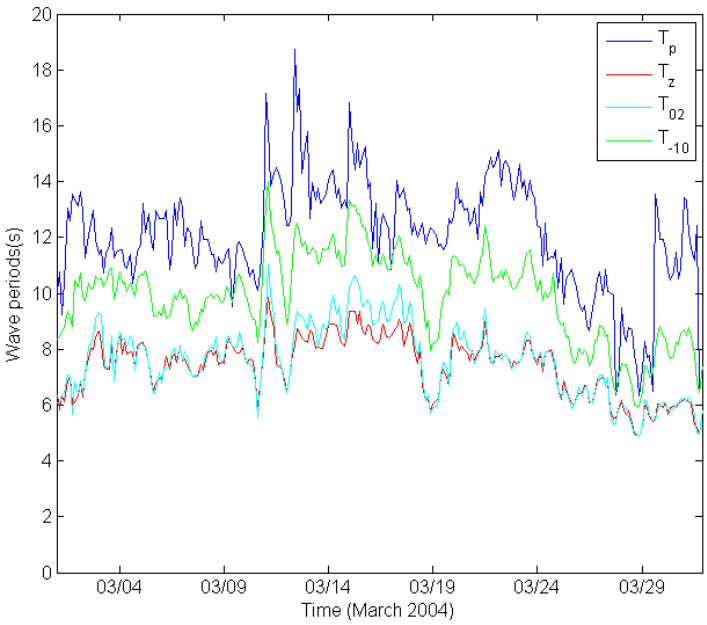

Figure 2.16: Time evolution of wave periods T_p, T_z, T_{02} and T_{-10} at Nazaré (March 2004).

Figure 2.15 illustrates the evolution of the main wave parameters throughout the month of March 2004, namely the significant wave height H_s, peak period T_p, mean energy period T_{-10}, Goda's peakedness factor Q_p and energy flux by unit of wavefront (or omnidirectional wave power) in finite water depth P_w, calculated as (Mollison, 1985)

$$P_w = \rho g \int_0^\infty c_g(f) E(f)\, \mathrm{d}f \tag{2.57}$$

where $c_g(f)$ denotes the group celerity of waves ($m.s^{-1}$) corresponding to frequency f, and commonly expressed in $kW.m^{-1}$. It is defined as

$$c_g = \frac{\mathrm{d}\omega}{\mathrm{d}k} \tag{2.58}$$

and computed thanks to the *dispersion equation* drawn from linear theory

$$\omega^2 = gk \tanh(kh) \tag{2.59}$$

Hence, for given circular frequency ω and water depth h, this yields

$$c_g(\omega, h) = \frac{\omega}{2k}\left(1 + \frac{2kh}{\sinh(2kh)}\right) \tag{2.60}$$

$$= \frac{c_\phi}{2}\left(1 + \frac{2kh}{\sinh(2kh)}\right) \tag{2.61}$$

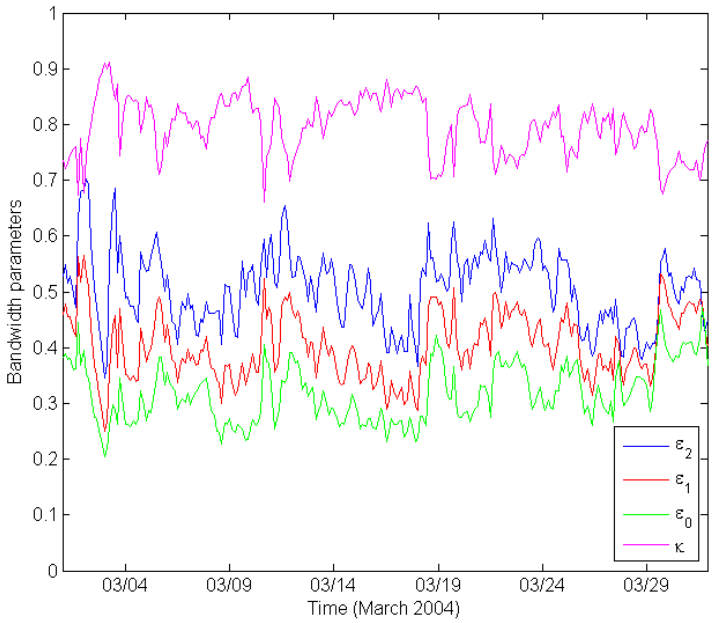

Figure 2.17: Time evolution of spectral parameters ε_0, ε_1, ε_2 and κ at Nazaré (March 2004).

where $c_\phi = \omega/k$ is the phase (or crest) celerity of waves.

As stressed hereabove, the spectral computation of parameters as Q_p is licit since monopeaked spectra are mostly observed at the considered location. Moreover, the estimated energy densities are smoothed with a 25-points moving average, that is 2×25=50 degrees of freedom, so that the bias on the computation of Q_p is significantly reduced. The figures highlight two major energetic events around the $13^{th}$and $23^{rd}$of March, where H_s exceeds $3.5m$ and P_w reaches $100kW/m$. An important variability is also noticed for parameters Q_p (1.3 to 3.9) and P_w (4 to $134kW/m$) although both do not seem to be correlated anyhow. The evolution of mean periods T_p, T_z, T_{02} and T_{-10} are given in figure 2.16, where the correlation of parameters T_z and T_{02} is well identified, especially for the lowest values.

The evolution of spectral parameters ε_0, ε_1, ε_2 and κ is illustrated in figure 2.17. The ε-type parameters are small when the bandwidth is narrow, wheread the correlation parameter κ must be high; this is well observed in the figure. It is also manifest that the ε-type parameters – moreless correlated to each other – follow similar fluctuations, which are found to be larger for ε_2.

The scatter plot in figure 2.18 depicts these three parameters against κ and shows that the best correlation is observed for ε_0. A clear correlation is quite observable for each parameter however, namely because the sea-states are mostly monopeaked here. It may be expected that in case of more complex sea-states (multimodal seas), the cor-

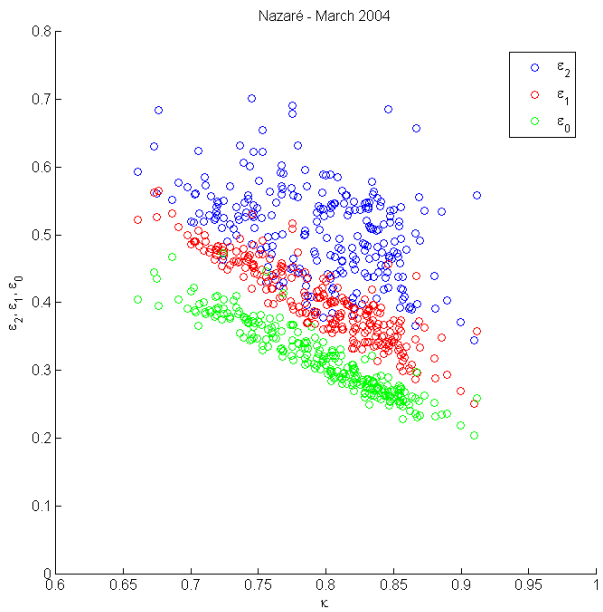

Figure 2.18: Parameters ε_0, ε_1, and ε_2 against κ at Nazaré (March 2004).

relation with κ may be less marked. Parameters B_w and β are compared to each other in figure 2.22; they show a certain agreement with a bias for the weakest bandwidths though: let us remark both parameters should match only if the estimated wave spectra followed the exponential shape defined by Prevosto (1988), which is apparently not the case in Nazaré when bandwidth is low. Let us also invoke the possible distorsion due to the fitting technique of the envelope spectra.

In view of observing the links between groupiness parameters in both frequency and time domain, a particular focus is made on parameters B_w, β, C, GF_{Hilb} (Eq. (2.35)&(2.36)), GF_{SIWEH} (Eq. (2.39)), GF_{Π} et GF_{IE} (id. GF_{SIWEH} for $\Pi(t)$ and $IE(t)$ respectively), whose time evolution is illustrated in figure 2.19. We namely notice that:

- B_w and β are very correlated to each other, with more variability for B_w;
- factor C is quite correlated to parameters H_s and P_w (see Fig. 2.15) as expected according to equation (2.46);
- groupiness factor GF_{Hilb} is found to oscillate around its theoretical value (~ 0.74, Eq. (2.36));
- factor GF_{Π} is also found to oscillate around its theoretical value (=1, according to the expressions of envelopes mean value derived by Tayfun and Lo, 1989);
- factors GF_{Hilb} and GF_{IE} seem quite correlated to each other.

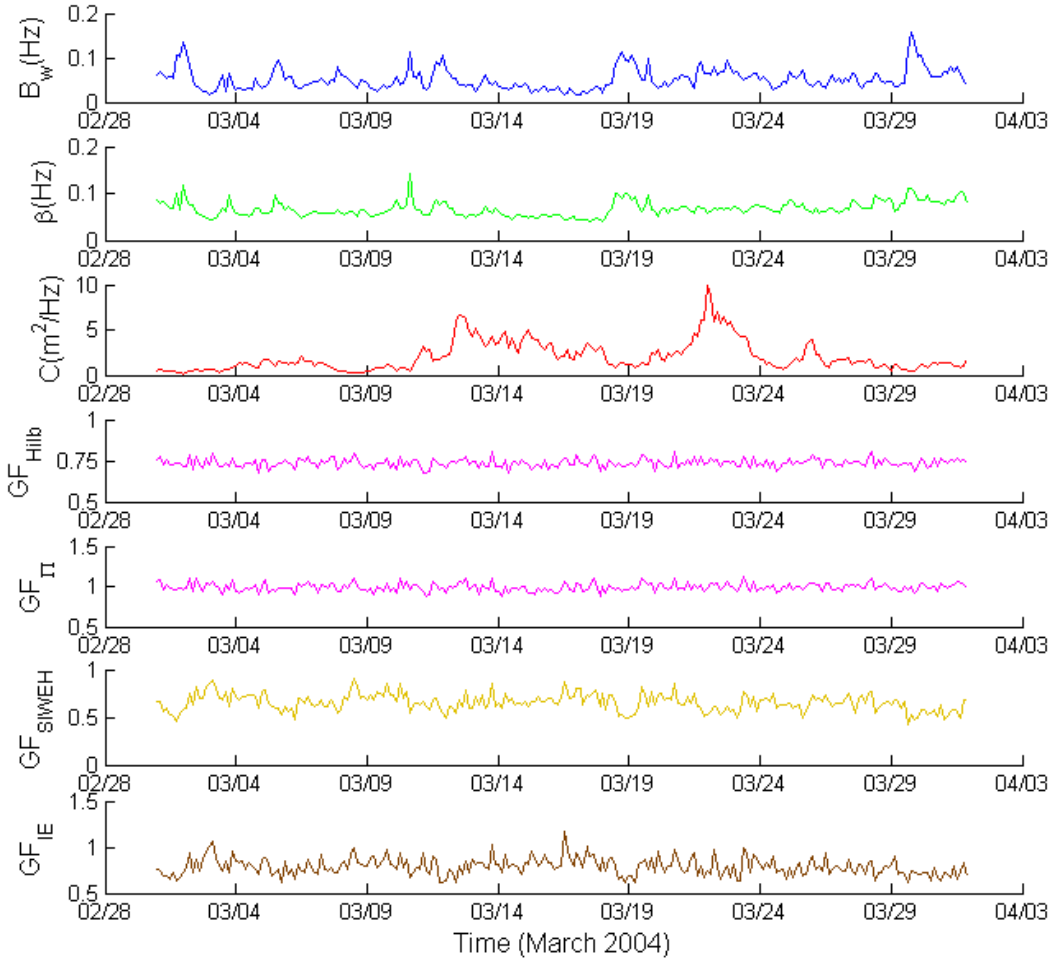

Figure 2.19: Time evolution of groupiness parameters B_w, β, C, GF_{Hilb}, GF_{Π}, GF_{SIWEH} and GF_{IE} at Nazaré (March 2004).

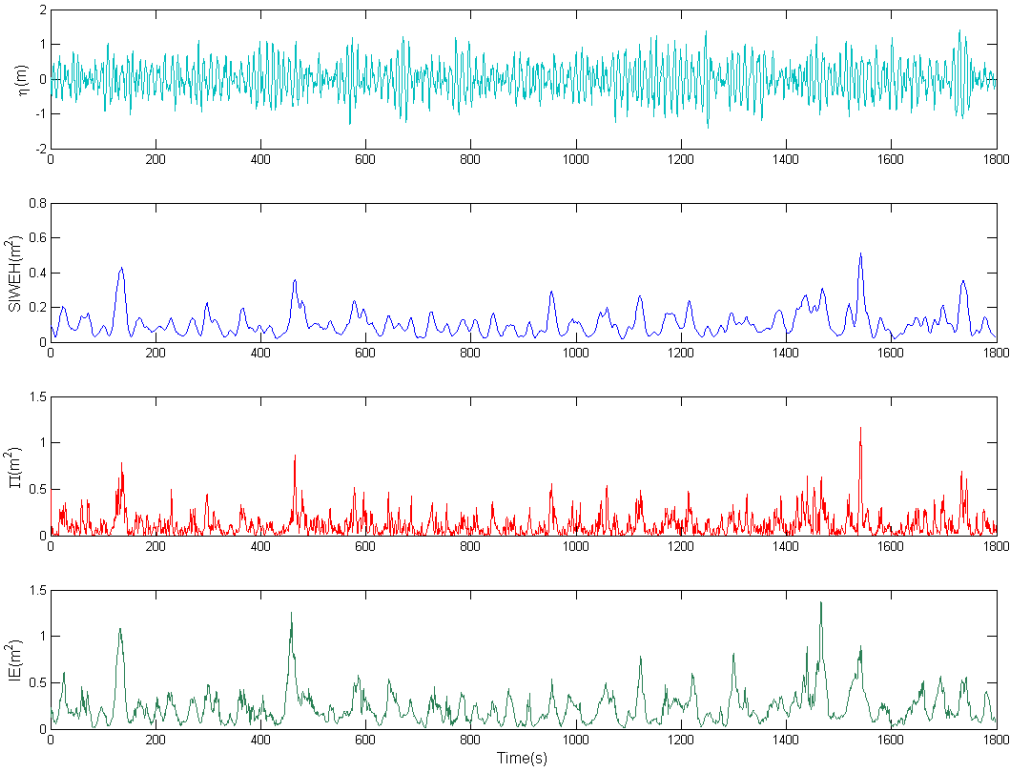

Figure 2.20: Signals $\eta(t)$, $SIWEH(t)$, $\Pi(t)$, and $IE(t)$ obtained at Nazaré on the $1^{st}$of March, midnight).

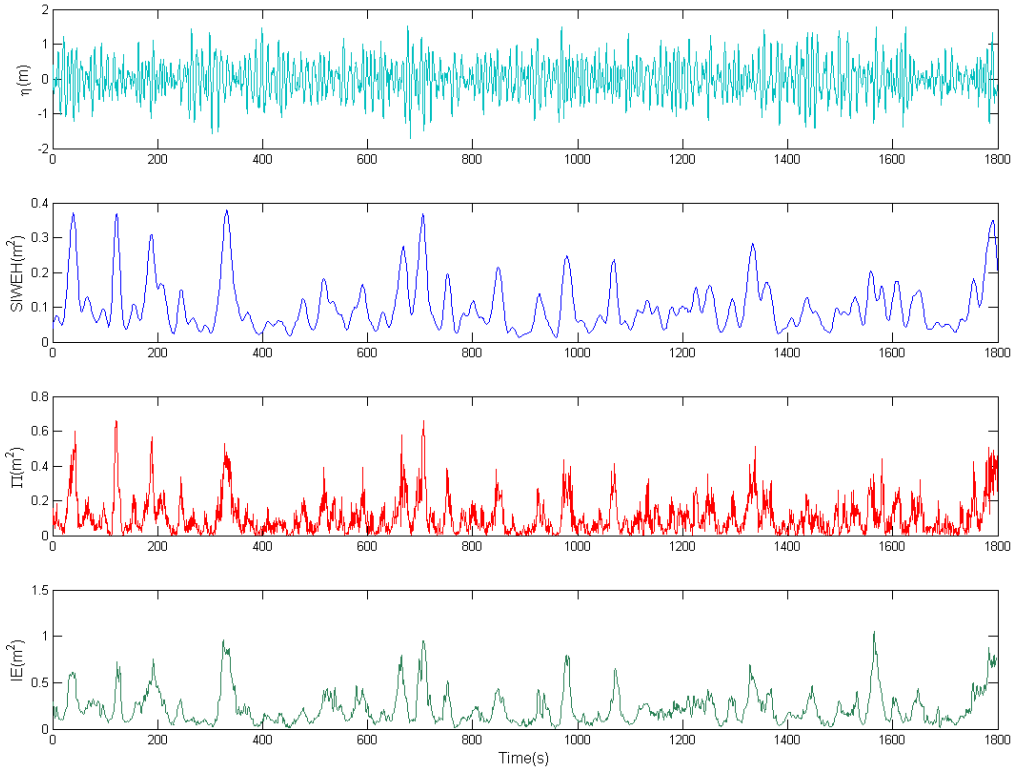

Figure 2.21: Signals $\eta(t)$, $SIWEH(t)$, $\Pi(t)$, and $IE(t)$ obtained at Nazaré on the $3^{rd}$of March, 9AM).

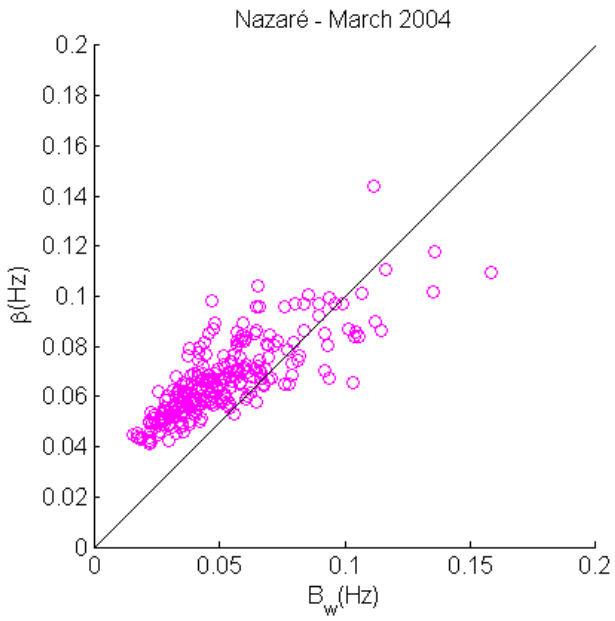

Figure 2.22: Factor β against B_w at Nazaré (March 2004).

Groupiness factors GF_{Hilb} and GF_{Π} do not seem to be very interesting parameters for their value is a priori fixed by theory (see for instance Eq. (2.36)). The variations they exhibit are therefore due to a default of stationarity and/or Gaussianity of the measured processes. On the contrary, groupiness factors GF_{SIWEH} and GF_{IE} exhibit more variability. Figure 2.23 compares both factors to each other, which emphasizes their similarity (with a bias).

Figures 2.20 & 2.21 show the time evolution of signals $\eta(t)$, $SIWEH(t)$, $\Pi(t)$, and $IE(t)$ simultaneously for two particular measurements: on the $1^{st}$of March, midnight, and on the $3^{rd}$of March, 9AM. At both dates, it is easy to see that signals $SIWEH(t)$, $\Pi(t)$ and $IE(t)$ are well correlated, as detecting the same significant wave groups. $\Pi(t)$ show more noise since it is linked to the square of the Hilbert envelope function. The less noisy signal is $SIWEH(t)$, because of the Bartlett filter. Signal $IE(t)$ however introduces a different sensitivity to wave groups, namely to the most energetic ones. Indeed, the energy peaks between two groups are not identified in the same way: $IE(t)$ may isolate two groups of equivalent intensity when both $SIWEH(t)$ and $\Pi(t)$ discriminate one of the two groups, and conversely. Accordingly, it can be said that the Hilbert-Huang spectral analysis may bring – through the calculation of $IE(t)$ – an alternative way of identifying wave groups in wave records from the instantaneous wave energy history.

Figures 2.24 & 2.25 compare the values of spectral parameters ε_0, κ, Q_p and B_w to groupiness factors GF_{SIWEH} and GF_{IE} respectively. It is then established that a clear correlation exist, which is even more pronounced for factor GF_{SIWEH}. Let us remind that $SIWEH(t)$ is a priori smoother than $IE(t)$ due to the moving-average filtering.

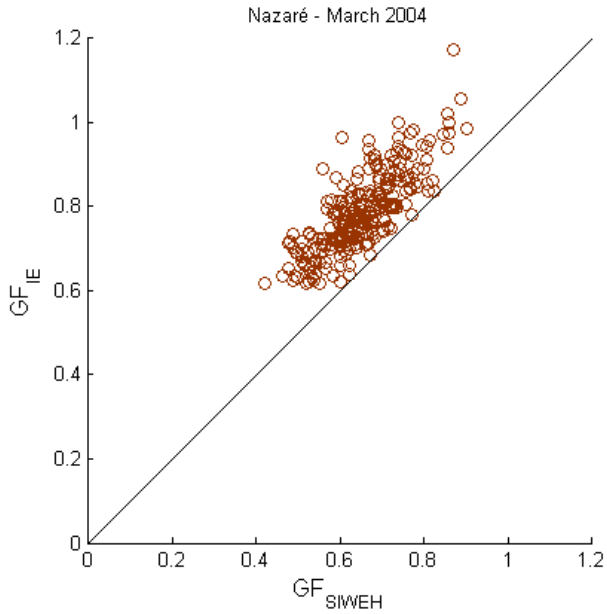

Figure 2.23: Factor GF_{IE} against groupiness factor GF_{SIWEH} at Nazaré (March 2004).

This illustrates how the groupiness of waves observed in wave records may be related to bandwidth (or narrowness, peakedness...) properties of the corresponding estimated spectral density $E(f)$. In particular, a nice correlation is found for some parameters such as ε_0 and κ – which are themselves quite correlated to each other here. Let us recall the elevation process is estimated here with 50 degrees of freedom and the occurring sea-states are mostly monopeaked. The estimation of parameters such as Q_p or B_w (see Appendix A) is licit and hardly subject to numerical biases. However, the obtained results do not seem to exhibit any correlation between wave energy level and groupiness/spectral bandwidth characteristics (Fig. 2.15&2.19).

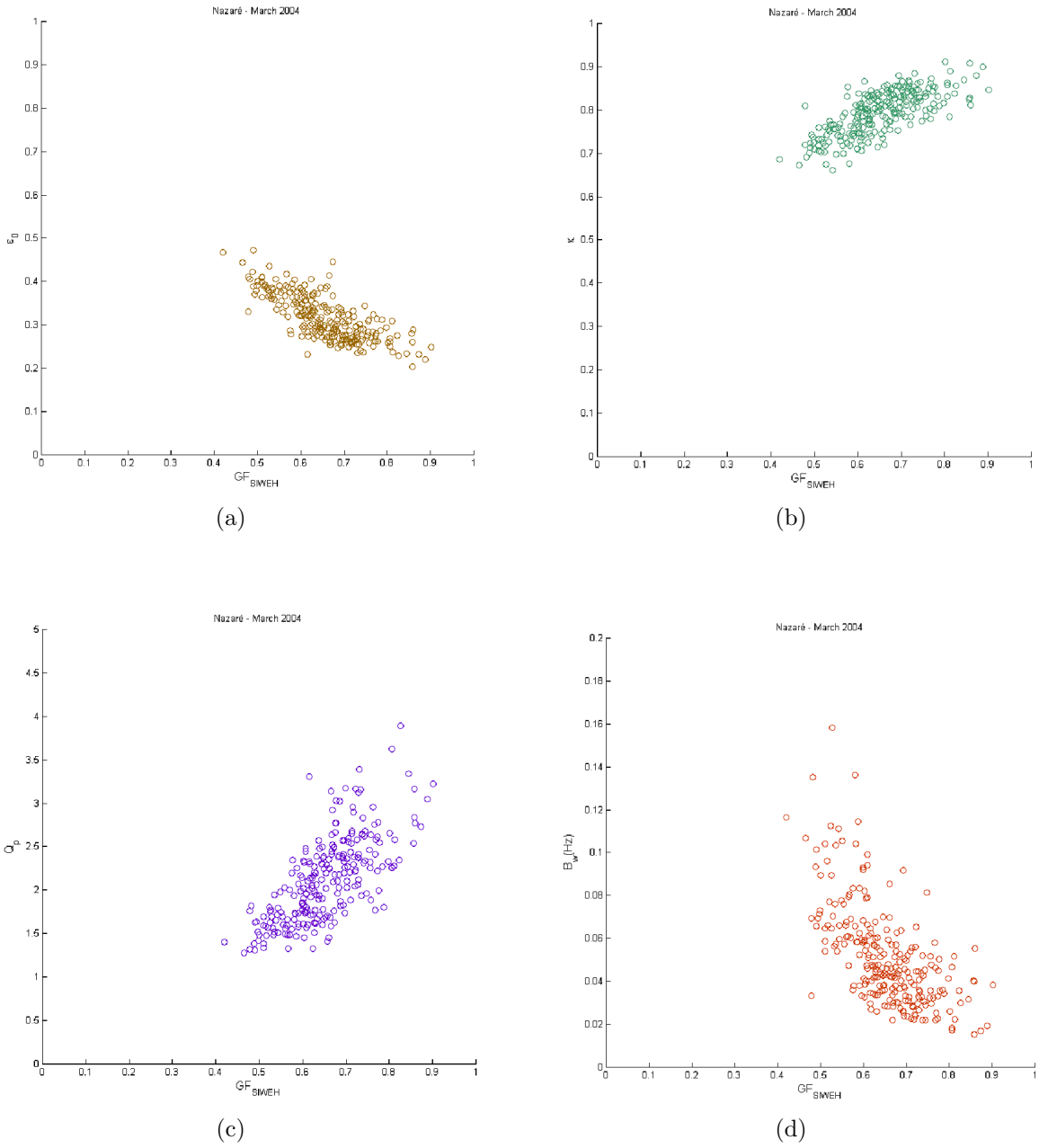

Figure 2.24: Spectral parameters ε_0 (a), κ (b), Q_p (c) and B_w (d) against groupiness factor GF_{SIWEH} at Nazaré (March 2004).

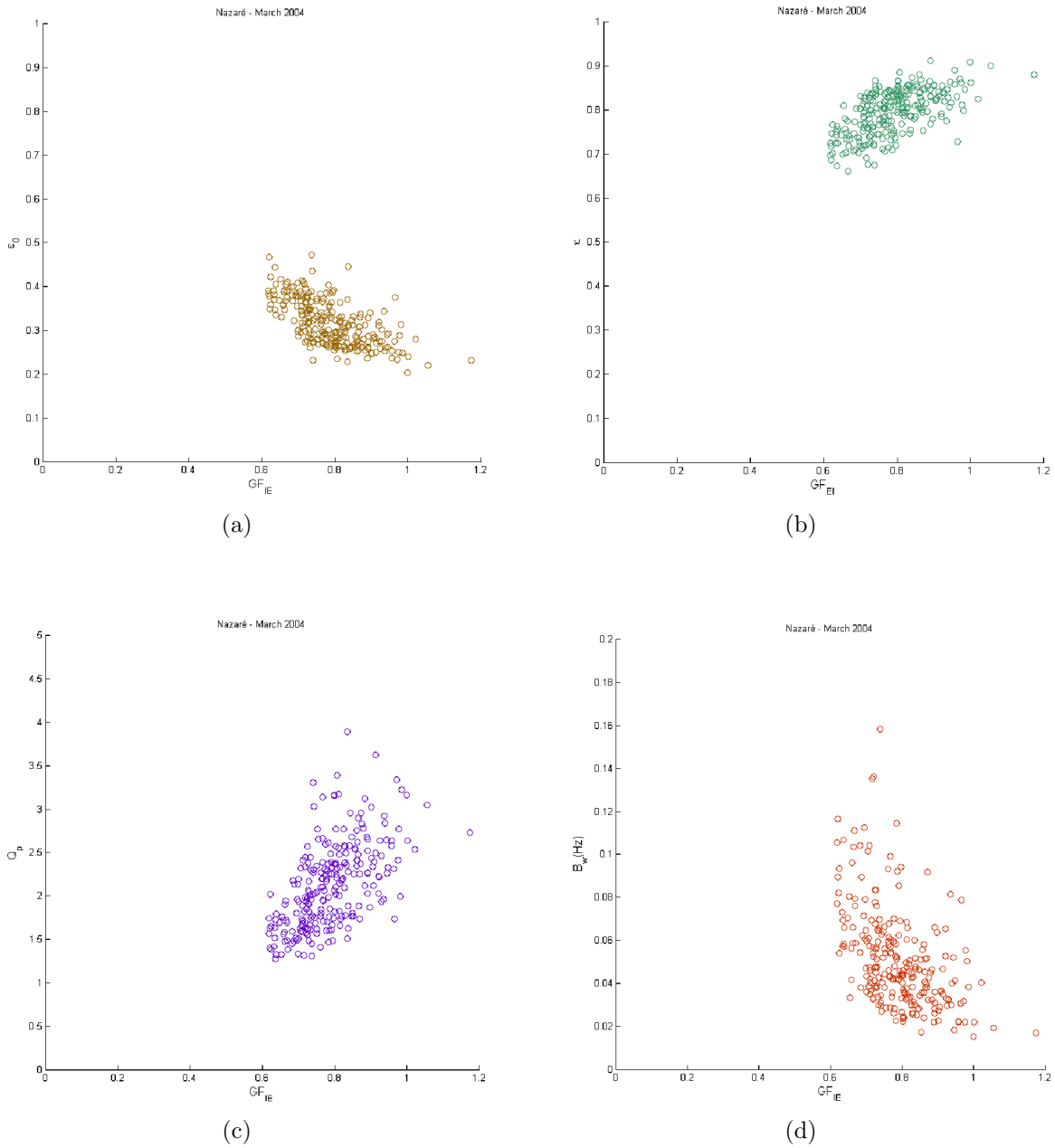

Figure 2.25: Spectral parameters ε_0 (a), κ (b), Q_p (c) and B_w (d) against groupiness factor GF_{IE} at Nazaré (March 2004).

2.10 Conclusion on the wave groupiness spectral characterisation

This first chapter permits to underline the theoretical and practical links existing between the groupiness phenomenon and the spectral bandwidth of wave spectrum, whatever the method (successive wave heights, envelopes, instantaneous wave energy histories, ...).

Appendix A reviews the main groupiness and bandwidth parameters that were proposed in the literature so far – some of them having been already introduced in the present chapter. Nine parameters are therefore introduced: the appendix exposes the origins of each parameter, its formulation(s), as well as the practical limits encountered in their numerical computation, like the smoothing effect on the parameter estimation. Indeed, it is shown that the computation of parameters like Q_p is systematically biased when lead on estimated spectral densities (influence of the estimates' precision, as *degrees of freedom*), whereas that of the spectral moments m_n is not. Moreover, a stability study is presented following previous investigations of Rye (Rye, 1977), which stresses the sensitivity of each parameter to cut-off in the high-frequency tail. It is notably emphasized that "ε" parameters are quite unstable except ε_0, while the other parameters exhibit a good stability.

Chapter 3

Global spectral shape and mean power extraction of WECs

3.1 Introduction

The present chapter is focussed on the relation between the global spectral shape of sea-states and the mean production of an offshore WEC figured by its mean output power. It namely aims at showing – using various simplified dynamic models like axi-symmetric heaving point absorbers here – how the behaviour of such systems is influenced by spectral shape variations, which are summarised through a set of three characteristics: *energy* (as m_0 or $H_{m0} \equiv H_s$), *mean period* (as $T_{-10} \equiv T_e$, T_z or T_p), and *spectral bandwith/wave groupiness* (see Chapter 2 and Appendix A).

First, a straightforward theoretical approach is lead in the frequency domain (stochastic modelling of linear systems) in order to emphasize the fact spectral bandwidth variations – while energy and mean period are kept fixed – are not sufficient to account for the WEC production variability, but only approximately depending on the proper dynamic response of the body (mechanical impedance or *transfer function*). This is illustrated on a simple heaving WEC with various impedances standing for various sensitivities in sea-states observed at two different locations (Portugal and North-Sea). Then, the Hilbert envelope theory for narrow-banded Gaussian processes is applied to the output signals of a linear system (heave motion and velocity here) and used to derive mean group statistics on the peaks of instantaneous power extracted from waves.

When the numerical modelling of WECs needs to be refined, non-linearities often must be taken into account. This is namely the case when one wants to equip the WEC with a latching control system, or with realistic PTO equipments (water/air turbines, hydraulic circuits, linear direct generation...), or any other external effort (2nd-order wave efforts, hydrodynamic non-linearities, moorings, extreme loads, wind, currents...). Including such non-linearities into the model requires a dynamic description in time domain thanks to integro-differential equations, which allow to simulate the full device in

a given wave field over a finite duration. Now, it will be shown that the global spectral bandwidth of the wave field also plays a significant role in the temporal simulation of Gaussian signals like $\eta(t)$, which is the main – excitation – input of the dynamic equation system. It therefore may have an impact on the estimation of mean power extracted by linear as well as non-linear WECs. Finally, the sensitivity of systems equipped with capacitive energy converters to wave groups is observed: the PTO devices are modelled as simple inertial flywheels or short-term energy storage reservoirs, which are likely to make the whole system highly non-linear.

3.2 Modelling of a 1-DOF linear WEC

The simplest WEC model is a one degree of freedom (DOF) linear WEC oscillating in heave thanks to the wave action, and rigidly linked to the sea bottom. It is excited by the incident waves $\eta(t)$ – whose amplitudes are small enough in relation to wavelength to satisfy the linear theory conditions. The energy absorption is performed through a linear damper (C_{PTO}) so that the whole system may be seen as a linear filter. In addition, the WEC is supposed to be punctual (*point absorber*) and axi-symmetric with respect to the vertical axis (orthogonal to the waterplane at rest): it is thus supposed to be absolutely insensitive to wave directionality.

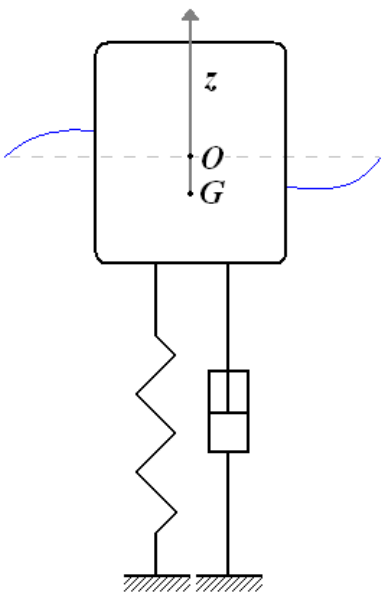

Figure 3.1: Mechanical scheme of a simple 1-DOF linear point absorber in heave.

In figure 3.1, O denotes the origin of the space coordinate system ($Oxyz$), with $z = 0$ set to the waterplane at rest, and G the float's centre of gravity. The mechanical

equation against vertical axis (Oz) (with positive z going upwards) in time domain may be written as

$$m\ddot{z}(t) = F_e(t) + F_r(t) + F_h(t) + F_{PTO}(t) \tag{3.1}$$

where m is the float's mass, $F_e(t)$ the vertical wave excitation force exerted on the float, $F_r(t)$ the vertical radiation force (i.e. the force exerted by the hull on waves when oscillating), $F_h(t)$ the hydrostatic restoring force in the sea-water (relative Archimede's force), and $F_{PTO}(t)$ the vertical effort of the PTO device (here, a pure damper) on the float. As each of these forces is linear with respect to the float's vertical motions, if one considers a harmonic excitation of circular frequency ω, equation (3.1) in the frequency domain simplifies to

$$\underline{z}(\omega) = \underline{H_{z\eta}}(\omega)\underline{\eta}(\omega) \tag{3.2}$$

where

- $\underline{z}(\omega)$ is the complex amplitude of the float's vertical motion z (heave), that is,

$$z(t) = \Re\{\underline{z}(\omega)e^{i\omega t}\} \tag{3.3}$$

- $\underline{\eta}(\omega)$ the complex amplitude of the water elevation η at point O, that is,

$$\eta(t) = \Re\{\underline{\eta}(\omega)e^{i\omega t}\} \tag{3.4}$$

- $\underline{H_{z\eta}}(\omega)$ the complex transfer function that links elevation η to heave motion z.

Transfer function $\underline{H_{z\eta}}(\omega)$ is made of mechanical terms that stand for the efforts listed in equation (3.1), among others. Equation (3.2) may be generalised to systems with two degrees of freedom or more: in such cases, $\underline{H_{z\eta}}(\omega)$ is expected to involve coupling terms (e.g. sway-roll, surge-pitch...).

Instead of displacement z, it is more convenient to consider velocity $\dot{z} = \mathrm{d}z/\mathrm{d}t$ when dealing with energy extraction. The instantaneous extracted power from waves is directly related to the velocity indeed. From equation (3.2), the velocity complex amplitude is taken as the first time derivative of the displacement, so that

$$i\omega\underline{z}(\omega) = i\omega\underline{H_{z\eta}}(\omega)\underline{\eta}(\omega) = \underline{H_{\dot{z}\eta}}(\omega)\underline{\eta}(\omega) \tag{3.5}$$

where $\underline{H_{\dot{z}\eta}}(\omega)$ is the transfer function linking water elevation η to heave velocity $\dot{z}$. It is also called *complex mechanical impedance* of the system. The typical expression of such a transfer function for a 1-DOF linear WEC as that depicted in figure 3.1 is (see e.g. Falnes, 2002; Falcão, 2005, 2007)

$$\underline{H_{\dot{z}\eta}}(\omega) = \frac{\underline{\Phi}(\omega)}{[B(\omega) + C_{PTO}] + i\left[\omega(m + A(\omega)) - \frac{\rho g S}{\omega}\right]} \tag{3.6}$$

where

- $\underline{\Phi}(\omega)$ denotes the complex transfer function linking elevation η to excitation force $F_e(t)$, with $F_e(t) = \Re\{\underline{F_e}(\omega)e^{i\omega t}\}$, thus

$$\underline{F_e}(\omega) = \underline{\Phi}(\omega)\underline{\eta}(\omega) \tag{3.7}$$

- $A(\omega)$ is the float's added mass,
- $B(\omega)$ is the float's radiation coefficient,
- C_{PTO} is the PTO damping coefficient,
- ρ is the sea water mass density,
- S is the waterplane area, that is, the cross-sectional area defined by intersecting the waterplane and the float at rest.

Coefficients $A(\omega)$ et $B(\omega)$ may be approached with the aid of boundary elements method (BEM) numerical softwares which solve the linearised Navier-Stokes equations (WAMIT, Aquadyn...) or by Fourier transform of the impulse responses obtained with time-domain hydrodynamic codes (ACHIL3D, TIMIT...), or even by using theoretical and empirical formulae derived for elementary hull shapes in infinite water depth (see e.g. Evans, 1976).

As elevation $\eta(t)$ is Gaussian and centred, the output signals $z(t)$ and $\dot{z}(t)$ are also Gaussian and centred thanks to the linearity property of the system. As a consequence, the related energy spectral densities are respectively expressed as

$$E_{zz}(f) = |\underline{H_{z\eta}}(f)|^2 E(f) \tag{3.8}$$

and

$$E_{\dot{z}\dot{z}}(f) = |\underline{H_{\dot{z}\eta}}(f)|^2 E(f) = (2\pi f)^2 |\underline{H_{z\eta}}(f)|^2 E(f) = (2\pi f)^2 E_{zz}(f) \tag{3.9}$$

Hence, the system filters the excitation signal $\eta(t)$ and its motions are known as soon as the impedance function $\underline{H_{\dot{z}\eta}}(\omega)$ is known. The energy spectral densities of the motions are likely to be narrower than the input wave spectrum, namely because of the natural bounds of the response interval (Fig. 3.2).

The linear PTO exerts on the system the instantaneous force

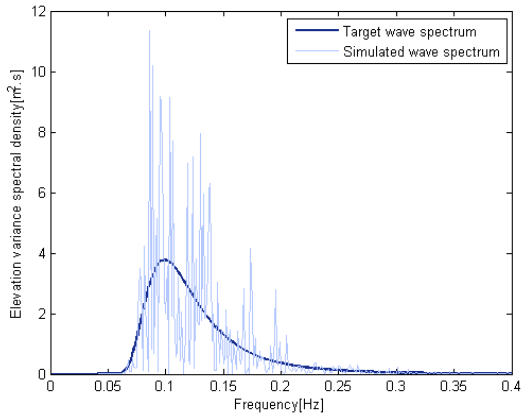

(a)

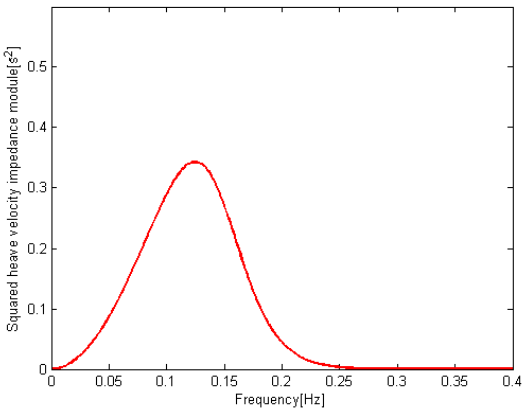

(b)

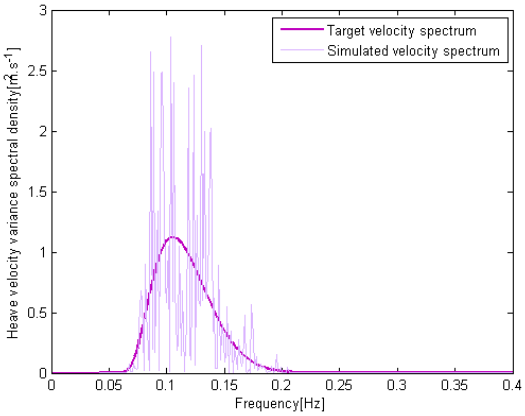

(c)

Figure 3.2: Target (Bretschneider, dark blue line) and simulated (light blue line) energy spectra of water elevation η (a), squared modulus of heave velocity impedance (b), and target (dark purple line) and simulated (light pruple line) energy spectra of the buoy's heave velocity.

$$F_{PTO}(t) = -C_{PTO}\dot{z}(t) \tag{3.10}$$

and hence, the instantaneous power absorbed by the system

$$P_{PTO}(t) = -F_{PTO}(t)\dot{z}(t) = C_{PTO}\dot{z}^2(t) \tag{3.11}$$

Since $\dot{z}$ is supposed to be Gaussian and centred, the mean extracted power is

$$\overline{P_{PTO}(t)} = \overline{C_{PTO}\dot{z}^2(t)} = C_{PTO}\overline{\dot{z}^2(t)} = C_{PTO}\sigma_{\dot{z}}^2 \tag{3.12}$$

where

$$\sigma_{\dot{z}}^2 = \int_0^\infty E_{\dot{z}\dot{z}}(f)\,\mathrm{d}f = m_{\dot{z}0} = \int_0^\infty |\underline{H_{\dot{z}\eta}}(f)|^2 E(f)\,\mathrm{d}f \tag{3.13}$$

which yields

$$\overline{P_{PTO}(t)} = \overline{P_{PTO}} = C_{PTO}\int_0^\infty |\underline{H_{\dot{z}\eta}}(f)|^2 E(f)\,\mathrm{d}f \tag{3.14}$$

Accordingly, the mean power extracted by such a system from waves is directly proportional to the variance of the heave velocity (the converter's DOF here), that is, the integral of the squared modulus of $\underline{H_{\dot{z}\eta}}(f)$ times the input wave spectrum $E(f)$. Besides, as these both functions are real, positive and square integrable, it is interesting to notice that the Cauchy-Schwartz inequality may be applied, as

$$\begin{aligned}\overline{P_{PTO}} = C_{PTO}\int_0^\infty |\underline{H_{\dot{z}\eta}}(f)|^2 E(f)\,\mathrm{d}f &\leq \sqrt{\int_0^\infty C_{PTO}^2 |\underline{H_{\dot{z}\eta}}(f)|^4\,\mathrm{d}f}\cdot\sqrt{\int_0^\infty E^2(f)\,\mathrm{d}f} \\ &\leq \Pi_{PTF}\cdot\frac{m_0}{\sqrt{\Lambda}}\end{aligned} \tag{3.15}$$

where the term Π_{PTF} depends on the dynamics of the system only, and where the equivalent spectral bandwidth parameter $\Lambda(Hz)$ is defined as

$$\Lambda = \frac{m_0^2}{\int_0^\infty E^2(f)\,\mathrm{d}f} \tag{3.16}$$

(also introduced in Appendix A, Section A.1). This inequality allows to determine an upper bound to the mean extracted power figure $\overline{P_{PTO}}$, whose terms separately refer to the sea-state and the linear system's dynamics. Thus, if one considers a sea-state whose energy (m_0 or H_{m0}) and spectral bandwidth (Λ) are known on the one hand, and the dynamic term Π_{PTF} is computable on the other hand, then the mean power performance of the device may be easily upper-bounded. The terms at both sides of inequality (3.15) become equal as soon as $|\underline{H_{\dot{z}\eta}}(f)|^2$ and $E(f)$ are linearly related: in other words, the inequality becomes an equality as both spectral shapes look more and more similar and match in frequency. When this occurs – or nearly – the mean power

(Eq. (3.11)) may be approached by the upper bound $\Pi_{PTF} \cdot \frac{m_0}{\sqrt{\Lambda}}$.

When considering equation (3.11), it is clear that $P_{PTO}(t)$ is a random value following a χ^2-distribution with one degree of freedom, whose variance is

$$\begin{aligned}\sigma^2_{P_{PTO}} &= \overline{\left(P_{PTO}(t) - \overline{P_{PTO}(t)}\right)^2} \\ &= 2\overline{P_{PTO}}^2 \\ &= 2C^2_{PTO}\sigma^4_{\dot{z}}\end{aligned} \tag{3.17}$$

It results that the variations of $PTO(t)$ increase with mean power $\overline{P_{PTO}}$. Accordingly, the groupiness of $\dot{z}(t)$ – which influences $\sigma^2_{\dot{z}}$ – is the most important to account for the performance of the WEC, much more than the own groupiness of elevation $\eta(t)$. This first simple approach lead in the frequency domain explains why the incident wave groups may or not have an impact on the WEC's production, according to the dynamics of the system at the scale of a sea-state.

Before closing this section, let us derive the analytical expression of the energy spectrum of the instantaneous power signal $P_{PTO}(t)$, $E_{P_{PTO}}(f)$. Let $y(t)$ be the square of a Gaussian and centred signal $x(t)$, as: $y(t) = x^2(t)$. It may be decomposed as

$$y(t) = \overline{y(t)} + \tilde{y}(t) \tag{3.18}$$

where $\overline{y(t)}$ is the mean value and $\tilde{y}(t)$ denotes the zero-mean varying part of the signal. The autocorrelation function $R_{\tilde{y}\tilde{y}}(\tau)$ of $\tilde{y}(t)$ is then written as (Eq.(2.1))

$$\begin{aligned}R_{\tilde{y}\tilde{y}}(\tau) &= \overline{\tilde{y}(t)\tilde{y}(t+\tau)} = \overline{\left(y(t) - \overline{y(t)}\right)\left(y(t+\tau) - \overline{y(t+\tau)}\right)} \\ &= \overline{y(t)y(t+\tau)} - \overline{y(t)}^2 \\ &= \overline{x(t)x(t)x(t+\tau)x(t+\tau)} - \overline{y(t)}^2 \\ &= \overline{x(t)x(t)}^2 + 2\overline{x(t)x(t+\tau)}^2 - \overline{y(t)}^2 \\ &= 2\overline{x(t)x(t+\tau)}^2 \\ &= 2R^2_{xx}(\tau)\end{aligned} \tag{3.19}$$

where the following property for two gaussian and centred signal $x(t)$ et $y(t)$ (see Papoulis, 1991)

$$\overline{x^2(t)y^2(t)} = \overline{x^2(t)} \cdot \overline{y^2(t)} + 2\overline{x(t)y(t)}^2 \tag{3.20}$$

has been applied. Calculating the Fourier transform of autocorrelation function $R_{\tilde{y}\tilde{y}}(\tau)$ is similar to calculating the convolution product of $R_{xx}(\tau)$ (i.e. the two-sided energy spectral density of $x(t)$, $G_x(f)$, Eq. (2.4)) with itself, thus

$$
\begin{aligned}
G_{\tilde{y}}(\omega) &= \frac{1}{2\pi}\mathcal{F}\{R_{\tilde{y}\tilde{y}}(\tau)\}(\omega) \\
&= \frac{1}{2\pi}\cdot 2\mathcal{F}\{R_{xx}(\tau)R_{xx}(\tau)\}(\omega) \\
&= \frac{1}{\pi}\cdot\frac{1}{2\pi}\mathcal{F}\{R_{xx}(\tau)\}(\omega) * \mathcal{F}\{R_{xx}(\tau)\}(\omega) \\
&= \frac{1}{2\pi^2}\cdot(2\pi)^2\, G_x(\omega) * G_x(\omega) \\
&= 2\int_{-\infty}^{\infty} G_x(\omega-\sigma)G_x(\sigma)\,\mathrm{d}\sigma \\
&= \frac{1}{2}\int_{-\infty}^{\infty} \tilde{E}_x(\omega-\sigma)\tilde{E}_x(\sigma)\,\mathrm{d}\sigma \\
&= \frac{1}{2}\int_{-\infty}^{\infty} \tilde{E}_x(\sigma)\tilde{E}_x(\omega+\sigma)\,\mathrm{d}\sigma
\end{aligned}
\tag{3.21}
$$

where $\tilde{E}_x(\omega)$ is the two-sided energy spectrum defined as $\tilde{E}_x(\omega) = 2G_x(\omega)$ over $]-\infty;\infty[$ (and whose integral is $2m_{x0}$), since $G_x(\omega)$ is real and even by definition. Therefore, the one-sided energy spectral density of $\tilde{y}(t)$ is ($\omega > 0$)

$$
\begin{aligned}
E_{\tilde{y}}(\omega) &= 2G_{\tilde{y}}(\omega) \\
&= \int_{-\infty}^{\infty} \tilde{E}_x(\sigma+\omega)\tilde{E}_x(\sigma)\,\mathrm{d}\sigma \\
&= \int_{0}^{\infty} E_x(\sigma)\left(E_x(\sigma+\omega) + E_x(|\sigma-\omega|)\right)\,\mathrm{d}\sigma
\end{aligned}
\tag{3.22}
$$

[Such a formulation may be found in e.g. Tayfun and Lo (1989).]

For the particular case $y(t) = C_{PTO}\dot{z}^2(t) = P_{PTO}(t)$, that is, $y(t) = (C_{PTO}^{\frac{1}{2}}\dot{z}(t))^2$, which is the square of a Gaussian and centred signal, the following spectrum (expressed against frequency in Hz) is derived

$$
E_{P_{PTO}}(f) = C_{PTO}^2 \int_{-\infty}^{\infty} \tilde{E}_{\dot{z}}(\phi+f)\tilde{E}_{\dot{z}}(\phi)\,\mathrm{d}\phi \tag{3.23}
$$

where $\tilde{E}_{\dot{z}}(f)$ represents the two-sided energy spectrum of $\dot{z}(t)$. This expression shall be used in the following sections to compare the theoretical "power" spectrum to the estimated one in given sea-state realisations.

3.3 Sensitivity of a 2-DOF heaving linear point absorber to spectral shape

From the previous section, it is expected that if the WEC's impedance modulus exhibits a (broad) resonance peak around the main period of the incident waves, the system's motions (displacements, velocities...) will be fairly correlated to their natural groupiness. On the contrary, if the WEC's impedance is narrow and not tuned to the main waves' period band, wave groupiness will hardly account for the device's performance.

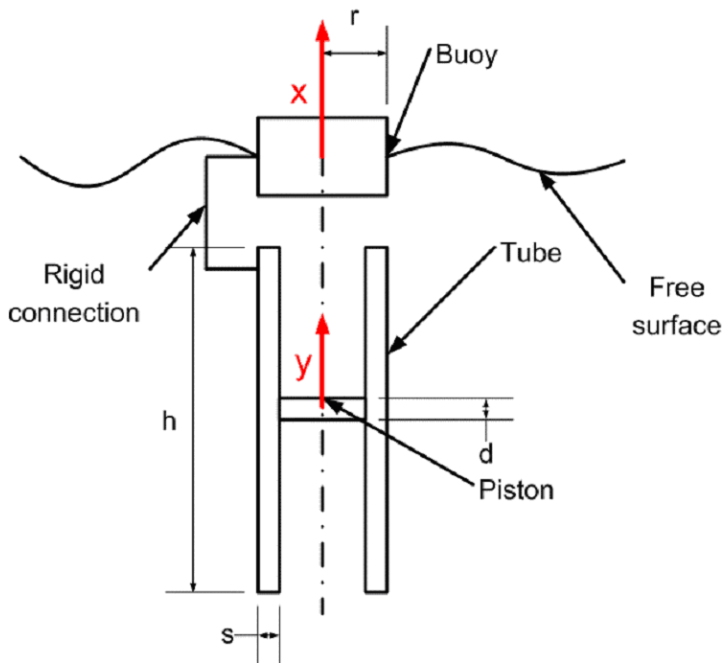

Figure 3.3: Scheme of IPS heaving buoy.

A study on the sensitivity of a linear 2-DOF heaving point absorber WEC to wave groupiness (and spectral bandwidth) was carried out. The model is close to an IPS buoy[1] and is composed of a heaving buoy of diameter $5m$ (1^{st}DOF, x) rigidly connected to a $10m$-long submerged vertical cylinder housing a piston, which can freely oscillate inside (2^{nd}DOF, y), as depicted in figure 3.3. A linear damper C_{PTO} is applied to the relative heaving motion $\delta = x - y$ as a PTO device. For more details about the device modelling, we refer to Saulnier et al. (2007a,b).

The complex impedance linking $\eta(t)$ to the relative heave $\delta(t)$ is obtained from the hydrodynamic coefficients of each moving part (buoy+tube and inner piston) computed

[1]For industrial applications, see the IPS *OWEC Buoy* (`http://www.ips-ab.com/`) or AquaBuOY (`http://www.finavera.com/`) websites.

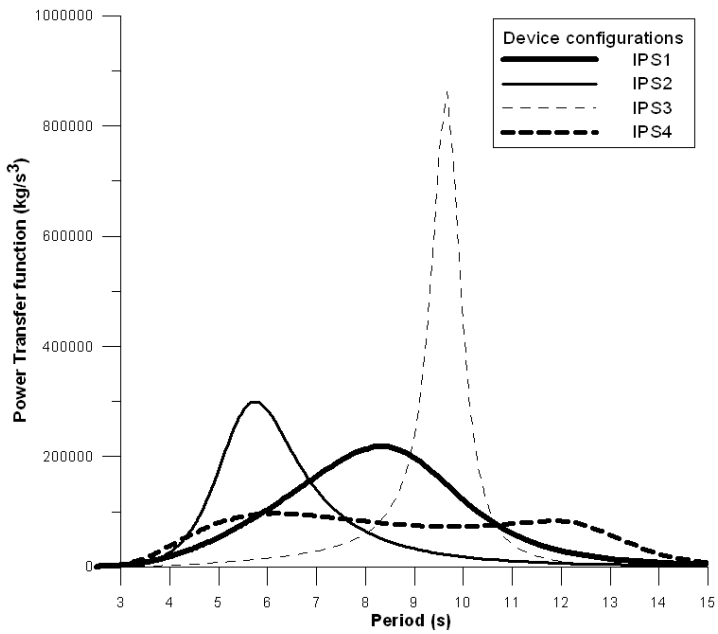

Figure 3.4: IPS buoy configurations (IPS1, 2, 3 et 4): power transfer functions (PTF).

with the aid of the WAMIT BEM code. Four particular PTO configurations (transfer functions) are envisioned by modifying the restoring and damping coefficients K_{PTO} and C_{PTO} respectively. Figure 3.4 illustrates the four power transfer functions $PTF(f)$ against wave period, which are defined as

$$PTF(f) = C_{PTO}|\underline{H_{\dot{z}\eta}}(f)|^2 \tag{3.24}$$

Hence, according to equation (3.14),

$$\overline{P_{PTO}} = \int_0^\infty PTF(f)E(f)\,\mathrm{d}f \tag{3.25}$$

These four configurations are respectively called IPS1, IPS2, IPS3 and IPS4:

- IPS1: mean broad-banded response with resonance around 8-9s;
- IPS2: mean narrow-banded response with resonance around 6s;
- IPS3: high narrow-banded response with resonance around 9-10s;
- IPS4: low broad-banded response with resonance within [5s;12s].

The sensitivity of each WEC configuration to spectral width has been observed on energy spectra estimated by accelerometric buoys that were deployed at two locations:

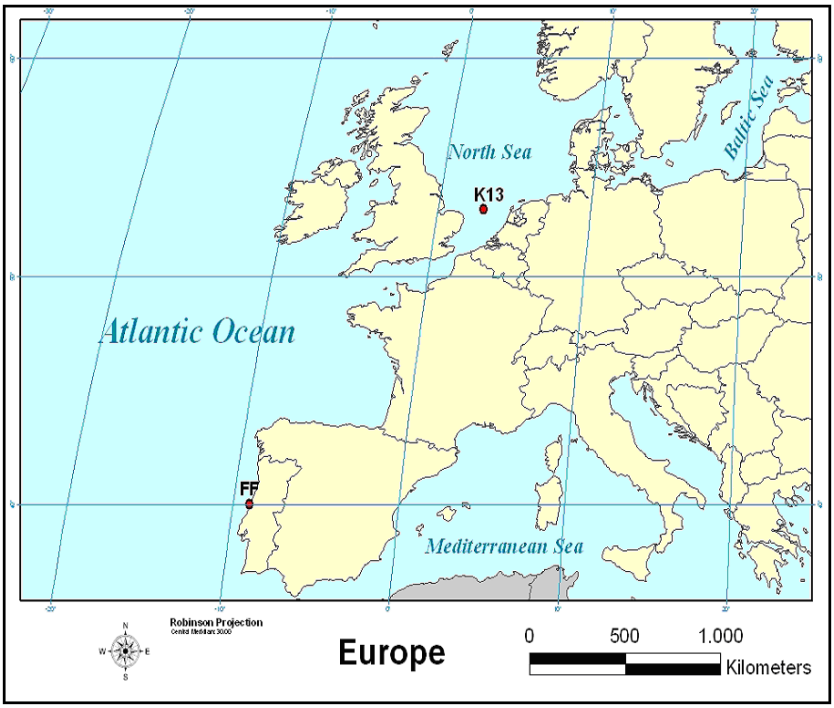

Figure 3.5: Buoy measurements locations: FF (Figueira da Foz, Portugal) and K13 station (North Sea, Netherlands).

western coast of Portugal (*FF*, Figueira da Foz, $40\,°13'33''N, 09\,°06'00''W$) and North-Sea (*K13*, dutch station, $53\,°12'17''N, 03\,°03'10''E$). The FF data were processed by the Portuguese *Hydrographic Institute* whereas the North-Sea data were provided by the Dutch National Institute for Marine and Coastal Management (*Rijswaterstaat*[2]). The water elevation measurements at FF were carried out over the period 1981-1994 ($\sim$26500 spectra) with Wavec and Waverider buoys, at a water depth of $90m$ on average. At K13 station, the Wavec buoy has been installed and recording over the period 1993-2002 ($\sim$23300 spectra) at $\sim 30m$ water depth. A map showing both locations is given in figure 3.5.

To evaluate the sensitivity of each configuration to spectral width, it is necessary to define a performance parameter that does not depend on the incident (omnidirectional) wave power P_w (Eq. (2.57)). From equations (2.61)&(2.59) (wave dispersion) in deep water ($h \to \infty$), the group celerity of waves simplifies to

$$c_g = \frac{g}{4\pi f} \tag{3.26}$$

which yields

$$P_w = \frac{\rho g^2}{4\pi} m_{-1} = \frac{\rho g^2}{4\pi} H_{m0}^2 T_{-10} \approx 0.4906 H_{m0}^2 T_{-10} \tag{3.27}$$

[2] `http://www.rijkswaterstaat.nl`

Deep water conditions may be assumed at FF indeed for the depth is large enough, so that equation (3.27) may be used. At K13 however, the low depth requires the exact computation of the group celerity in finite depth conditions (Eq. (2.61)) in equation (2.57). Once the incident wave power is known, the following ratio

$$\chi_P = \frac{\overline{P_{PTO}}}{P_w} \tag{3.28}$$

may be formed and is called *capture width* for it is homogeneous to a wave-front width (m). This ratio is independent of the wave spectrum's energetic contents (m_0). The only parameters that may have an influence on it are indeed the mean period of waves and spectral bandwidth. By fixing the wave period (here, T_{-10}), only the spectral shape variations may a priori influence χ_P. Thanks to this performance parameter, it becomes possible to compare the performance of each WEC configuration at both locations for fixed wave energy periods.

For each location, spectra having T_{-10} approximately ($\pm 2\%$) equal to {5s,5.5s, ...,14.5s,15s} at FF, and {3.5s,4s, ...,9s,9.5s} at K13, are grouped together in respectively 21 and 13 period sub-samples. Each one of those never contains less than fifty spectra, which ensures a good representativity of the local wave climate within each sub-sample. Capture width χ_P is computed for each sea-state $E(f)$ in each sub-sample at both locations and for the four WEC configurations. Figures 3.6 and 3.7 depict the distribution of χ_P against energy period T_{-10}, as the mean value bounded by its $5^{th}$and 95th percentiles. For each configuration, the distributions obtained at FF (left) and K13 (right) are displayed side-by-side in order to allow for joint inspections. The capture width obtained using a Bretschneider as input wave spectrum (see Appendix C) is also reported in the figures.

The wave climates at both locations have very different characteristics. While the western coast of Portugal is continuously facing long swells generated by remote storms (in the North-Atlantic: Caribbean islands, North-America, Greenland, Azores...), the North-Sea sea-states are generally dominated by local wind-sea systems of variable breadths, which sometimes may result in very energetic sea conditions. For these reasons, the waves are found to be longer and more monocrested at FF than at K13. This is why the energy periods of definition in figures 3.6 and 3.7 do not exactly match at both locations. Nevertheless, both wave climates coincide in the range [5s;9.5s], where the χ_P-distributions show some similarities. The slight differences may be partly due to the definition of P_w at both places (infinite – Eq. (3.27) – and finite – Eq. (2.57) – water depths respectively) as well as local particularities in terms of spectral shape (swell and wind-sea peakednesses have proper spectral characteristics indeed). In these figures, the influence of the spectral width variability on the WECs' capture width is clearly emphasized. Furthermore, the sensitivity manifestly increases when the wave period is close to the own WEC configuration's resonance (see Fig. 3.4). This is par-

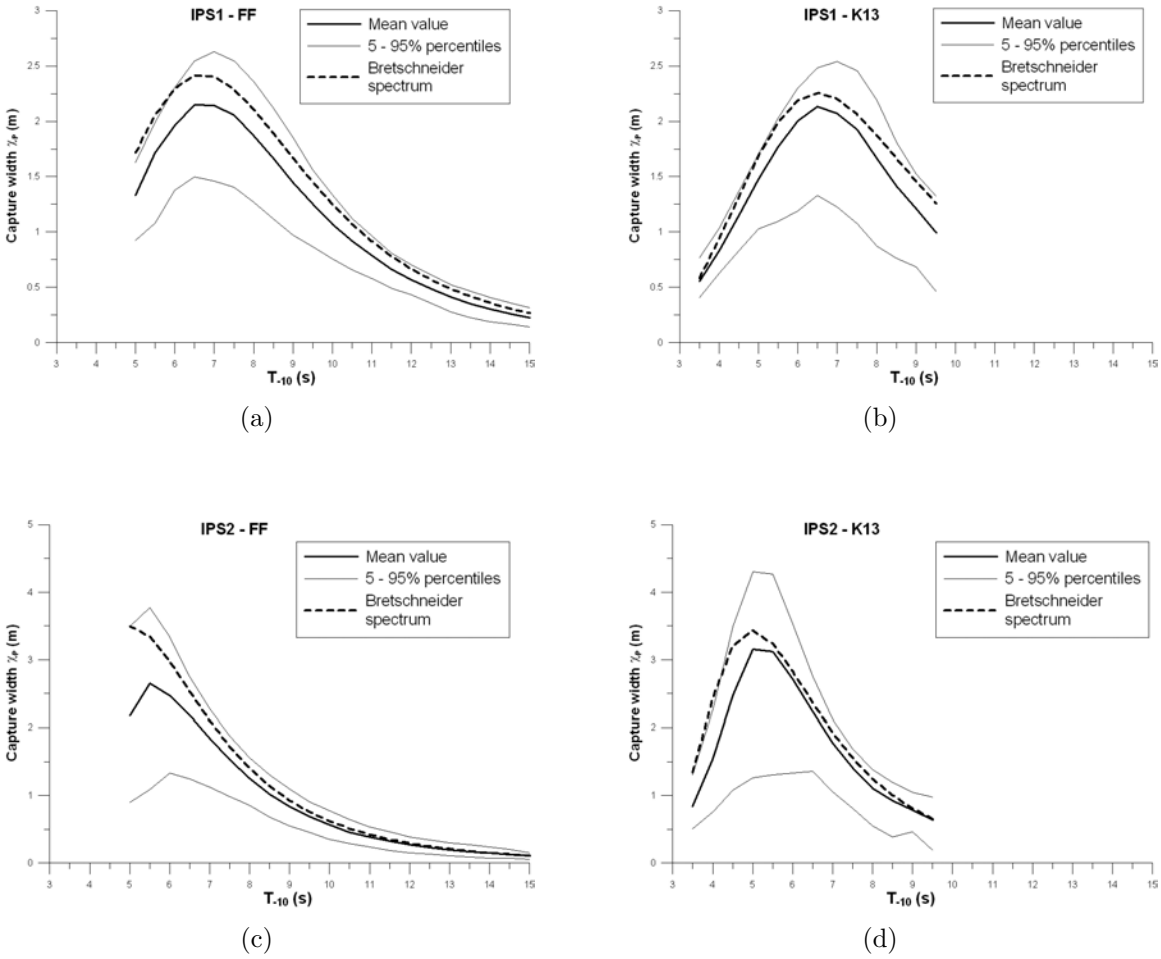

Figure 3.6: χ_P distribution for configurations IPS1 and IPS2 at FF (left) and K13 (right): mean value, 5th and 95th percentiles, and results obtained with standard Bretschneider sea-state as wave input.

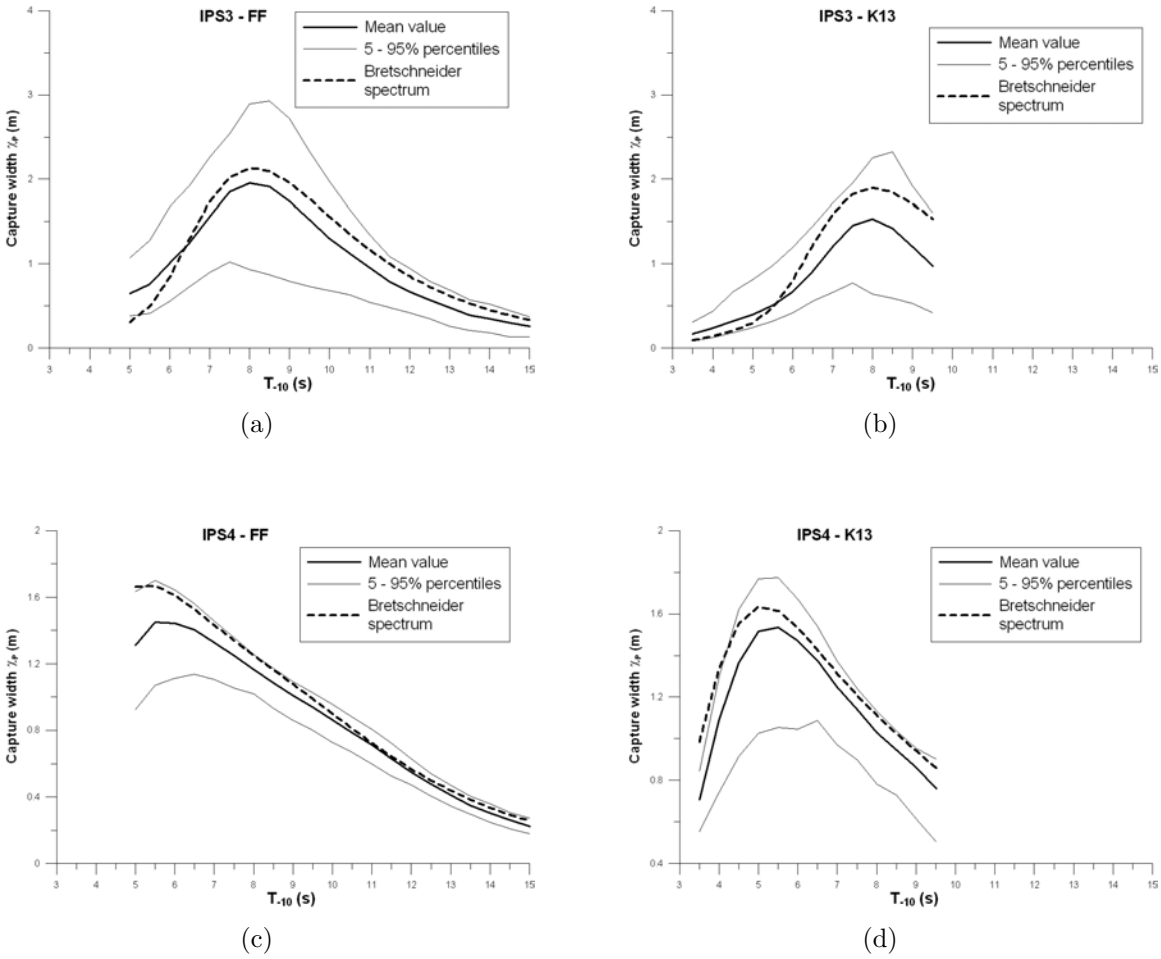

Figure 3.7: χ_P distribution for configurations IPS3 and IPS4 at FF (left) and K13 (right): mean value, 5th and 95th percentiles, and results obtained with standard Bretschneider sea-state as wave input.

ticularly visible in figure 3.6. Consequently, the spectral shape/bandwidth of sea-states definitely is an influent parameter on the wave energy conversion here, especially when the sea-state's main wave period interval matches the resonance band of the WEC. As both bands mismatch, this influence vanishes: in such cases, spectral width and wave groupiness are not relevant characteristics with respect to production anymore.

The capture width curves obtained by considering Bretschneider input sea-states globally overestimate the mean curves of the sub-samples. Performance predictions based on a fixed input sea-state defined such as the Bretschneider spectrum therefore may lead to biased estimations compared to reality (see Part II).

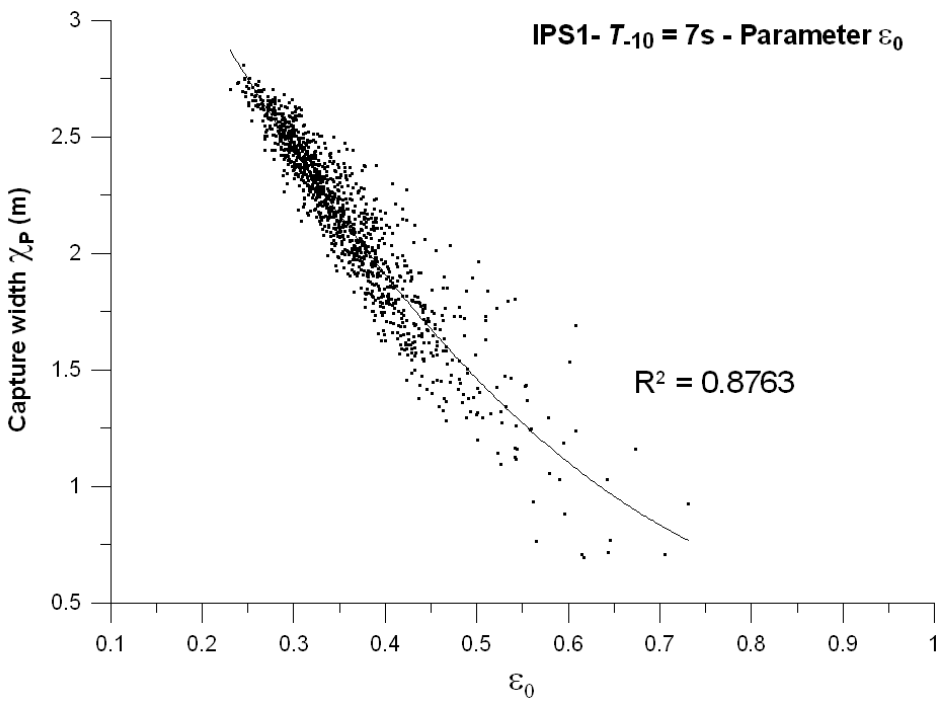

Figure 3.8: Capture width χ_P against ε_0 at FF for $T_{10} = 7s$ and WEC configuration IPS1; quadratic trend fitting and determination coefficient R^2.

Let us now investigate the WEC sensitivity to spectral bandwidth by means of a spectral parameter among the period sub-samples at both locations. To this aim, the following parameters were also computed along with χ_P on each spectrum $E(f)$: $\{\varepsilon_0,\varepsilon_1,\varepsilon_2,Q_p,\kappa,B_w\}$. In each sub-sample, the obtained dispersion is fitted with a quadratic trend (least squares method). Then, the correlation of the capture width to each of these parameters is assessed through the value of the corresponding coefficient of determination R^2. Figure 3.8 illustrates the nice correlation to parameter ε_0 found for WEC configuration IPS1 within the FF sub-sample of $T_{-10} = 7s$. Coefficient R^2 is used here as a correlation indicator: if χ_P is very sensitive to the parameter (high correlation), the quadratic trend fitted on the scatter plot yields a value of R^2 close to 1; on the contrary, if the scatter plot looks isotropic (almost no correlation), the fit will be poor and R^2 will

be low (0 for uncorrelated data). In figure 3.8, the dispersion is weak and the fit seems good so that R^2 comes close to 0.9, as confirmed by a quick visual inspection: one can conclude that capture width is well correlated to parameter ε_0 at FF for sea-states with T_{-10} around $7s$.

The determination coefficient R^2 is calculated for each sub-sample of both locations FF and K13, for each parameter of $\{\varepsilon_0,\varepsilon_1,\varepsilon_2,Q_p,\kappa,B_w\}$, and for each WEC configuration (IPS1 to IPS4). Figures 3.9, 3.10, 3.11 and 3.12 present the various sensitivities (R^2) obtained against mean energy period. The sub-sample mean extracted power (red spots) is added to each figure for indication. As well as in figures 3.6 and 3.7, the curves are plotted within the same period range to allow comparisons between FF and K13.

In order to make these plots easier to understand, one can consider the sensitivity (or the correlation) as good as soon as the value of R^2 exceeds 0.70. It is then straightforward to identify the parameters that seem able to account for the capture width level, namely ε_0, ε_1 and B_w here. Once again, the sensitivity is somewhat subject to the response interval of each configuration. For instance, χ_P is quite correlated to ε_0 over [5s;9s] for IPS1 at FF and K13 (Fig 3.9). Correlation parameter κ yet shows good correlations for intervals unrelated to the response interval, as one can see at FF for configurations IPS1 to IPS3 (Fig. 3.9(a), 3.10(a), 3.11(a); not observable at K13 because of the upper period limit). These "sensitivity intervals" generally coincide with the response interval of the devices. Thus, they are found to be as broad as the WECs' PTF, and conversely (Fig. 3.4). Configurations IPS3 – narrow-banded over [8s;11s] – and IPS4 – broad-banded over [4s;14s] – constitute two extreme cases, which exhibit respectively narrow (Fig. 3.11(a)) and broad (Fig. 3.12) sensitivity intervals. The same is observed for configurations IPS1 and IPS2 (Fig. 3.9&3.10), IPS2 being broader than IPS1.

As a conclusion, it can be said that the broader the device's resonance interval, the higher the sensitivity to spectral bandwidth and parameters like ε_0, ε_1 and B_w. A practical implication of such a conclusion is that if the WEC is able to tune its response to the incident waves, and provided its PTF is not too narrow – highly desirable in practice –, the energy conversion operated by such a device shall be always correlated with spectral bandwidth, and therefore, wave groupiness. In addition, some similarities are noticeable on the previous graphics related to both FF and K13: this means that the spectral width characterisation through some well chosen spectral parameters is relevant whatever the wave climate. A spectral parameter is likely to be less sensitive to spectral shape particularities (spectral slopes and tails, noise) than the global distribution of energy against frequency. Parameters ε_2, Q_p and κ are not recommended for these purposes however, either because their correlation with capture width is too low (ε_2, Q_p), or because it is not high over relevant period intervals (κ).

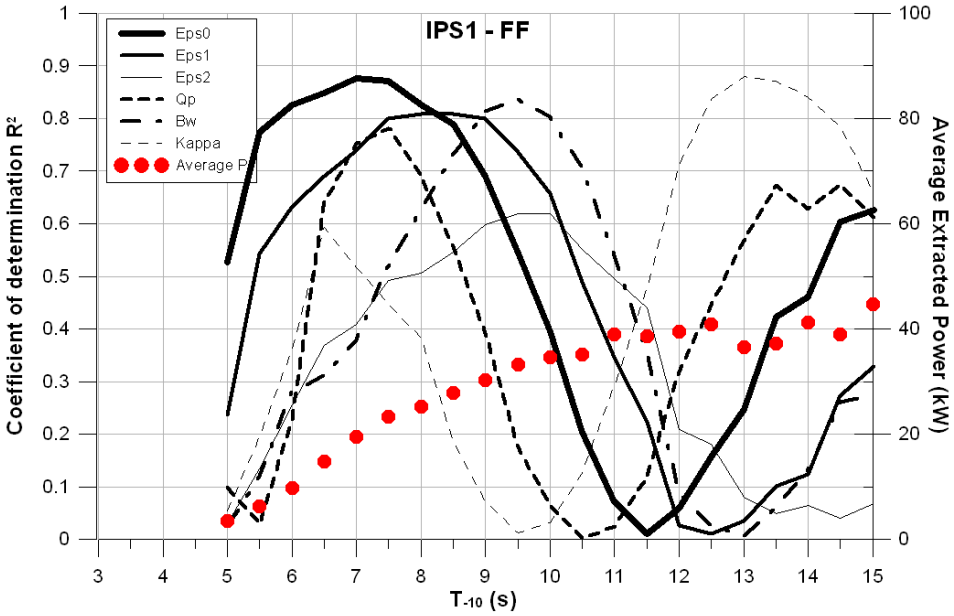

(a)

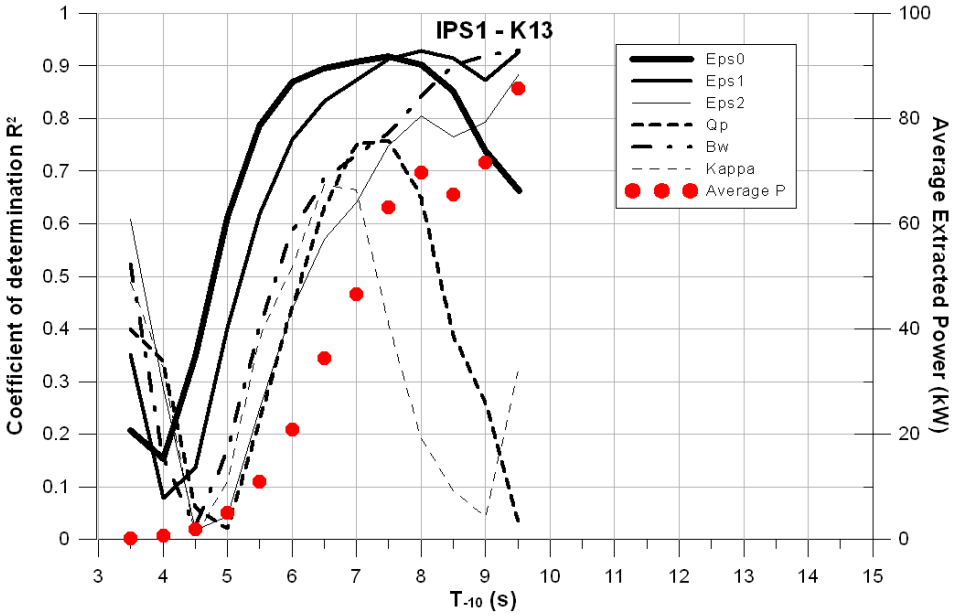

(b)

Figure 3.9: Coefficient R^2 of χ_P-distribution fitted with a quadratic law against T_{-10} for each spectral parameter and configuration IPS1 at FF (a) and K13 (b); sub-sample mean extracted power (kW) (red spots).

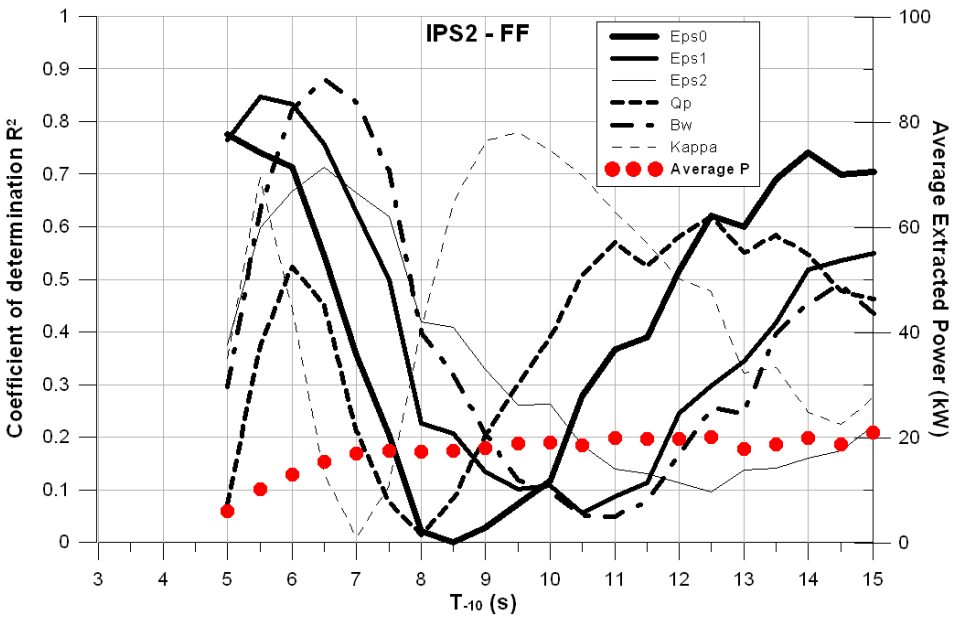

(a)

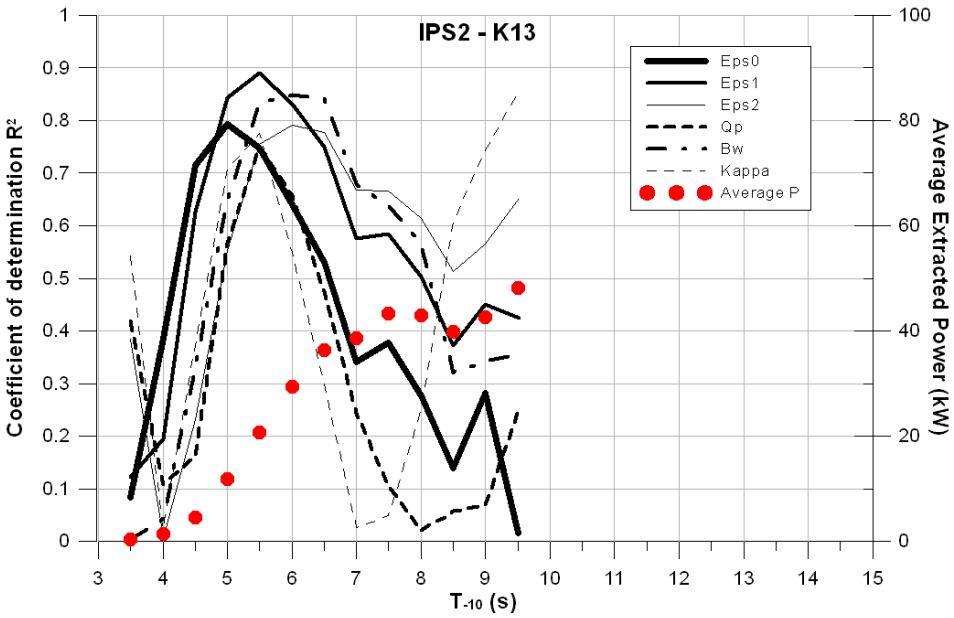

(b)

Figure 3.10: Id. Fig. 3.9 for configuration IPS2.

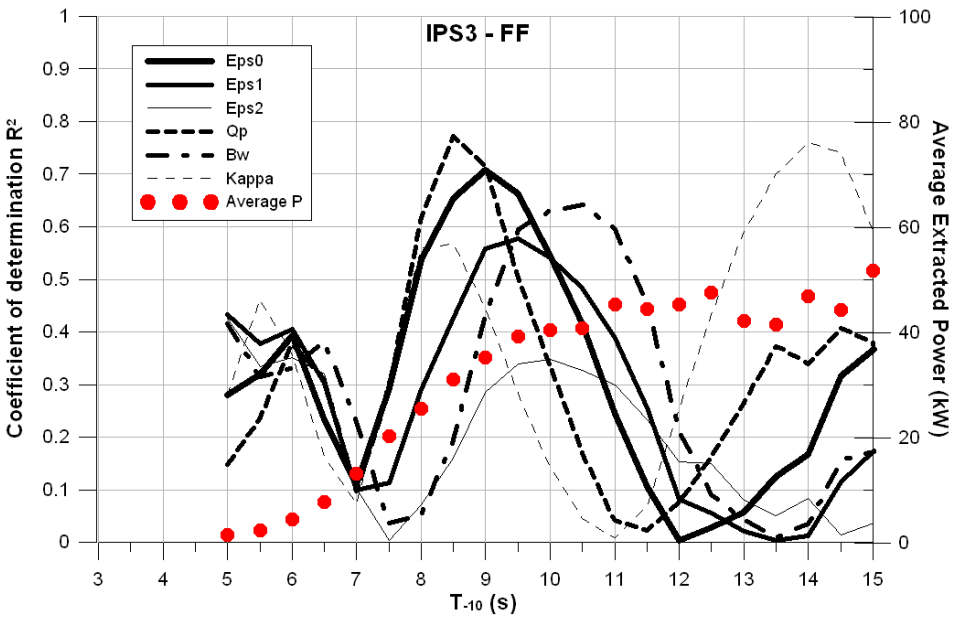

(a)

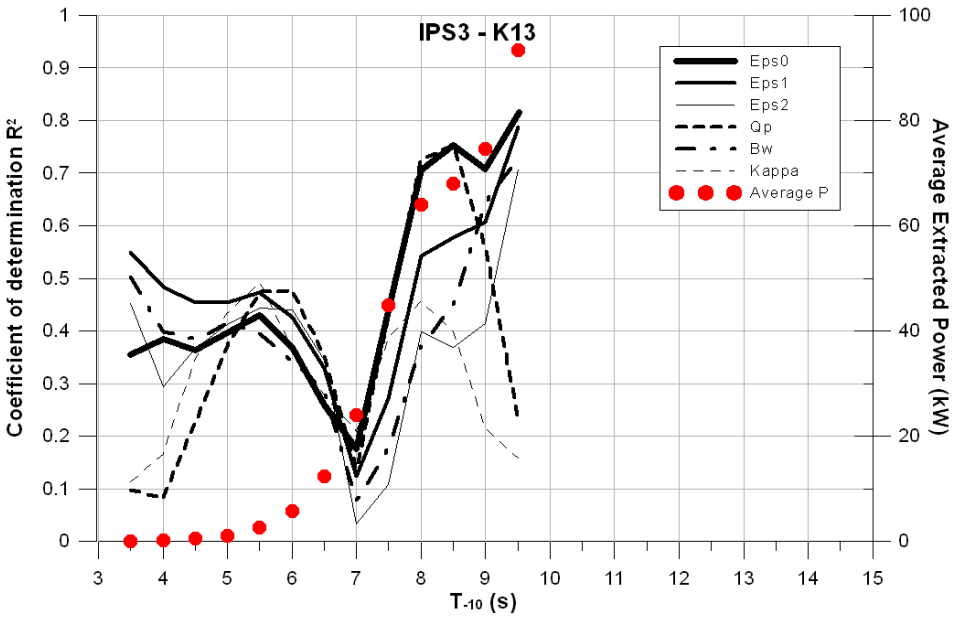

(b)

Figure 3.11: Id. Fig. 3.9 for configuration IPS3.

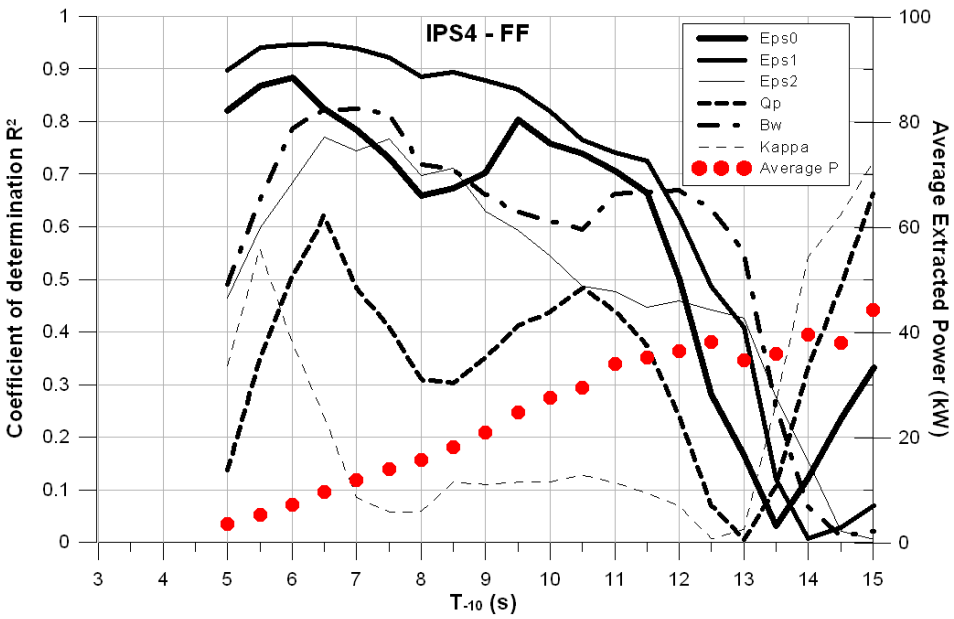

(a)

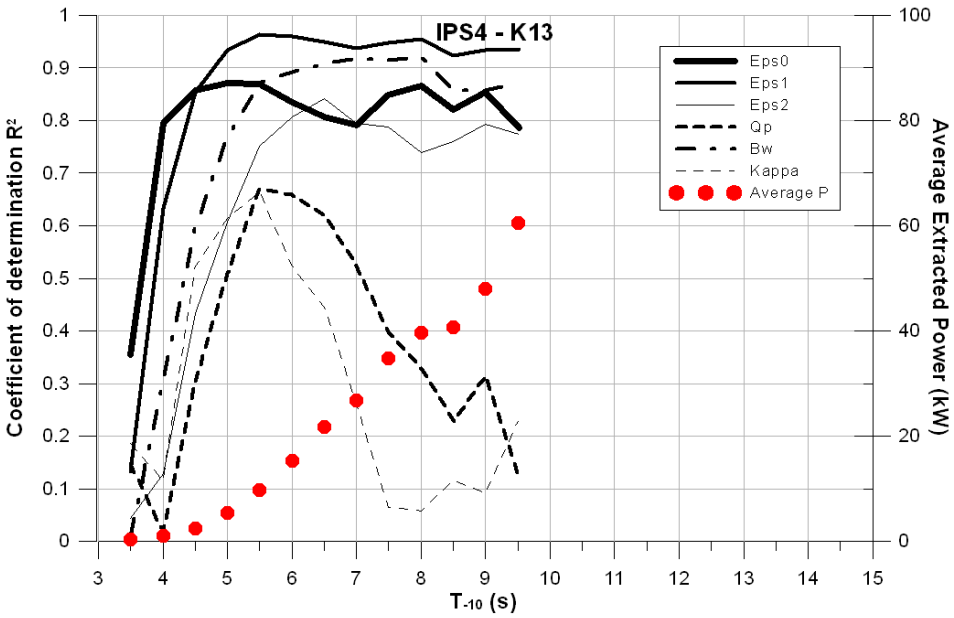

(b)

Figure 3.12: Id. Fig. 3.9 for configuration IPS4.

3.4 Groupiness statistics for a linear WEC

Some spectral methods for groupiness studies presented in Chapter 2 can be applied to the output signals of a WEC (e.g. displacements, velocities...) instead of the wave signal. Mean statistics on motion and velocity amplitudes can be easily obtained as soon as those signals satisfy the assumptions required by the selected method. This enables to derive a highly relevant design information concerning extreme motions (physical limits of the structure) as well as the power peaks output from the PTO mechanism ($P_{PTO}(t)$), among others. In this case, the Hilbert envelope method for Gaussian narrow-banded processes (see Section 2.5.1) is implemented for both signals $z(t)$ and $\dot{z}(t)$ of the 1-DOF linear system described in Section 3.2, which requires the computation of corresponding spectral moments, respectively as

$$\begin{aligned} m_{zn} &= \int_0^\infty f^n E_z(f)\,\mathrm{d}f \\ &= \int_0^\infty f^n |H_{z\eta}(f)|^2 E_\eta(f)\,\mathrm{d}f \end{aligned} \tag{3.29}$$

and

$$\begin{aligned} m_{\dot{z}n} &= \int_0^\infty f^n E_{\dot{z}}(f)\,\mathrm{d}f \\ &= 4\pi^2 \int_0^\infty f^{n+2} |H_{z\eta}(f)|^2 E_\eta(f)\,\mathrm{d}f \end{aligned} \tag{3.30}$$

Assuming the output signals $z(t)$ and $\dot{z}(t)$ – obtained by "filtering" the waves – are reasonably narrow-banded, the following statistics are derived for the threshold levels ρ_z^* and $\rho_{\dot{z}}^*$ (Eq. (2.33)) respectively as

$$\overline{H}_z = \frac{1}{\sqrt{2\pi}}\left(\frac{\sqrt{1+\nu_z^2}}{\nu_z}\right)\frac{\sqrt{m_{z0}}}{\rho_z^*} \qquad \overline{G}_z = \frac{1}{\sqrt{2\pi}}\left(\frac{\sqrt{1+\nu_z^2}}{\nu_z}\right)\frac{\sqrt{m_{z0}}}{\rho_z^*}e^{\rho_z^{*2}/2m_{z0}} \tag{3.31}$$

and

$$\overline{H}_{\dot{z}} = \frac{1}{\sqrt{2\pi}}\left(\frac{\sqrt{1+\nu_{\dot{z}}^2}}{\nu_{\dot{z}}}\right)\frac{\sqrt{m_{\dot{z}0}}}{\rho_{\dot{z}}^*} \qquad \overline{G}_{\dot{z}} = \frac{1}{\sqrt{2\pi}}\left(\frac{\sqrt{1+\nu_{\dot{z}}^2}}{\nu_{\dot{z}}}\right)\frac{\sqrt{m_{\dot{z}0}}}{\rho_{\dot{z}}^*}e^{\rho_{\dot{z}}^{*2}/2m_{\dot{z}0}} \tag{3.32}$$

for groups of successive heights related to signals $z(t)$ and $\dot{z}(t)$ – as mean length of high runs ($\overline{H}_z$, $\overline{H}_{\dot{z}}$) and total runs ($\overline{G}_z$, $\overline{G}_{\dot{z}}$) –, where narrowness parameters ν_z and $\nu_{\dot{z}}$ are respectively defined as (Eq. (2.34))

$$\nu_z = \sqrt{\frac{m_{z0}m_{z2}}{m_{z1}^2} - 1} \tag{3.33}$$

$$\nu_{\dot{z}} = \sqrt{\frac{m_{\dot{z}0} m_{\dot{z}2}}{m_{\dot{z}1}^2} - 1} \tag{3.34}$$

Group statistics on the instantaneous extracted power $P_{PTO}(t)$ – with respect to threshlod level P^*_{PTO}) – may be inferred by making the assumption 1) a height of $\dot{z}(t)$ (crest-to-trough) is roughly equal to twice the envelope value at the same instant, which is valid as soon as the signal is considered as narrow-banded ($\nu_{\dot{z}}^2 <<1$), and 2) the fact two power peaks correpond to one velocity height. Hence,

$$\overline{H}_{P_{PTO}} = \sqrt{\frac{2}{\pi}} \left(\frac{\sqrt{1+\nu_{\dot{z}}^2}}{\nu_{\dot{z}}} \right) \frac{\sqrt{m_{\dot{z}0}}}{\rho^*_{\dot{z}}} \tag{3.35}$$

$$\overline{G}_{P_{PTO}} = \sqrt{\frac{2}{\pi}} \left(\frac{\sqrt{1+\nu_{\dot{z}}^2}}{\nu_{\dot{z}}} \right) \frac{\sqrt{m_{\dot{z}0}}}{\rho^*_{\dot{z}}} e^{\rho^{*2}_{\dot{z}}/2m_{\dot{z}0}} \tag{3.36}$$

where $\rho^*_{\dot{z}} = \sqrt{P^*_{PTO}/C_{PTO}}$ (see Eq. (3.11)).

In order to assess the relevance of this application, the behaviour of the 1-DOF heaving buoy in a Bretschneider sea-state ($H_{m0} = 2m$, $T_p = 8s$, *method a*, see Appendices B&D) is simulated over $3600s$. The theoretical statistics on wave groups (Eq. (2.33)) and groups of power peaks (Eq. (3.35)&(3.36)) are calculated on unfiltered spectral estimations of both $E(f)$ and $E_{\dot{z}}(f)$ (parameter $\varepsilon_{\dot{z},2}$ instead of $\nu_{\dot{z}}$) and are then compared to those derived from the envelopes' calculation in the simulation.

The results are depicted in figures 3.13(a-d). As the simulation is quite long ($3600s$) and spectra $E(f)$ and $E_{\dot{z}}(f)$ are rather narrow-banded ($\varepsilon_2 \approx 0.39$, $\varepsilon_{\dot{z},2} \approx 0.19$), a nice agreement is found between both theoretical and numerical statistics. Equally, the theoretical power peaks statistics are satisfactorily predicting those obtained in the simulation (through the envelope of $\dot{z}$), except for very large values of power, which would require much longer simulations.

In this sea-state, the mean number of power peaks exceeding the mean extracted power ($P^*_{PTO} = \overline{P_{PTO}}$) is 4, which is repeated every 8 peaks on average (i.e. every 4 waves). For threshold level $P^*_{PTO} = 5\overline{P_{PTO}}$, 2-peaks groups are observed on average, which are repeated every 26 peaks (or 13 waves, approximately). An excerpt of the 1-DOF linear buoy simulation is depicted in figure 3.14 as the instantaneous extracted power (kW) along with the multiples (gray levels) of the mean value $\overline{P_{PTO}(t)}$ (red level).

Thanks to the spectral approach, it is therefore possible to derive statistics on groups of power peaks as soon as the motions of oscillating WEC models – as those described so far – can be assumed as narrow-banded. This kind of information may be of great interest when dimensioning more realistic PTO converters with short-term energy storage, as those described in Section 3.6.

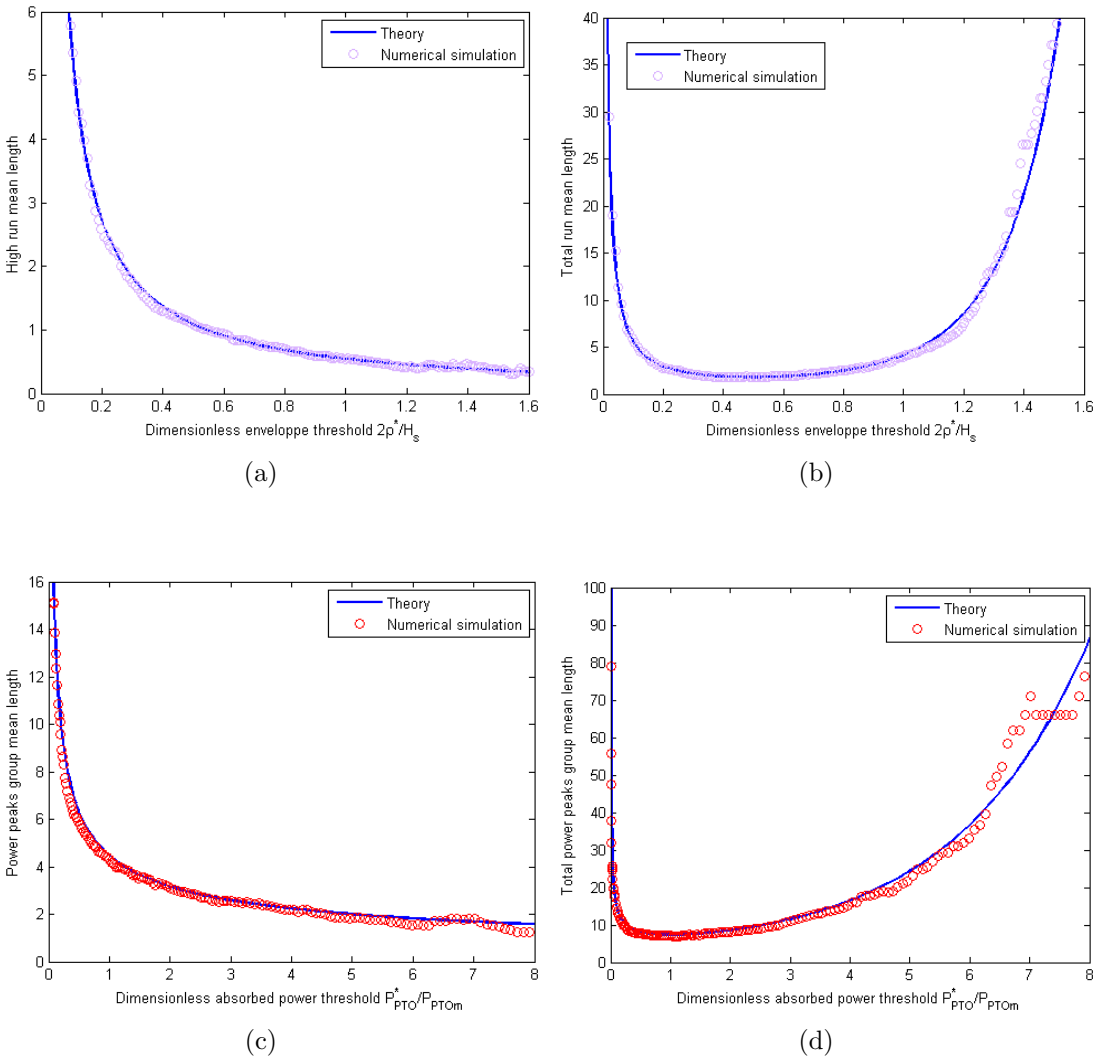

Figure 3.13: Statistics on groups of successive wave heights (top) and power peaks (bottom) for $\eta(t)$ and $P_{PTO}(t)$ simulated over 3600s (Bretschneider target sea-state); the mean lengths of high runs (a) and total runs (b) are given against the dimensionless height $2\rho^*/H_s$; the mean lengths of high peaks runs (c) and total runs (d) are given against the dimensionless power $P^*_{PTO}/\overline{P_{PTO}}$; the theoretical curves obtained from equations (2.33), (3.35)&(3.36) are plotted in blue.

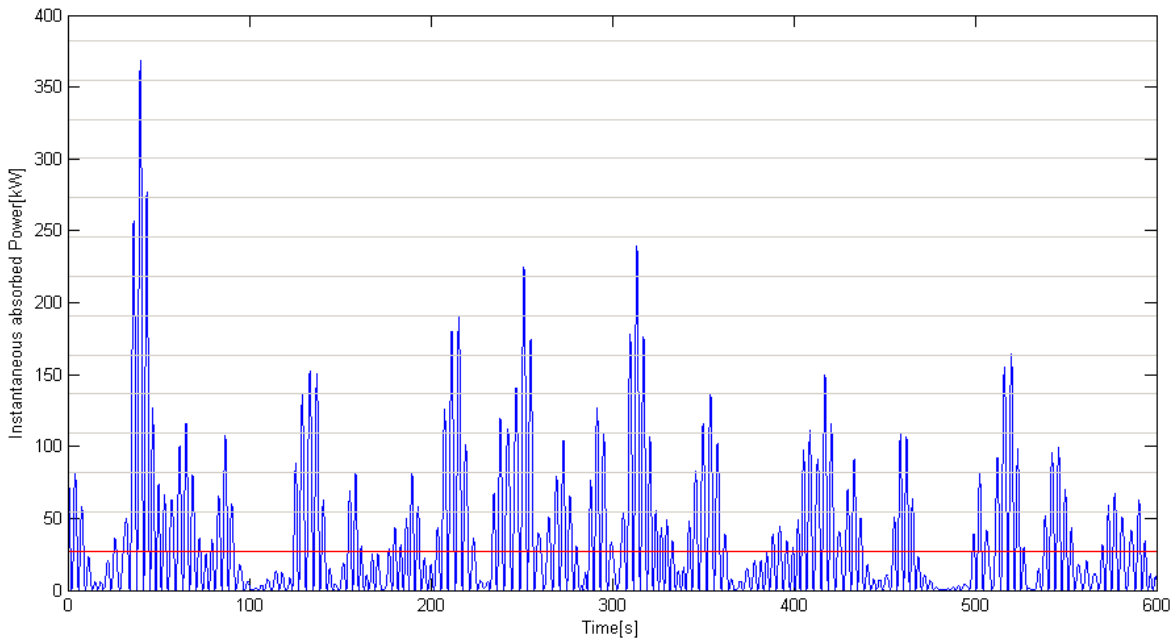

Figure 3.14: Numerical simulation of an axi-symmetric heaving buoy: instantaneous extracted power (kW) and multiples (gray levels) of mean extracted power $\overline{P_{PTO}(t)}$ (red level).

3.5 Influence of spectral bandwidth in wave numerical simulations

This section investigates the practical estimation of mean power $\overline{P_{PTO}}$ extracted by a WEC modelled in time domain, whose input information is the water elevation $\eta(t)$ simulated from a target wave spectrum. It is shown that the spectral bandwidth of the sea-state, once again, plays an important role in the power estimation's accuracy.

3.5.1 Estimation error on the variance of a simulated Gaussian centred signal

Let us remind that water elevation $\eta(t, x, y)$ is generally assumed as a stationary, homogeneous and ergodic centred Gaussian process. The property of ergodicity namely permits to state that the mean value obtained in a time realisation $\eta_T(t)$ of a given process over $[0; T]$ is an *unbiased* estimation of the theoretical mean (0 here, since the process is centred), to which it should converge as $T \to \infty$ (see Papoulis, 1991). In the case of simple linear hydro-mechanical models such as those described so far, it may be concluded that any signal $u(t)$ output from the system is *ipso facto* centred and Gaussian. The following results – derived for a signal $u(t)$ – are therefore valid for $\eta(t)$ as well as e.g. $\dot{z}(t)$, the velocity process of the DOF related to the energy conversion mechanism of the 1-DOF WEC (Fig. 3.1).

It can be shown (see e.g. Max, 2004; Papoulis, 1991) that the variance of the auto-correlation function $R_{uu}(\tau)$ of $u(t)$ estimated on a – sufficiently long – interval $[0; T]$ for a time-lag τ is approached by the integral expression

$$\sigma^2_{R_{uu}(\tau)} = var\left[R_{uu}(\tau)\right] \approx \frac{1}{T}\int_{-\infty}^{\infty}\left[R^2_{uu}(\theta) + R_{uu}(\theta+\tau)R_{uu}(\theta-\tau)\right]\,\mathrm{d}\theta \tag{3.37}$$

Let us indicate that in the frame of the present purposes, the numerical simulations are always considered as "sufficiently long" so that the approximation in equation (3.37) is considered as an equality[3]. As $\overline{u^2(t)} = \sigma^2_u = R_{uu}(0)$, we obtain for $\tau = 0$

$$\sigma^2_{R_{uu}(0)} = \frac{2}{T}\int_{-\infty}^{\infty} R^2_{uu}(\theta)\,\mathrm{d}\theta \tag{3.38}$$

[3]As stressed in Papoulis (1991), the degree of approximation in equation (3.37) is related to $1/T$; the equality is therefore assumed as soon as T is sufficiently long.

As exemplified in Max (2004), if one considers a B-wide white noise – that is, a signal whose spectral density is constant over this interval and 0 elsewhere – of length T, the variance of estimated $R_{uu}(0)$ simplifies to

$$\sigma^2_{R_{uu}(0)} = \frac{R^2_{uu}(0)}{BT} \tag{3.39}$$

In other words, the estimation of $R_{uu}(0)$ carried out in a realisation $u_T(t)$ over $[0;T]$ will converge to the theoretical value (characteristic of the process) as both length T and spectral bandwidth B increase. The estimation error is therefore proportional to the square root of their product. As recalled by this author, it is necessary to insist on that point for the idea the simulation must be as long as the simulated frequencies are low is still widely – and erroneously – admitted. At given simulation length T, only the spectral bandwidth is responsible for the estimation precision.

By the same manner, for a Gaussian random process $u(t)$ characterised by its energy spectral density $E_u(f)$, it is shown in the following that the error committed on the estimation of $R_{uu}(\tau)$ only depends on T and the spectral shape of $E_u(f)$ (bandwidth and energy). If the density is known, the variance of $R_{uu}(0)$ may therefore be exactly calculated against T.

Indeed, as the continuous function $R_{uu}(\tau)$ is defined in $\mathbb{R}$ and square integrable (even, bounded and rapidly converging to 0), the Parseval's theorem (see Appendix B, Eq. (B.11)) may be applied, as

$$\begin{aligned}
\int_{-\infty}^{\infty} R^2_{uu}(\theta)\,\mathrm{d}\theta = \int_{-\infty}^{\infty} \left|R^2_{uu}(\theta)\right|\,\mathrm{d}\theta &= \frac{1}{2\pi}\int_{-\infty}^{\infty} \left|\mathcal{F}\{R_{uu}(\theta)\}(\omega)\right|^2\,\mathrm{d}\omega \\
&= \frac{1}{2\pi}\int_{-\infty}^{\infty} \left|2\pi G_u(\omega)\right|^2\,\mathrm{d}\omega \\
&= 2\pi\int_{-\infty}^{\infty} \left|G_u(\omega)\right|^2\,\mathrm{d}\omega \\
&= 2\pi\int_{-\infty}^{\infty} G^2_u(\omega)\,\mathrm{d}\omega \\
&= 2\int_{0}^{\infty} G^2_u(f)\,\mathrm{d}f \\
&= \frac{1}{2}\int_{0}^{\infty} E^2_u(f)\,\mathrm{d}f
\end{aligned} \tag{3.40}$$

according to equations (2.2)&(2.5). Hence, this yields from equation (3.38)

$$\begin{aligned}
\sigma^2_{R_{uu}(0)} &= \frac{2}{T}\cdot\left(\frac{1}{2}\int_{0}^{\infty} E^2_u(f)\,\mathrm{d}f\right) \\
&= \frac{1}{T}\int_{0}^{\infty} E^2_u(f)\,\mathrm{d}f
\end{aligned} \tag{3.41}$$

Besides, it may be shown (see e.g. Ochi, 1988) that the estimator of variance σ_u^2

$$\hat{\sigma}_u^2 = \frac{1}{N_{PTS}} \sum_{i=i}^{N_{PTS}} {}^i u_T^2$$

calculated in a given N_{PTS}-points realisation $({}^i u_T)$ of $u(t)$ (whose length is therefore $T = (N_{PTS} - 1)\Delta t \approx N_{PTS}\Delta t$ as $N_{PTS} >> 1$) is a χ^2-distributed random value with N_{PTS} degrees of freedom. Accordingly, its expectation and variance are σ_u^2 and $\frac{2}{N_{PTS}}\sigma_u^4$ respectively; furthermore, its distribution should tend to a normal law as $N_{PTS} \to \infty$. This is exact however if the hypothesis of statistical independency of $({}^i u_T)$ is assumable only. Now, as time step Δt decreases, the dependency between two successive simulation points ${}^i u_T$ and ${}^{i+1} u_T$ is likely to increase. Let us denote the variance under statistical independency assumption by $\sigma^2_{R_{uu}(0)-i.s.}$, it may be written

$$\begin{aligned}
\sigma^2_{R_{uu}(0)-i.s.} &= \frac{2}{N_{PTS}}\sigma_u^4 = \frac{2}{N_{PTS}} m_{u0}^2 \\
&= \frac{2m_{u0}^2}{1 + \frac{T}{\Delta t}} \\
&\approx \frac{2\Delta t}{T} m_{u0}^2
\end{aligned} \tag{3.42}$$

Let us now introduce the *equivalent spectral bandwidth* Λ_u (Hz) of process $u(t)$ defined as (see Eq. (3.16) and Appendix A, Eq. (A.16))

$$\Lambda_u = \frac{m_{u0}^2}{\int_0^\infty E_u^2(f)\,\mathrm{d}f} \tag{3.43}$$

By combining equations (3.41), (3.42) and (3.43), it yields

$$\begin{aligned}
\sigma^2_{R_{uu}(0)} &= \frac{1}{T}\int_0^\infty E_u^2(f)\,\mathrm{d}f \\
&= \frac{1}{T}\frac{m_{u0}^2}{\Lambda_u} \\
&= \sigma^2_{R_{uu}(0)-i.s.}\frac{N_{PTS}}{2T\Lambda_u} \\
&= \frac{\sigma^2_{R_{uu}(0)-i.s.}}{2\Delta t\Lambda_u} \\
&= \sigma^2_{R_{uu}(0)-i.s.}\frac{f_{Nyq}}{\Lambda_u}
\end{aligned} \tag{3.44}$$

where f_{Nyq} represents the Nyquist frequency, defined as the highest detectable frequency at sampling frequency f_e, as $f_{Nyq} = f_e/2 = 1/(2\Delta t)$ (with Δt expressed in s). The exact

variance of the signal's variance estimator is then proportional to the variance derived under statistical independency hypothesis, whose multiplicative factor is equal to the ratio of f_{Nyq} over equivalent spectral bandwidth Λ_u. In case both are equal (i.e. the time step is adjusted to the process' spectral bandwidth), it may be considered that the independency hypothethis is roughly admissible. However, this latter remains very sensitive from a process to another, and consequently is too strong for the present applications.

3.5.2 Application to the numerical estimation of H_{m0}^2 and $\overline{P_{PTO}}$ (linear system)

Let us now successively consider the two following centred Gaussian processes: $u_a(t) = 4\eta(t)$ and $u_b(t) = \sqrt{C_{PTO}}\dot{z}(t)$. For the first one, we have

$$\begin{aligned} R_{u_a u_a}(0) &= \overline{u_a^2(t)} = 16\overline{\eta^2(t)} \\ &= 16R(0) \\ &= 16m_0 = H_{m0}^2 \end{aligned} \tag{3.45}$$

By the same manner for the second one,

$$\begin{aligned} R_{u_b u_b}(0) &= \overline{u_b^2(t)} = C_{PTO}\overline{\dot{z}^2(t)} \\ &= C_{PTO}R_{\dot{z}\dot{z}}(0) = C_{PTO}\sigma_{\dot{z}}^2 \\ &= C_{PTO}m_{\dot{z}0} = \overline{P_{PTO}(t)} = \overline{P_{PTO}} \end{aligned} \tag{3.46}$$

Therefore, the standard deviation of both H_{m0}^2 and $\overline{P_{PTO}}$ estimators within a large sample containing T-long simulations $u_{aT}(t)$ and $u_{bT}(t)$ is known, as

$$\begin{aligned} \sigma_{H_{m0}^2} &= \frac{16}{\sqrt{T}}\sqrt{\int_0^\infty E^2(f)\,\mathrm{d}f} \\ &= \frac{16m_{u0}}{\sqrt{T\Lambda}} \\ &= \frac{H_{m0}^2}{\sqrt{T\Lambda}} \end{aligned} \tag{3.47}$$

– where parameter Λ is obtained on the wave spectrum $E(f)$ –, and

$$\begin{aligned}\sigma_{\overline{P_{PTO}}} &= \frac{C_{PTO}}{\sqrt{T}}\sqrt{\int_0^\infty E_{\dot{z}}^2(f)\,\mathrm{d}f} \\ &= \frac{C_{PTO}m_{\dot{z}0}}{\sqrt{T\Lambda_{\dot{z}}}} \\ &= \frac{\overline{P_{PTO}}}{\sqrt{T\Lambda_{\dot{z}}}}\end{aligned} \tag{3.48}$$

where parameter $\Lambda_{\dot{z}}$ is derived from the velocity spectrum $E_{\dot{z}}(f)$. The (unbiased) expectations of H_{m0}^2 and $\overline{P_{PTO}}$ are exactly known thanks to the 0th-order spectral moments in equations (3.45)&(3.46).

These formulations clearly emphasize the estimation error on both parameters is diretcly influenced by the spectral bandwidth of densities $E(f)$ and $E_{\dot{z}}(f)$ respectively. Of course, the most interesting results for the purposes of this work concern the mean extracted power, but it seems also of great interest to compare the numerical estimations with theory in the case of a wave parameter such as H_{m0}^2. Figures 3.15(a-f) depict the obtained distributions of H_{m0}^2 estimator for 300 simulations of length $T = 100$ to $3600s$ with a $\Delta t = 0.1s$ time step. The simulation method used to generate the wave realisations is the – correct – one described in Tucker et al. (1984) and presented in Appendix B (referred to as *method a*). For each simulation, both amplitudes and phases are randomly selected indeed, as Rayleigh- and uniformly distributed respectively. The simulated target sea-state $E(f)(= S(f))$ is a Bretschneider with $H_s = 2m$ and $T_p = 10s$. Figures 3.16(a&b) summarise – as absolute (a) and relative (b) values – the previous results against simulation duration T (more durations were simulated for a better visualisation). An excellent agreement is found between the sample estimation characteristics and theory, which validates *method a* as a consistent simulation method against theory. In particular, the $T^{-1/2}$ standard deviation decrease with simulation length is clearly observed. Equation (3.44) is also verified in the sample results, with $f_{Nyq} = 5Hz$ and $\Lambda = 0.115Hz$.

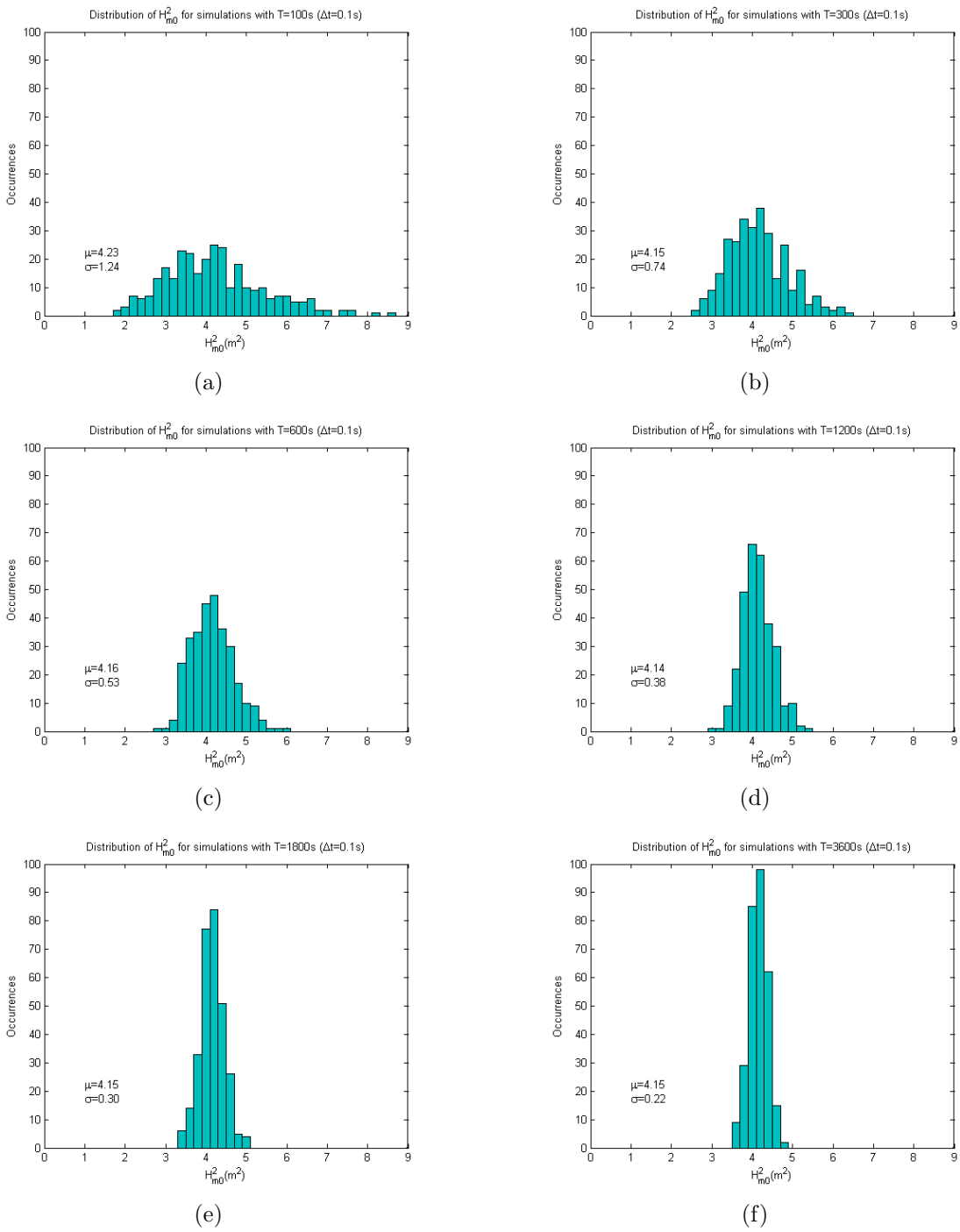

Figure 3.15: H^2_{m0} estimator distributions obtained in 300 wave simulation samples of duration $T = 100, 300, 600, 1200, 1800$ and $3600s$ (a-f); mean value (μ) and standard deviation (σ) of the distributions (m^2).

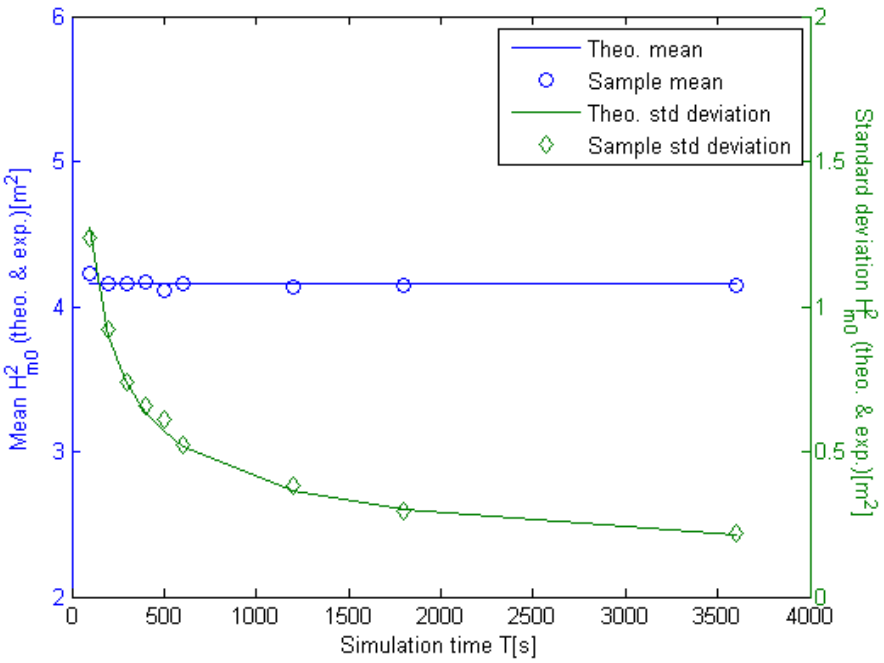

(a)

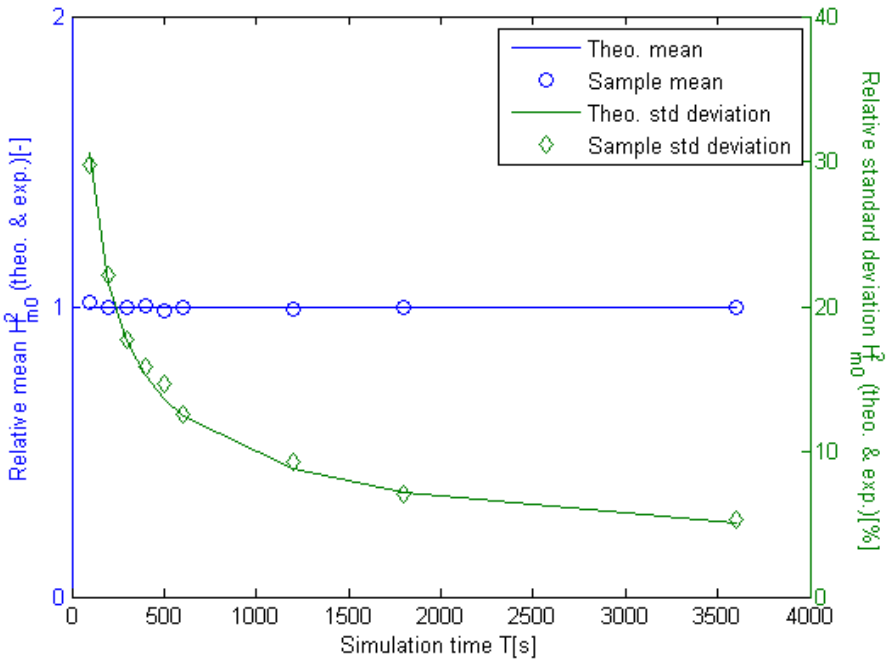

(b)

Figure 3.16: Theoretical (plain line) and sample (markers) mean values (left Y-axis) and standard deviations (right Y-axis) related to wave parameter H^2_{m0}; results in absolute [m^2] (a) and relative (b) value (non-dimensionalised by the theoretical mean value); Bretschneider target sea-state ($H_{m0} = 2m$ et $T_p = 10s$, *method a*).

For a given linear system, we know that the velocity spectral density $E_{\dot{z}}(f)$ can be calculated as soon as the wave spectral contents $E(f)$ are available (Eq. (3.9)). Hence, as well as for parameter H_{m0}^2, the estimation error on $\overline{P_{PTO}}$ averaged from simulation samples should also decrease as the square root of both simulation length T and spectral bandwidth $\Lambda_{\dot{z}}$ increase, following equation (3.48). The error is also expected to increase with mean value $\overline{P_{PTO}}$. Figures 3.18(a-e) illustrate the distributions of $\overline{P_{PTO}}$ estimator obtained in 300-simulations samples of an axi-symmetrical heaving buoy for the same durations as H_{m0}^2 and Bretschneider target spectrum with $H_s = 2m$ and $T_e = 7s$ (i.e. $T_p \approx 8.2s$). The main difference with H_{m0}^2 here lies in the fact the velocity signal is not calculated as a Fourier series, unlike $\eta(t)$ – this would then lead to the same kind of results as H_{m0}^2 (see Appendix D) –, but rather obtained as the solution of the Cummins' equation in time-domain (see Eq. (3.1) and Cummins, 1962). This WEC model (Ricci et al., 2008; Saulnier et al., 2009) is cylindrical and characterised by $5m$-radius and draft. The PTO mechanism is modelled as a linear damper ($C_{PTO} = 200000kg.s^{-1}$). [More information about the WEC modelling as well as the Cummins' equation resolution scheme can be found in the two papers cited hereabove.] For each simulation, the initial transient regime is left out due to the rest conditions of the buoy at $t = 0$, and arbitratily fixed to $T_{RT} = 200s$, so that the simulations actually are run over $T + T_{RT} = T + 200s$: the mean values and standard deviations of the resulting estimator distributions are therefore calculated on the permanent regime corresponding to the T last seconds of each simulation. As the mechanical system is modelled as linear, the mean and standard deviation values of $\overline{P_{PTO}}$ estimator are exactly known from the model's impedance and target wave-spectrum. It is then possible to compare the samples' estimation parameters to theory, which are depicted in figure 3.17. Once again, a very good agreement is found when simulating waves with *method a*. Another wave simulation method – called here *method b*, commonly adopted in offshore engineering, see Olagnon et al. (1990) – is also implemented, which only selects random phases (the amplitudes are fixed as in Eq. (2.28)). Such a simplification – only correct in the limit $T \to \infty$ – permits to significantly reduce the estimator dispersion, as shown in that figure, while it does not seem to imply any bias in the mean power estimation. The question of the wave simulation method is particularly pointed out in the author's paper (Saulnier et al., 2009).

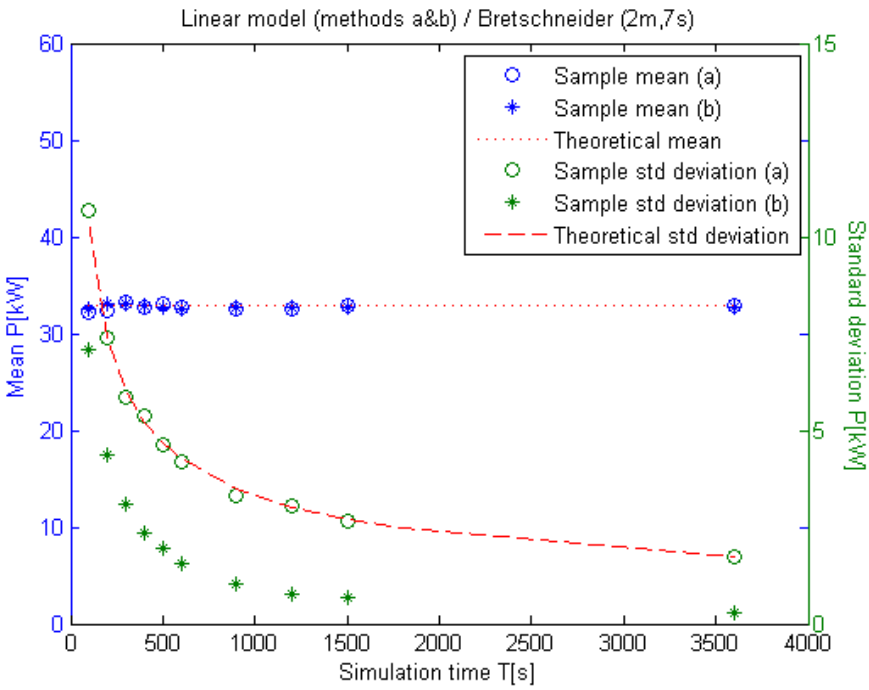

Figure 3.17: Theoretical (dotted line) and sample (circles) mean values (left Y-axis) and standard deviations (right Y-axis) related to mean power $\overline{P_{PTO}}$ in a Bretschneider target sea-state ($H_{m0} = 2m$ and $T_e = 7s$, *method a*) after transient regime of the linear WEC buoy modelled in the time domain; results obtained with *method b* are plotted with stars.

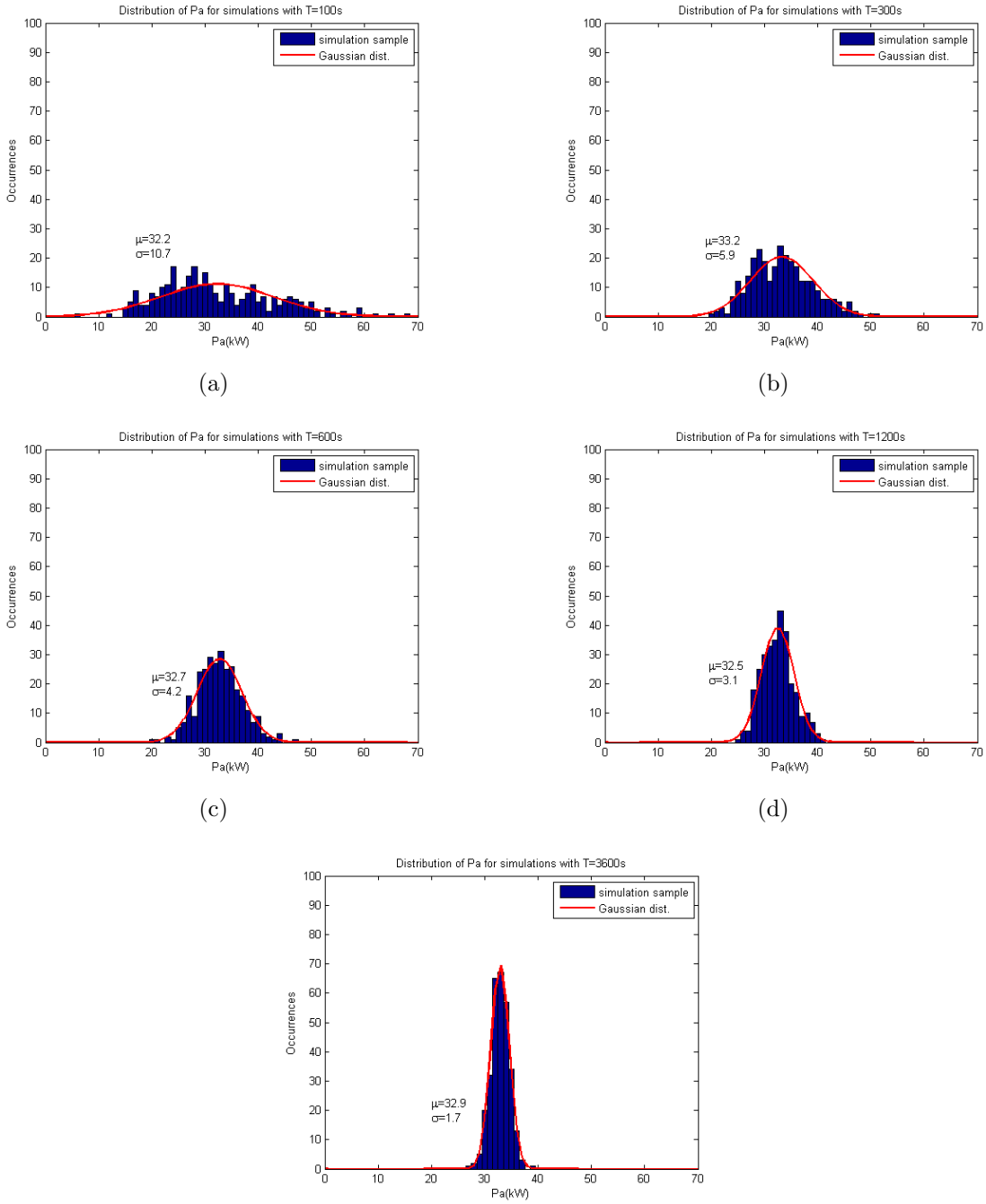

Figure 3.18: $\overline{P_{PTO}}$ estimator distributions obtained in 300 wave simulation samples of duration $T = 100, 300, 600, 1200$ and $3600s$ (a-e) after transient regime of the linear WEC buoy modelled in the time domain; mean value (μ) and standard deviation (σ) of the distributions (kW), and Gaussian-law fitting.

3.5.3 Application to the numerical estimation of $\overline{P_{PTO}}$ (non-linear system)

It is now of interest to observe the same results that are obtained when dealing with more realistic – and therefore somewhat non-linear – WEC devices and sea conditions. Here, the case of the cylindrical buoy esquipped with a non-linear PTO (hydraulic circuit with low- and high- pressure gas accumulators) is investigated in sea-states estimated by means of accelerometric buoys. [This work can also be integrally found in Saulnier et al. (2009).]

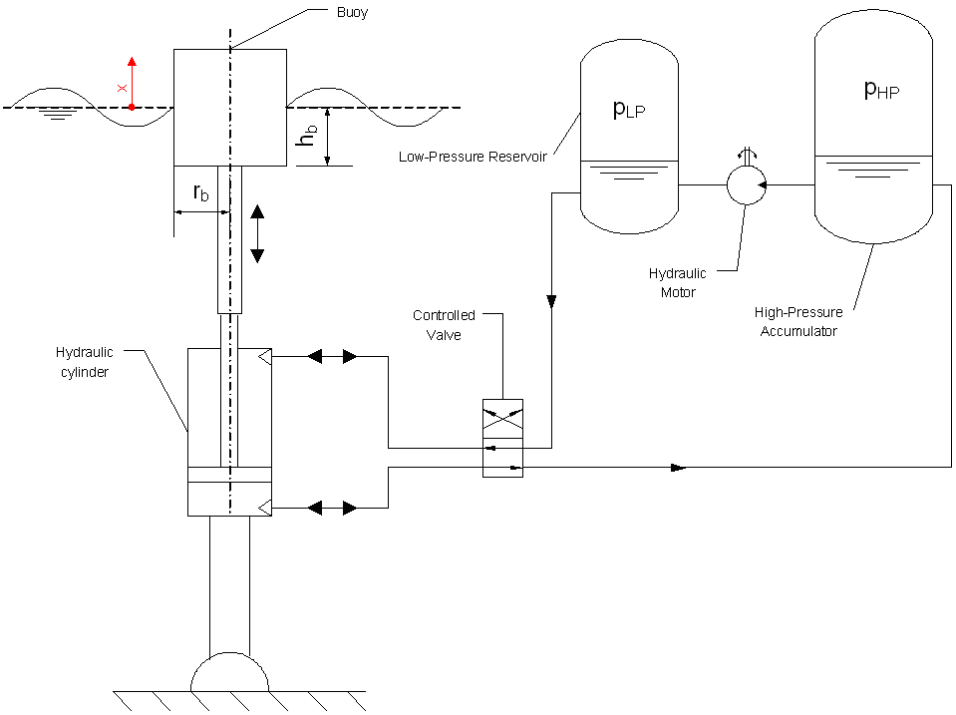

Figure 3.19: Heaving buoy WEC equipped with a hydraulic PTO device (low- and high-pressure gas accumulators coupled to a hydraulic motor, as described in Ricci et al., 2008; Saulnier et al., 2009).

This system is very similar to the previous – linear – one since the heaving float's shape is the same. However, the energy absorption is now operated by a piston which pumps oil from the low- to the high-pressure gas accumulator, so that the absorbed mechanical energy in heave is converted into hydraulic energy, as short-term stored high-pressure oil flowing between both accumulators and actuating the hydraulic motor (Fig. 3.19). The inertia of such a device is therefore determined by the accumulators' dimensions, the low- and high-pressure inside both, and the maximum flow rate into the hydraulic motor. For more details about this PTO scheme, the author namely refers to Falcão (2005, 2007), and Henderson (2006) (PTO equipping the Pelamis WEC). This results in quite a complex non-linear equation system to be solved in the time domain,

whose resolution is thoroughly described in Ricci et al. (2008) and Saulnier et al. (2009) (Prony's method with ODE variable-step integration by 5th-order Runge-Kutta algorithm).

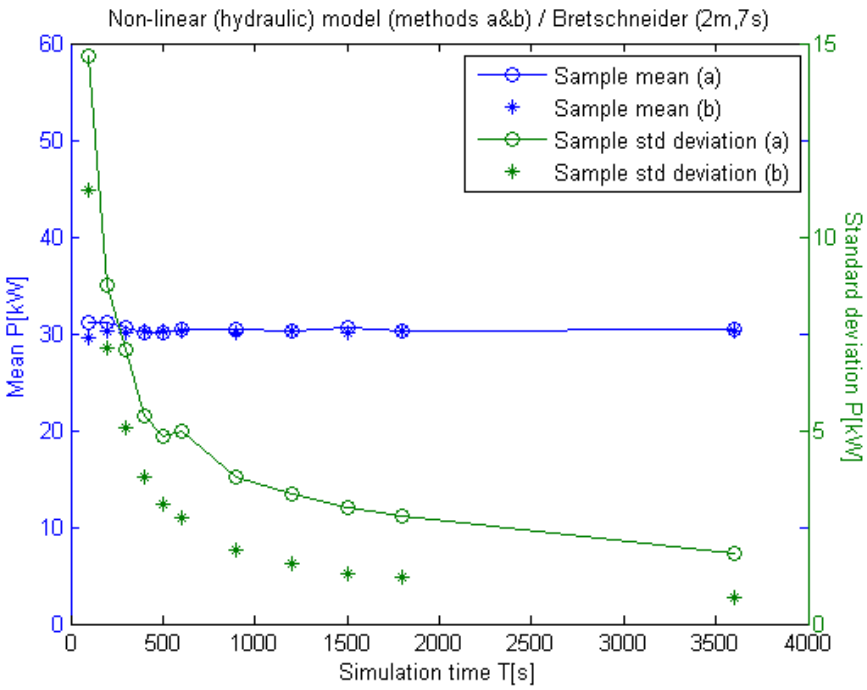

Figure 3.20: Sample (circles) mean values (left Y-axis) and standard deviations (right Y-axis) related to mean power $\overline{P_{PTO}}$ in a Bretschneider target sea-state ($H_{m0} = 2m$ and $T_e = 7s$, *method a*) after transient regime of the non-linear WEC buoy modelled in the time domain; results obtained with *method b* are plotted with stars.

First, the mean power extracted by the system is estimated in a Bretschneider sea-state ($H_{m0} = 2m$ and $T_e = 7s$) for various 300-simulations samples of fixed duration T, as previously. Again, a $200s$ transient regime is disregarded for the calculation of mean extracted power, and the wave field is simulated using both methods a and b. As in figure 3.17, the results related to the non-linear WEC are plotted in figure 3.20. As the model is not linear anymore, no theoretical curve can be derived for both the mean value and standard deviation of the power estimator; equations (3.14)&(3.48) cannot be applied here. However, the trends observed in figure 3.20 are very similar to those in figure 3.17. Indeed, the standard deviation's decrease (green circles and stars) remains unchanged, while, once again, *method b* leads to a reduction of the estimator dispersion, which seems to decrease even more as T increases. Last, the mean power estimation does not seem to be biased anyhow when using *method b* for the input waves simulation.

Let us now consider more realistic sea-states, by simulating waves from three target spectral densities estimated from buoy measurements off Figueira da Foz, at a $\sim 82m$

Table 3.1: Spectral characteristics of three spectra estimated off Figueira da Foz, Portugal (Saulnier and Pontes, 2006).

Ref.	FF198310261200	FF198912070000	FF199404240900
$H_{m0}(m)$	0.93	1.86	2.35
$T_{-10}(s)$	9.22	10.77	8.48
$T_p(s)$	9.41	13.33	8.70
ε_0	0.286	0.342	0.368
κ	0.615	0.492	0.354
$\Lambda(Hz)$	0.081	0.087	0.137
$P_w(kW/m)$	4.0	19.6	23.8

water depth. The spectral data related to these "representative" sea-states are drawn from the WAVETRAIN deliverable n°5 (see Saulnier and Pontes, 2006, public data, Fig. 3.21(a,c,e)) and the main wave parameters are listed in table 3.1 (parameter Λ is added in the table for the purpose of the study). The correponding estimation results are given in figures 3.21(b,d,f). According to these figures, one can reasonably deduce that both the WEC non-linearities (hydraulic PTO) and realistic sea conditions (possibly multi-peaked spectra) are not resulting in far different estimation patterns from the previous ones. The standard deviation's decrease still is noticeable and more pronounced for *method b* than for *method a*, as previously. Similarly, *method b* does not apparently lead to biased mean power estimations.

In order to observe the influence of the target wave spectra's bandwidth, the spectral parameter Λ_v related to the velocity process of an equivalent linear system (Eq. (3.48)) is calculated against duration T, as

$$\Lambda_v(T) = \frac{1}{T} \cdot \left(\frac{\overline{P_{PTO}}(T)}{\sigma_{\overline{P_{PTO}}}(T)} \right)^2 \tag{3.49}$$

For the case of the Bretschneider sea-state ($H_{m0} = 2m$ and $T_e = 7s$), this parameter is derived from figure 3.20, and similarly for the three estimated spectra from figure 3.21. The value taken by this parameter against T along with its mean value obtained over all the samples are depicted in figures 3.22(a-d) for both simulation methods (a in blue, b in red) and the four sea-states. For each of these sea-states, Λ_v is found to be almost constant over T using *method a*: this indicates that the standard deviation of the mean power estimator still follows a $T^{-1/2}$ decrease law – as well as a linear system. On the contrary, the same parameter found by simulating waves with *method b* is unstable, which is due to the fact the related standard deviation decreases more abruptly against T.

In figure 3.23, the mean value $\overline{\Lambda_v}(Hz)$ is plotted against the spectral bandwidth parameters Λ, ε_0 and κ corresponding to the Bretschneider ($H_{m0} = 2m$ and $T_e = 7s$), FF198310261200, FF198912070000, and FF199404240900 sea-states. Even if the related spectra exhibit far different mean energy periods T_{-10} (from $7s$ to $10.8s$), a non-negligible

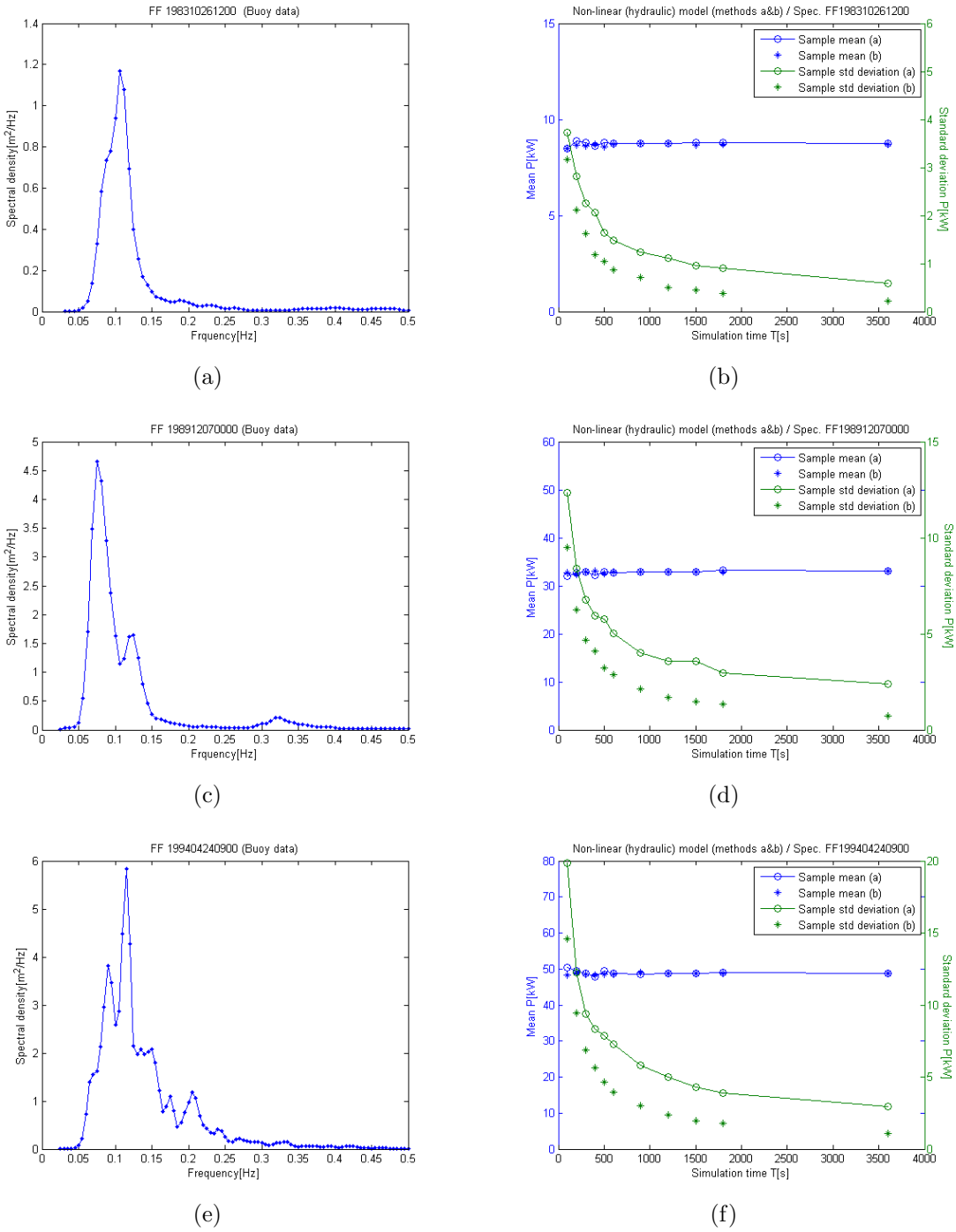

Figure 3.21: Sea-state spectral densities estimated by buoy measurements off Figueira da Foz (Portugal): $26^{th}$of October 1983, 12AM (a), $7^{th}$of December 1989, 0AM (c) and $24^{th}$of April 1994, 9AM (e) (Saulnier and Pontes, 2006); id. Fig. 3.20 for the corresponding estimated spectra (a,c,e).

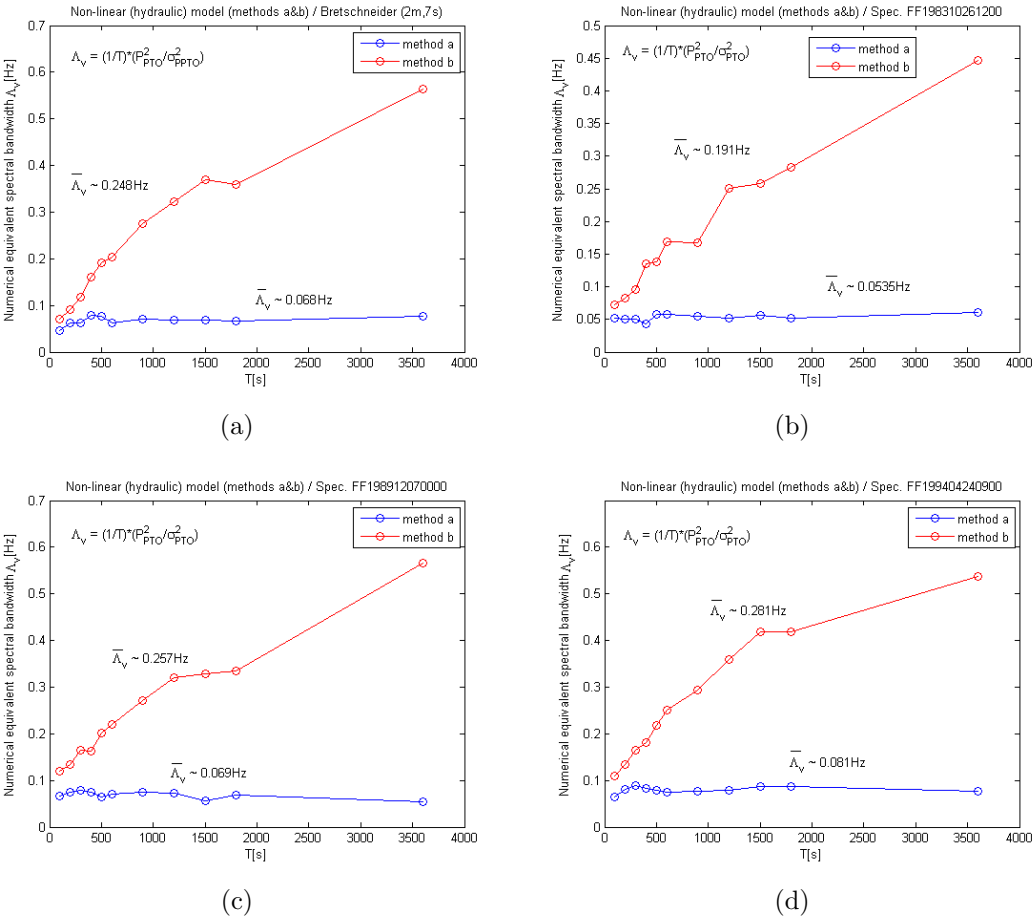

Figure 3.22: Spectral bandwidth parameter related to the heave velocity of an equivalent linear system against T (Eq. (3.49)) obtained from simulations of the target spectra: Bretschneider ($H_{m0} = 2m$ et $T_e = 7s$)(a) and Figueira da Foz sea-states (FF198310261200, FF198912070000, and FF199404240900 resp.)(b,c,d).

correlation of $\overline{\Lambda_v}$ with any of the three wave bandwidth parameters is noticeable. Accordingly, when the sea-state's spectral bandwidth increases – and provided the system is sensitive to the main waves – the response bandwidth of the equivalent linear system (Eq. (3.49)) tends to increase also, while the power estimator's dispersion is expected to decrease, as for a simple linear system.

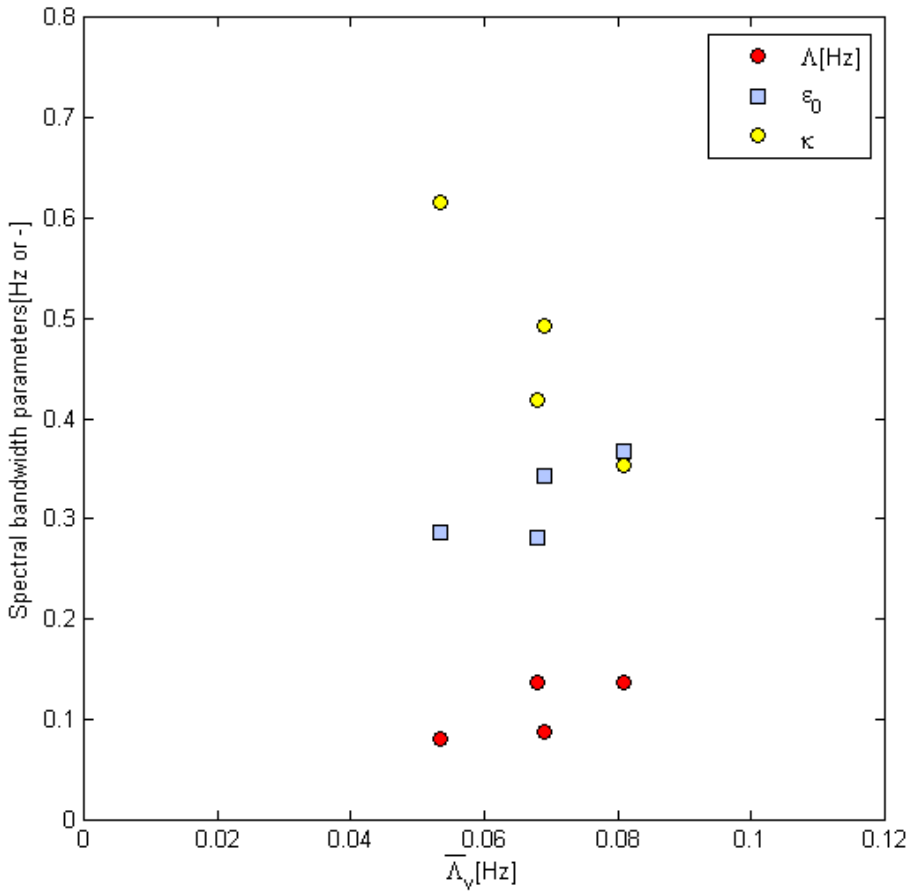

Figure 3.23: Wave spectral bandwidth parameters $\Lambda(Hz)$, ε_0 and κ against mean velocity spectral bandwidth of the linear equivalent system $\overline{\Lambda_v}(Hz)$ (Eq (3.49)) for the four sea-states Bretschneider ($H_{m0} = 2m$ and $T_e = 7s$), FF198310261200, FF198912070000, and FF199404240900.

3.6 Inertial WEC modelling and groupiness characterisation

One of the advantages of the linear modelling in frequency domain – also called *stochastic modelling* – is its straightforward numerical implementation once the structure's hydrodynamic coefficients are known. The statistics related to any degree of freedom may be derived from the wave spectral density, as formulated in the previous sections. If the wave spectrum is estimated from e.g. buoy measurements and considered as representative of the actual target sea-state process (stationary over 1 to 3 hours), the probable mean behaviour of the device in such a sea-state is automatically known through its mechanical impedance (and holds over the same duration).

On the contrary, solving the dynamic equations in time domain presents several drawbacks, among which the fact it may be significantly computer time consuming. Besides, the fact long and/or numerous simulations are necessary to obtain averaged estimations of dynamic parameters in the ongoing sea-state (estimation error decreases with simulation time, as shown in Section 3.5), unless the frequency modelling, which directly yields probabilistic values. However, as soon as a more realistic – and consequently, more complex – modelling, aiming at refining the description of the PTO mechanisms for instance, as hydraulic circuits with gas accumulators and hydraulic motors (Falcão, 2005; Henderson, 2006; Josset et al., 2007), air turbines for oscillating water columns (Falcão, 2002), low-head water turbines for overtopping systems (e.g. Wave Dragon, Kofoed, 2002) or direct generation converters (e.g. AWS, Polinder et al., 2005)... the frequency domain turns out to be impracticable.

Out of the physical principles on which they are based, any WEC is generally equipped with a PTO mechanism converting the extracted energy from waves into electricity and mostly inducing a short-term energy storage – related to the so-called *inertia* of the whole system. This can be easily illustrated by considering different energy converters installed on e.g. a simple heaving buoy as those described so far, as a linear direct generator (low inertia) or a hydraulic conversion system (possibly high inertia). In the first case, the mechanical heave energy is directly converted into electricity: the mechanical power fluctuations are integrally transmitted to the electrical generator's output, which accordingly exhibits the same fluctuations. In the second case, the mechanical heave energy is converted into hydraulic energy, as oil pumped and stored within a high-pressure gas accumulator, which in turn supplies a hydraulic motor through a constant flow-rate valve: the gas accumulator stores energy at short-term and the corresponding inertia therefore depends on the PTO characteristics as accumulator dimensions, inner pressure, nominal flow rate, ... As a consequence, the input power fluctuations are damped by the buffering device whereas the linear generator stores almost no energy at short-term, neither electrically nor mechanically.

This point is of a quite major interest, because if inertia is too low, a complex power

electronics assembling is required to smooth the output power (including choppers, rectifiers, inverters...) – which may induce electrical losses as well as be expensive. If inertia is too high, the output power is likely to be quite stabilised but may restrain the performance of the whole WEC due to possible mechanical, hydraulic, electrical... internal losses. Accordingly, the developers must find the best compromise between these both extremes, and adapt it to the particular features of their WEC, sometimes resorting to control laws. In that field, wave groupiness is a major concern for the design of WEC components, which is addressed in the present section.

3.6.1 Instantaneous power filtering by inertial flywheel

The short-term energy storage operated by a simple WEC can be modelled by introducing a flywheel of variable inertia coupled to the system's output. The instantaneous – mechanical – absorbed power $P_{PTO}(t)$ is considered here as input power $P_a(t) = P_{PTO}(t)$ supplying energy to the flywheel through equation (and neglecting all kind of losses, for the sake of simplicity)

$$P_{PTO}(t) \equiv P_a(t) = P_e(t) + \frac{I}{2K}\frac{\mathrm{d}P_e(t)}{\mathrm{d}t} \tag{3.50}$$

where $P_e(t)$ is the instantaneous electrical power obtained on the flywheel's rotor, which depends on the instantaneous rotational speed $\Omega(t)$ through an arbitrarily fixed control law: $P_e(t) = K\Omega^2(t)$, I denoting the flywheel's inertia against its rotation axis ($kg.m^2$) and K the control law constant ($kg.m^2.s^{-1}$). By also neglecting energy losses by friction on the rotor (see Falcão, 2002), it yields for the dynamic equation

$$P_a(t) - P_e(t) = I\Omega(t)\frac{\mathrm{d}\Omega(t)}{\mathrm{d}t} \tag{3.51}$$

which is similar to equation (3.50). The conveter's inertia may be defined here as the time constant $\mu = I/2K$ (s). Indeed, equation (3.50) is analogous to a RC electrical circuit with resistor $R(\equiv 1/2K)$ and capacitor $C(\equiv I)$, for which the product $\tau = RC$ characterises the circuit's time constant, that is, the time the system needs to reach ~63% of the permanent regime voltage. For given control law K, the higher the flywheel's inertia (I), the higher the short-term energy storage (μ).

By energy conservation, assuming rest conditions for the wheel at the beginning and end of the simulation, we have

$$\overline{P_{PTO}(t)} = \overline{P_a(t)} = \overline{P_e(t)} \tag{3.52}$$

what is observed in practice when simulation time T is much greater than time constant μ.

Let $E_{P_{PTO}}(f)$ be the energy spectral density of the power signal $P_{PTO}(t)$ (Eq. (3.23)). It is easy to show that the density related to the rotor's electrical power $E_{Pe}(t)$ is

$$E_{Pe}(f) = \frac{E_{P_{PTO}}(f)}{1 + \left(\frac{I}{2K}\right)^2 4\pi^2 f^2} = \frac{E_{P_{PTO}}(f)}{1 + (2\mu\pi f)^2} \tag{3.53}$$

As for the RC circuit, the flywheel performs a high-frequency filtering (low-pass filter). At given frequency $f(>0)$, $E_{Pe}(f) < E_{P_{PTO}}(f)$ so that the variance of $P_e(t)$ is always inferior to that of $P_{PTO}(t)$: the electrical output fluctuations therefore turn out to be reduced. In addition, $E_{Pe}(f)$ tends to zero against frequency much faster than $E_{P_{PTO}}(f)$, which results in lower output power mean frequencies. The electrical power signal $P_e(t)$ looks more smoothed ans stabilised than absorbed power $P_{PTO}(t)$.

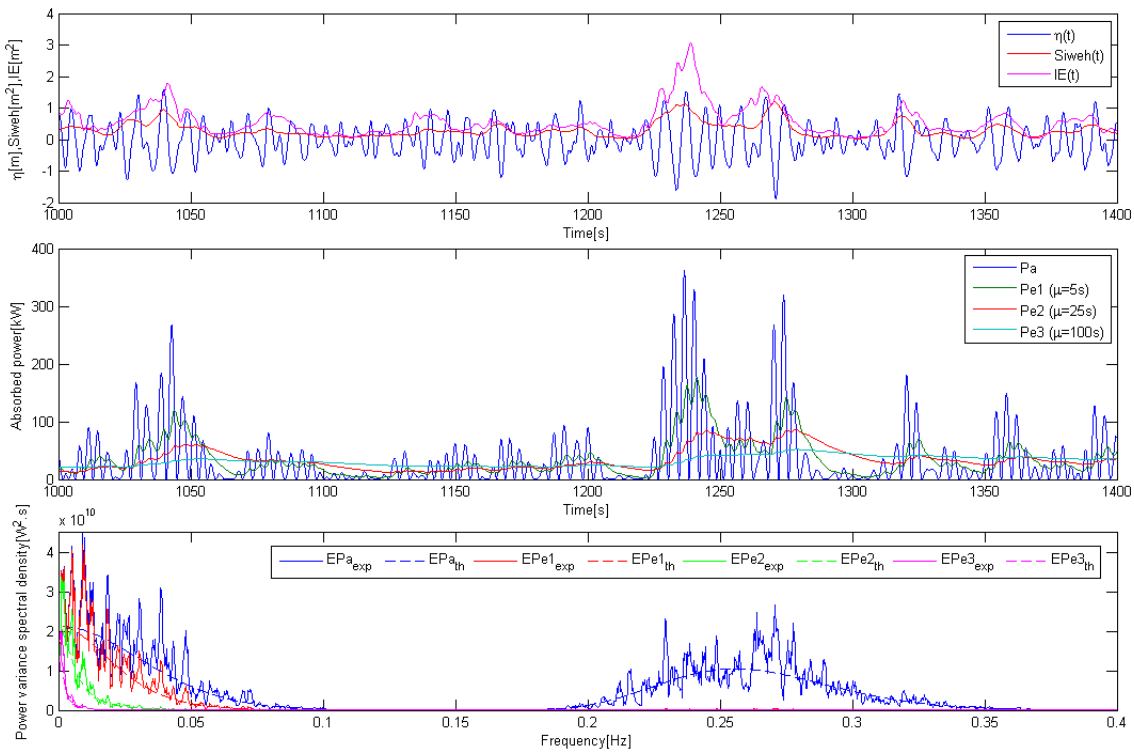

Figure 3.24: Simulation of a heaving axi-symmetric WEC equipped with a flywheel of inertia: $\mu = 0$ (no inertia), $\mu = 5s$ (low inertia), $\mu = 25s$ (mean inertia), and $\mu = 100s$ (high inertia) in a Bretschneider sea-state ($H_s = 2m$, $T_p = 8s$).

The axi-symmetric heaving linear WEC (see Section3.2) equipped with a flywheel with variable inertia is simulated in two different sea-states in figures 3.24 & 3.25 (after transient regime and neglecting losses in the energy conversion chain). Four inertial configurations are simulated: no inertia (linear damped system, $\mu = 0$), low inertia ($\mu = 5s$), mean inertia ($\mu = 25s$) and high inertia ($\mu = 100s$). Both sea-states (Fig. 3.26) are simulated over $3600s$ according to *method a*: the first one is unimodal (swell: $H_s = 2m$, $T_p = 8s$, and $Q_p = 2$, Fig. 3.24), while the second is bimodal (swell: $H_s = 1m$, $T_p = 11s$, and $Q_p = 5$; wind-sea: $H_s = 1m$, $T_p = 5s$, and $Q_p = 2$, Fig. 3.25). The spectral shapes are obtained using peakedness-variable Bretschneider spectra (Q_p-spectra, see Appendix C). The theoretical (Eq. (3.23)&(3.53)) and estimated rotor electrical power

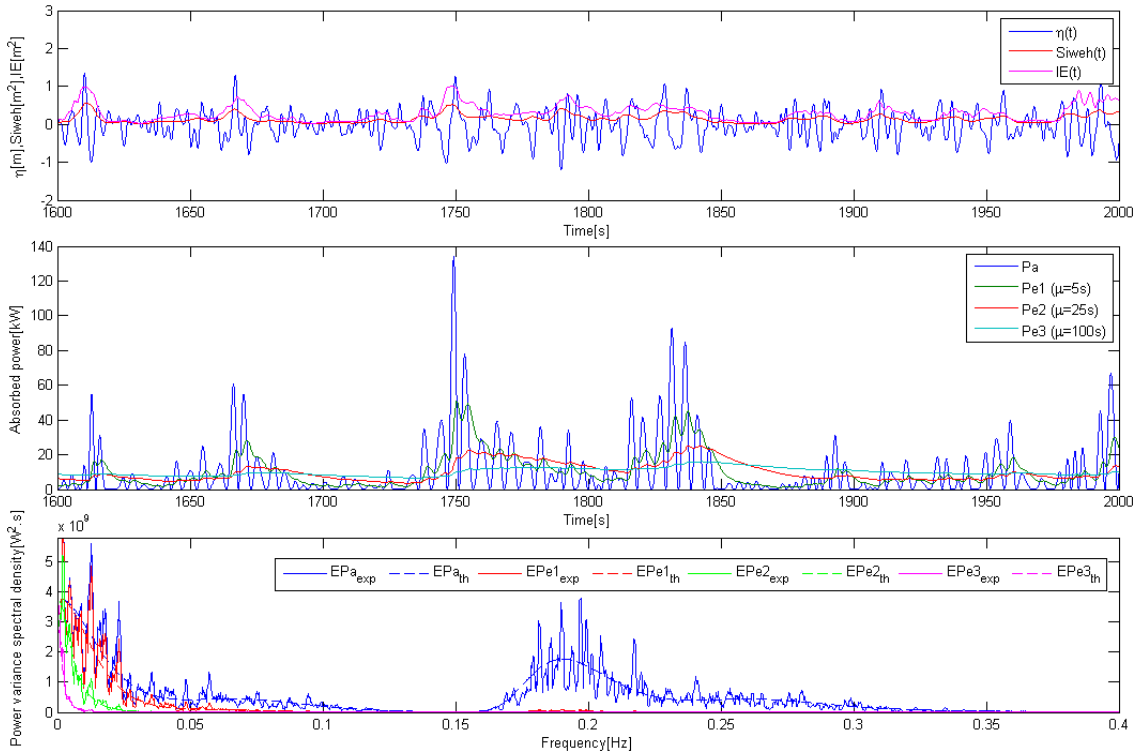

Figure 3.25: Id. Fig. 3.24 in a mixed sea-state (swell: $H_s = 1m$, $T_p = 11s$, $Q_p = 5$; wind-sea: $H_s = 1m$, $T_p = 5s$, $Q_p = 2$).

$P_e(t)$ spectral densities are also plotted at the bottom of these figures.

The four ouput power signal $P_e(t)$ exhibit quite different looks: the smoothing operated by the inertial flywheel is evident, since from high fluctuations in signal $P_a(t)$ ($\mu = 0$) showing very important power peaks ($> 300kW$), the flywheel filter outputs more and more stabilised electrical power signals $P_{e1}(t)$, $P_{e2}(t)$, and $P_{e3}(t)$. Indeed, $P_{e3}(t)$ is almost constant and close to its mean value ($29.1kW$ and $10.1kW$ in the uni- and bimodal sea-states respectively). The PTO sensitivity to wave groupiness is therefore likely to decrease as inertia μ increases.

In order to validate this assertion, figures 3.27(a&b) depict the inter-correlation function of (centred and normalised) power signals $P_{e1}(t)$, $P_{e2}(t)$ and $P_{e3}(t)$ with the (centred and normalised) instantaneous wave-energy signals $SIWEH(t)$ and $IE(t)$ (see previous Chapter). By considering two signals $x(t)$ et $y(t)$, this function is here defined as (see Eq. (2.1))

$$R_{yx}(\tau) = \lim_{T\to\infty} \frac{1}{T} \int_{-\frac{T}{2}}^{\frac{T}{2}} x(t)y(t-\tau)\,\mathrm{d}t \tag{3.54}$$

averaged over the numerical integration interval ("unbiased" estimation in Matlab). In these figures, the target sea-state is the unimodal Bretschneider in figure 3.26. For both energy signals, it is noticed that the inter-correlation between power and wave groups

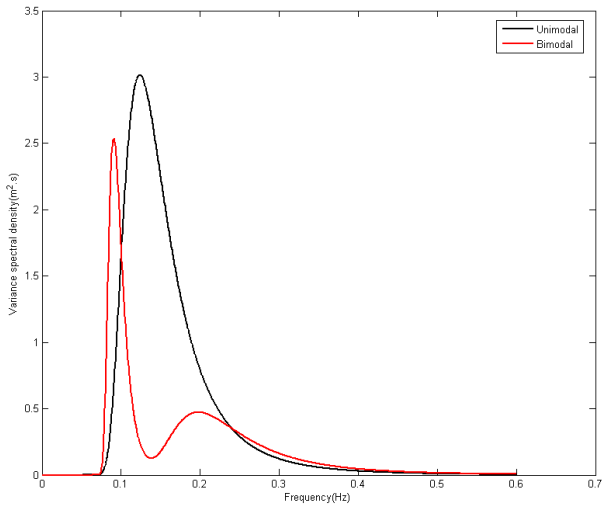

Figure 3.26: Target spectra of the simulated sea-states in figures 3.24 & 3.25: swell (black line) and mixed sea swell/wind-sea (red line).

vanishes as inertia increases; the best corelation is found here for the low inertia configuration $\mu = 5s$. Because of the flywheel's smoothing effect, the inter-correlation is even more pronounced in this last case than for no inertia at all ($P_{PTO}(t)$). It is also of interest to remark that the inter-correlation peaks occur at increasing time lags against inertia ($5s$, $8s$ and $11s$ for $P_{e1}(t)$, $P_{e2}(t)$ and $P_{e3}(t)$ respectively when inter-correlated with $SIWEH$). Accordingly, energy signals such as $SIWEH(t)$ or $IE(t)$ (among others) can be used in time domain to detect wave groups influencing the PTO output power. As seen here, the ouput power signals and wave energy groups are significantly correlated indeed, namely in sea-states whose main waves match the response interval of the buoy – which is the case of the sea-state simulated in this section.

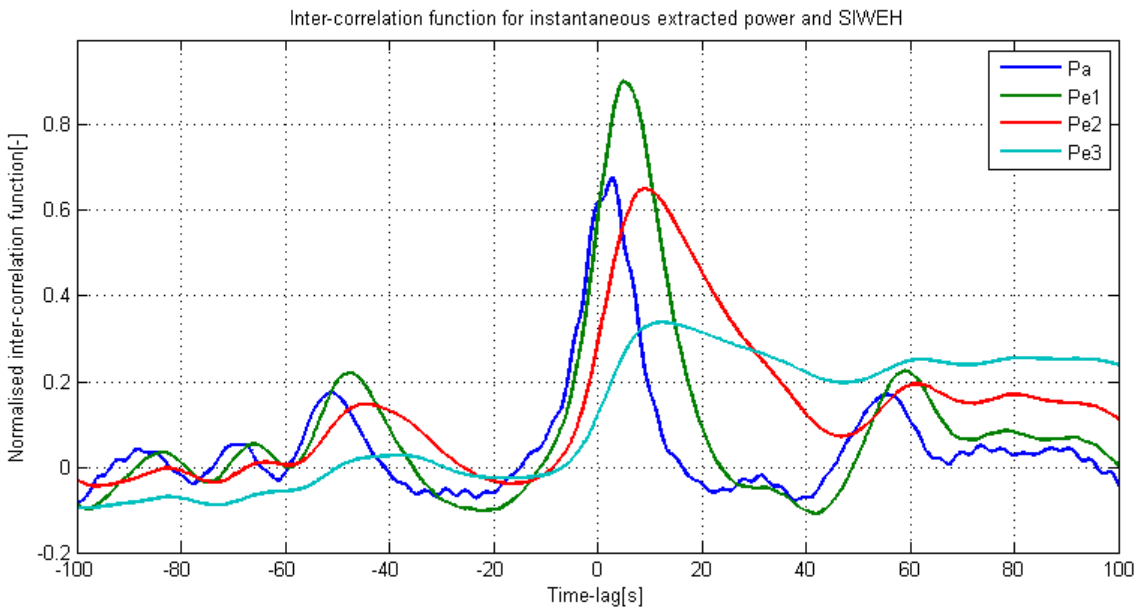

(a)

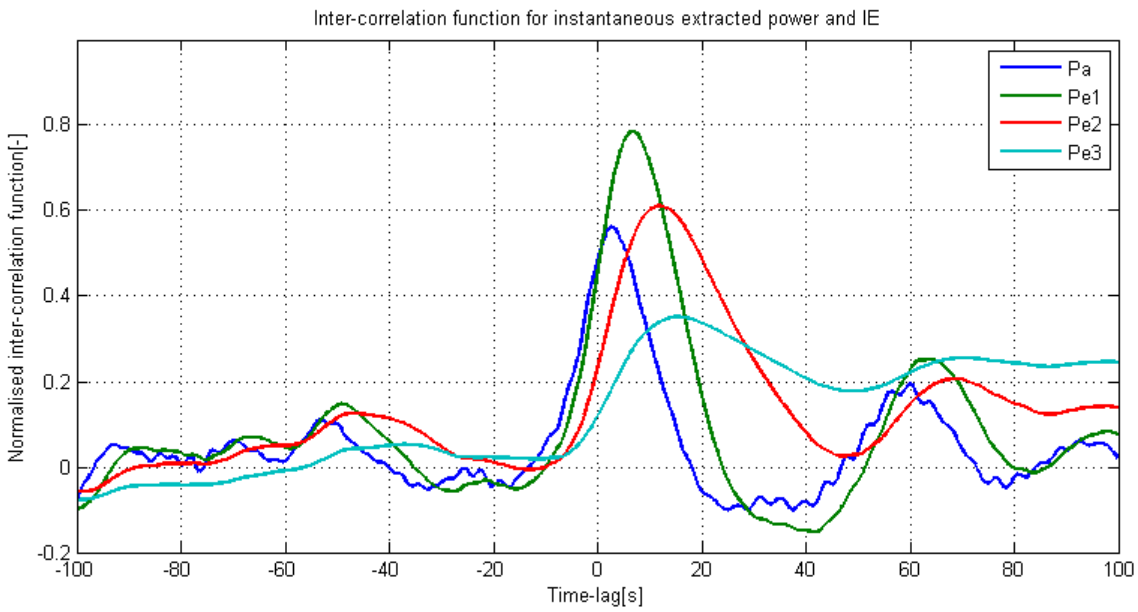

(b)

Figure 3.27: Inter-correlation function of the (centred and normalised) electrical power signals $P_{e1}(t)$, $P_{e2}(t)$ $P_{e3}(t)$ output from the flywheel with (centred and normalised) instantaneous wave energy signals $SIWEH(t)$(a) and $IE(t)$(b).

3.6.2 Short-term energy storage reservoir with nominal output power

Another possible model for inertial PTO mechanism connected to an electrical grid is by considering its output power $P_s(t)$ as binary (hydraulic motor): either it is equal to nominal power P_{nom}, or it is zero. In this last case, the system is in charge thanks to a short-term energy storage reservoir of instantaneous potential energy $E_{capa}(t)$ (kJ). If the output power is not zero, the system is in charge only if the instantaneous power absorbed by the mechanical converter is superior to P_{nom}. It is in discharge otherwise, in which case the energy default is compensated for by the energy already stored in the reservoir. At each instant i_t of the numerical simulation, the whole system is subject to an algorithm as the following:

<u>If</u> $E_{capa}(i_t) > E_{min}$ and charge at $i_t - 1$
<u>or</u> $E_{capa}(i_t) > P_{nom}\Delta t$ and discharge at $i_t - 1$, Do

- $P_s(i_t) = P_{nom}$
- Status at i_t = discharge
- $E_{capa}(i_t + 1) = E_{capa}(i_t) + (P_{PTO}(i_t) - P_{nom}) * \Delta t$

<u>Otherwise</u> Do

- $P_s(i_t) = 0$
- $E_{capa}(i_t + 1) = E_{capa}(i_t) + P_{PTO}(i_t) * \Delta t$

<u>End If</u>

[E_{min} is arbitrarily choosen here such as $E_{min} = P_{nom} * T_{min}(20s)$, and $E_{capa}(0) = 0$]. No energy upper bound is imposed to the reservoir first. As expected, the output power $P_s(t)$ is intermittent as shown in figure 3.28 for a $1200s$-simulation of the linear heaving buoy in a Bretschneider target sea-state ($H_s = 2m$ and $T_p = 8s$) simulated with *method a*.

On a given simulation of length T, we denote by $\Phi_{q,P_{nom}}(T)[\%]$ the *quality factor* (or nominal operating rate) corresponding to the nominal output power $P_{nom}[kW]$ as

$$\Phi_{q,P_{nom}}(T) = \frac{\sum \tau\left(P_s = P_{nom}\right)}{T} \tag{3.55}$$

that is, the ratio of the total cumulated time where $P_s(t) = P_{nom}$ over simulation length T. Such a factor is clearly dependent on the wave-groupiness properties of the wave

field. It may therefore be seen as a relevant groupiness parameter towards wave-energy conversion. The nominal power is here taken equal to the mean power absorbed by the linear WEC in the envisioned target wave process ($P_{nom} = \overline{P_{PTO}}$, see Eq. (3.14)). For the sake of simplicity, the notation of the quality factor is simplified to $\Phi_q(T) = \Phi_{q,\overline{P_{PTO}}}(T)$.

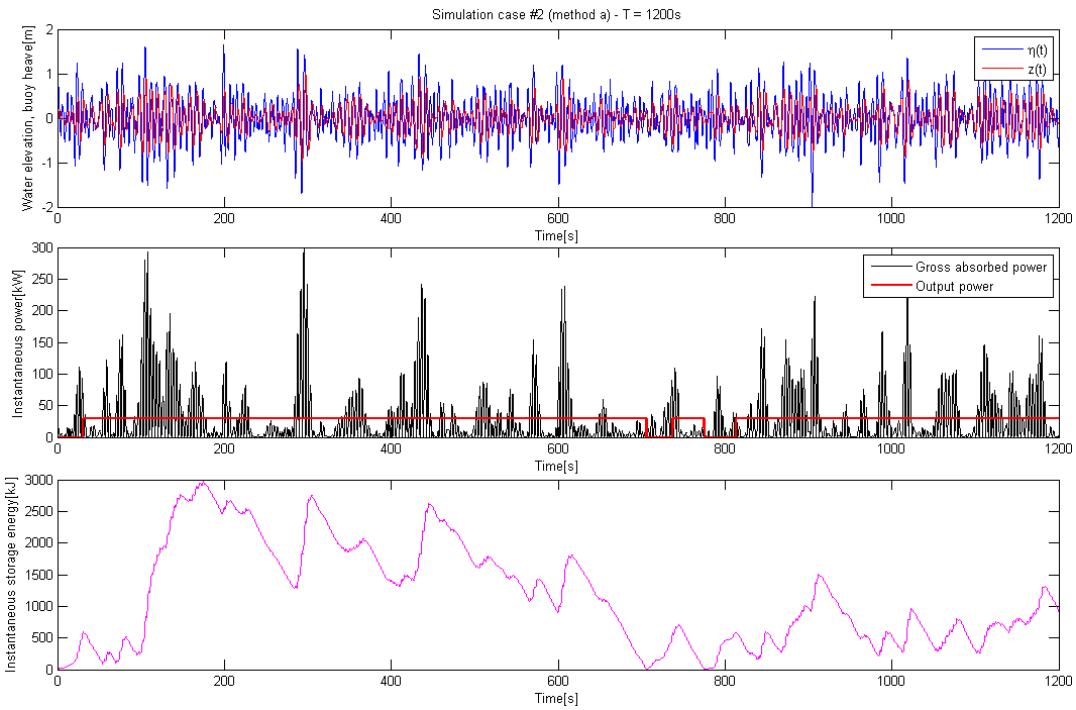

Figure 3.28: Simulation of an axi-symmetrical heaving buoy coupled to a short-term energy reservoir (without upper limit) in a Bretschneider sea-state ($H_s = 2m$, $T_p = 8s$, *method a*).

First, the influence of the wave simulation method (a or b) on the estimation of expected quality factor $\mathrm{E}\left[\Phi_q(T)\right]$ is observed in a sea-state where the theoretical power extracted by the buoy is $29.1kW$ (no inertia) for different simulations lengths (300-simulations samples). The distribution results (mean value and standard deviation) are plotted in figure 3.29: *method b* induces a slight positive bias with respect to *method a* in the factor's estimation, but reduces the estimator's dispersion. For both methods, the quality factor expectation increases against simulation length T, beyond 90%. An asymptotic value is hard to determine though, for the convergence is not perfectly reached in both curves. One can conclude that the more representative of the process the simulation is, the higher the quality factor's expectation $\mathrm{E}\left[\Phi_q(T)\right]$.

Let us observe now the variability of the $\Phi_q(600s)$ expectation against spectral bandwidth of input waves, through peakedness parameter Q_p. Figure 3.30 gives the results obtained with 300-simulations samples for various Q_p values (1 to 7) along with the corresponding narrowness parameters ε_2 and $\varepsilon_{\dot{z},2}$. This figure exhibits a clear decreasing trend – almost linear – of $\mathrm{E}[\Phi_q(600s)]$ against Q_p. From the conclusions drawn in

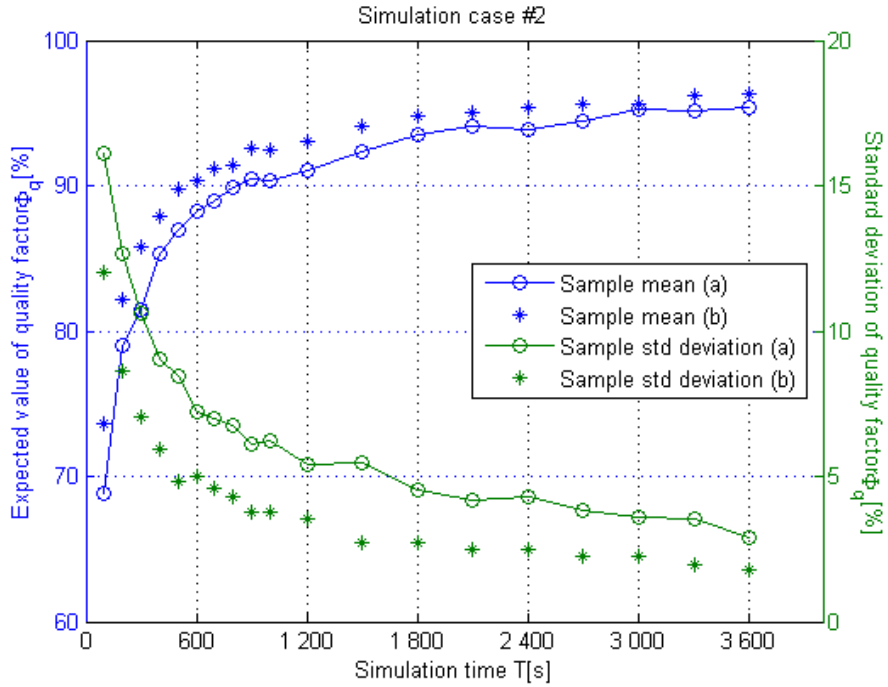

Figure 3.29: Expectation (left axis, blue line) ans standard deviation (right axis, green line) of the estimation of quality factor Φ_q obtained in 300-simulations samples of the heaving buoy with both methods a(circles) and b(stars) against simulation-length T.

Section 3.5, we know that, for the same estimator precision level, the simulation time length has to increase as the waves' spectral bandwidth increases (Eq. (3.47) & (3.48)). In other terms, let us say that: "the larger the spectral bandwidth, the longer the simulation".

Figures 3.31(a-c) illustrate various groupiness statistics related to the quality factor history against the selected nominal power non-dimensionalised by $\overline{P_{PTO}}$, as the expectation of $\Phi_{q,P_{nom}}(1200s)$(a), the mean duration (s) of discharge events (i.e. where $P_s = P_{nom}$)(b), and mean discharged energy during those events ($P_{nom} * \tau(P_s = P_{nom})$, in kJ)(c). In each figure, the 10th and 90th percentiles of the samples are also plotted. All of these statistics are obtained from a 1200s-simulation of the device using *method a*. The dispersion of $\Phi_{q,P_{nom}}(1200s)$ estimator seems quite low, according to figure 3.31(a). Moreover, a clear threshold – slightly inferior to 100% – up to $P_s^* = 1$ is noticed. Beyond, the factor's expectation decreases exponentially, and ends up with 12% for $P_s^* = 8$. The mean duration of discharge events (Fig. 3.31(b)) reaches a maximum value for $P_s^* = 1$ and then decreases in the same way. Similarly, the mean discharge energy has a peak value for $P_s^* = 1$ and then increases again for higher P_s^*. As a conclusion, the criterion $P_s^* = 1$ appears as an optimal compromise for the design of the PTO when the reservoir's energy is unlimited.

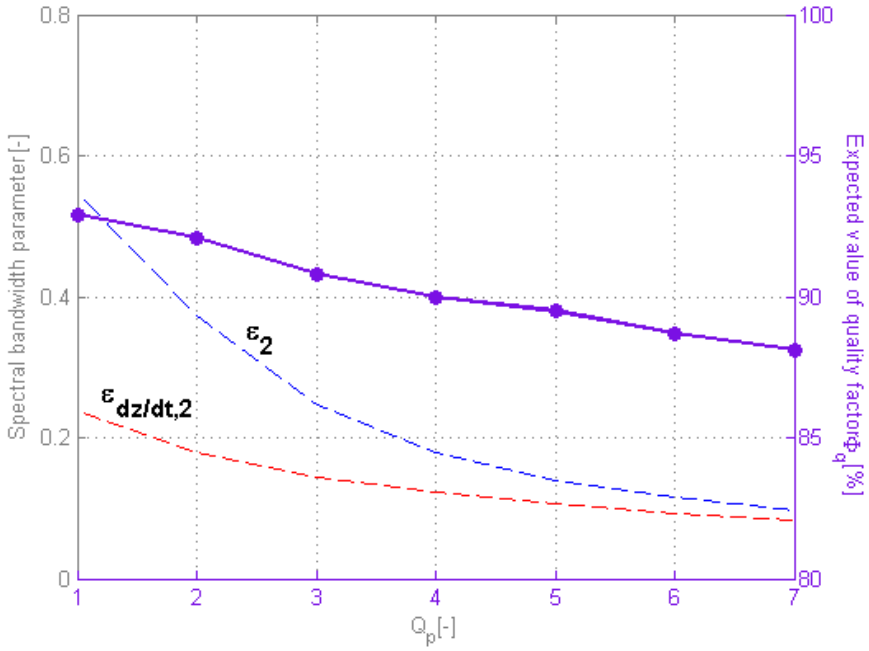

Figure 3.30: Expectation of quality factor $\Phi_q(600s)$ (right axis, purple line) in Bretschneider target sea-states with increasing Q_p (1 to 7) estimated from 300-simulations samples of the heaving buoy; corresponding narrowness parameters ε_2 and $\varepsilon_{\dot{z},2}$ (left axis, lue and red dashed lines).

In reality, the capacity of the reservoir is much likely to be limited. Let us therefore fix an arbitrary energy storage limit (kJ), which may appreciably modify the power output, as shown in figure 3.32 for a maximum stored energy of $1000kJ$ (to be compared to Fig. 3.28). These simulation results emphasize that quality factor is generally reduced, just as the own reservoir's capacity.

Figure 3.33 represents $\mathrm{E}[\Phi_q(1200s)]$ against energy storage limit E_{max} in the reservoir for both simulation methods a and b for the same target sea-state as previously. As the reservoir's capacity increases with E_{max}, the obtained trends are logically increasing against this parameter. An estimation bias is observed from $E_{max} = 1500kJ$ on when using *method b*, which overestimates the results drawn from *method a*, once again.

In the case of the inertial flywheel as well as the energy storage reservoir (Fig. 3.27(a&b)), the wave groupiness characteristics in time manifestly have a direct influence on the power signals output from the PTO mechanism. When the wave field is simulated according to *method a*, the expectation of performance parameter estimators – like the mean extracted power or the quality fator presented hereabove – correspond to the target value of the wave-process (unbiased estimation); the observed dispersion is thereore due to the variability of the simulated spectral shapes. For *method b* however, as the wave field energy is the same in each simulation – the simulated spectrum is equal to the target one – first, a bias with respect to *method a* may be noticed for some parameters

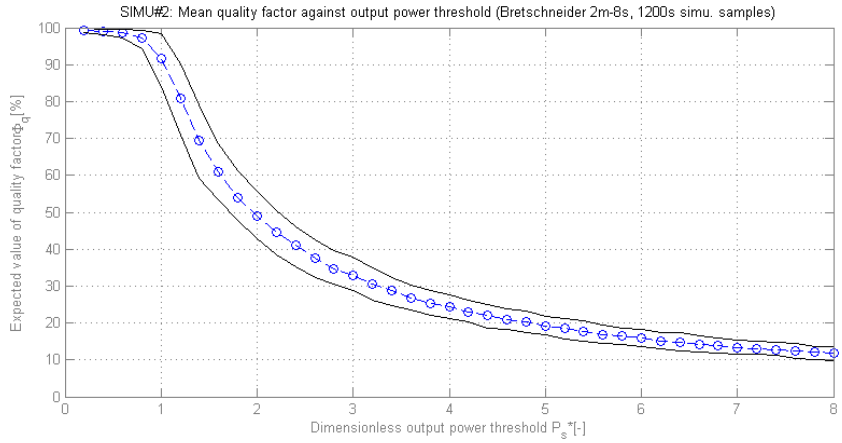

(a)

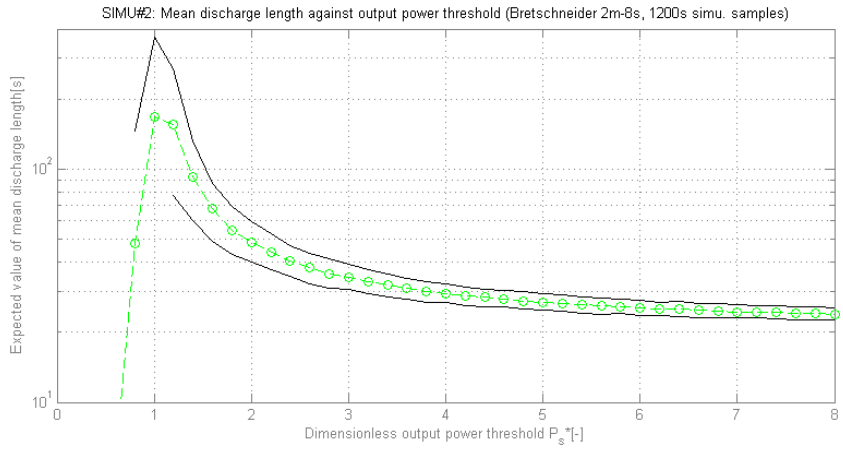

(b)

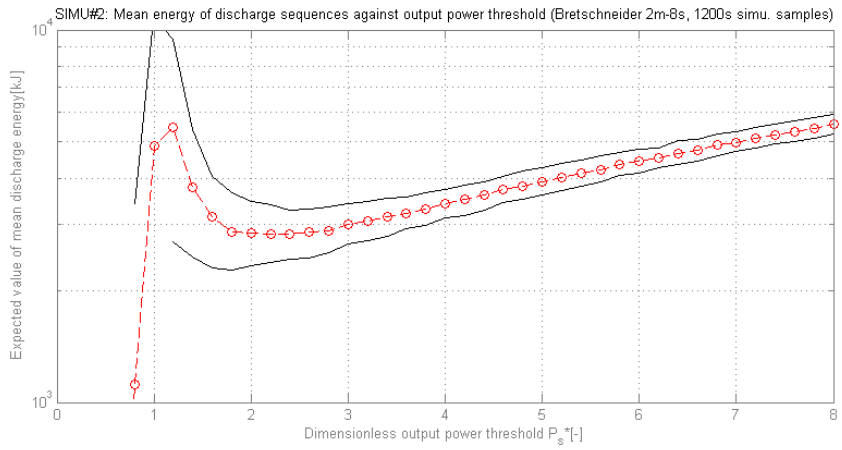

(c)

Figure 3.31: Groupiness statistics on power output from the reservoir against dimensionless nominal power $P_s^* = P_{nom}/\overline{P_{PTO}}$: expectation of $\Phi_{q,P_{nom}}(1200s)$(a), mean discharge lengths (log. scale)(b), and mean discharged energy (log. scale)(c).

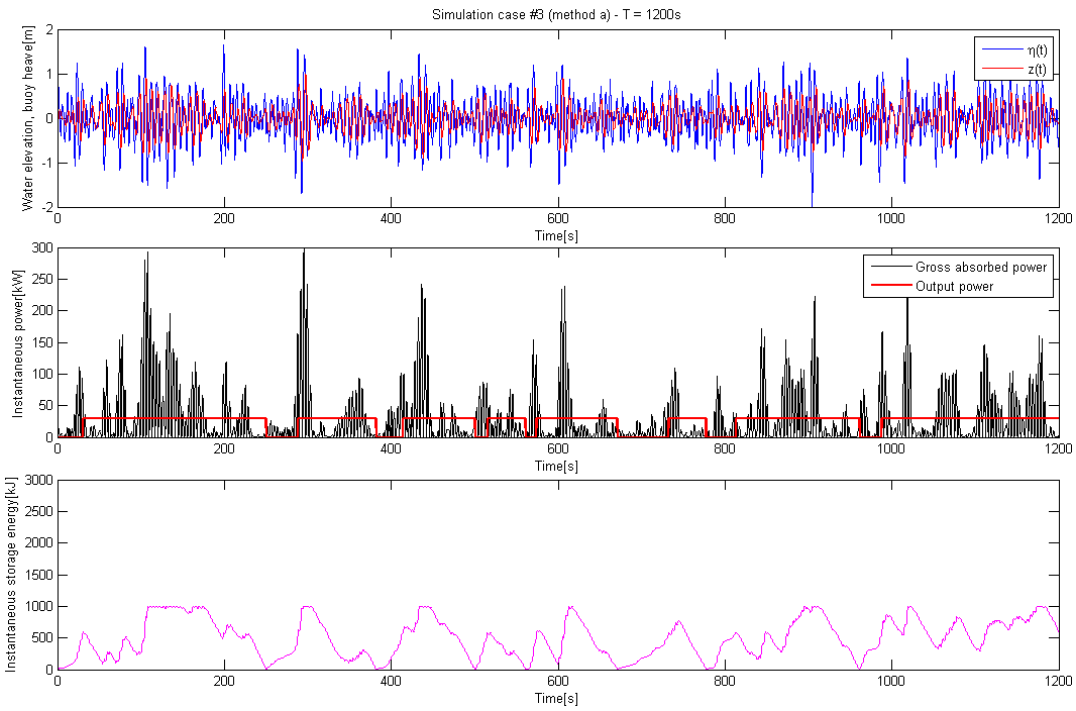

Figure 3.32: Simulation of an axi-symmetrical heaving buoy coupled to a short-term energy reservoir (with $1000kJ$ energy-storage limit) in a Bretschneider sea-state ($H_s = 2m$, $T_p = 8s$, *method a*).

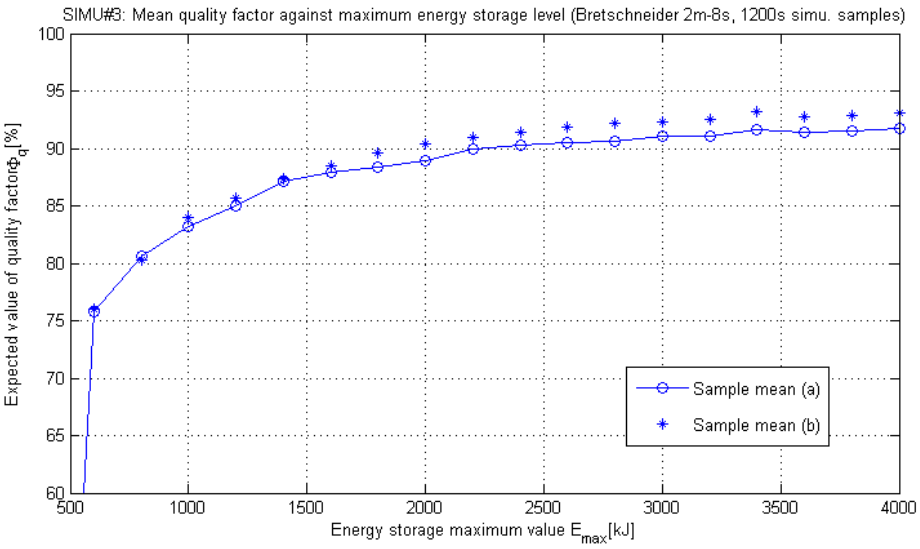

Figure 3.33: Expectation of quality factor $\Phi_q(1200s)$ against energy-storage limit $E_{max}(kJ)$ in the reservoir from 300-simulations samples in a Bretschneider target sea-state ($H_s = 2m$, $T_p = 8s$) simulated with both methods a and b.

(as the quality factor), and second, the dispersion of estimators is exclusively due to the phases' distribution in the Fourier series of $\eta(t)$, that is, to wave groupiness, according to Funke and Mansard's experiments. Hence the following interrogation: if the WEC's response (here, the output power) is reasonably correlated to the wave groups' variations in a wave energy signal such as $SIWEH(t)$, is the value of the estimator in a *method b* simulation related to the corresponding groupiness factor (GF_{SIWEH}) ? [That question also applies to any other instantaneous wave-energy signal, but as all these signals are somewhat highly correlated (see Chapter 2), it is here restrained to $SIWEH(t)$, for exemplification].

In order to have a first guess answer to that question, the correlation of quality factor $\Phi_q(1200s)$ estimator and groupiness factor GF_{SIWEH} is observed in a 500-simulations sample in the same sea-state as previously using *method b* and without any limitation to the reservoir's capacity. The calculation of $SIWEH(t)$ is lead on the entire wave simulation, so that no transient regime has to be considered for all parameters (as it is the case until now). The result is given in figure 3.34, where it is quite manifest that the scatter plot exhibit strictly no correlation. From that example, on can deduce that groupiness factor GF_{SIWEH} (and by extension, any other groupiness factor based on the same formulation, as GF_{IE}, $GF_{\Pi}\ldots$) are unable to account for the groupiness, itself responsible for the performance estimator variability when the input spectrum's shape is fixed. Let us remind that groupiness factors are defined as variability coefficients of the instantaneous wave energy signal. A better groupiness parameter – correlated to the performance estimators – should be defined.

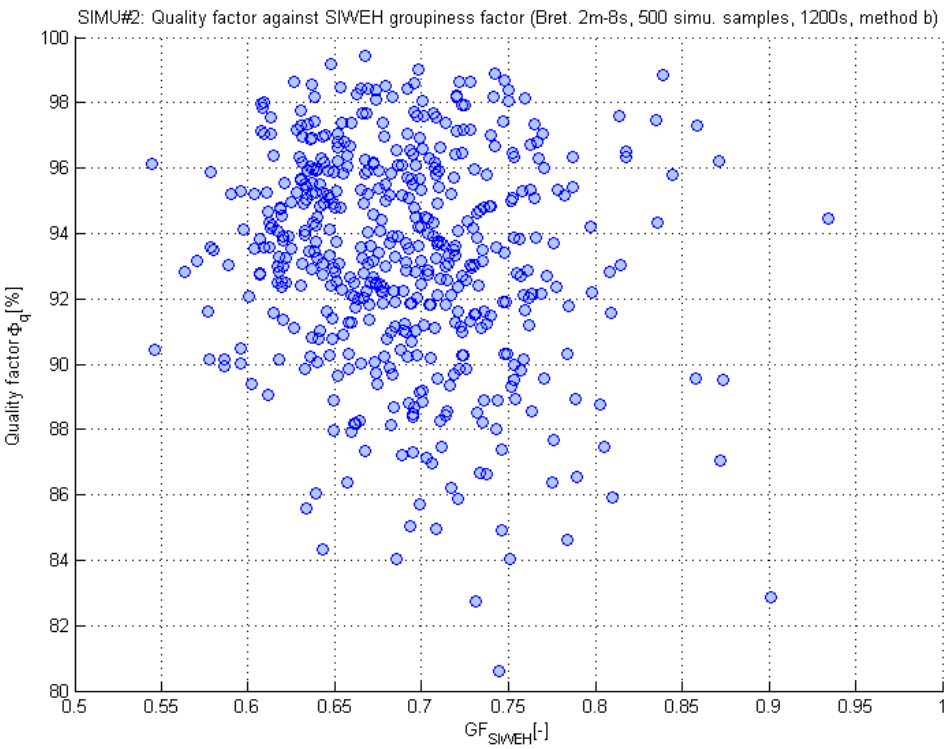

Figure 3.34: Estimator of quality factor $\Phi_q(1200s)$ against groupiness parameter GF_{SIWEH} of the water elevation signal in a 500-simulations sample and in a Bretschneider target sea-state ($H_s = 2m$, $T_p = 8s$) simulated with *method b*.

3.7 Conclusion about the global spectral shape of sea-states and its influence upon the mean power extracted by WECs

This chapter has provided a better understanding of the sensitivity of oscillating WECs to the overall spectral width of the sea-states. In particular, it has been shown that the sensitivity to spectral width was more strongly marked when the response band of the WECs was tuned to the main incoming wave frequencies. Besides, it appeared that the sensitivity was even greater when the width of the own WECs' response band was broader (case of IPS4). Under such conditions, spectral bandwidth parameters such as ε_0 and ε_1 have shown to be relevant to account for the performance of the systems (through the capture width parameter) while the significant wave height H_s and energy period T_e were both fixed. The chapter ended by considering simplified capacitive energy converters (flywheels, gas accumulators, etc.) in the time domain. It was notably observed that the higher the inertia of the WEC (e.g. air turbines with variable control law), the lower the correlation of both the – fluctuating – output electrical power and the incident wave energy groups – identified through instantaneous wave energy signals such as $SIWEH(t)$ and $IE(t)$ (but not groupiness factors such as GF_{SIWEH} however) – and the longer the inter-correlation time lag. In the case of a capacitive converter with nominal power output (e.g. a gas accumulator feeding a hydraulic motor) it has been shown that, on the one hand, the mean quality factor of the whole device was increasing with the simulation time T, and on the other hand, it was increasing also with the spectral bandwidth of the sea-state for a given T (provided that the mechanical system be reasonably excited by the main wave frequencies).

In parallel, this chapter has illustrated the implementation of a wave grouping spectral method (enveloppe method) applied to groups of velocity heights (of the degree of freedom related to the PTO converter), which in turn have yield theoretical statistics on groups of instantaneous power peaks. A wave by wave analysis of the motion results has been carried out on long simulations of a linear WEC, which satisfactorily validated the theoretical formulations.

Then, the importance of the overall spectral bandwidth in the estimation of mean wave parameters, and *a fortiori* mean WEC performance parameters from simulations run in the time domain, was clearly emphasized. It was underlined that in time-domain modelling, the spectral bandwidth of the sea-states had not only an influence on the mean WEC response, according to its resonance regime, but also on the dispersion of the mean converted power estimator. Indeed, the broader the bandwidth, the narrower the dispersion, and, therefore, the better the precision of the power estimation. In this study, it has been also noticed that simulating the wave field using *method b* was not leading to biased mean performance estimations against *method a*, while the dispersion of the estimator was reduced.

This chapter closes this first part of the thesis, which is devoted to the global spectral bandwidth of sea-states and its effect upon the performance of WECs that are little sensitive to wave directionality (by axi-symmetry here): this constitutes a first important step in the refinement of the wave climatology, when the sea-states are represented by their spectral density $E(f)$ only. The next part goes further in refining the climatology by considering and characterising each individual wave systems of the sea-state. This, of course, involves the directional dimension, for directional spectral data $E(f, \theta)$ are now used to represent the sea-states.

Part II

Refined sea-state description and wave systems space and time tracking

Chapter 4

Uni- and multimodal sea-state representations

4.1 Unimodal representation

Most of design studies and ship or offshore structures dimensioning are based on a unimodal representation of sea-states. Historically, the description of the sea conditions is limited to basic parameters like significant wave height, mean or peak wave period and direction, which are far enough to provide indications about the sea-state's severity. Significant wave height H_s for instance was estimated by seamen onboard (Hogben and Lumb, 1967) long before the mean sea surface excursion be measured by scientific procedures (as buoys, radars, probes, altimeters and satellites...). So, the spectral shape is mostly unknown, and any sea-state is modelled as a single wave system, which can be modelled thanks to parametric shapes against frequency and direction to obtain the spectrum $S(f)$ or directional one $S(f, \theta)$.

A lot of such parametric shapes against frequency have been proposed in the literature – some of them even were introduced in the previous chapters –, which are governed by global parameters such as wave height and period (and possibly wind information when available). The JONSWAP spectrum (Hasselmann et al., 1973) is one of the most famous examples, along with the Pierson-Moskowitz (Pierson and Moskowitz, 1964), Bretschneider (Bretschneider, 1959), or Wallops (Huang et al., 1981) spectra among others. The directional wave spectrum $S(f, \theta)$ is then straightforward to derive, as the following decomposition

$$S(f, \theta) = S(f) \cdot D(f, \theta) \tag{4.1}$$

where $D(f, \theta)$ denotes the directional distribution function –, which can possibly depend on frequency, and satisfies the normalisation condition

$$\int_0^{2\pi} D(f, \theta)\, \mathrm{d}\theta = 1 \tag{4.2}$$

Several parametric directional shapes may also be found in the literature, as e.g. in Benoit et al. (1997), Krogstad et al. (1997) or in the C.O.S.T. report (Kahma et al., 2005, 2.5, p. 35-50): cos^{2s}, Gaussian, wrapped-normal, Poisson, von Mises... Each distribution may be defined from the mean wave direction and spreading of the sea-state. The most common formulation in offshore engineering is certainly the cos^{2s} distribution (Mitsuyasu et al., 1975), defined as

$$D(\theta) = D(f,\theta) = \frac{\Gamma\left(s+1\right)}{2\sqrt{\pi}\Gamma\left(s+\frac{1}{2}\right)} \cdot cos^{2s}\left(\frac{\theta-\bar{\theta}}{2}\right) \tag{4.3}$$

around mean wave direction $\bar{\theta}$, where Γ denotes the Gamma function defined in Appendix C, and where the spreading parameter s increases when the distribution becomes narrow over directions (see Fig. 4.1). In figure 4.2, an example of synthetic Bretschneider and cos^{2s} ($s = 2$, large spreading) unimodal wave spectrum is depicted.

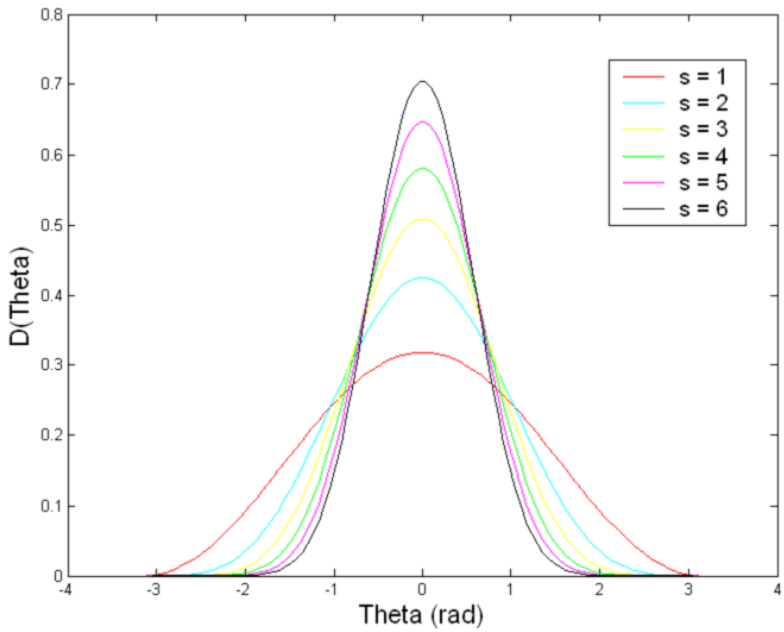

Figure 4.1: cos^{2s} distribution for $s = 1 \ldots 6$.

When spectral density $E(f)$ is estimated from spectral analysis of in situ measurements, it is not easy to accurately assess the directional distribution function against frequency. For instance, a directional accelerometric buoy records its own absolute motions as three degrees of freedom (heave/roll/pitch, or heave/surge/sway) and therefore enables to compute only the four first coefficients (1st and 2nd orders) of the Fourier series decomposition of $D(f,\theta)$. Some methods have been implemented to evaluate this function through the limited knowledge of the four Fourier coefficients, which are

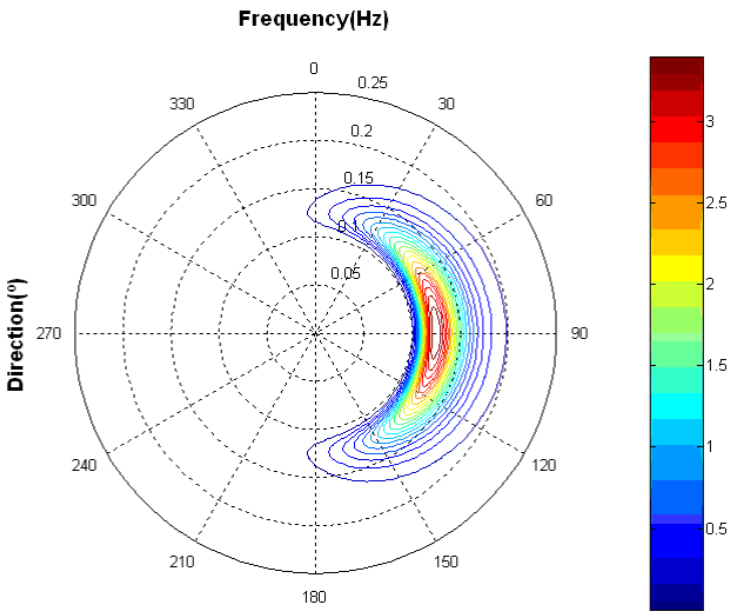

Figure 4.2: Synthetic directional wave spectrum $[m^2.s/rad]$ as the product of a Bretschneider spectrum with cos^{2s} directional distribution function for $s = 2$.

thouroughly reviewed in Benoit et al. (1997) (truncated direct Fourier decomposition, maximum likelihood, maximum entropy, Bayesian method...). Considering the relative complexity of their numerical implementation (complex algorithms) as well as the technical deployment (buoys, probes, networks) required to ensure a good accuracy on the sea-state spectral contents, unimodal parametric methods – based on a simplified characterisation, as energy, frequency, direction, and possibly frequency and directional spreading – turn out to be extremely convenient for the design of naval, offshore, nearshore and coastal structures.

From WAM-model results, Oliveira-Pires et al. (1999) estimate the mean directional spreading coefficient s at each of the 85 locations of the wave-energy atlas WERATLAS (Pontes et al., 1997; Pontes, 1998). This allows to slightly refine the sea-state description provided by the atlas for the Atlantic Ocean and Mediterranean Sea.

The consideration of the sea-state's spectral shape as a key-information divides both oceanographers and hydrodynamicists. When oceanographers investigate with much care the dynamics of wave systems interactions, hydrodynamicists are only interested in the distribution of the sea-state energy contents for offshore design purposes. Now, as seen in the previous chapter, the wave energy distribution might not be systematically simplified to a unimodal representation. Otherwise, the simulated sea-states are likely to differ a lot from the real ones.

For a better understanding of this fact, let us have a look at the frequency of unimodal (or, conversely, bi- or multimodal) sea-state occurrences at given locations, which has

been reported by some authors. Guedes-Soares (1984) collected spectral observations from previous studies lead in the Atlantic Ocean, and obtained – according to the level of sea severity – a bimodal sea-state frequency included in 10–30% (with average around 22%), which increases with H_s. Similarly, Kerbiriou (2007), using spectral Bay of Biscay data output from the WaveWatch III hindcast model (Tolman, 2002) over the year 2005, extracted and identified the wave systems (thanks to the SPOP application, see Section 5) in order to derive refined climatological statistics, such as those given in Table 4.1. These show that: 38% of the time, the sea-states may be considered as unimodal; 38% of the time also, the sea-states may be considered as bimodal (swell + wind-sea, two swells), and the rest of the time, the sea-states are multimodal with at least three systems. Accordingly, the unimodal sea-state hypothesis seems to be of low realism when predicting the behaviour of floating structures at sea, at least for the Atlantic Ocean.

Table 4.1: Statistics on the sea-state composition (occurrences of swells "SW" and wind-seas "WS") observed in the Bay of Biscay for year 2005 from WaveWatch III spectral data (Kerbiriou, 2007).

		SW		
		0	**1**	**2**
WS	**0**	0	34%	9%
	1	4%	29%	11%
	2	n.c.	8%	n.c.

4.2 Sensitivity to unimodal sea-state modelling of a directional linear WEC

This section addresses the impact of the unimodal sea-state representation on the behaviour of a fictive directional linear WEC, whose (power) directional transfer function is known (Fig. 4.3). The WEC is a linearised version of the SEAREV device (presented in Section 8), which converts wave energy through its pitching mode through a linear damping mechanism.

The response of the WEC is observed here over a two-months WaveWatch III spectral dataset (from the 1st of January 2008, midnight, to the 3rd of March 2008, 9AM, by 3h time-steps) related to a $31m$ water-depth nearshore location near Yeu Island (France, 46.68 °N,2.38 °W). To obtain the mean extracted power in a given sea-state, the directional wave spectra $S(f,\theta)$ are simply convoluted with function $PTF(f,\theta)$ – assuming the WEC's bow faces the local mean waves, arising from direction $\beta = 270\,°$ – according to

$$\overline{P_{PTO}} = \int_0^{2\pi} \int_0^{\infty} PTF(f,\theta) S(f,\theta)\, \mathrm{d}f\, \mathrm{d}\theta \tag{4.4}$$

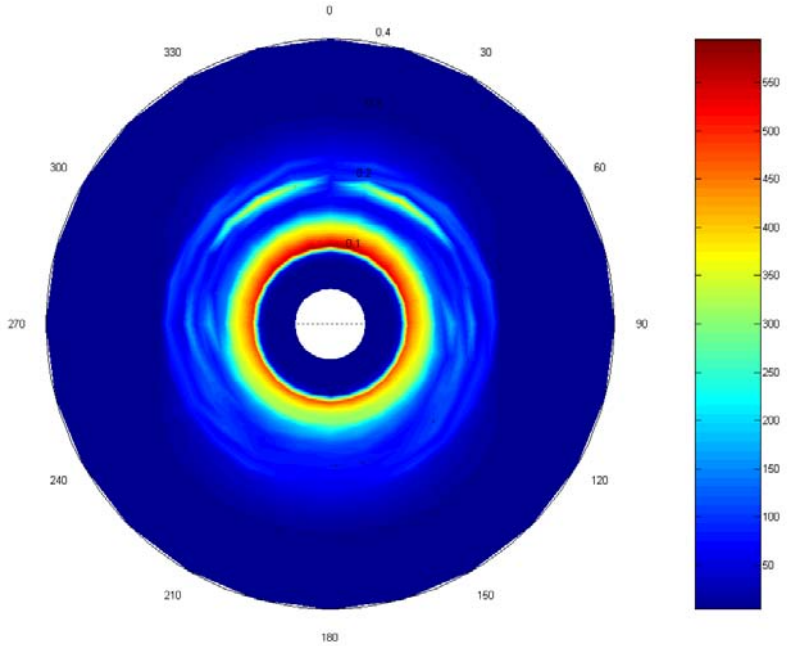

Figure 4.3: Power directional transfer function $[kW.m^{-2}]$ of a linearised SEAREV WEC (polar plot: frequency increases with radius); the bow is here aligned with the geographical North (0 °).

which derives from the omnidirectional equation (3.25) extended to the frequency-direction plane. Also, global wave parameters H_{m0} and T_p are calculated in view of modelling the corresponding unimodal sea-state thanks to a Bretschneider spectral shape ($Q_p = 2$) and cos^{2s} directional distribution function ($s = 40$), according to the mean characteristics of the climate at that location.

In figures 4.4(a&b), two particular sea-state cases are depicted: a unimodal swell (a) and a bimodal swell-dominated sea-state (b), along with their corresponding unimodal representation (on the right hand side). In case (a), the structure remains unchanged since both representations exhibit one peak – related to the same swell wave system. Then, differences may appear in terms of spectral shape, just as the frequency-dependent directional distribution, which cannot be reproduced by the cos^{2s} model here: the spectral peak therefore appears underestimated compared with reality, and shows a broader spectral bandwidth. In case (b), the sea-state is bimodal, as made of one swell and one wind-sea following two distinct directions of propagation: in such a case, the unimodal sea-state modelling appears somewhat inappropriate since it neglects both the actual wind-sea energy and perturbations caused by the wave systems interaction, and allocates the whole energy to the main peak – that is, the dominating swell system – which turns out to be overestimated.

The mean power output from the WEC computed using both the "real" WWIII and associated synthesized unimodal spectra over the two months of data is plotted

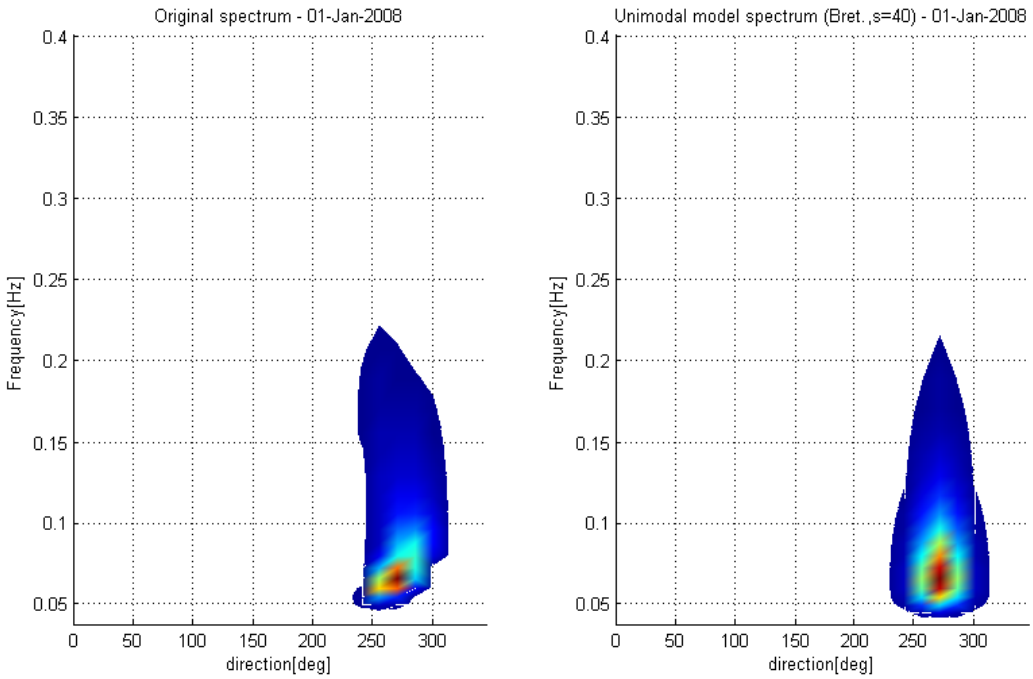

(a)

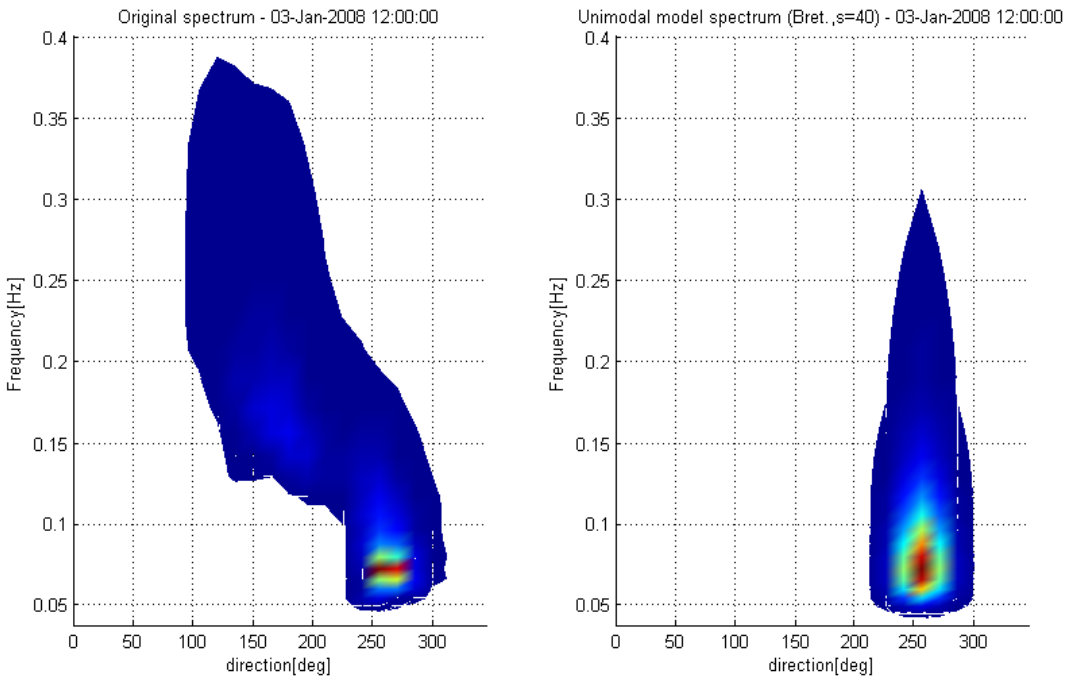

(b)

Figure 4.4: WWIII wave spectra (left) and unimodal model (right) near Yeu Island at two dates : 1st of January, midnight (a) and 3rd of January 2008, 12AM (b); the unimodal shapes are synthesized from Bretschneider ($Q_p = 2$) and cos^{2s} ($s = 40$) shapes.

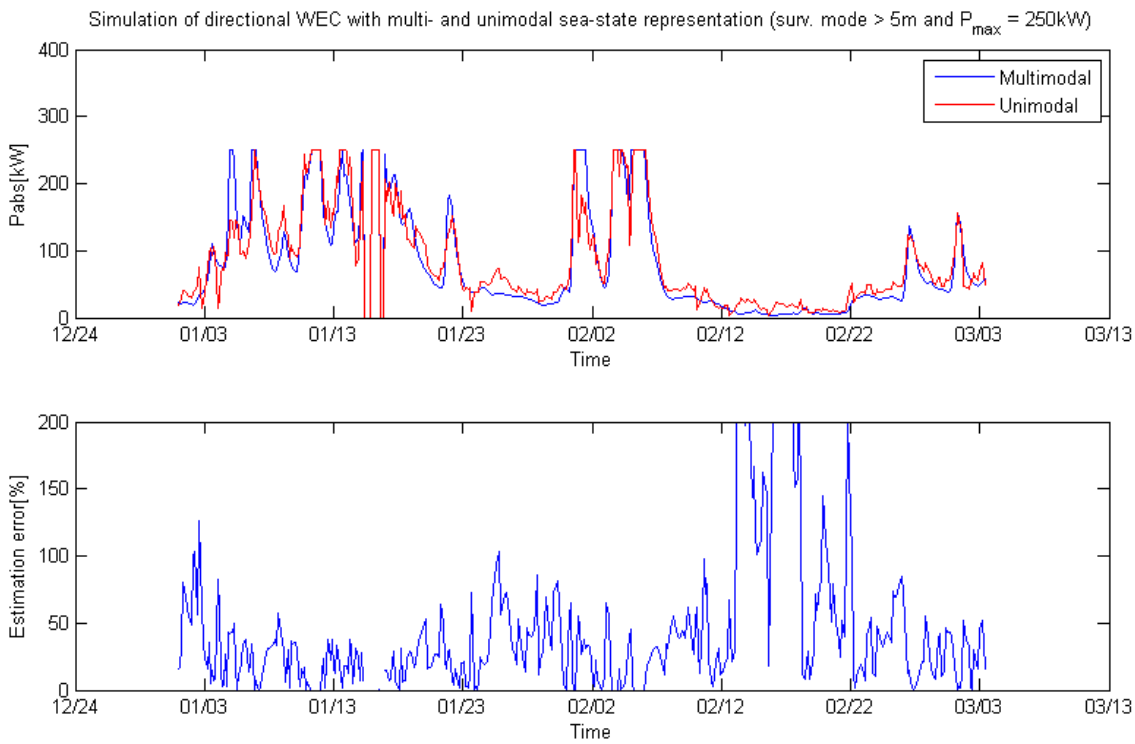

Figure 4.5: Exact (blue curve) and estimated (unimodal sea-state prepresentation, red curve) mean production (kW) operated by the linear directional WEC over the two-months WWIII dataset at Yeu Island (top); relative error (%) between both figures (bottom).

in figure 4.5(top). Let us stress that the WEC was set up such as the survival mode ($\overline{P_{PTO}} = 0$) be activated as soon as the significant wave height exceeds $5m$, and the maximal converter output power is arbitrarily fixed at $250kW$. Hence, the occurrence of power thresholds and sudden power cuts. As one can observe, discrepancies are noticeable when comparing both (blue and red) power curves, while the relative error sometimes reaches high percentages, especially when production is low. The unimodal representation results in either under- or overestimated power levels with respect to reality. Thus, it only provides an approximation of the expected values, yet one can concede they are not always absolutely uncorrelated. The actual mean extracted power over the considered weather window is around $85.5kW$, whereas it only reaches $80.8kW$ when modelling the sea-states with unimodal spectra, which corresponds to a relative estimation error about 5.7%.

Further examples that underline the inappropriateness of the unimodal representation in other wave energy conversion purposes are presented later on in Part III (Section 7).

4.3 Multimodal representation

It is possible to represent more accurately the spectral shape of sea-states by considering the individual wave systems it is made of (swells and wind-sea) separately, which are assumed to be unimodal. This implies the systems must be extracted from the (directional or not) wave spectra – which is more particularly addressed in the next chapter.

First, in agreement with the previous remarks, several authors have suggested analytical bimodal frequency spectra, namely Ochi and Hubble (1976), Guedes-Soares (1984), Torsethaugen and Haver (2004), among others. Appendix C also provides an alternative formulation, as the superposition of two peakedness-variable Bretschneider spectra ("Q_p-spectra"). Whatever the formulation, it always boils down to defining at least six parameters, three for each wave system, related to energy (H_{m0}), peak (f_p) or mean frequency, and spectral bandwidth or narrowness (e.g. the peak enhancement factor γ for JONSWAP spectra). If one wants to reduce that number, arbitrary assumptions must be made on the system's status (e.g., the swell spectrum's peakedness may vary, whereas that of the wind-sea is fixed as developped sea with $\gamma = 1$, equivalent to a Pierson-Moskowitz/Bretschneider spectrum).

More generally, a certain number of descriptive wave parameters similar to the unimodal model has to be set if one wishes to represent a n-systems multimodal sea-state, as state vectors: $\vec{p_i} = \{H_{m0i} \quad f_{pi} \quad \theta_{pi} \ldots\}^t$. Then, the sea-state is simply modelled as the matrix

$$\Sigma = [\vec{p_1} \quad \vec{p_2} \quad \ldots \quad \vec{p_n}] \tag{4.5}$$

In practice, sea-states with more than four or five significant coexisting wave systems are seldom observed at sea. However, the representation becomes heavier and heavier as the number of parameters in the systems' state vectors increases. It would therefore seem reasonable to limit oneself to the following characteristics: *significant wave height* (H_{m0i} or m_{0i}), *peak frequency* (f_{pi}), *spectral width* (particular shape factors as: γ_i, $Q_{pi}\ldots$), *peak direction* (θ_{pi}), *directional spreading* (coefficient s_i, see Eq. (4.3), standard deviation $\sigma_i\ldots$), assuming the directionality of each system (direction and spreading) is not dependent of frequency. This yields a maximum set of 25 parameters for each sea-state (five wave systems).

The SPOP application – presented in next Chapter – enables such as decomposition from raw directional wave spectra. Each identified wave-system is fitted with parametric shapes such as original and modified JONSWAP spectra (more abrupt low-frequency decreases for young swells), which ensures a fine characterisation of the sea-state's components at each time-step. Figure 4.6 illustrates how it is possible to compress the information of a whole directional spectrum into a synthetic matrix, where each column stands for a given wave system through a reduced set of descriptive parameters –, and which in turn allows to reconstruct the original spectrum. In the present case, the sea-

state is made of three wave-systems: two north-western swells and a western wind-sea. The wind-sea's directional spreading is more pronounced than for both swells, and the peakedness value γ is very different for each: the first – and quite young (i.e. the first observable frequency components of the wavetrain) – swell is narrow-banded whereas the second one – older and persistent – is quite broad-banded ($\gamma \approx 1$, as for a fully developped wind-sea); the wind-sea is probably growing, as the corresponding factor γ is superior to 1.

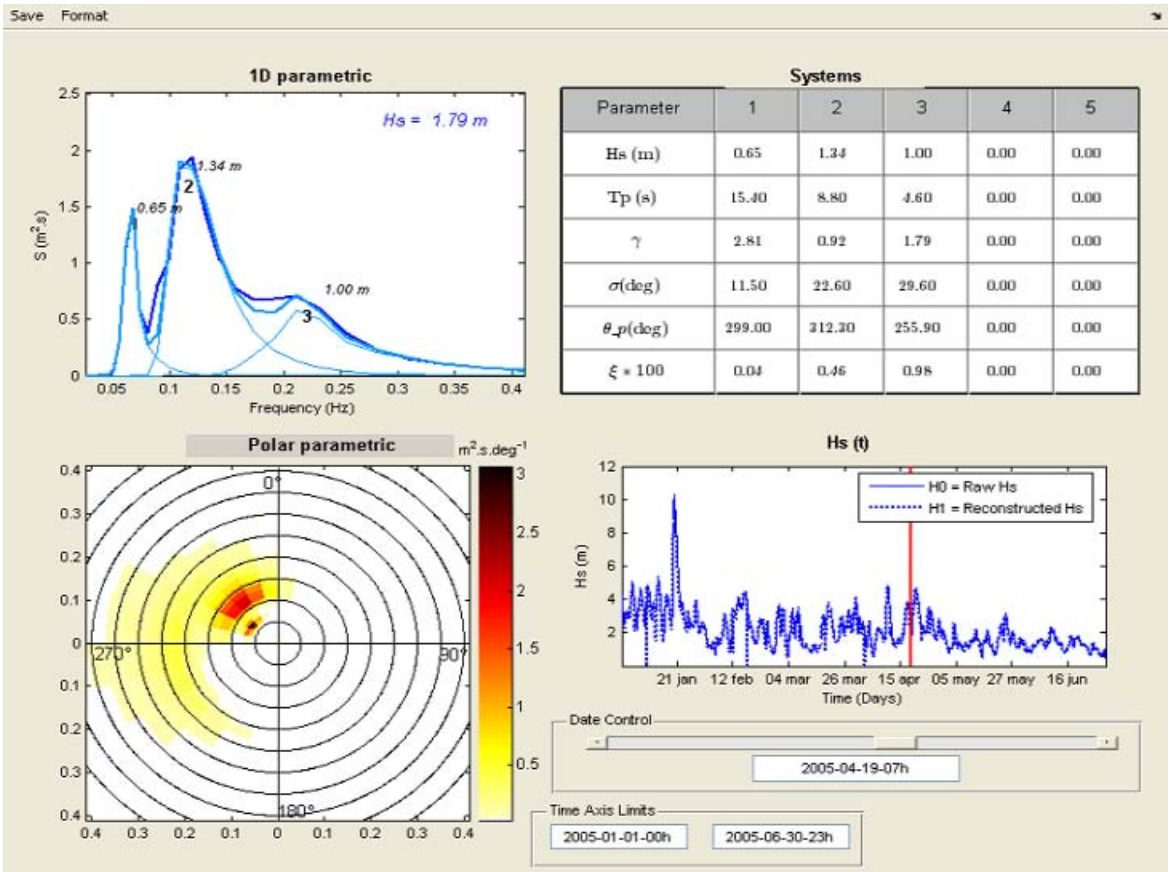

Parameter	1	2	3	4	5
Hs (m)	0.65	1.34	1.00	0.00	0.00
Tp (s)	15.40	8.80	4.60	0.00	0.00
γ	2.81	0.92	1.79	0.00	0.00
σ(deg)	11.50	22.60	29.60	0.00	0.00
θ_p(deg)	299.00	312.30	255.90	0.00	0.00
$\xi * 100$	0.04	0.46	0.98	0.00	0.00

Figure 4.6: Example of sea-state decomposition into individual wave systems, operated by SPOP (Kerbiriou et al., 2007).

4.4 Conclusion about the uni- and multimodal sea-state representations

This chapter has addressed two possible spectral representations of the sea states. The first one of those – commonly adopted in offshore engineering – consists in modelling the sea-states as unimodal in both frequency and direction from a set of overall wave parameters (H_s, T_p or T_e, θ_p). Such a representation does not allow to adequately reproduce the ocean physics (the sea-states are not always unimodal in reality) and, as a consequence, this may lead to erroneous and biased performance estimation results when simulating the behaviour of WECs in given exploitation sites. The second representation – multimodal, still very little implemented –, characterises each sea-state by separating each modal component (swells and wind-sea), which enables to recompose the whole sea-state in a very precise way. Such a representation therefore appears much more relevant from a physical point of view, and was illustrated in this chapter by results obtained with the SPOP application.

Chapter 5

Wave systems extraction, time tracking and identification

This part exposes the main steps that enable to extract time-coherent wave systems from a sequence of successive directional spectra $E(t, f, \theta)$ (obtained from propagation models or in situ measurements), which allows a better identification of ongoing wave-trains. Some of these steps are illustrated with results drawn from the SPOP application, developped at *IFREMER* (Kerbiriou, 2007), which performs the full processing sequence automatically, from the raw spectral data to the building of refined climatological statistics.

5.1 Wave systems extraction

This first step – the extraction – consists in partitioning (or clustering) a wave spectrum $E(t, f, \theta) = E(f, \theta)$ at instant t, that is, dividing the components of a frequency-direction matrix (with directional overlapping) into a finite number of connex partitions, which all represent given wave systems coexisting in the same sea-state. Some numerical techniques were proposed to deal with the automatic partitioning procedure for both directional and omnidirectional spectra ($E(f, \theta)$ and $E(f)$ respectively), and are comprehensively summarised in the recent paper of Portilla et al. (2009). The main referred authors in that field are Gerling (Gerling, 1992), Hasselmann et al (Hasselmann et al., 1996), Voorrips et al (Voorrips et al., 1997), Hanson and Phillips (Hanson and Phillips, 2001), and Aarnes and Krogstad (Aarnes and Krogstad, 2001). Let us also cite Rodríguez and Guedes-Soares (Rodríguez and Guedes-Soares, 1999) and Wang and Hwang (Wang and Hwang, 2001), among others, who have more precisely investigated on the multimodal partitioning in omnidirectional spectral densities $E(f)$, when directional information is not available.

5.1.1 Partitioning of directional spectra $E(f, \theta)$

Gerling's arborescent structure

Gerling (Gerling, 1992) proposed an arborescent method for the extraction of wave systems in directional spectra, which regards the systems' dependence scheme as the ramifications of a tree. From the zero-level (the "root", or "basis"), the method seeks the successive energy levels above which the emerging part of the spectrum is not connex anymore: new systems are defined as branches of the root, which sometimes may be of non-negligible energy indeed. Therefore, such an algorithm allows to extract wave systems but does not partition the spectrum into complementary sub-ensembles, as stressed in Aarnes and Krogstad (2001).

Steepest ascent path and catchment area techniques

An algorithm is proposed by Hasselmann (Hasselmann et al., 1996) – and reexploited later on by several authors, like Hanson and Phillips (2001) and Voorrips et al. (1997) –, which partitions the discretised wave spectrum $E(f, \theta)$ by allocating to each spectral component the reference of the nearest maximum value to which it leads by following the steepest ascent path. This can be simply performed by seeking back through the successive adjacent maxima up to the local peak, as illustrated in figure 5.1. The resulting partitions are therefore complementary and the full wave spectrum may be reconstructed by assembling the partitions together again. If one turns the spectrum upside down so that peaks become troughs and conversely, such an algorithm is similar to determining *catchment areas* for topographic purposes, that is, zones where falling water is likely to store according to gravity. Such a routine is available in Matlab (*watershed* toolbox), which was retained and implemented in SPOP for the wave systems extraction step.

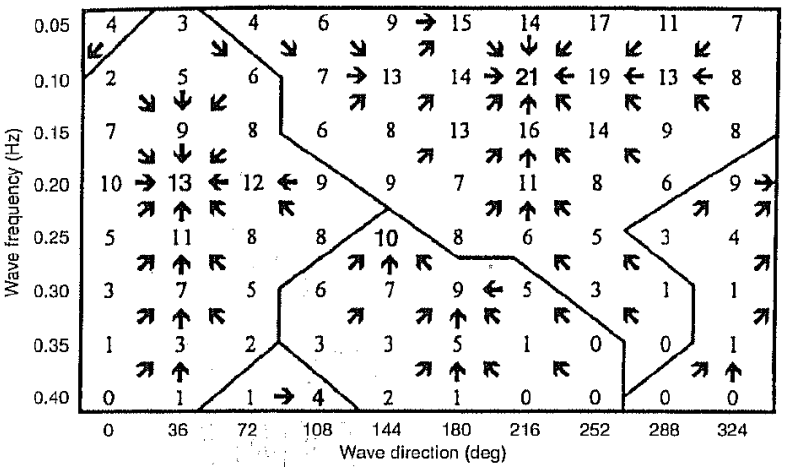

Figure 5.1: Wave systems partitioning by steepest ascent path (or *catchment area*) algorithm*[from Hanson and Phillips (2001)]*.

5.1.2 Partitioning of omnidirectional spectra $E(f)$

For the case of omnidirectional spectral densities $E(f)$, the same kind of algorithms may be used (Voorrips et al., 1997), although the results are not expected to be as consistent as those obtained from directional wave spectra. Integrating energy over directions indeed implies some distortion onto the global spectral shape against frequency. Therefore, extracting wave systems by peaks separation does not always lead to partitions consistent with reality. As addressed later on (Subsection 5.2.1), it is theoretically possible to distinguish swell and wind-sea systems in a spectrum $E(f)$ by defining a so-called *separation frequency* (in Hz), above which the spectral components are assumed to be part of the local wind-sea system. When such data – related to local winds – is not available, other methods were proposed to cope with the systems partitioning just from the spectral characteristics of the sea-state. Two of them are evoked herebelow.

Statistical discrimination criterion of spectral peaks (Rodríguez and Guedes-Soares, 1999)

When estimating an energy spectral density such as $E(f)$ from a given wave record, noise is always found in the spectral estimates, so that a smoothing step is needed to better observe the spectrum's shape. Smoothing can be carried out through block spectral analysis or moving average for instance, but must not be too strong in order to keep most of the original spectral information. Basically, it is assumed that to each spectral peak corresponds a wave system – as actual energy peak of the sea-state. Now, in practice, spectral peaks resulting from the spectral analysis are always noticed, which may remain visible even after having smoothed the raw spectral density properly (*artefacts*). Furthermore, the statistical variability of the spectral estimates increases as the wave sample's size – generally characterised by the density's *degrees of freedom* – decreases. Accordingly, the less the degrees of freedom of the original spectral estimates, the more they need to be smoothed in order to reduce the artefacts' significance. Following this, Rodríguez and Guedes-Soares (1999) deduce that if one wants to know if a spectral peak – in a smoothed spectral density – is "true", it is sufficient to check that its logarithmic height (with respect to the nearest previous saddle point) is superior to some criterion which depends on the estimation precision (degrees of freedom) for a given confidence interval on the statistical variability of the spectral estimates, which follow a χ^2 distribution according to linear theory (see Appendix A). Such a logarithmic criterion has the advantage of being frequency-independent by definition and consistent with the numerical estimation process for Gaussian-assumed wave signals. However, the recommended number of degrees of freedom is quite high in general (>18) and somewhat depends on the arbitrarily fixed confidence interval.

Maximal wave steepness criterion (Wang and Hwang, 2001)

Wang and Hwang (2001) proposed a criterion for separating swells from wind-sea under deep water assumptions, which is based on the determination of the maximum value of a wave steepness function $\alpha(f^*)$ (formed by the ratio of the significant wave height H_{m0} over the mean wavelength $\lambda_{02} = gT_{02}^2/2\pi$ in deep water) from frequency f^* on, expressed as

$$\alpha(f^*) = \frac{H_{m0,f\geq f^*}}{\lambda_{02,f\geq f^*}} = \frac{4\sqrt{m_{0,f\geq f^*}}}{\left(\frac{gT_{02,f\geq f^*}^2}{2\pi}\right)} = \frac{8\pi m_{2,f\geq f^*}}{g\sqrt{m_{0,f\geq f^*}}} \tag{5.1}$$

where index "$_{f\geq f^*}$" means that the parameter is otained by integration over the frequency interval $[f^*; +\infty[$. By plotting $\alpha(f^*)$ against frequency, a maximum value appears for some frequency, which is related to the actual separation frequency, possibly through some correction coefficient according to the data. This method therefore allows to separate wave systems (swells/wind-sea) without working on spectral peaks, but rather on an smoothed frequency-dependent parameter. It has been implemented namely by the *National Data Buoy Center* (N.D.B.C.) to process spectral data estimated by numerous accelerometric buoys deployed along the North American coastlines. Good results were found by the NDBC for growing and strong wind-seas compared with locally measured wind data. Yet, the method may overestimate the actual separation frequency in case of decaying wind-seas and light winds in swell-dominated sea-states[1].

5.2 Wave systems evolution and time tracking

5.2.1 Wind-sea and swell systems dynamics

Wind-sea systems

In linear wave theory, high-frequency wind-generated waves propagate and disperse according to equation (2.59) within quite a broad angular sector – *short-crested waves* – following the rapid strength and direction changes of local winds. These waves store the energy transmitted by wind as the time goes by, and are themselves suject to non-linear wave-wave interactions, so that on the one hand, the peak frequency of the generated wavetrains decreases, and on the other hand, the related significant wave height increases, as illustrated in figures 5.2(a&b).

[1] `http://www.ndbc.noaa.gov/windsea.shtml`

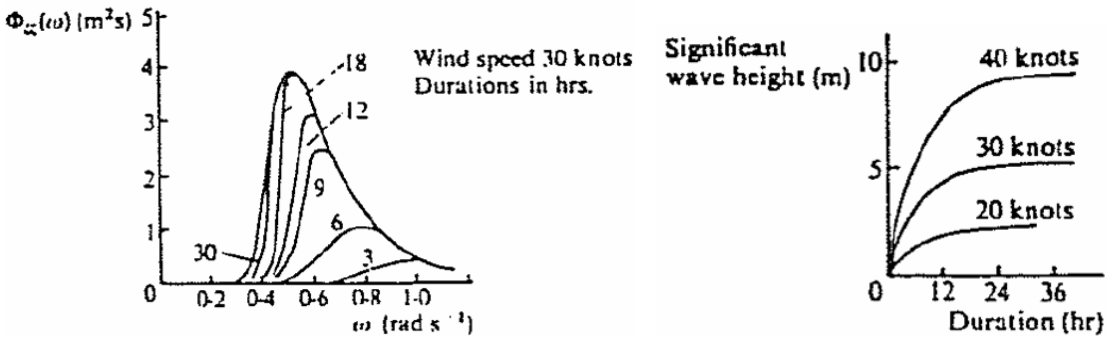

(a) (b)

Figure 5.2: Time evolution of peak frequency ($rad.s^{-1}$) of waves generated by a $30kn$-wind (a) and significant wave height for three wind velocities and fixed fetch (b) *[from Price and Bishop, 1974].*

As peak frequency decreases, the sea-state's spectral shape come closer and closer to a JONSWAP (with $\gamma = 1$) or Pierson-Moskowitz/Bretschneider spectrum. The sea is then said to be "fully developped", which means that the wave energy sources (positive wind energy input on the sea surface) and sinks (non-linear wave-wave interactions, white-capping dissipation and turbulences, wave/current and wave/internal wave interactions, bottom friction in shallow water...) are almost exactly compensated for.

It is common to characterise a wind-sea through the mean velocity U_w of the local wind (generally estimated at some height from the mean sea level, between 10 and $20m$) assuming the wave phase celerity c_ϕ defined as (see Eq. (2.59) in deep water)

$$\begin{aligned} c_\phi &= \frac{\omega}{k} \\ &= \frac{g}{\omega} \\ &= \frac{g}{2\pi f} \end{aligned} \tag{5.2}$$

cannot exceed a certain fraction β of U_w, that is

$$c_\phi = \frac{g}{2\pi f} \leq \beta U_w \tag{5.3}$$

which is also called *local wave age* (ratio of wave and wind celerities) criterion. Parameter β is generally given a value between 1 and 1.5 – the most widely used value being 4/3. This criterion may be refined by introducing the relative wind and wave directionality, denoted by δ and equal to the minimum relative angle separating θ_w (wind) and $\bar{\theta}$ (waves). If this value is inferior to a certain sector (e.g. $\delta \leq 90\,°$), the wind-sea components are therefore defined such as

$$c_\phi \leq \beta U_w cos\delta \tag{5.4}$$

which – according to equation (5.2) – allows to define the separation frequency

$$f_s = \frac{g}{2\pi\beta U_w cos\delta} \tag{5.5}$$

Without directional information, one can let hold the less restrictive condition (5.3) – equivalent to (5.4) assuming both mean wind and waves are aligned together ($\delta = 0$) –, which therefore yields

$$f_s = \frac{g}{2\pi\beta U_w} \tag{5.6}$$

Hence, if one considers a persistent wind of mean velocity $U_w = 10m.s^{-1}$ over a given extended area, it will generate a wind-sea whose lowest wave frequencies are close to $0.12Hz$, i.e. a maximum wavelength of about $110m$ in deep water. Lower wave frequencies will then be considered as belonging to one or more swell(s) system(s).

Swell systems

A swell is defined as the result of propagated and dispersed waves generated by high-energetic wind events (storms) in remote locations. These wavetrains – which are very conservative – can travel over thousands of kilometres and cross oceans. Such long swell waves are frequently observed along the western coast of Europe as the result of very strong storms likely to have occurred in the Caribbean islands, along the eastern coast of the United States and Canada up to Greenland. At the observation point (*receiver*), as the bending radius (i.e. the distance to the *transmitter* zone along the great paths circles) is quite high, the directional spreading of swells is found to be significantly reduced compared with that of the first wavetrains generated at the transmition point. Hence, swells are characterised as *long-crested waves* parallel to each other. It may be assumed (see Hanson and Phillips, 2001) that swell energy is roughly conveyed at the wave group velocity corresponding to the main frequency of the train, and can therefore be equalled to the mean wave celerity needed to cover the transmission-reception distance d_{prop} at instant t over duration $t - t_0$ (t_0 being the generation instant), which yields, according to equation (3.26) in deep water

$$\frac{d_{prop}}{t - t0} = \frac{g}{4\pi f} \tag{5.7}$$

In other words, the peak frequency of a swell train observed at the reception point increases as time passes by as quick as the transmition zone is close. This phenomenon may be easily comprehended when dropping a stone into the water: the lowest wave frequencies (the longest and fastest waves) propagate first, followed by higher and higher frequencies in tighter and tighter concentric ripples. Equation (5.7) is used to derive estimations of the generation distance to the observation point. Then, thanks to the system's directional information, a gross geographical estimation of the generation zone where the climatic events occurred can be achieved (see Fig. 5.3). For applications as

well as numerical implementations of this theory, the reader is namely referred to Hanson and Phillips (2001) and Kerbiriou (2007).

Figure 5.4 illustrates the ideal and typical peak frequency time evolution of both a swell and wind-sea systems, starting with a growing wind (f_s decrease). One can notice here that after some time both systems come close to each other, so that in case their respective directions are close too, the one is likely to merge with the second. Due to the wind fluctuations as well as the various perturbation factors occurring during the wave propagation (meteorology, currents, geography...), such a pattern is not always observable. This may then complicate the swell and wind-sea systems time tracking and identification steps.

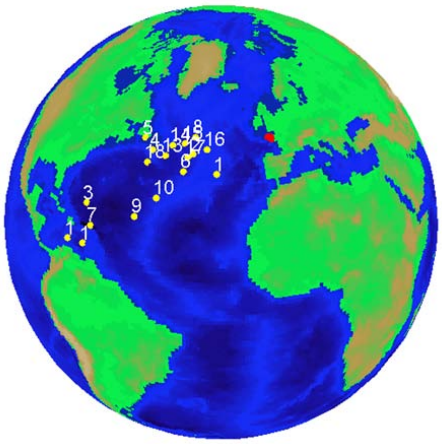

Figure 5.3: Swell generation zones estimated from western Europe wave data *[from Kerbiriou (2007)]*.

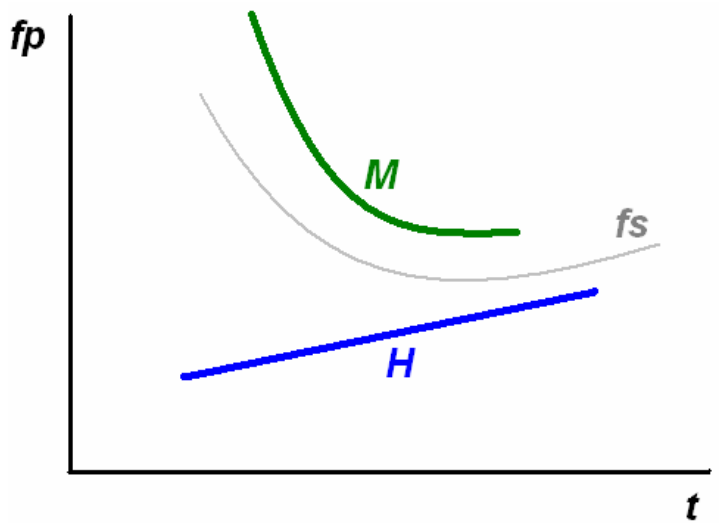

Figure 5.4: Typical peak frequency time evolution of swell ("H") and wind-sea ("M") with separation frequency ("f_s").

5.2.2 Partitions grouping, parameterisation and time tracking

Partitions grouping

A swell partition is defined as a partition whose peak frequency is lower than the swell/wind-sea separation frequency, which can be set to a default value (e.g. $0.12--0.15Hz$ according to the local climate) when wind information is not available. Conversely, a wind-sea partition is characterised by a peak frequency higher than separation frequency.

When two partitions extracted from a wave spectrum – namely thanks to the catchment area technique – are considered as too close in both frequency and direction, it is often relevant to merge then as one and the same partition. Hasselmann et al. (1996) consider that two swell partitions, such that the distance (as module in the complex representation) between their respective peaks is inferior to a fraction (0.5) of the mean spectral spreading of both partitions, may be grouped together. Similarly, if the height of the *saddle point* – that is, the lowest observable value of the spectrum between both peaks – is superior to a fraction (∼0.7) of the smallest peak, both partitions can be grouped together. Last, partitions satisfying condition (5.4) are automatically gathered into a unique wind-sea partition.

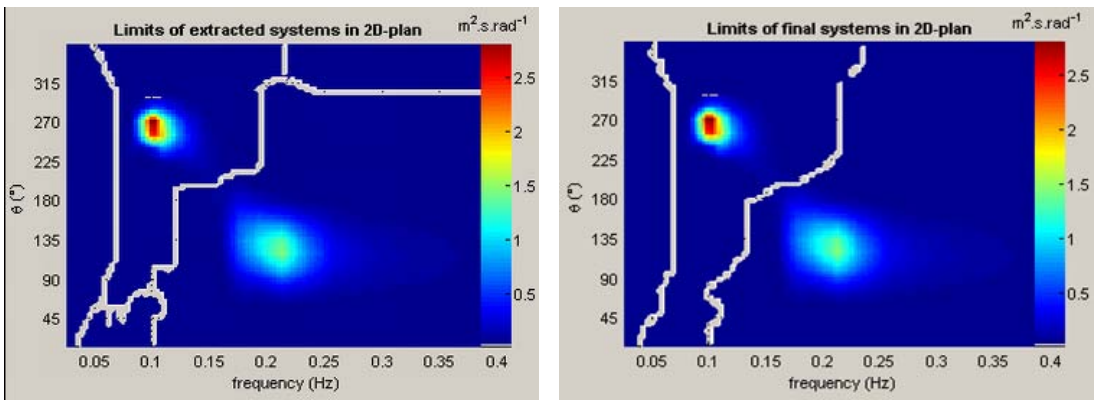

(a) (b)

Figure 5.5: Wave spectrum partitioning with catchment area technique (*watershed*) operated by SPOP: for a multimodal sea-state before (a) and after (b) partitions grouping; here, a swell and a wind-sea partition – both of very low energy – have been grouped to the closest respective swell and wind-sea partitions of the sea-state.

In SPOP, Kerbiriou (2007) similarly sets default (user-controlled) frequency and direction intervals as grouping criteria, such that two partitions are grouped if: 1) the angular distance between both peaks does not exceed 40 ° and 2) the frequency distance is lower than 2 frequency bins (this allows to avoid discriminating swell and wind-sea cases when dealing with frequencies defined as a geometric progression). If the partition

corresponds to a negligible part of the global spectrum's energy (e.g. 4% by default), it is automatically grouped together with the most significant and closest (in frequency) partition. Figure 5.5(a&b) gives an example of wave spectrum partitioning before and after partitions grouping.

Partitions parameterisation

After extraction and grouping of partitions, the information may be reduced to energy, peak period and direction at a minimum, that is, a number of parameters limited to three times the number of partitions. Hence for a given time sequence of wave spectra, these parameters are used to track the systems' time evolution through those three characteristics (see Hanson and Phillips, 2001; Aarnes and Krogstad, 2001, among others).

However, it is of interest to go further in the parameterisation step for at least two reasons. The first one of those is that the wave system is identified through its partition, which is nothing but a spectral portion extracted as with a die-cutter in the directional spectrum, and – by hypothesis – not related to the surrounding spectral components, which is physically not always admissible. It could be so if the system were absolutely separated from any other in the frequency-direction plane, so that the border values of the partition were almost zero. A wave system actually spreads itself and interacts with possible coexisting others beyond its own boundaries. For each frequency-direction component, the spectrum is therefore made of the superposition of all the systems' energy contributions, even negligible. A partition must then be "purified" from all external energy contributions. Conversely, it is necessary to know its own external influence on the surrounding systems. Such a procedure is called in SPOP *mutual influences correction*, which can be carried out on the directional spectrum as well as on the omnidirectional frequency spectrum. The second reason – which is directly linked to the first one – is that the previous synthetic dataset characterising each partition does not enable to *reconstruct* the original spectrum with accuracy. By fitting the partitions with well-chosen parametric spectral shapes (such as JONSWAPs and $cos^{2s}\ldots$), it is first possible to parameterise the partition in a much finer way (through frequency and directional spreading parameters governing these shapes), and second, to fully reproduce the original spectrum from such shapes with a minimal residual error. This is namely true when the mutual influences between partitions have been taken into account and corrected beforehand. Otherwise, the reconstructed sea-state may appear more energetic than the original one (see Fig. 5.6(a)). The optimal parametric shapes must therefore be found in order to, first, end up with a global spectral shape that matches as best as possible the original one, and second, have parametric shapes whose total energy corresponds to that of the related partition (Fig. 5.6(b)).

In SPOP, a JONSWAP (for wind-seas) or modified JONSWAP (with higher decrease-powers around the peak for swells) spectral shape is first fitted to the partition in fre-

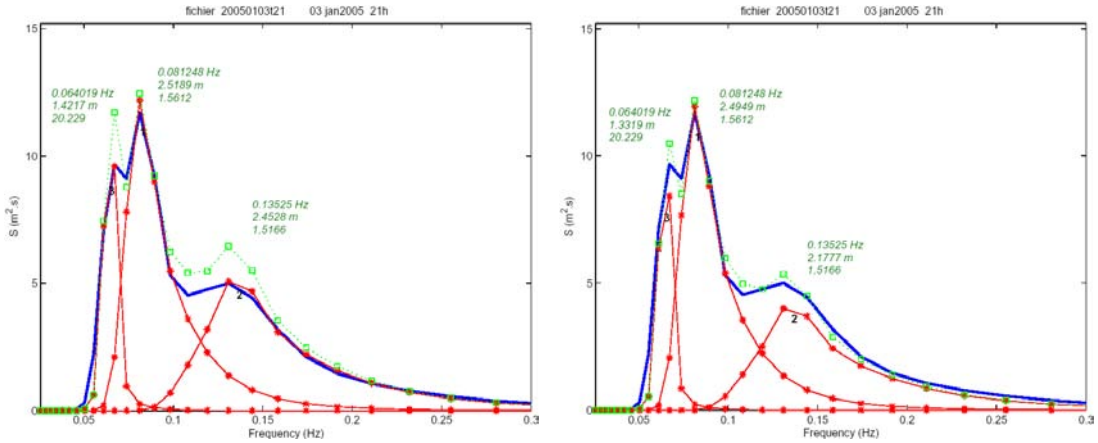

(a) (b)

Figure 5.6: Example of parametric shapes (against frequency – red curves) fitting wave partitions extracted from a given spectrum with (a) and without (b) mutual influences correction; the blue and green curves respectively refer to the original and reconstructed (superposition of the fitting parametric shapes) spectral densities *[from Kerbiriou, 2007]*.

quency, then a directional distribution (such as cos^{2s}) to the same partition integrated over frequencies. The spectro-directional parametric shape is then simply obtained as the product of both, according to equation (4.1). The most optimal fitting of each partition leads to a set of descriptive parameters as $\{H_{m0}, f_p, \gamma, \theta_p, s\}^t$. To take the possible mutual influences of systems into account for the spectrum's reconstruction – sum of all the systems –, one can for instance adjust the energy of the partitions in order to minimise the quadratic error with the original target spectrum. In SPOP, a routine solving non-negative least squares constraints (as an approached solution of a matrix equation $A \cdot X = B$) is implemented to compute the optimal correction coefficients for each partition based on the spectrum's peak values (see Kerbiriou, 2007, p. 37): the sum of the corrected fitting spectral shapes at the peaks must be as close as possible to the original values. Indeed, the resulting matrix equation system is not always solvable due to the inherent dependence of the terms of the matrix. This is why, in practice, only an approached solution is expectable to deal with the mutual influences issue.

Wave systems time tracking

Thanks to the wave systems extraction and grouping steps, and thanks to the determination of a separation frequency (from wind data with Eq. (5.5) or (5.6), or set to a default value), a first identification procedure is possible by sorting wave systems into "swell" or "wind-sea". Nevertheless, certain contentious cases force to look at the systems' time evolution in view of confirming or not the first identification, namely through the consideration of parameters like f_p, θ_p and H_s, along with the local wind

characteristics (mean velocity and direction), when available.

Gerling (1992) details a first approach for the cross-assignment of two partitions within a given space and time window. On the one hand, if two partitions are close enough in space and time (typically, by an interval separating two consecutive measurements), and on the other hand, if their descriptive parameters are close too (in relative or absolute value), they are assigned to each other. Such arbitrary criteria may obviously differ from a dataset to another, according to the local wave climate particularities.

Voorrips et al. (1997) adopt a similar point of view and add another condition, based on the correspondence of both system types (swell or wind-sea). Then it is not possible anymore to reconsider the previous identification since it is assumed as exact. Such a method was namely implemented by Aarnes and Krogstad (2001).

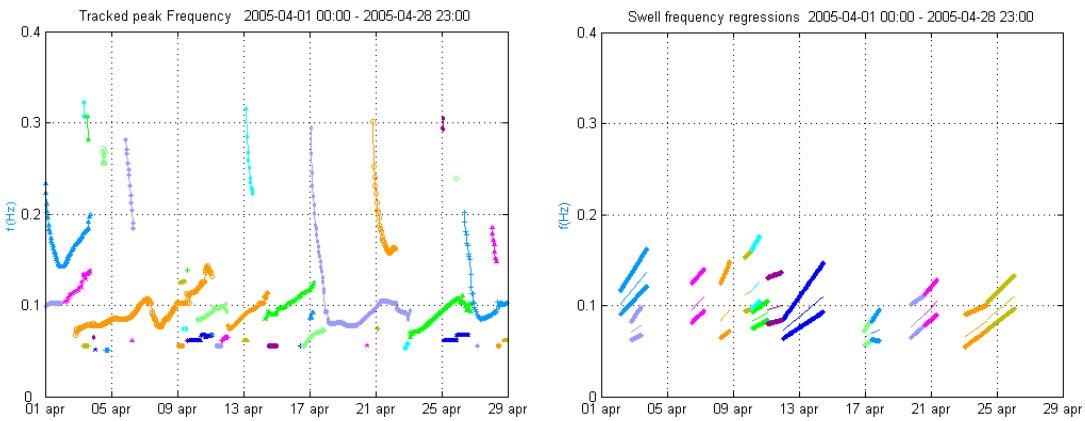

(a) (b)

Figure 5.7: Peak frequency time evolution (a) of wave systems extracted by SPOP in the Bay of Biscay in March 2005; linear regressions applied to the frequency evolution of identified swells with corresponding cut-off frequencies (b) (see Gjevik et al., 1988) [The colour system is not the same in both figures].

Once again in SPOP, Kerbiriou (2007) used the same kind of criteria without any test on the partitions' nature though. Time tracking results related to spectral data in the Bay of Biscay (April 2005) are depicted in figures 5.7(a&b), 5.8(a&b) and 5.9. It becomes then possible to definitely state on the real nature of a wave system, by inspecting the total time the peak frequency lies above or below the separation frequency (Fig. 5.7): for instance, if the peak frequency remains above f_s more than 70% of its total lifetime, then it is identified as a wind-sea at each time step, and conversely. Linear regressions – possibly piecewise – can be carried out on the peak frequency time evolution of wave systems identified as swells, which allow to determine the space and time origins of the related wavetrains, or generation zone, thanks to equation (5.7) (Fig. 5.9). To be exhaustive, let us add (Gjevik et al., 1988) that the spectral bandwidth time evolution of swells theoretically enables also to derive information about the mean dimensions and

durations of the storms which originated these systems.

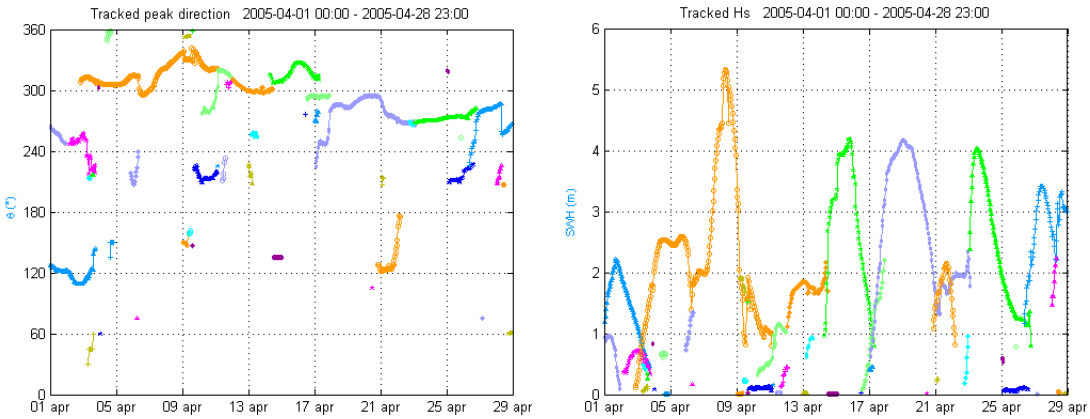

(a) (b)

Figure 5.8: Peak direction (a) and significant wave height (b) time evolutions of wave systems extracted by SPOP in the Bay of Biscay in March 2005.

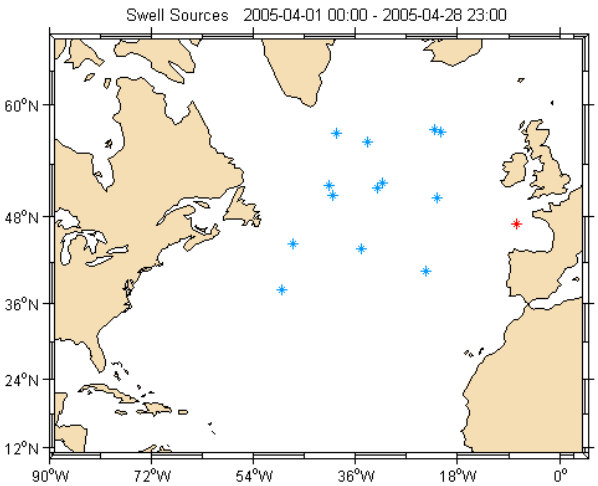

(a)

Figure 5.9: Estimated generation zones corresponding to the swells identified in figure 5.7(b).

This illustration (from wave propagation model results) confirms the theoretical wave systems time evolution patterns developped in Section 5.2.1 (Fig. 5.4). The low-frequency swells mostly come from a wide western angular sector (Fig. 5.9) – with a noticeable time continuity – whereas the high-frequency isolated wind-seas arise from much more random directions (Fig. 5.8(a)). The time evolution of their significant wave height generally is increasing and decreasing successively, as figure 5.8(b) notably suggests. The energy time evolution of swells is a bit more complex for it may be distorted by merging close wind-seas, as occurred near the 18th of April where the algorithm assigned the turning wind-sea to the frequency-close ongoing swell. Figure 5.7(a) however

shows that some swells are not entirely tracked during their whole existence. This is due to several reasons, among which the continuity cuts in case of missing dates (where the extraction step failed), inappropriate time tracking criteria for some very particular cases, etc. Nevertheless, the space correlation of wave systems observed in a few sea locations may help overcome such failures. This may induce distortions in the global statistics derived from the multisystem analysis.

5.3 Conclusion about the extraction, time tracking and identification of wave systems

This chapter – as an introduction to Chapter 6 – permitted to briefly review the state-of-the-art related to the wave systems extraction procedures applied to time sequences of directional spectra $E(t, f, \theta)$. A particular attention notably was paid to the method of wave systems time tracking, which yields a better identification and was once again exemplified with results drawn from SPOP. The acquired knowledge about the time evolution of wave systems is indeed a good prerequisite before tackling the spatiotemporal coherence analysis, which provides a finer and more complete tracking. It is addressed in detail in the next chapter.

Chapter 6

Wave systems coherence and spatiotemporal tracking

6.1 Geostatistics and variographic analysis

To tackle the study of space coherence of wave systems, one can start by drawing its inpiration from the geostatistics field and its most common techniques (see namely Cressie, 1993). Most of geostatistical studies are based on the variographic analysis, which is briefly presented in the following.

6.1.1 semi-variogram and covariogram

Let $Z(\vec{s})$ be a real random value defined at point $\vec{s} = (x, y) \in \mathbb{R}^2$ and distributed according to some particular law. A finite ensemble of such values $(\vec{s})$ – that is, a spatial domain $\mathscr{D} \subset \mathbb{R}^2$ – is called a *random function*: $\{Z(\vec{s}), \vec{s} \in \mathscr{D}\}$. This can deal with temperature fields, rainfall rates, ore concentrations... It is then assumed that:

- the function is **continue** over $\mathscr{D}$, and
- the function is **2nd-order stationary** over $\mathscr{D}$, which means that its 1st- (mean value) and 2nd- (variance, covariance, variogram) orders do not depend on the absolute position in space but only on the separation distance.

The less extended the spatial region, the more the stationarity hypothesis can be invoked. In the following, it will also be assumed that the function is *isotropic*, which means that the field correlation is not influenced by the directionality of the points (along certain axes), but only by their relative distance.

The semi-variogram $\gamma(h)$ is defined as the difference of the total variance and covariance of the random function, as

$$\gamma(h) = C(0) - C(h) \tag{6.1}$$

where $C(h)$ denotes the covariance function – also called *covariogram* –, which only depends on the Euclidean distance $h = \|\vec{s_1} - \vec{s_2}\|$ for any pair $(\vec{s_1}, \vec{s_2}) \in \mathscr{D}^2$, that is

$$\begin{aligned} C(h) = C(\vec{s_1}, \vec{s_2}) &= C(\|\vec{s_1} - \vec{s_2}\|) \\ &= E\left[(Z(\vec{s_1}) - m(\vec{s_1}))(Z(\vec{s_2}) - m(\vec{s_2}))\right] \end{aligned} \tag{6.2}$$

and

$$\begin{aligned} C(0) = C(\vec{s_1}, \vec{s_1}) &= E\left[(Z(\vec{s_1}) - m(\vec{s_1}))^2\right] \\ &= var\left[Z(\vec{s_1})\right] \end{aligned} \tag{6.3}$$

or, since the stationarity hypothesis permits to write $m(\vec{s_1}) = m(\vec{s_2})$,

$$\begin{aligned} \gamma(h) &= C(0) - C(h) \\ &= var\left[Z(\vec{s_1})\right] - C(\vec{s_1}, \vec{s_2}) \\ &= E\left[(Z(\vec{s_1}) - m(\vec{s_1}))^2\right] - E\left[(Z(\vec{s_1}) - m(\vec{s_1}))(Z(\vec{s_2}) - m(\vec{s_2}))\right] \\ &= \frac{1}{2} \cdot E\left[(Z(\vec{s_1}) - Z(\vec{s_2}))^2\right] \\ &= \frac{1}{2} \cdot var\left[Z(\vec{s_1}) - Z(\vec{s_2})\right] \end{aligned} \tag{6.4}$$

Hence the name *semi-variogram*, or more simply – and abusively – *variogram*. The variogram describes both the continuity and correlation of the spatial structure of field Z in $\mathscr{D}$. It generally increases with inter-distance h and is characterised by the following properties (Fig. 6.1):

range: distance from which the field values can be considered as uncorrelated (zero covariance) and where γ becomes equal to the variance of function Z;

sill: asymptotic value (equal to the variance of Z) in the limit $h \to +\infty$;

nugget: value taken by γ as $h \to 0^+$ (discontinuity at $\gamma(0) = 0$) which corresponds to variability at very small scale as the measurement error.

In practice, the isotropic semi-variogram is estimated as

$$\hat{\gamma}(h) = \frac{1}{2N(h)} \cdot \sum_{\|\vec{s_i} - \vec{s_j}\| = h} (Z(\vec{s_i}) - Z(\vec{s_j}))^2 \tag{6.5}$$

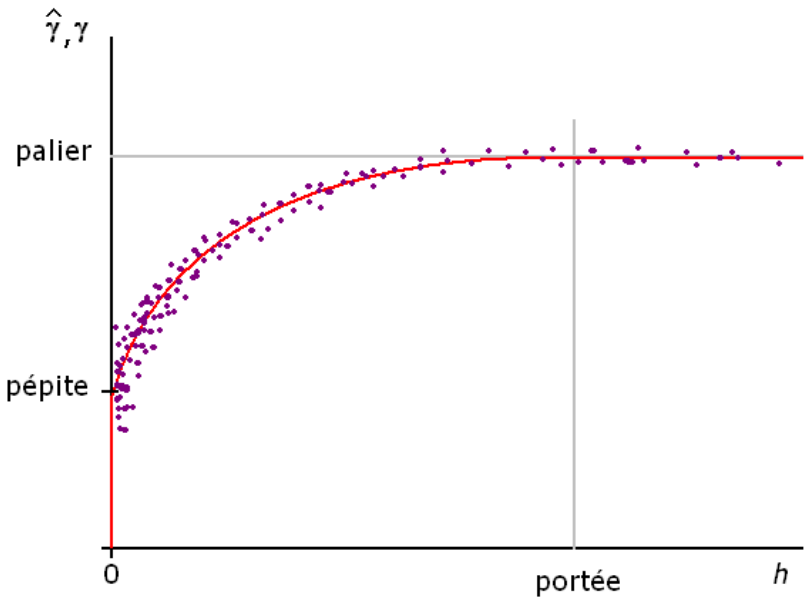

Figure 6.1: Estimated and modelled semi-variogram.

in which a certain tolerance is assumed on h, in order to deal with a sufficient number of pairs $(\vec{s_i}, \vec{s_j})$ while estimating $\gamma(h)$ (the number of points is finite). The resulting estimated variogram (scatter plot $\hat{\gamma}$) is then fitted with a parametric model (as nugget, power, spherical, Gaussian, exponential... see e.g. Cressie, 1993). The variogram modelling certainly constitutes the most sensitive and fussiest part of the variographic analysis for it is aimed at describing the correlation of the whole field for further works, like spatial interpolation techniques (*kriging*). In the present thesis, the concept of variogram and covariogram shall be retained to characterise the similarity of two wave parameters.

In order to illustrate the use of variograms, let us focus on an integrated wave parameter such as H_{m0} estimated over a vast maritime zone (44 sea points in the South of French Brittany through WWIII 3-hourly spectral densities, see Fig. 6.2 and Ardhuin et al., 2008). The stationarity hypothesis cannot hold if the mean value (in time, here) of the random variable is space-dependent within $\mathscr{D}$, which is observed in practice (see Fig. 6.3). To overcome this problem, it is common to work with zero-mean normalised variables, such as $h_{m0} = \frac{H_{m0} - \overline{H_{m0}}}{\sigma_{H_{m0}}}$, where $\overline{H_{m0}}$ and $\sigma_{H_{m0}}$ respectively denote the mean and standard deviation of H_{m0} in time (calculated over roughly five months of data – January to May 2008 –, see Fig. 6.3&6.4). Figures 6.5(a-d) represent the variograms estimated (Eq. (6.5)), and fitted with a Gaussian parametric model (see Section 6.2.3, Eq. (6.12)) on the 1st of January, midnight (a), 13th of January, 9AM (b) and 10th of February 2008, midnight (c&d). According to the cases, the variogram exhibits either a mono-(b) or multi-field (a&c) structure. Figures 6.5(a&c) moreover highlight the fact the model is not appropriate to the geographical domain, which would deserve to be divided into more homogeneous sub-regions where another model may better fit the data

(Fig. 6.5(d)). Obviously, the South Brittany region is too wide to let the stationarity hypothesis be invoked when applying kriging techniques on wave parameters like H_{m0}.

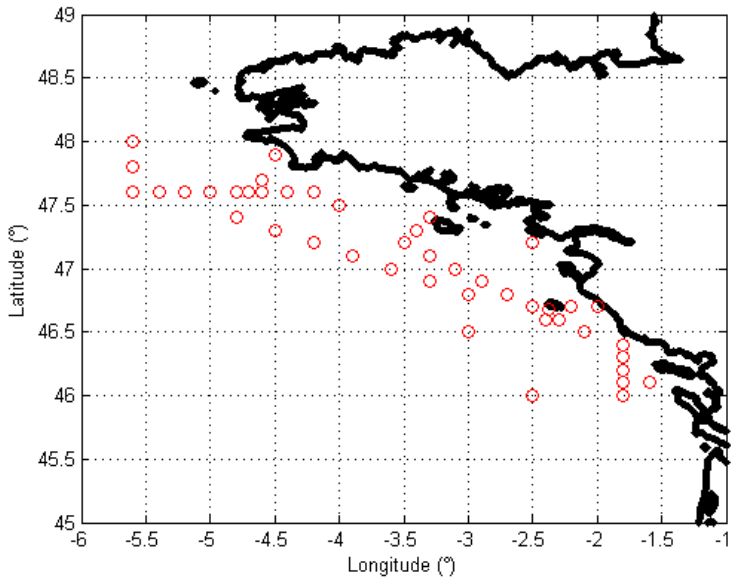

Figure 6.2: WWIII control points in South Brittany (France).

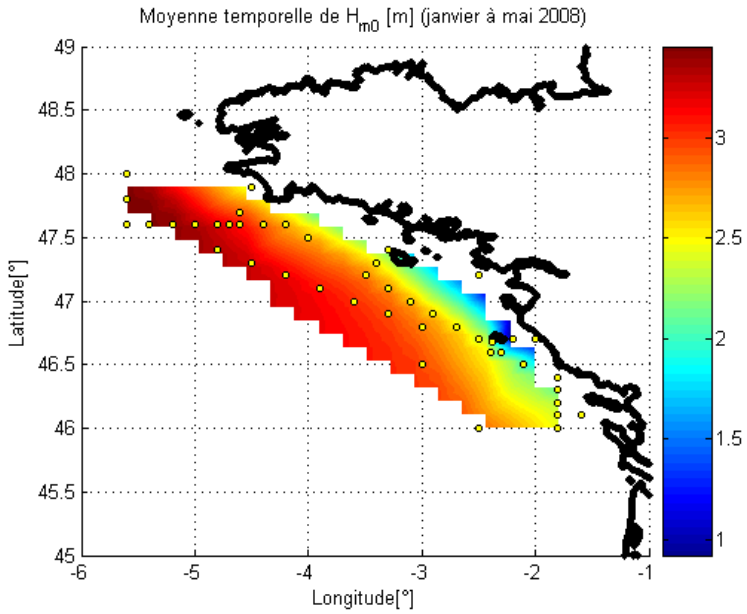

Figure 6.3: Distribution of (time) mean significant wave height H_{m0} in South Brittany from January to May 2008.

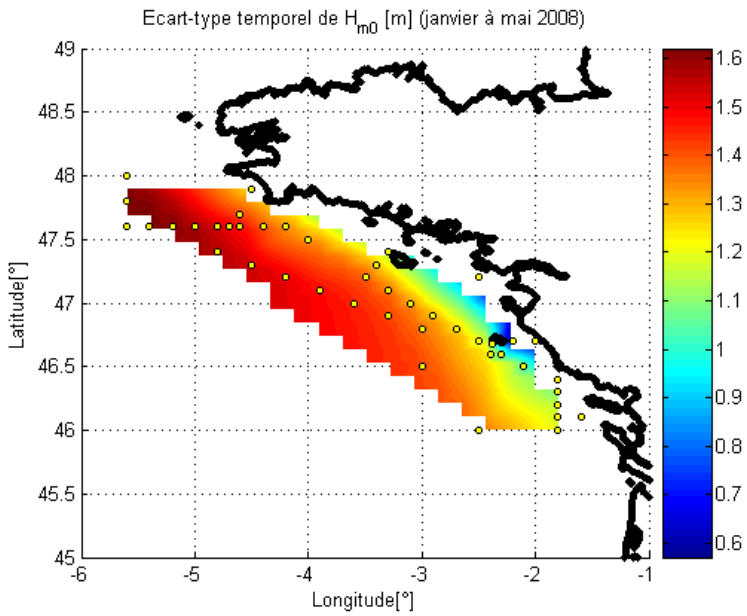

Figure 6.4: Distribution of significant wave height H_{m0} (time) standard deviation in South Brittany from January to May 2008.

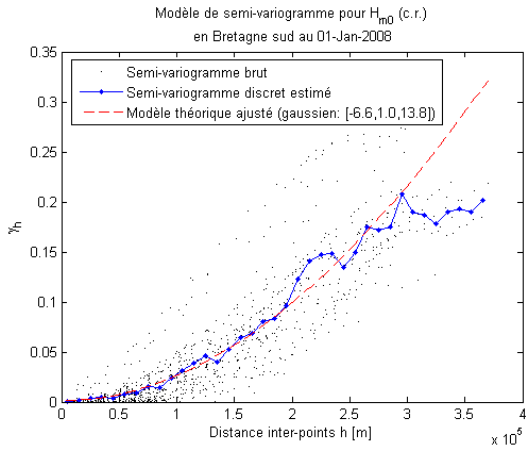

(a)

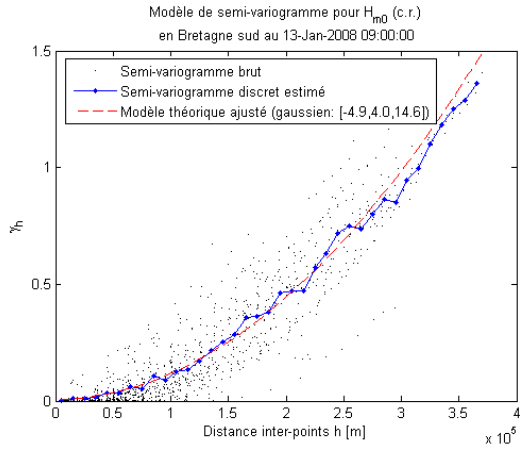

(b)

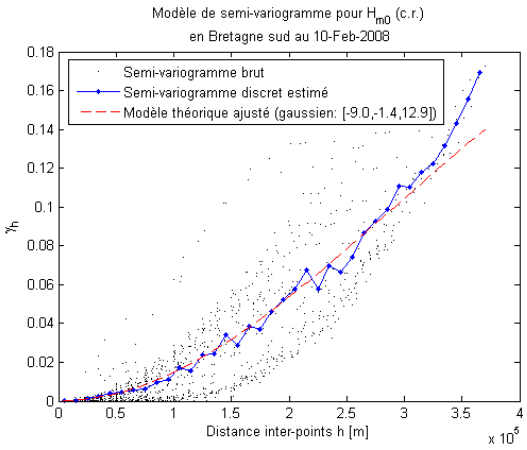

(c)

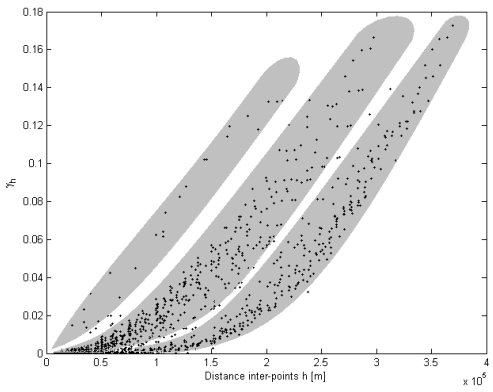

(d)

Figure 6.5: Variograms of centred and normalised significant wave height H_{m0} estimated and Gaussian-fitted in South Brittany on the 1st of January, midnight (a), 13th of January, 9AM (b), and 10th of february, midnight (c); homogeneous scatter zones highlighted in gray (d).

6.1.2 Specificity of the sea-state spatial coherence study

As exemplified in the previous subsection, both the continuity and stationarity hypotheses can be invoked on principle when studying the time and space evolution of global wave parameters such as the significant wave height, wave power, mean direction... Now, studying the space and time coherence of sea-states – which are based on a refined multisystem description – presents a double difficulty:

- the characterisation of a wave system through a single parameter (H_{m0}, $P_w \ldots$) is not sufficient: an ensemble of N_{par} parameters has to be considered instead – as the system's state-vector : $\vec{p} = \{f_p \quad \theta_p \quad m_0 \ldots\}^t \in \mathscr{G}$, where $\mathscr{G} \subset \mathbb{R}^{N_{par}}$ denotes the domain of definition of state vectors $\vec{p}$;

- a sea-state is often made of the superposition of several wave-systems; in others terms, at given point $P(\vec{s})$ in $\mathscr{D}$ and given instant t, the sea-state may be synthesized by the state matrix (Eq. (4.5))

$$\Sigma_{(\vec{s},t)} = [\vec{p}_{\vec{s},t,1} \quad \vec{p}_{\vec{s},t,2} \quad \ldots \quad \vec{p}_{\vec{s},t,n}]$$

  where $n = n(\vec{s}, t)$ is the number of individual systems composing the sea-state. At instant t over the oceanic region $\mathscr{D}$ described through N_P observation points, an ensemble of N_P matrices $\Sigma_{(\vec{s},t)}$ is therefore to be considered, whose columns number may vary from one point to another.

Therefore, the spatial coherence of sea-states rapidly becomes inextricable if one wants to use common variographic tools based on one or even two (like in *co-kriging* purposes) variable(s) only. In the following, an explorative approach in proposed to cope with the space and time coherence of sea-states in small-scale regions where continuity and stationarity conditions can be assumed on principle for any wave variable.

6.2 Space and time tracking of extracted wave systems

6.2.1 Spatiotemporal cross-assignment of wave systems at small scale (local)

Let $\mathscr{F} = \mathscr{D} \times \mathscr{T}$ be a spatiotemporal window, where $\mathscr{D} \subset \mathbb{R}^2$ describes the spatial (geographical) domain and $\mathscr{T} \subset \mathbb{R}$ the study time window. It is assumed that the wave systems are quasi-stationary in $\mathscr{F}$, especially since $\mathscr{F}$ is small.

The wave fields are described in a finite number of spatiotemporal observation points N_c, and such that $N_c = N_t \times N_P$, with N_t the number of observation instants and N_P the number of geographical points defined by the spatial discretisation. Here, this will be restrained to fixed a discretisation in both space and time (i.e. fixed grid and constant time interval, 1-3h), typically as data output from wave propagation models like WaveWatch III or WAM models.

At each sea-point $P_{i,j} = P(\vec{s_i}, t_j)$, let us set the maximum extractable number of wave systems to n_{smax}, that is, a total of N_s systems over $\mathscr{F}$, with $N_c \leq N_s \leq N_c n_{smax}$. The following function is then defined

$$\begin{aligned} A : \mathscr{G} \times \mathscr{G} &\longrightarrow [0;1] \subset \mathbb{R} \\ (\vec{p_1}, \vec{p_2}) &\longmapsto \lambda \end{aligned} \tag{6.6}$$

where the scalar λ accounts for the assignability of two extracted wave systems $\vec{p_1}$ et $\vec{p_2}$. It can deal with a linear combination of the type

$$\lambda = A(\vec{p_1}, \vec{p_2}) = \sum_{i=1}^{N_{par}} \lambda_i g_i(\vec{p_1}, \vec{p_2}) \tag{6.7}$$

where functions $g_i(\vec{p_1}, \vec{p_2})$ are comparative applications, whose values are included in $[0;1] \in \mathbb{R}$ such that $g_i(\vec{p_1}, \vec{p_2}) \to 1$ as $\vec{p_1} \to \vec{p_2}$, and λ_i are weighting coefficients such that $\sum_i \lambda_i = 1$, which permit to adjust the relative influence of each descriptive wave parameter (components of the state vector) in the comparison. By applying this cross-assignment function to each pair of wave systems observed in $\mathscr{F}$ (i.e. N_s systems, thus $\frac{1}{2}(N_s - 1)(N_s - 2)$ pairs), the results can be summarised into a matrix form – spatiotemporal cross-assignment matrix $M_{A_{\mathscr{F}}}$ – as

$$M_{A_{\mathscr{F}}} = \begin{pmatrix} A(\vec{p_1}, \vec{p_1}) & A(\vec{p_1}, \vec{p_2}) & \dots & A(\vec{p_1}, \vec{p_{N_s}}) \\ A(\vec{p_2}, \vec{p_1}) & A(\vec{p_2}, \vec{p_2}) & \dots & A(\vec{p_2}, \vec{p_{N_s}}) \\ \vdots & \vdots & \ddots & \vdots \\ A(\vec{p_{N_s}}, \vec{p_1}) & A(\vec{p_{N_s}}, \vec{p_2}) & \dots & A(\vec{p_{N_s}}, \vec{p_{N_s}}) \end{pmatrix} \tag{6.8}$$

This matrix is symmetrical due the own symmetry properties of function A, whose diagonal terms are equal to unity. Then, let us set a threshold $A_{min} \in [0;1]$ to define matrix $\hat{M}_{A_{\mathscr{F}}}$ such that $\hat{M}_{A_{\mathscr{F},ij}} = 1$ if $M_{A_{\mathscr{F},ij}} \geq A_{min}$, and 0 otherwise. This second matrix is also symmetric and binary, by definition: it describes the gross spatiotemporal cross-assignment structure of the wave systems observed in $\mathscr{F}$. However, the matrix needs to undergo some transformations in order to be perfectly consistent. For the moment indeed, if three wave systems $\vec{p_i}$, $\vec{p_j}$ and $\vec{p_k}$ extracted within the window $\mathscr{F}$ such as $\hat{M}_{A_{\mathscr{F},ij}} = \hat{M}_{A_{\mathscr{F},jk}} = 1$, $\hat{M}_{A_{\mathscr{F},ik}}$ is not prevented from being zero. Now, it would seem relevant to assign $\vec{p_k}$ to $\vec{p_i}$ indirectly – even if they are not assigned to each other

directly. Determining those indirect assignments requires some numerical operations on the matrix that are exposed in Appendix E. It deals with an iterative procedure until convergence to matrix $\tilde{M}_{A_{\mathscr{F}}}$, which is block-diagonalisable. This latter synthesizes the final spatiotemporal cross-assignment structure of wave systems, which are gathered in disjointed ensembles.

6.2.2 Cross-assignment by homogeneous structures tracking at meta-scale (global)

In a given spatiotemporal window $\mathscr{F}$ characterised by space and time dimensions of respectively a few hours and tens of square kilometers, the first local step permits to regroup the wave systems belonging to homogeneous and coherent structures at small (or micro-) scale: this step was called *local cross-assignment*. At a superior scale (window Φ) – or "meta-scale" – the coherence or such structures observed in sub-windows $\{\mathscr{F}_i\}$ such that $\forall i, \mathscr{F}_i \subset \Phi$, may in turn be processed by *global cross-assignement*. The grouping of coherent structures is therefore lead from the smallest to the widest scale, for well-chosen space and time dimensions. However, the meta-scale approach differs from the previous one for several reasons:

- As any globalising process, local particularities disappear as scale increases to the detriment of the physical resolution, so that the number of comparative wave parameters at meta-scale – mean structure values in each local window – may be reduced. For instance, parameters like peak frequency, peak direction and significant wave height are necessary to determine homogeneous structures at small scale ($\mathscr{F}$); at meta-scale though, their coherence may be limited to the consideration of the mean structure frequency and direction;

- furthermore, contrary to the small-scale approach where the wave systems' stationarity may be assumed on principle, this latter is less and less assumable as scale increases, so that the spatiotemporal proximity of windows $\mathscr{F}_i \subset \Phi$ has now to be taken into account.

The scales used in this work are the following:

- **small-scale:** one time interval separating two spectral measurements for time scale (typically 1 to $3h$, during which the sea-states stationarity assumptions generally hold for offshore and coastal engineering purposes) and a geographical zone contained within a square of side up to a few hundreds of kilometers for spatial scale;

- **meta-scale:** from a few days to a few months for the time scale; no geographical extension for spatial scale.

In this particular scheme, the local coherence corresponds to that of the wave systems in space coherence at given instant (or sea-state time interval), whereas the global coherence corresponds to that of the homogeneous structures in time, following a chronological progression (two successive time discretisation instants). This scheme represents one possibility among many others. It has been chosen for the sake of programmation simplicity, and directly refers to the scheme adopted by Kerbiriou (Kerbiriou et al., 2007) in SPOP, where the spatial observation is limited to one single sea-point (pure time coherence). The structure of the implemented algorithm here is presented in the following subsection.

6.2.3 Spatiotemporal wave systems tracking algorithm

The proposed algorithm is structured in three successive steps: the first one performs an auto-adaptative partitioning in homogeneous wave systems at each time step; the second step refines these groupings namely by characterising the spatial structures as "fixed" or "floating"; last, the third step performs the structures' time tracking.

Auto-adaptative spatial partitioning

The first – spatial – step mostly follows the previously exposed sequence, which is based on parameters as peak frequency (f_p), peak direction (θ_p) and significant wave height (H_s ou H_{m0}) of each wave system extracted by SPOP. Each wave system is therefore represented by a state vector $\vec{p} = \{f_p, \theta_p, H_s\}^t$.

Let $(\vec{p_1}, \vec{p_2}) = (\vec{p}_{\vec{s_1},t}, \vec{p}_{\vec{s_2},t})$ be the state vectors of two systems observed at the respective sea points $\vec{s_1}$ and $\vec{s_2}$ at instant t such that $\vec{p_1} = \{f_{p1}, \theta_{p1}, H_{s1}\}^t$ and $\vec{p_2} = \{f_{p2}, \theta_{p2}, H_{s2}\}^t$ respectively. The spatial cross-assignment function $A(\vec{p_1}, \vec{p_2})$ (Eq. (6.6)) is calculated by default as

$$\begin{aligned} A(\vec{p_1}, \vec{p_2}) = a_{fs} * & \left[\frac{\min(f_{p1}, f_{p2})}{\max(f_{p1}, f_{p2})}\right] + \\ a_{ts} * & \left[1 - \frac{\min(|\theta_{p1} - \theta_{p2}|, 360 - |\theta_{p1} - \theta_{p2}|)}{180}\right] + \\ a_{hs} * & \left[\frac{\min(H_{s1}, H_{s2})}{\max(H_{s1}, H_{s2})}\right] \end{aligned} \tag{6.9}$$

where a_{fs}, a_{ts}, and a_{hs} are weighting coefficients related to the wave systems' state parameters, and such that $a_{fs} + a_{ts} + a_{hs} = 1$. As peak frequency is rather a homogeneous and stationary parameter for the considered physical phenomenon, coefficient a_{fs} may be assigned more relative weight. On the contrary, as the significant wave height may susbstantially vary from a location to another nextby one due to the natural variability of wind regimes and possible – and random – distortion induced by the wave partitioning step (catchment area partitioning technique, systems grouping, mutual influence correction...), less weight may be given to coefficient a_{hs}. Hence the general inequality

$$a_{hs} \leq a_{ts} \leq a_{fs} \tag{6.10}$$

The physical similarity criteria therefore are merged into one single (scalar) coefficient, which takes the joint and relative proximity of all parameters in a row, contrary to static empirical and independents criteria that were proposed by some autors for the same type of study (see Section 5.2.2). Here, the results are not constrained to some arbitrary physical criteria, but derive from a qualitative grouping of systems without strong physical limitations. This namely allows to reconsider the common swell/wind-sea separation criteria, which may happen sometimes to be inappropriate.

Expression (6.9) is proposed as a default function, but other ones may be envisioned acording to the most adopted variographic models by geostatisticians: Gaussian, exponential, spherical... (see Baillargeon, 2005), namely for peak frequency and significant wave height. The comparative function related to peak direction is kept as in equation (6.9) (linear model). As an illustration, let us list some other possible covariograms (with zero-nugget) formulated for peak frequency:

- *linear model:*

$$g(f_{p1}, f_{p2}) = 1 - \frac{2\,|f_{p1} - f_{p2}|}{f_{p1} + f_{p1}} \tag{6.11}$$

- *Gaussian model:*

$$g(f_{p1}, f_{p2}) = \exp\left[-4\left(\frac{|f_{p1} - f_{p2}|}{f_{p1} + f_{p1}}\right)^2\right] \tag{6.12}$$

- *exponential model:*

$$g(f_{p1}, f_{p2}) = \exp\left[-\frac{|f_{p1} - f_{p2}|}{f_{p1} + f_{p1}}\right] \tag{6.13}$$

- *spherical model:*

$$\begin{aligned} g(f_{p1}, f_{p2}) &= 1 - \frac{3}{2}\rho - \frac{1}{2}\rho^3, \quad \rho \leq 1 \\ &= 0, \quad \rho > 1 \end{aligned} \tag{6.14}$$

with

$$\rho = \frac{|f_{p1} - f_{p2}|}{\frac{f_{p1}+f_{p1}}{2}}$$

- *extrema model (default):*

$$g(f_{p1}, f_{p2}) = \frac{\min(f_{p1}, f_{p2})}{\max(f_{p1}, f_{p2})}, (f_{p1}\, f_{p2}) \neq (0, 0) \tag{6.15}$$

Each model is depicted in figures 6.6(a-e). As one can see, each bivariable function is equal to 1 when both input parameters are equal ($y = x$ axis) and decreases as both parameters differ from each other up to zero. To each model corresponds a particular sensitivity: according to the model, the sill ($= 1$) is moreless sharp and the decrease from 1 moreless abrupt. By sorting these models qualitatively from the most "discriminating" to the most "tolerant", it yields respectively: spherical, extrema, exponential, linear and Gaussian. These five models are then tested in the wave systems and homogeneous structures cross-assignment (for parameters f_p and H_s).

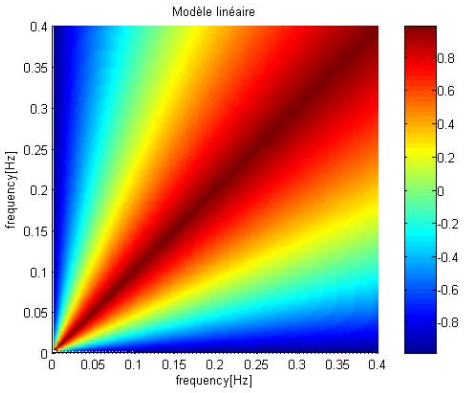

(a)

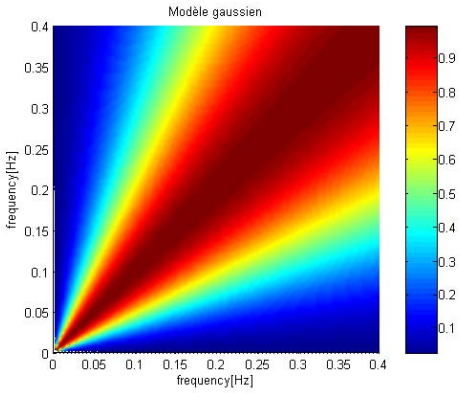

(b)

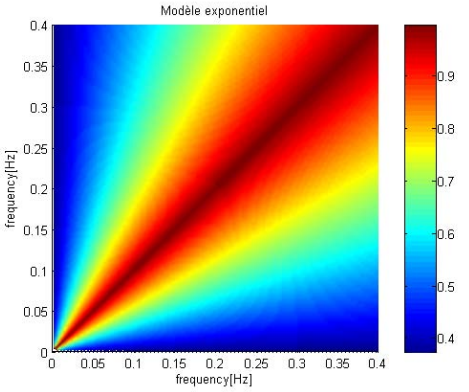

(c)

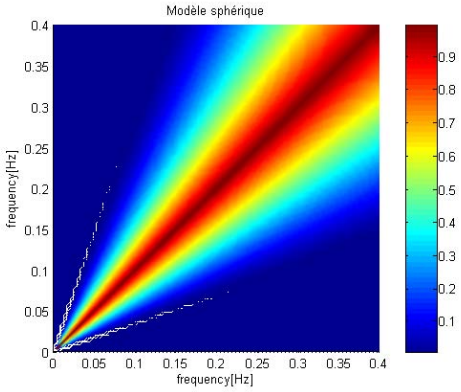

(d)

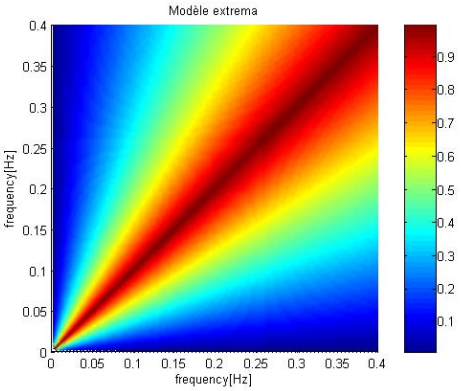

(e)

Figure 6.6: Models of covariograms related to peak frequency parameter f_p: linear (Eq. (6.11)), Gaussian (Eq. (6.12)), exponential (Eq. (6.13)), spherical (Eq. (6.14)) and extrema (default, Eq. (6.2.3)).

From the extracted systems at instant t in the envisioned spatiotemporal domain, the cross-assignment matrix M_A can be easily obtained. A minimum assignment threshold-level A_{min} (e.g. 0.8) is defined in order to determine whether two wave systems are cross-assigned or not. From the gross matrix M_A, the binary matrix $\hat{M}_A$ is formed and processed so that all indirect associations are set to 1, as described previously. Then, it is checked in M_A that the new indirect associations correspond to assignments values sufficiently high, as greater than a threshold $A_{minind} < A_{min}$ (e.g. 0.6). The ensemble of wave systems is therefore partitioned into a finite number of disjointed sub-ensembles characterising *homogeneous structures*.

If the spatial partitioning besides does not induce geographical redundancy – that is, if the associations do not regroup two wave systems observed at the same sea point –, it is considered as relevant. Otherwise – in case there is one geographical redundancy at least and/or if the minimum indirect assignment value in M_A is lower than threshold A_{minind} –, threshold A_{min} is slightly incremented (e.g. 1%) and the whole procedure is repeated. When incrementing A_{min}, the cross-asignment conditions become more restrictive: the number of partitions is therefore expected to increase while the occurrences of geographical redundancy decrease. The procedure may be iterated several times until the stopping criteria be met. That is why the method is called *auto-adaptative*.

In the end of an iteration, all ungrouped wave systems are seen as isolated individual structures. For the next steps (meta-scale), all the structures are characterised through their mean peak frequency and peak direction mean values (once again, significant wave height is not kept for it may vary a lot within a structure).

Re-processing of spatial partitioning by differentiation of fixed and floating structures

Before the spatial structures time coherence step, it is necessary to look back in the previous partitioning step to determine, for each structure, if it has to be merged with another ot not in the same sea-state. Indeed, the previous iterative procedure, which groups together coherent wave systems, tends to isolate them from each other for it avoids before all any geographical redundancy. The present *post-spatial* step is therefore useful when the extraction algorithm punctually detected two "close" systems, which are most probably artefacts corresponding to one and the same structure. It is therefore important to reconsider the spatial partitioning results, by separating here the resulting structures into "fixed" and "floating" elements.

A homogeneous structure is called *fixed* if its physical reality is undeniable (typically, a homogeneous swell observed in most sea points). A homogeneous structure is called *floating* if its physical reality is doubtful, either because too few sea points are involved in the structure (on or two, for instance), or because the wave parameters involved show an important variability. By definition, a floating structure may be retrospectively

grouped together with a fixed structure, but not the contrary. Similarly, two floating structures cannot be merged with each other, neither two fixed structures, which have to remain independent as long as possible.

In the present algorithm, several criteria for classifying structures as fixed or floating are used, all of them being initially assumed as floating. The first criterion classifies a structure as fixed if the number of grouped wave systems is significant: for example, if it is higher than 70% of the total geographical points under consideration. A second criterion also classifies a structure as fixed if it is sufficiently far (in frequency) from another fixed structure, without any intermediary structure in between. When two structures – with one fixed – are complementary in space (no geographical redundancy induced by merging both) while their respective mean frequency and directions are close, both structures are grouped with each other. This procedure is iterated over all the time window until no new grouping occurs anymore. The structures' mean characteristics (frequency f_{pm} and direction θ_{pm}) are recalculated according to the new spatial partitioning.

Time tracking of homogeneous structures

This very last step consists in linking the coherent homogeneous structures to each other between two successive time steps. First, it is checked that the very first instant corresponds to a set of fixed structures only. In case it is not, this is taken into account in the results interpretation regarding the first instants of observation. Each structure is referenced with a code name (four digits), a colour (for graphical visualisation) and an age (persistency length from its apparition to instant t, in time steps).

At each time step $i_t > 1$, $n_{sid}(i_t)$ denotes the number of homogeneous structures and the time tracking matrix $\hat{M}_{B_{\mathscr{F}}}$ ($n_{sid}(i_t - 1)$ rows and $n_{sid}(i_t)$ columns) – similar to $\hat{M}_{A_{\mathscr{F}}}$ – is formed, whose terms are unity if (zero otherwise)

$$B_{ij} = a_{ft} * \left[\frac{\min(f_{pm,i}, f_{pm,j})}{\max(f_{pm,i}, f_{pm,j})}\right] + a_{tt} * \left[1 - \frac{\min(|\theta_{pm,i} - \theta_{pm,j}|, 360 - |\theta_{pm,i} - \theta_{pm,j}|)}{180}\right] \geq B_{min} \tag{6.16}$$

where index i refers to the ith structure at time step $i_t - 1$ and j the jth at time step i_t. The frequency and direction weighting coefficients a_{ft} and a_{tt} respectively are such that $a_{ft} + a_{tt} = 1$ and may be adapted whether the structures are in located in low- or high-frequency (e.g. $(a_{ft}, a_{tt}) = (0.7, 0.3)$ for $f < 0.12Hz$ and $(a_{ft}, a_{tt}) = (0.3, 0.7)$ for $f > 0.12Hz$): this favours frequency groupings for swell systems and direction groupings for wind-sea. Initially, the time cross-assignment threshold B_{min} is arbitrarily fixed (e.g. 0.8).

In each row of the matrix – that is, for each homogeneous structure at $i_t - 1$ –, if at least two structures at i_t are associated with the current structure, no more than one must be fixed (*1st condition*). Then, it is checked that the spatial grouping of two structures at i_t does not imply geographical redundancies so that the maximal number of systems at each sea point exceeds 2, or, if it equals 2, the number of redundancy occurrences is superior to 70% of the total sea points number (*2nd condition*). While both conditions are not satisfied, the threshold B_{min} is incremented and a new $\hat{M}_{B_{\mathscr{F}}}$ matrix is calculated. As soon as they are, rows and columns are used to determine the final associations: if one structure at i_t has been associated with two structures or more at $i_t - 1$, the closest structure (in frequency) is retained only (the other terms become 0); if the sum of the column terms is nil, this means that a structure appeared, which is assigned a code name, colour and age. Last, looking at the rows of the matrix, each – not new-born – structure at i_t inherits the code name, colour and age of the corresponding structure at $i_t - 1$ from the one it has been associated.

6.2.4 Applications

The spatiotemporal tracking algorithm described hereabove is implemented in Matlab language, and process the data output from SPOP (*.mat* files) whose wave system extraction are above all needed (the punctual time tracking data are disregarded). The spectral data ($E(f, \theta)$) come from the wind-wave model WWIII run by both the *ARGOSS* company[1] as well as the *SHOM* (*Service Hydrographique et Océanographique de la Marine*, Brest, France, see Ardhuin et al., 2008). Two geographical zones are particularly focussed on: a wide region in the Bay of Biscay (nine points) and a more restrained one around Yeu island (France, four points) respectively for ARGOSS and SHOM data. In these datasets, the time step has been set to one and three hours respectively.

The spatiotemporal results as well as their sensitivity to the algorithm parameters are not easy to reproduce in a report. Consequently, the shown results refer to satisfying trackings obtained thanks to that method, which allows a deeper study on the spatiotemporal evolution of the wave systems observed at both locations.

Spatiotemporal tracking in the Bay of Biscay

The first zone under consideration is depicted in figure 6.7, through nine control points of a 1.25 °x1 °-grid (lon. x lat.). The ARGOSS spectral data used here describe the wave climate observed during the month of April 2005 with a time step of one hour (i.e. 670 wave spectra approximately).

[1] `http://www.argoss.nl/`

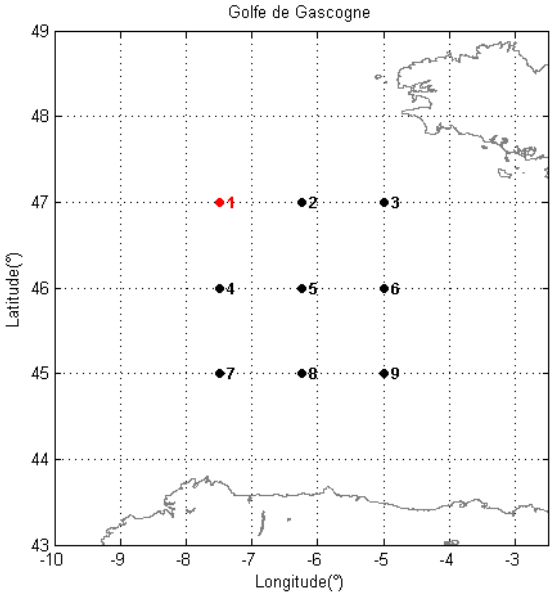

Figure 6.7: Bay of Biscay zone (1.25 °x1 °): 9 points (ARGOSS data).

The wave system extraction is lead with SPOP with all default values and options (JONSWAP-2, cos^{2s}, 1D mutual influences correction, constant directional spreading against frequency). A linear covariogram model ($(a_{fs}, a_{ts}, a_{hs}) = (0.7, 0.3, 0)$) is chosen to carry out the spatiotemporal analysis. Significant wave height is discarded as a descriptive wave system parameter for its variability is too high over such a geographical region.

The successive steps of the algorithm are illustrated in figures 6.8(a-d) which correspond to the sea-states occurring in the region on the 17th of April, 6PM, and where the Z-axis stands for peak frequency: spatial partitioning into homogeneous structures (a), structures time tracking (b), vector field representation of the structures (c) where the vector characteristics – norm, direction and Z-value – are related to the wave systems' significant wave height, peak direction and frequency respectively; figure (d) provides a bird's eye view representation (xOy projection) of figure (c) along with the corresponding multivariable covariogram (Eq. (6.9) with linear model for f_p and H_s, Eq. (6.11)) against the sea points' orthodromic inter-distance. In all figures, data related to wind are yellow-plotted, as separation frequency (Eq. (5.6)) and mean direction. These spatial graphics highlight the coexistence of a wind-sea and three swells that are well identified thanks to peak frequency. The vector field representation (Fig. 6.8(c)) allow to see that the swells propagate within quite a restrained angular sector, whereas wind-sea is following a far different direction. The multivariable covariogram (Fig. 6.8(d - right)) emphasizes the spatial coherence of the wave systems – which are compared to each other – at the same instant: correlation is high when inter-distance is small (and theoretically equal to 1 if the distance is zero) and then decreases as inter-distance increases, which is moreless pronounced according to the spatial correlation of the structure, as for a classical covariogram (see Eq. (6.1)&(6.2) and Fig. 6.1). Thus, one can notice that the

spatial correlation of the wind-sea structure is less pronounced than that of the swells – more homogeneous – exhibiting more important dispersion and decrease.

The time evolution of parameters f_p, θ_p and H_s of the wave systems is plotted in figures 6.9, 6.10, 6.11 and 6.12, which was obtain thanks to the spatiotemporal algorithm at sea points n°1, 3, 5 and 7 respectively (see Fig. 6.7). The coherence of the wave systems – and thus, of the sea-states – is clearly emphasized in these figures: the same wavetrains are therefore observed at each observation point, which most probably arise from the same original climatic events. The swell named 'BUDA', for instance, is tracked over seven days on average. Swell 'WANE' is cut in two parts and may therefore be regarded as the sequence of two separated swells; however, both are continuous in direction, and even linked at point n°3 (Fig. 6.10(a)), so that the algorithm eventually identified a unique swell. Let us also remark that for swell 'BUDA', the spatial correlation enables to reconsider the wave-systems extraction in SPOP, namely when the spectrum exhibited two close peaks – artefacts – instead of one only (around the 10th of April). The algorithm linked both swell portions, which probably belong to the same wave event.

Eventhough the spatial area under consideration is relatively wide (the most distant points are separated by aproximately $300km$), the coherence of some extended wind-sea systems is noticeably highlighted, like 'SICI', 'UUGE' or 'KIJU'. However, other events linked to local particularities of the wind field are not well identified within homogeneous structures, due to the important wave variability from a location to the next. For such systems, the resulting time tracking may be poor (see for instance the sequence 'KAWO', 'YAOU' and 'AITI' in figure 6.10(a)).

As predicted by theory on the swells time evolution (see Section 5.2.1), the peak frequency observed punctually increases against time. The sudden increases of frequency slope may be accounted for by the fact the swells generally closely coexist with wind-seas which propagate in the same direction, so that the spectral energy – and hence, the frequency peak – of the system's partition is moved to high-frequency. The fusion of swell 'SOCO' and wind-sea 'UUGE' is particularly interesting from this point of view, for it illustrates the tricky issue of system identification after such an event occurred: is it still a swell? or is it now a fully developed wind-sea? In terms of peak-frequency, it clearly deals with the following of swell 'SOCO', thus, a swell. In terms of energy (significant wave height), wind-sea 'UUGE' is more energetic than 'SOCO', which seems to be phagocyted and succeeded by the wind-sea: the observed system is therefore likely to be still wind-sea 'UUGE'. Both interpretations may be observed in output of the algorithm according to the selected assigment functions (or multivariable covariograms). Then, swell 'SOCO' may be seen as a wave system of long duration or not. Here, the continuity of swell 'SOCO' has been assumed, as "strengthened" and prolonged by the fusion with wind-sea 'UUGE'. The same may be observed for systems 'GEIU' (swell) and 'MUOI' (wind-sea).

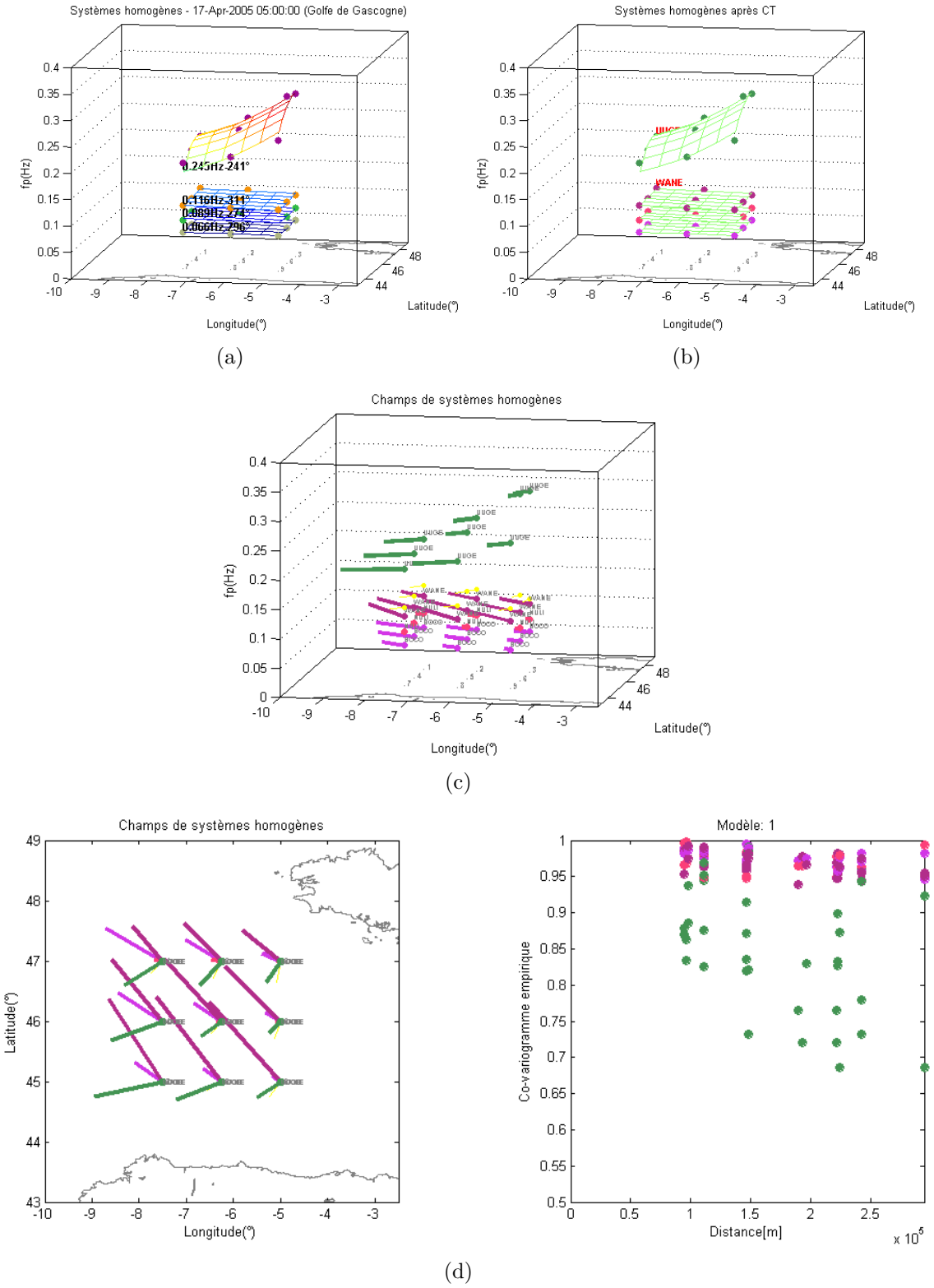

Figure 6.8: Grouping and spatiotemporal tracking of coherent wave systems: instantaneous structures grouping (a), structures time tracking (b), vector field representation (c) with bird's eye view (d - left) and multivariable covariogram of each structure (d - right) in the Bay of Biscay.

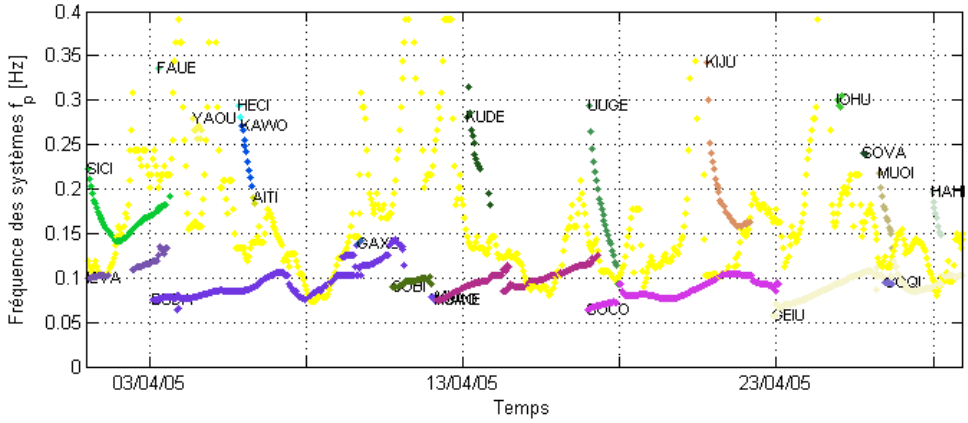

(a)

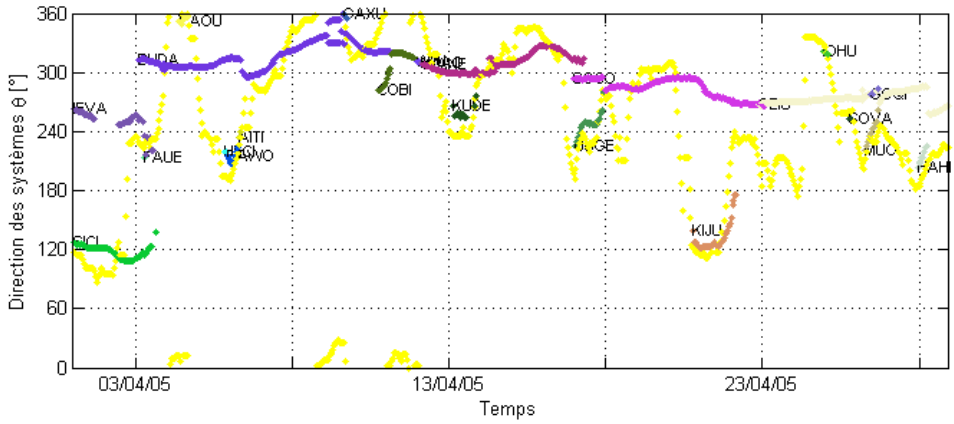

(b)

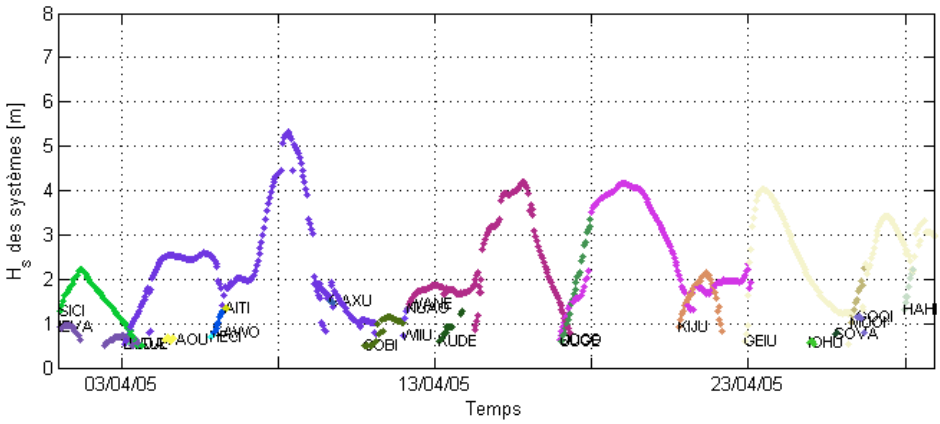

(c)

Figure 6.9: Wave systems tracking by spatiotemporal correlation in the Bay of Biscay (point n°1): peak frequency (a), peak direction (b), and significant wave height (c); wind data (separation frequency and mean direction are yellow-plotted (in Fig. (a) and (b) resp.).

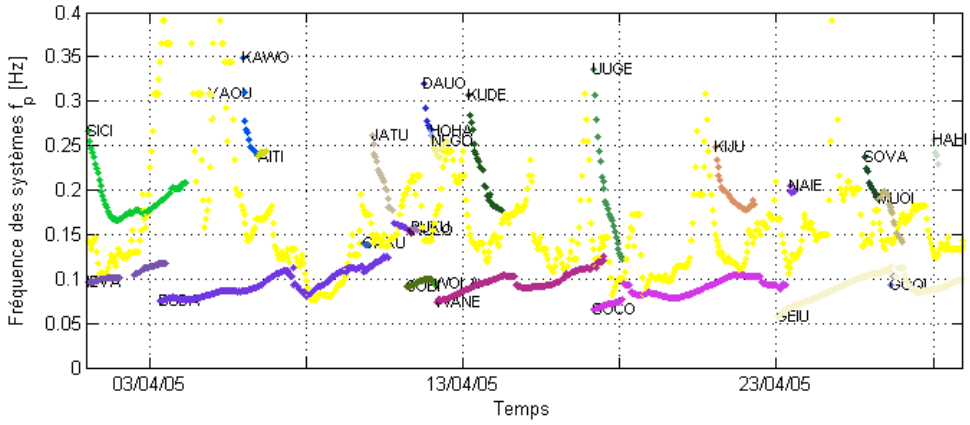

(a)

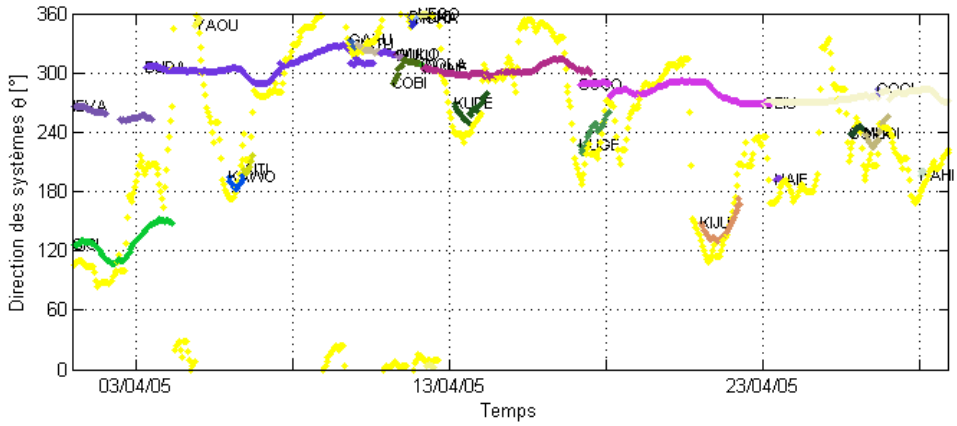

(b)

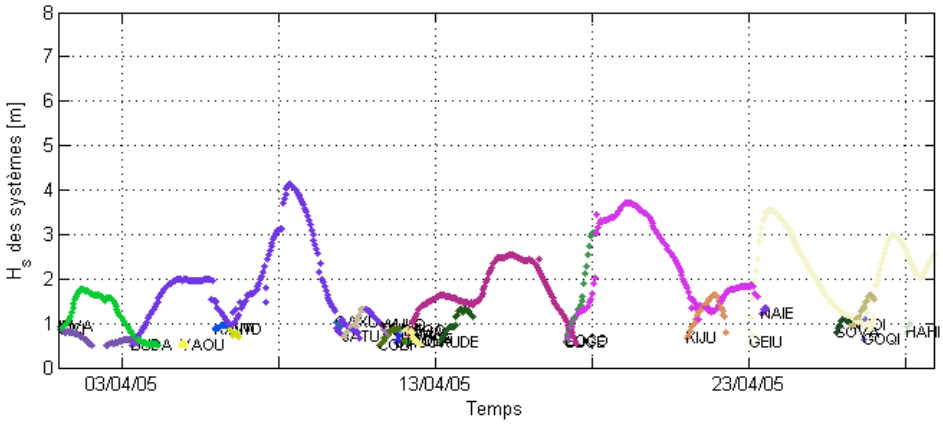

(c)

Figure 6.10: Id. Fig 6.9 for point n°3.

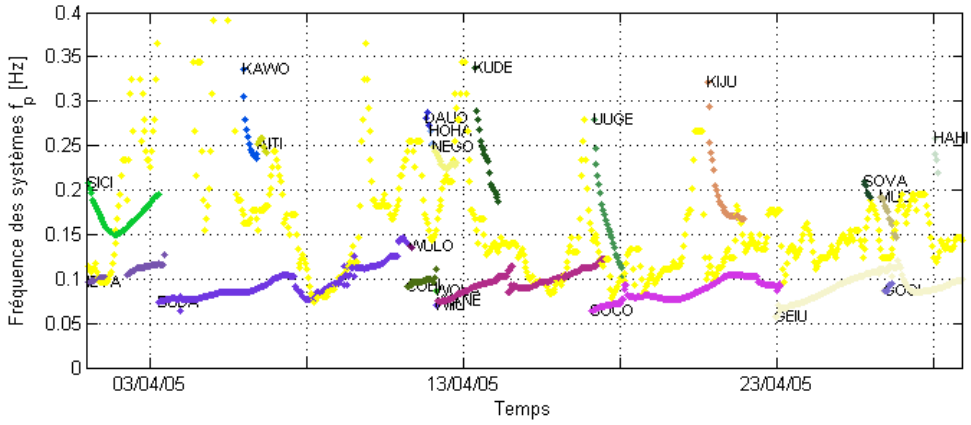

(a)

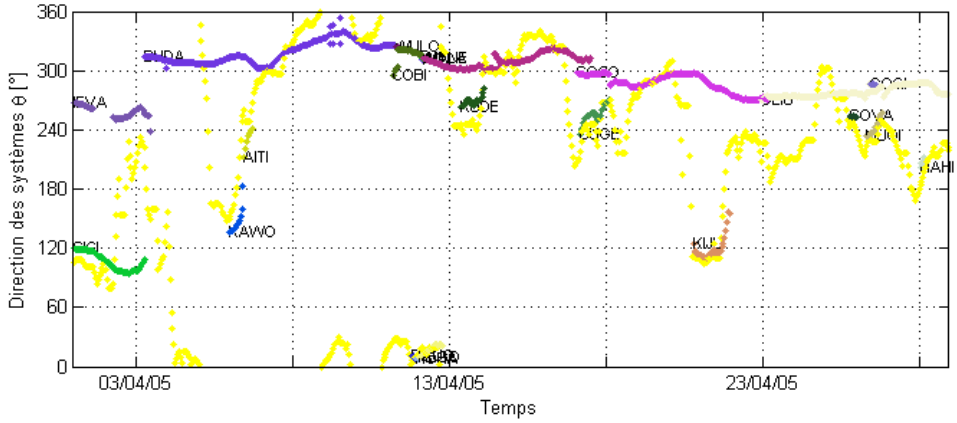

(b)

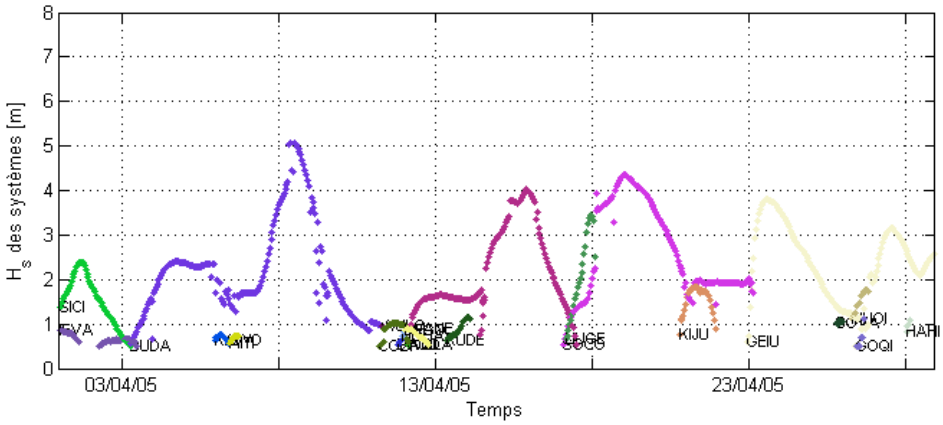

(c)

Figure 6.11: Id. Fig 6.9 for point n°5.

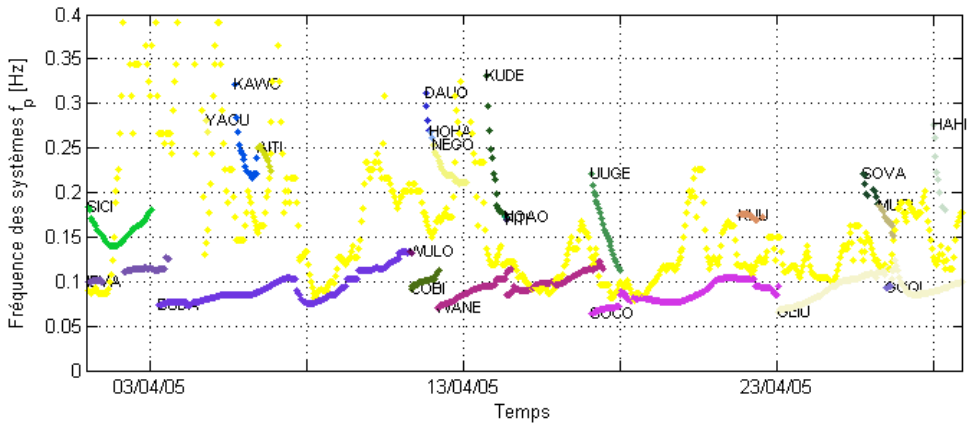

(a)

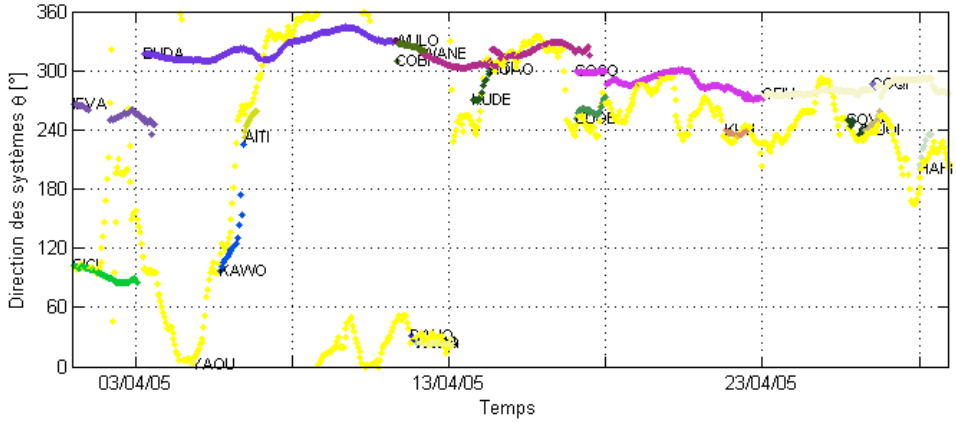

(b)

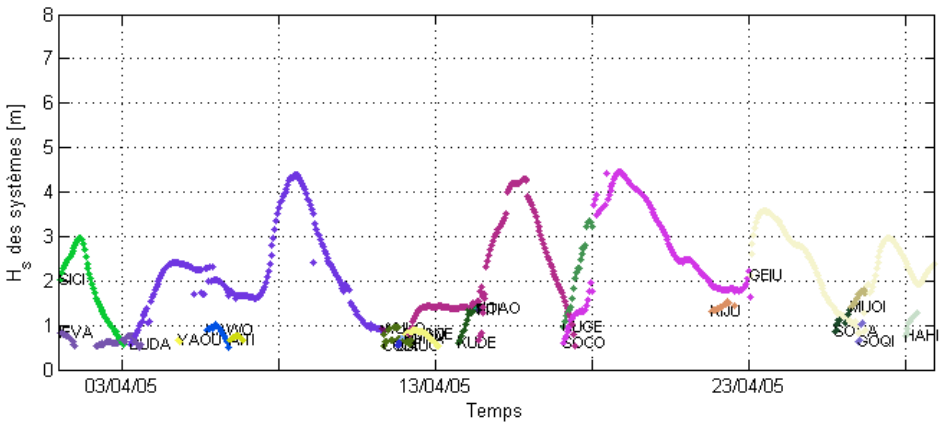

(c)

Figure 6.12: Id. Fig 6.9 for point n°7.

More generally, it is of interest to notice the time evolution of the systems' significant wave height, which mostly follow bell-shaped curves (increase, peak, decrease), whose energy peak coincides with a particular peak frequency. For swells (e.g. 'SOCO', 'GEIU'), the energy peak occurs somewhere in the middle of the sequence (median frequency) whereas for wind-seas (e.g. 'SICI', 'KIJU'), the energy peak mostly occurs at the end of the sequence – before possible fusion with a close swell –, or more generally, when peak frequency is the lowest.

To illustrate the spatiotemporal evolution of homogeneous wave systems in the Bay of Biscay during April 2005, we give in figures 6.13(a-f) a sequence of six time steps separated by $3h$, showing mixed seas with eastern wind-sea and western swell.

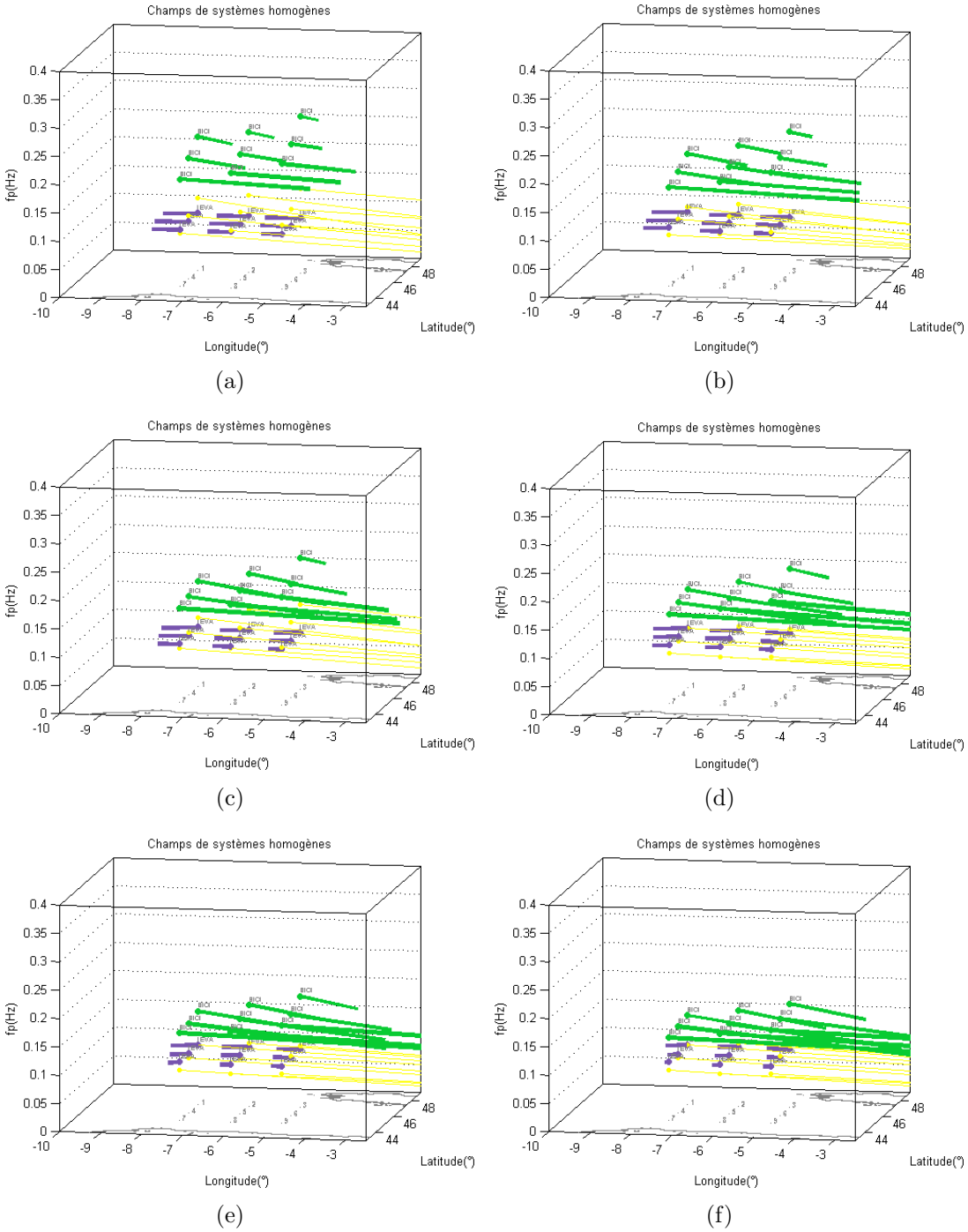

Figure 6.13: Sequence of sea-states with time tracking of space-coherent wave systems in the Bay of Biscay by $3h$ time steps on the 1st of April 2005 from midnight (a) to 3PM (f).

Spatiotemporal tracking near Yeu Island

The second zone under study is smaller than the previous one, as represented in figure 6.14, where four sea points near Yeu Island (France) are observed – two of them being located off the island. The wave spectra are provided by the SHOM (Ardhuin et al., 2008) and derive from the WWIII wind-wave model with *ECMWF* (*European Centre for Medium-Range Weather Forecasts*[2]) spatiotemporal wind fields as input. Here, the attention is focussed on the month of February 2008 (leap year) discretised in $3h$ time steps (hence, 240 spectra approximately).

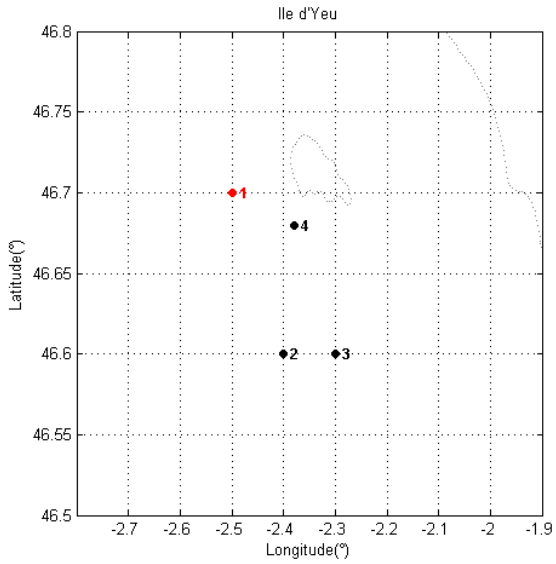

Figure 6.14: Yeu Island: 4 points (SHOM data).

Here again, the wave systems are extracted from the directional WWIII spectra using SPOP with all default settings. The spatiotemporal algorithm is run with a multivariable covariogram of type extrema, whose weighting coefficients are chosen as $(a_{fs}, a_{ts}, a_{hs}) = (0.7, 0.3, 0)$. As previously, the influence of significant wave height is not taken into consideration in the spatial partitioning.

The successive steps followed by the algorithm are illustrated in figures 6.15(a-d) which refer to the sea-states observed on the 17th of April 2008, 6PM, near Yeu Island. These plots underline the coexistence of a wind-sea and two swells. The main swell and the wind-sea ('PALA' and 'AIAU' respectively) are shown to propagate along two clearly different directions. Furthermore, the presence of a very local and slight wind-sea ('TAOO') is also noticed in sea points n°1&2: the separation frequency (yellow, Fig. 6.15(c)) suggests that system 'AIAU' refers to the local wind-sea, whereas it is very much likely to be rather an energetic swell system generated nextby, which is decaying as

[2] `http://www.ecmwf.int/`

wind is almost not supplying energy to it anymore (wind direction changed meanwhile). The local wind indeed is here only responsible for wave system 'TAOO'.

These observations as confirmed by examining the time evolution of wave systems parameters f_p, θ_p and H_s given in figures 6.16, 6.17, 6.18 and 6.19, which refer to sea points n°1 to 4 respectively (see Fig. 6.14). In this sequence, no wind-sea/swell fusion is observable contrary to the previous case: both types of system remain perfectly disjointed, and swells exhibit a certain continuity in direction, which lets guess that all these events are originally due to a same very wide and long-lasting climatic event. Let us say last that the dimensions of the spatiotemporal window seems here relevant to describe the joint space and time evolution of wave systems up to $0.35Hz$, that is, most of the extracted systems.

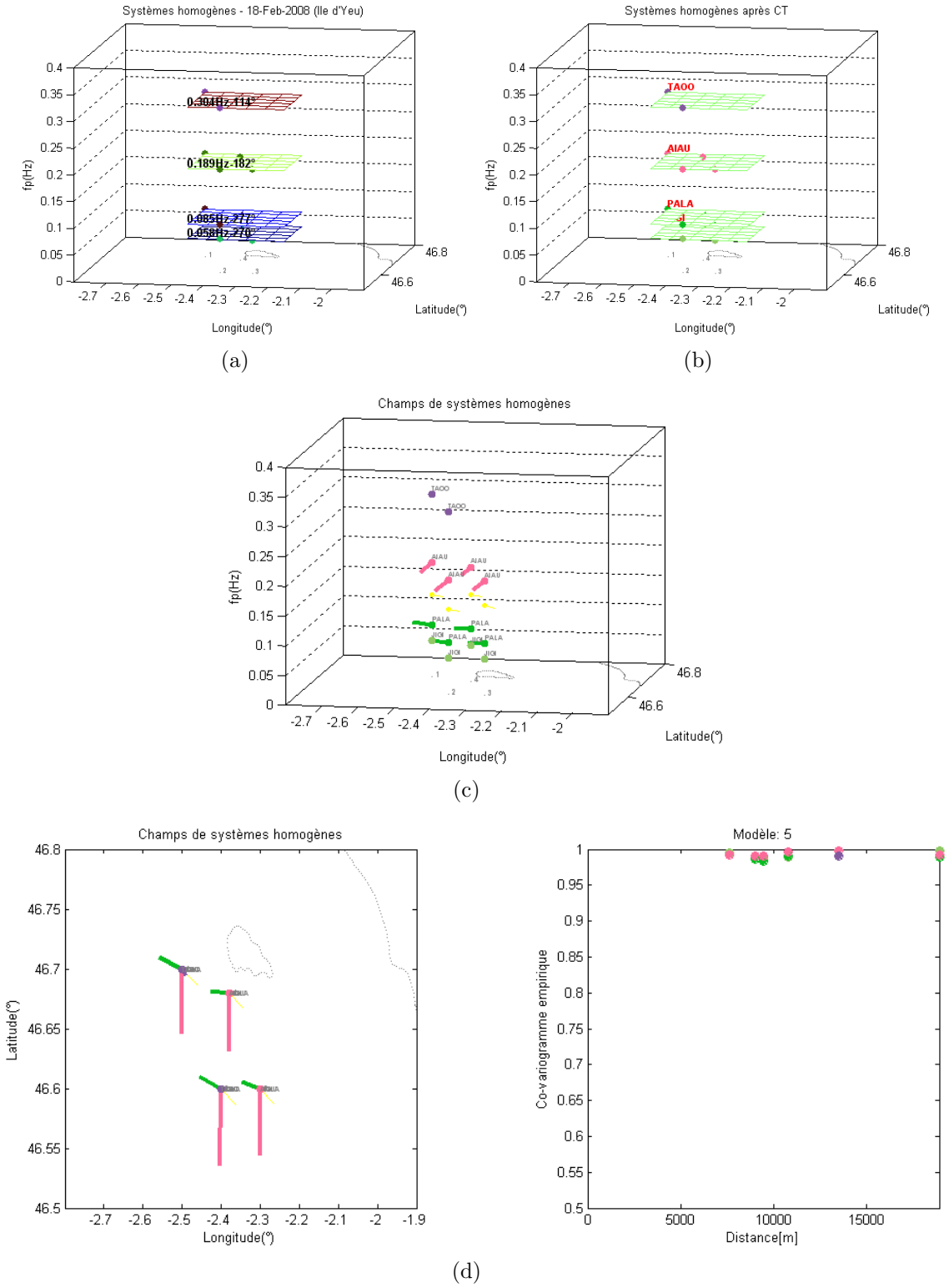

Figure 6.15: Grouping and spatiotemporal tracking of coherent wave systems: instantaneous structures grouping (a), structures time tracking (b), vector field representation (c) with bird's eye view (d - left) and multivariable covariogram of each structure (d - right) near Yeu Island.

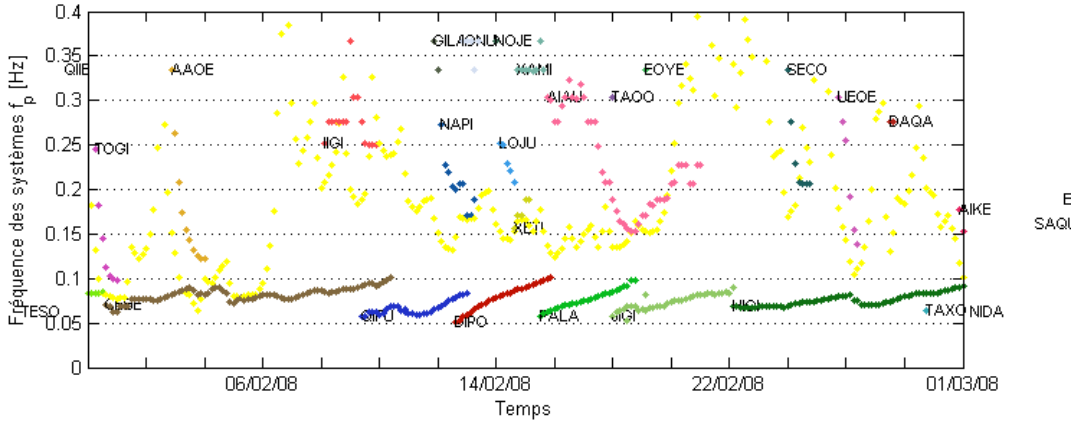

(a)

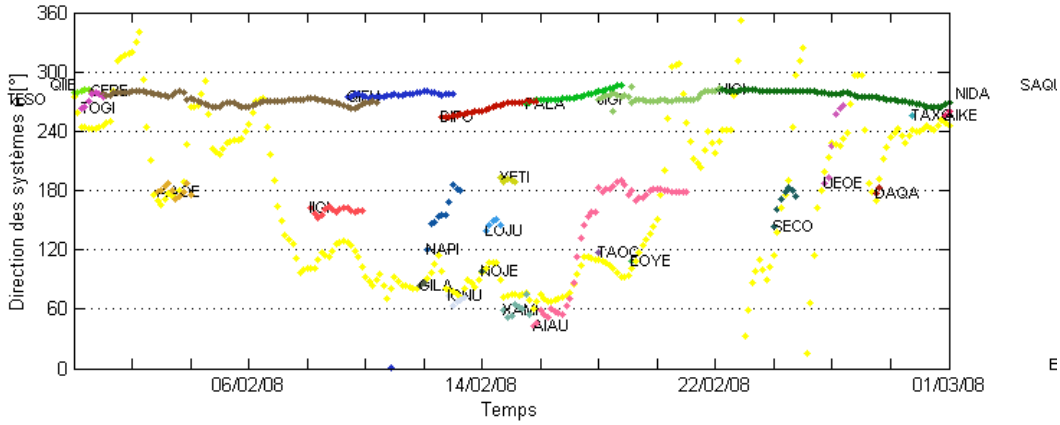

(b)

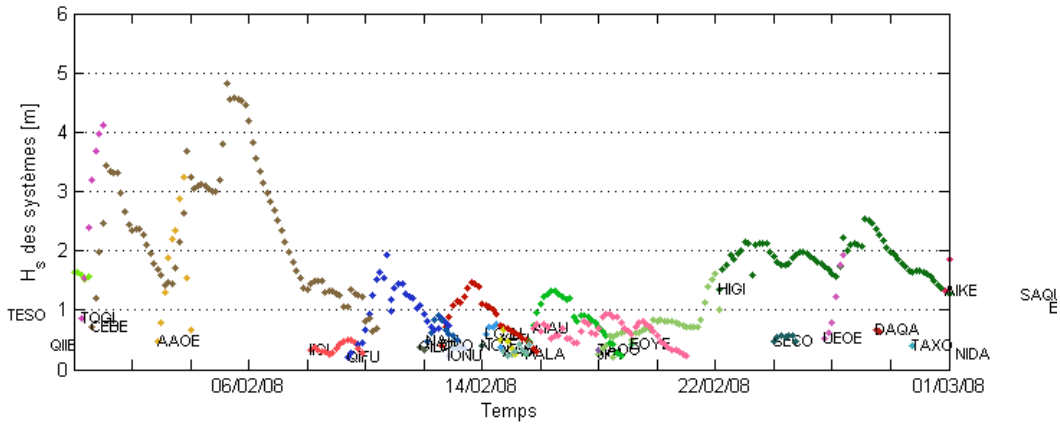

(c)

Figure 6.16: Wave systems tracking by spatiotemporal correlation in the Bay of Biscay (point n°1): peak frequency (a), peak direction (b), and significant wave height (c); wind data (separation frequency and mean direction are yellow-plotted (in Fig. (a) and (b) resp.).

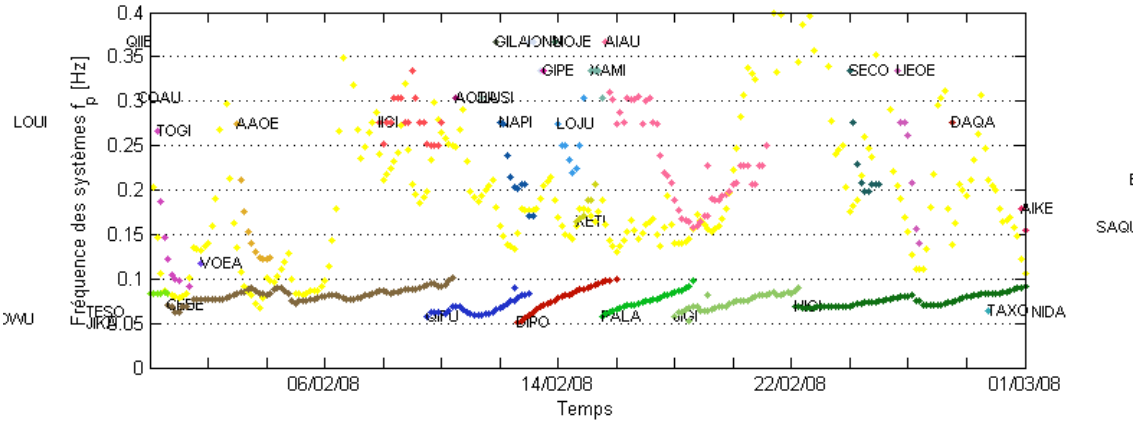

(a)

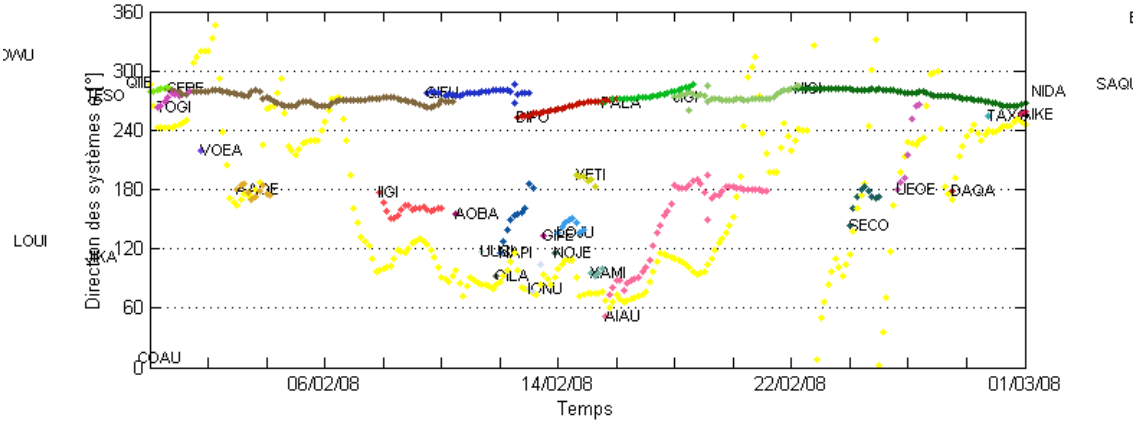

(b)

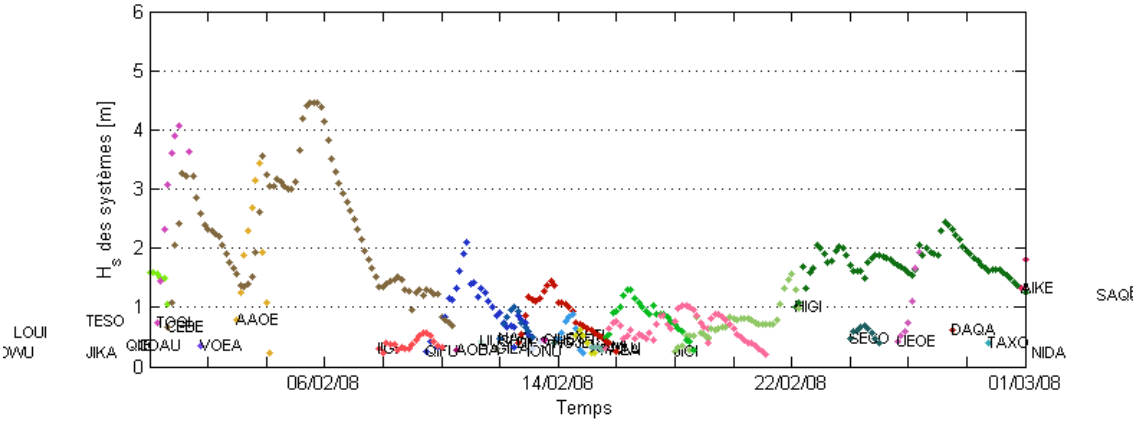

(c)

Figure 6.17: Id. Fig 6.16 for point n°2.

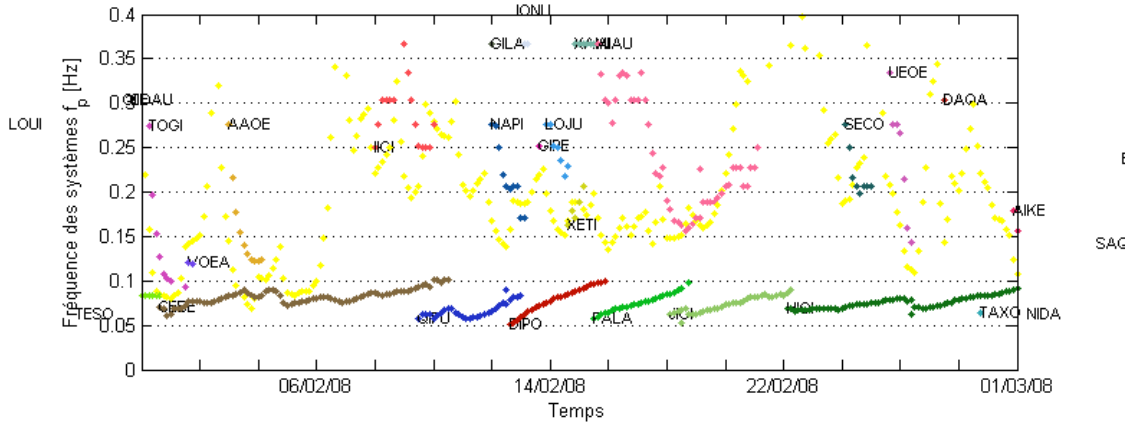

(a)

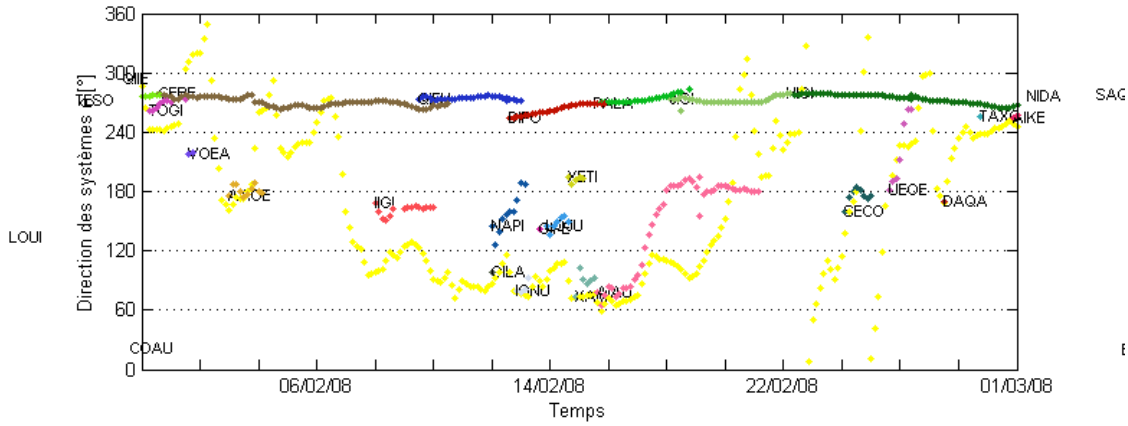

(b)

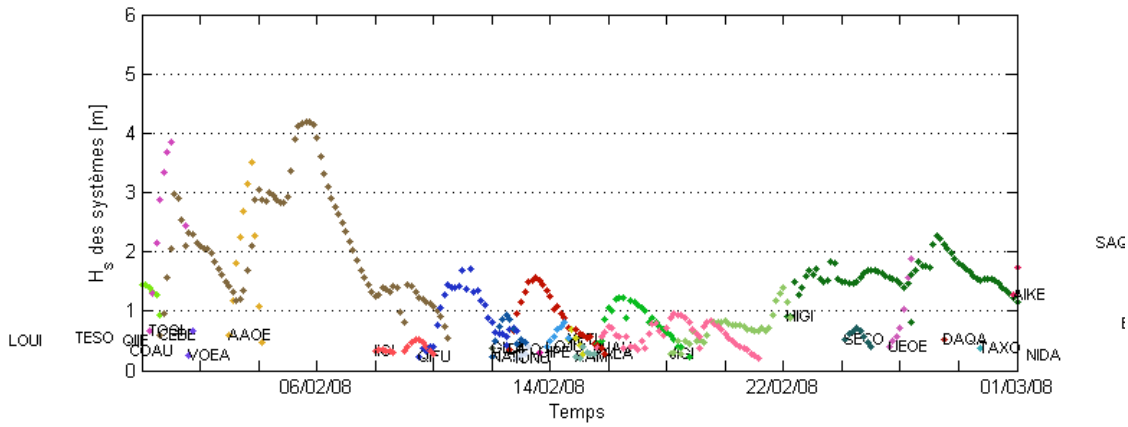

(c)

Figure 6.18: Id. Fig 6.16 for point n°3.

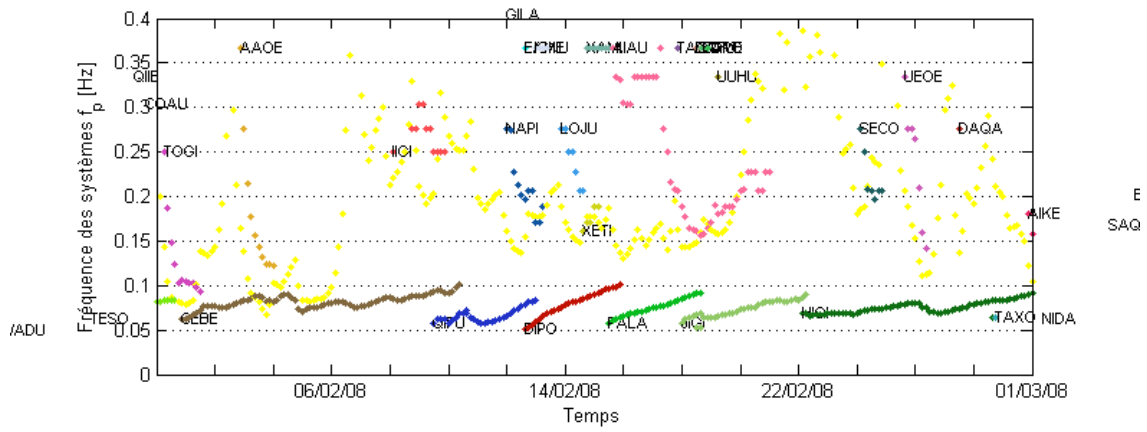

(a)

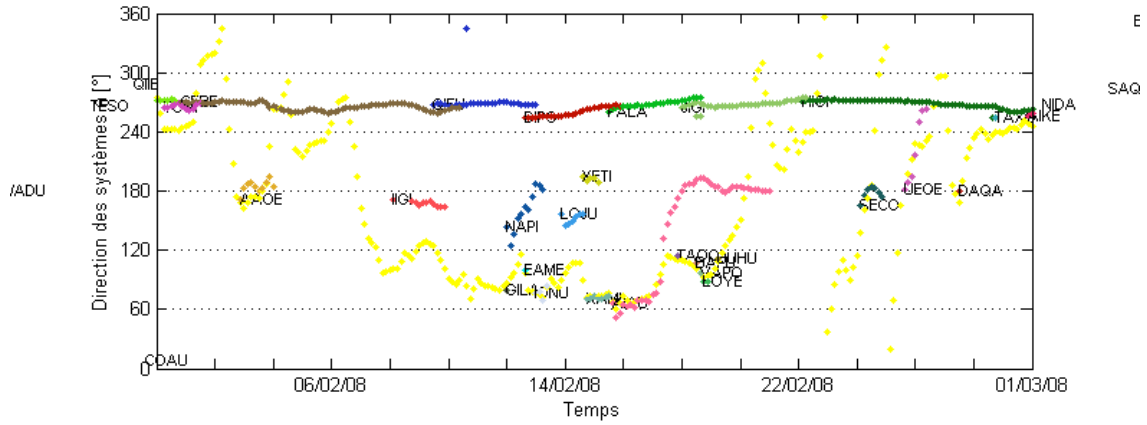

(b)

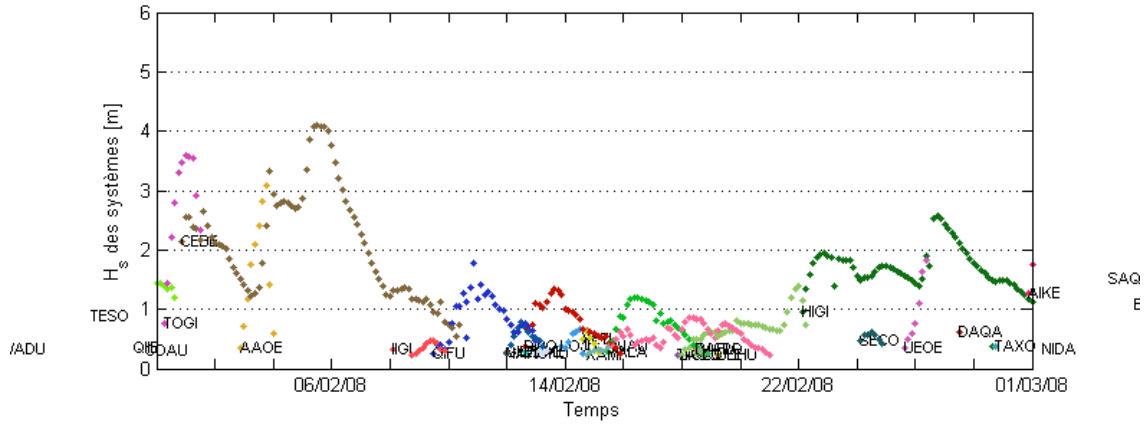

(c)

Figure 6.19: Id. Fig 6.16 for point n°4.

6.3 Conclusion about the spatiotemporal coherence and tracking of wave systems

In this chapter, an algorithm for the spatiotemporal tracking of wave systems – based on common tools widely adopted by geostatisticians (co-variograms) – has been proposed. It has been applied to two particular study zones, of different spatial extents (Bay of Biscay and Yeu Island respectively). The obtained results have highlighted the space coherence of wave systems as well as the time coherence of the related homogeneous structures in quite an efficient and satisfactory way. Accordingly, this – explorative – method was successfully validated.

Such a study has been made possible thanks to the multimodal description of sea states. Eventhough it is more related to pure oceanography, this study presents some very interesting and useful aspects in WEC performance estimation in realistic sea conditions. This second level of refinement in wave climatology is applied in the next chapters – as well as the first one, which is exposed through Chapters 2 and 3 – in order to improve the WEC performance estimation at both long and short term.

Part III

Effect of sea-state description refinements on WEC performance estimations

Chapter 7

Estimation of long-term production operated by linear systems

This chapter reviews two studies comparing the estimation of long-term production (annual estimations) operated by given WECs assuming shape-fixed sea-states to estimations including refined sea-state representations (unimodal shape-variable sea-states and multisystem representation).

7.1 Estimation of long-term production operated by axi-symmetrical WECs in shape-variable unimodal sea-states

In the continuity of the works exposed in Section 3.3, a comparative study at on various long-term performance estimation of the four axi-symmetrical WEC configurations IPS1 to IP4 has been lead and presented by the author jointly with P. Ricci (IST, Lisbon) in international conferences (see Saulnier et al., 2007a,b). It is reminded that, due to both the spectral data availability as well as the insensitivity of axi-symmetrical floats to wave directionality, this study involves omnidirectional spectra only, which were estimated by Waverider and Wavec buoys at locations FF (Figueira da Foz, Portugal, with ∼25300 spectra over thirteen years) and K13 (South of North Sea, near the Netherlands, with ∼23000 spectra over nine years). In both exploitation sites, it is assumed that most of the sea-states are dominated by swell and wind-sea respectively (unimodal spectral shapes).

Beforehand, the exact total performance figure over the whole spectral sample at both sites is calculated and scaled to the annual energy figure E_{ex} $(MWh/year)$ obtained by multiplying the annual mean power (sum of mean powers divided by the number of sea-states) to the total exploitation time over a year under nominal operat-

ing conditions (i.e. $365 \times 24h$=$8760h$). To this aim, it is assumed that the sea-states samples are homogeneous and representative of the local climate. The annual performance figure is used in the following as a reference to which other estimations methods detailed herebelow shall be compared to.

Long-term performance estimations here are based on the "classical" method, which resumes the wave energy ressource as joint occurrences tables $H_s - T_e$ (or $H_{m0} - T_{-10}$ here) multiplied cell-by-cell with the corresponding mean converted power table. The bins are here $0.5m$- and $1s$-spaced respectively for wave heights and periods in order to work with a fine climate description. Then, a third dimension is added to the tables, which accounts for spectral width – as parameters ε_0, ε_1, and B_w, among others –, and whose discretisation is different for each parameter (0.1-bins for ε_0 and ε_1, $0.025Hz$-bins for $B_w \ldots$). Accordingly, it is necessary to produce three-entry tables (significant wave height/energy period/spectal width) dealing with both the ressource (from buoy measurements) and mean production. Indeed, it is expected that for fixed H_{m0} and T_{-10} the mean production still is highly variable and may be in great part accounted for by the own variability of this third wave characteristic (see figures 3.6(a-d), 3.7(a-d)&3.8). The mean extracted power table (also called *power matrix*) is established using Q_p-spectra (see Appendix C) as representative sea-states of each cell: the value of factor Q_p which matches the central spectral width parameter of the cell is searched for by dichotomy. In figure 7.1, the performance results (capture width χ_P, Eq. (3.28)) of device IPS4 against spectral width parameter ε_1 for FF sea-states with $T_{-10} \approx 7.5s$ (+/-2%) are depicted, along with the results obtained by considering input Q_p-spectra of same T_{-10} (and indifferent significant wave height level since χ_P for a linear WEC does not depend on energy) whose Q_p is determined from the equivalent value of ε_1. In this example – among others –, the agreement of both results is fair and enables the use of such a shape-variable standard representative spectral model to draw the mean extracted power tables. Both ressource and power tables are constructed for each IPS configuration (see Section 3.3) at both locations FF and K13 for spectral parameters ε_0, ε_1 et B_w.

After, both kind of tables are convoluted cell-by-cell and the annual mean converted energy figure is derived. These three new estimations are respectively denoted by E_{Eps0}, E_{Eps1} and E_{Bw}. In addition, the annual figure E_{Bret} obtained using shape-fixed Bretschneider spectra as input sea-states is also derived for comparison purposes. The whole results are given in tables 7.1 & 7.2, in $MWh/year$ for E_{ex}, and percentage of error with respect to this reference for the estimation figures.

The results lead to several conclusions and remarks. First, configuration IPS1 seems appropriate for both locations FF and K13 as the annual performance reaches relatively satisfying levels in both cases. IPS2, however, seems more adapted to the North Sea wave climate where waves are are shorter on average. IPS3 appears extremely sensitive due to its particularly narrow response interval (at FF, the maximum production is found for this configuration, but at K13 its performance is the poorest). Last, IPS4 leads to mean results because of its broad and mean response interval: accordingly, it

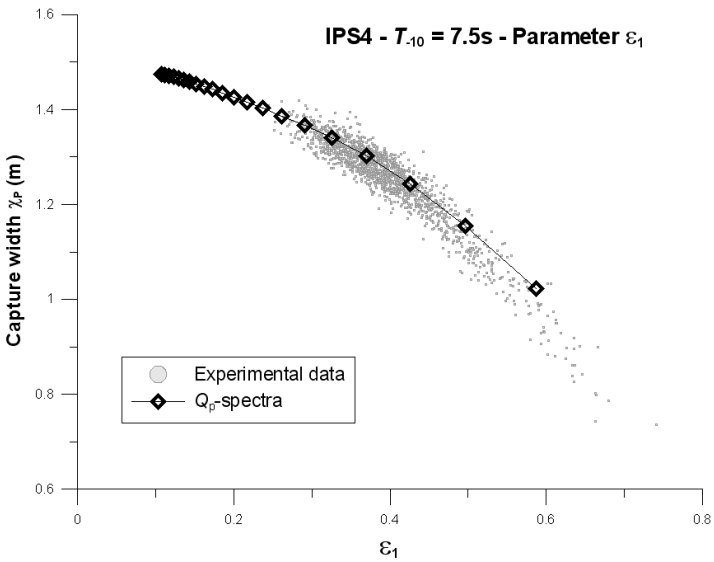

Figure 7.1: Capture width χ_P of WEC configuration IPS4 against parameter ε_1 computed for spectra with $T_{-10} \approx 7.5s$ estimated at Figueira da Foz and analytical shape-variable Q_p-spectra.

Table 7.1: Estimation error (%) on the annual converted energy of the four WEC IPS-configurations with respect to reference figure E_{ex} $(MWh/year)$ at Figueira da Foz for long-term production estimators E_{Bret}, E_{Eps0}, E_{Eps1} et E_{Bw}.

FF	IPS1	IPS2	IPS3	IPS4
E_{ex}	*251.4*	*156.4*	*266.6*	*193.1*
E_{Bret}	12.4%	5.2%	18.8%	4.8%
E_{Eps0}	5.8%	2.6%	10.7%	1.2%
E_{Eps1}	6.7%	6.2%	9.7%	1.1%
E_{Bw}	1.3%	5.9%	1.5%	-2.6%

is found to be less interesting than configurations IPS1 and IPS2.

Second, estimations based on Bretschneider spectra (E_{Bret}) may be adopted in North Sea locations where estimation errors are low (<1.4% except IPS3, which remains a very particular case). Nevertheless, they might not be used in Atlantic regions where the error sometimes exceeds 12% (12.4% for IPS1 and 18.8% for IPS3) by systematic overestimation of the reference figure. In all cases at FF, introducing spectral width in the sea-state characterisation seems crucial to improve the estimations. At K13, estimator E_{Bw} is not recommended; E_{Eps1}, though, seems quite precise (<1% except IPS3).

Let us remind that the wave parameter discretisation used in both ressource and mean converted power tables could have been even more refined. Here, a standard discretisation was adopted, which does not induce a too large set of joint occurrence cases

Table 7.2: Id. Table 7.1 at station K13.

K13	IPS1	IPS2	IPS3	IPS4
E_{ex}	*177.7*	*194.6*	*89.4*	*119.8*
E_{Bret}	1.4%	-0.5%	26.4%	1.2%
E_{Eps0}	-1.2%	-4.5%	24.5%	-1.4%
E_{Eps1}	0.1%	-0.1%	21.3%	0.8%
E_{Bw}	9.0%	13.1%	9.8%	7.1%

(the number of cells is determined indeed by the product of the three discretisations). Parameter Λ has not been included in the study at the time this work was carried out, so that no results related to it may be presented.

7.2 Comparison of uni- and multimodal sea-states representations for the long-term performance estimation of a linear directional WEC

Kerbiriou (2007) realised a study similar to that presented in Section 4.2 for the SEAREV device modelled in time domain over one year of observations (2004-2005) in the Bay of Biscay (ARGOSS data, WaveWatch III wind-wave model). She compared the annual mean power converted by the WEC considering unimodal input sea-states on the one hand, and multimodal sea-states derived from the wave systems extraction, identification and parameterisation operated by the SPOP application on the other hand. The device was set to various heading angles, and the results corresponding to the optimal one showed that the unimodal representation underestimated the parameterised multimodal one of about 8% ($103kW$ for multimodal vs. $95kW$ for unimodal). For more details about this work, the reader is referred to Kerbiriou (2007) and Kerbiriou et al. (2007).

7.3 Conclusion about the estimation of long-term production operated by linear systems

This chapter – quite short, indeed – permitted to illustrate the two refinement levels of wave climatology exposed in this thesis work, as unimodal with variable spectral width for the study of linear axi-symmetrical devices (using "Q_p"-spectra) and multimodal for that of a linear directional device. In the first case, it has been shown in particular

that introducing a third wave parameter as spectral bandwidth like ε_0 or ε_1 into the joint occurrences tables and power matrices was substantially improving the long-term performance estimation, provided the WECs do not have a narrow response interval (case of IPS3). Both kind of systems have clearly highlighted the lack of relevance of unimodal shape-fixed spectral models (e.g. Bretschneider) in long-term performance estimations, except in some very particular cases like in the North Sea, where modelling the sea states with full-developped sea spectra has led to very small estimation errors.

Chapter 8

Performance study of a non-linear directional WEC in a Californian site

8.1 Objectives and context

Another sensitivity study on the spectral width of sea-states is carried out in this chapter just as in Section 3.3, where this time:

- sea-state multimodality and
- non-linearities of WEC modelling (hydrodynamic non-linearities here)

are taken into account.

After having determined the wave system(s) to which the WEC is more sensitive – i.e., in which frequency intervals the WEC is more resonant – the spectral bandwidth of these systems is characterised, as well as that of the global wave spectrum. These systems are expected to be mostly wind-seas, as swells may have little influence on the WEC's dynamics (in particular when $f < 0.10Hz$). When the WEC is axi-symmetrical (omnidirectional), wave directionality has almost no impact on the device's response so that the global consideration of wave spectrum $E(f)$ is licit: this case was namely addressed in Section 7.1. In any other case, it may be more relevant to work closely with the wave system(s) that are harnessed by the WEC – and called *active systems* in the following for the sake of commodity – and which were obviously extracted from the directional wave spectrum.

If one is able to estimate the mean power extracted in a target sea-state characterised by the directional spectral density $E(f, \theta)$, it is then of interest to compare it to some

wave spectral properties, such as: energy (m_0, H_{m0}), mean energy frequency/period (T_{-10}, f_{-10}), spectral bandwidth (ε_0, κ, Q_p, $\Lambda\ldots$) and mean wave power (P_w). Directional parameters can also be added to this list although they are not required here, as shown in the following. Indeed, as the WEC is aligned with the active systems' main direction and does not exhibit much sensitivity to the directional variability of waves within quite a broad angular sector (restrained roll and yaw motions), the directional characteristics of waves may reasonably be disregarded. This is the case of the WEC under consideration throughout this chapter, whose pitch motions are essentially harnessed and whose roll and yaw motions are duly restrained.

Let us denote by $\overline{P_{PTO}} = E\left[\hat{P}_{PTO}\right](kW)$ the expectation of the mean – deterministic – power values (mean power estimators) estimated in each simulation of target spectrum $E(f,\theta)$. This figure is assumed to approach the exact – probabilistic – expectation obtained by simulating the device in the same sea-state an infinity of times. Let us define now (see Eq. (3.28))

$$\chi_{P,sa} = \frac{\overline{P_{PTO}}}{P_{w_{sa}}} \tag{8.1}$$

the WEC's capture width related to a particular input active wave system, where $P_{w_{sa}}$ denotes the mean power by unit of wavefront conveyed by this system ($P_{w_{sa}} \leq P_w$), which is computed in deep water conditions according to equation (3.27) as a function of the related significant wave height and mean energy period. Besides, parameter χ_P (see Section 3.3) is also calculated by considering wave power P_w of the global sea-state. Both parameters allow to measure the performance of the WEC in given sea-states towards the whole energy contents and that of the active system. These parameters – once again – are not expected to depend significantly on energy (H_{m0}^2) and wave period (T_{-10}) *a priori*.

The aim of this study is to observe the possible correlation existing between the WEC's capture width and the sea-state's spectral bandwidth characterised by parameters such as

- ε_2,ε_0
- Q_p,Q_e
- κ
- $\Lambda(Hz)$
- $B_w(Hz)$
- $\ldots$

Although the concept of capture width may intuitively be associated with a physical width related to the floating body's absorption, – and thus, to the length of incident wave crests somehow, – the WEC is not supposed to be sensitive to crest directionality. The variability of χ_P and $\chi_{P,sa}$ shall be accounted for only by that of the incident waves' spectral bandwidth.

8.2 Numerical WEC simulation code and hypothesis

The WEC simulated here corresponds to hull *DES1129* of the SEAREV WEC (S.E.A.R.E.V., *Système Electrique Autonome de Récupration de l'Energie des Vagues*, see Babarit, 2005) invented at ECN and illustrated in figure 8.1(a). This system has been designed to be essentially excited in pitch by waves. Its shape may recall the famous *ducks* developped in the 1970s by Salter (Salter, 1980). The hull is approximately cubic (of side around $15m$) and fixed by slack moorings at its four vertical sides. It houses a high-inertia pendulum (weight$\sim$ $400t$) whose rotation axis is parallel to the hull's own pitching axis, both with mismatching frequencies though. Accordingly, the relative motion α of the pendulum is harnessed (see Fig. 8.1(b)) to produce electricity thanks to a generator, modelled here simply as a linear damper with absorption coefficient $C_{PTO} = 10^7 kg.m^2.s^{-1}$ (or $N.m.s$).

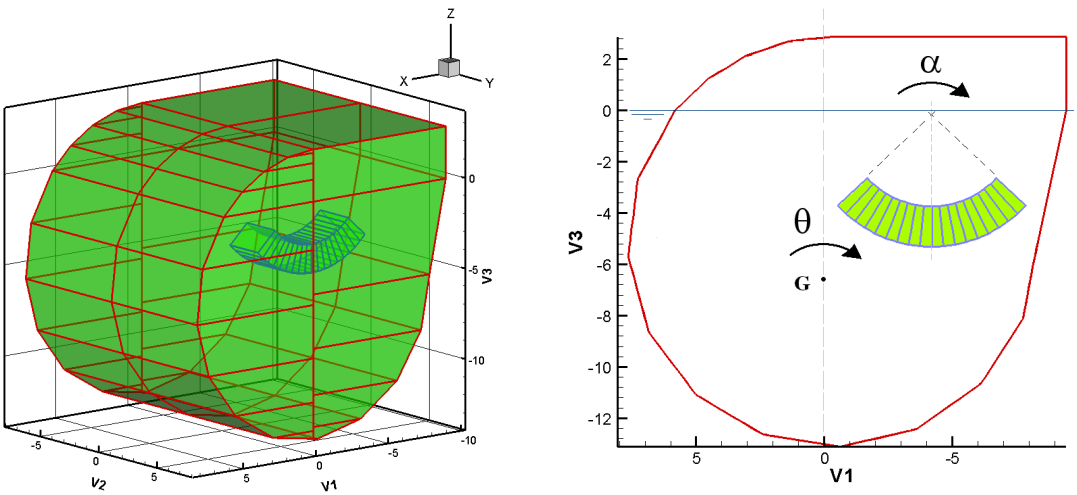

(a) (b)

Figure 8.1: 3D-view of hull *DES1129* of the SEAREV WEC (a) – incoming waves arising from negative x – and simplified technical sketch (lateral view xOz)(b).

In order to limit the roll and yaw motions in the simulations, fictive mechanical

stiffnesses are applied to these DOFs as the coefficients $K_{44} = 10^9 N.m.rad^{-1}$ (roll, φ), and $K_{66} = 10^8 N.m.rad^{-1}$ (yaw, ψ). As a consequence, pitching motions are favoured to the detriment of roll and yaw, which prevents the device from being disturbed by wave directionality. Thus, a fair focus can be made on the WEC sensitivity to spectral bandwidth, and hence, to wave groups.

A simulation code developped at ECN is used, which solves the dynamic integro-differential equation (Cummins, 1962) in time domain thanks to a 4th-order Runge-Kutta resolution scheme. The radiation (added masses and impulse responses) and diffraction (excitation forces of incident waves) efforts are obtained from previous results computed with the aid of 3D diffraction-radiation codes (also developped at ECN, **?**) applied to the hull at rest under deep water and small motions assumptions (linearised problem). The hydrodynamic non-linearities derive from the exact computation of the instantaneous Froude-Krylov efforts (fluid pressure forces exerted on the hull) at each time step. As these efforts often are of the same order as the own excitation efforts, it is crucial to figure out them precisely, even more when simulating a 3D-body against its six DOFs within moreless energetic real sea-states (possible large amplitudes of motion). It is more common, indeed, to linearise such a computation assuming the hull's shape does not vary a lot: this may however induce some discrepancies with the real dynamic behaviour of the body, namely when heave, pitch, and yaw motions are significant.

Throughout this work, it will be assumed that the WEC is deployed in a deep water zone. For each simulation, the chosen time step to solve the Cummins' equation is $\Delta t = 0.05s$, and the whole simulation is lead over $500s$ from initial rest conditions. A dynamic transient phase has to be estimated beforehand, during which the body moves from rest position to a permanent random regime. To this aim, the response of the SEAREV is observed in monochromatic waves for incoming wave incidences $\beta = 0$, 15, and 30 and crest-to-trough wave height $2m$, while wave periods range from $2s$ to $16s$. From figures 8.2(a-f) depicting the instantaneous extracted energy (kJ) by the WEC for cases $\beta = 0$ and $T_{exc} = 8, 10, 12s$ (a,c,e) on the one hand, and $\beta = 30$ and same periods (b,d,f) on the other hand, the mean power – i.e. the slope to which the instantaneous energy is converging as time goes by – seems reasonably stable in all cases as $t \geq 100s$. Accordingly, it shall be assumed in the following that the system – initially at rest position – lies in its permanent regime as soon as $t \geq T_{RT} = 100s$, whatever the sea-state. Thus, the 100 first seconds of the simulations (of length $T = T_{RT} + T_{simu}$) will not be taken into account in the power statistics, so that the realistic behaviour of the WEC is actually observed over $T_{simu} = T - T_{RT} = 400s$.

The nominal $500s$ simulation duration has been arbitrarily chosen: it yields an acceptable compromise between permanent regime duration (for the dynamic observation) and numerical run time. The code was implemented for a linear frequency vector definition, which corresponds to an arithmetic sequence such that $f_i = i * f_0$, with $f_0 = 1/T$ (Fourier harmonics). It is therefore not possible to define the input spectrum with freely distributed frequency vectors; also, refining the linear frequency discretisation is

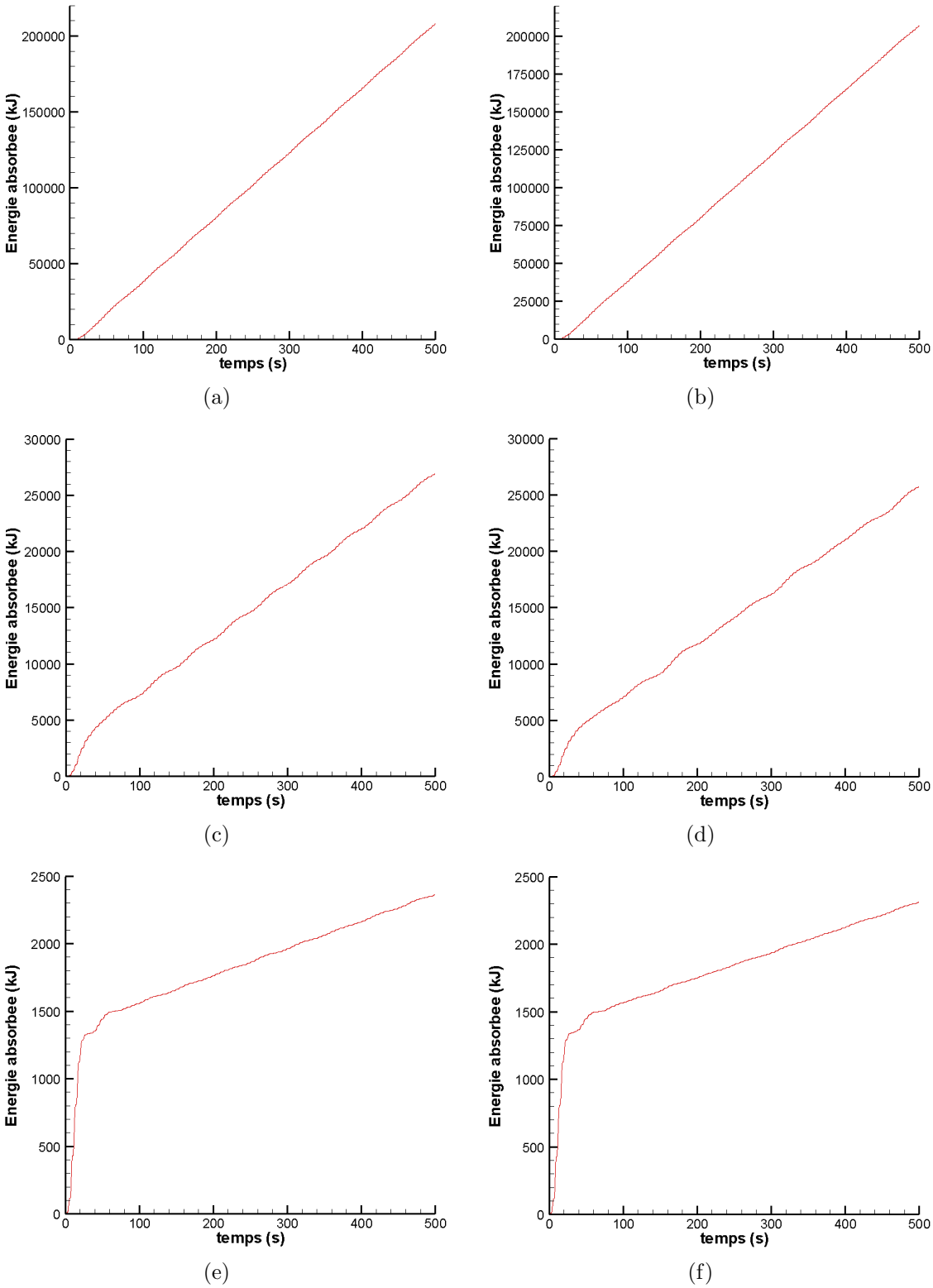

Figure 8.2: Instantaneous extracted energy (kJ) by the SEAREV simulated in monochromatic waves with ($\beta = 30$, right hand figures) and without ($\beta = 0$, left hand figures) incoming wave incidence, for periods $T_{exc} = 8s$(a,b), $10s$(c,d), and $12s$(e,f), and crest-to-trough wave height $2m$.

not recommended for the simulation run time may be unreasonably increased. Figure 8.3 illustrates the re-discretisation – or re-sampling – of the raw input directional wave spectrum (from WWIII model in California, on the 20th of January 2007, 3AM) on the left hand side, as linearly distributed frequency vector and filtered (low-energy directional components removal) wave spectrum on the right hand side. A slight energy loss is to be deplored yet after filtering and re-sampling. However, too long simulation durations would result if all directional components were taken into account, and that is why the directional filtering is necessary here. Last, let us stress that the input spectra are simulated up to a minimal cut-off frequency of $0.25Hz$.

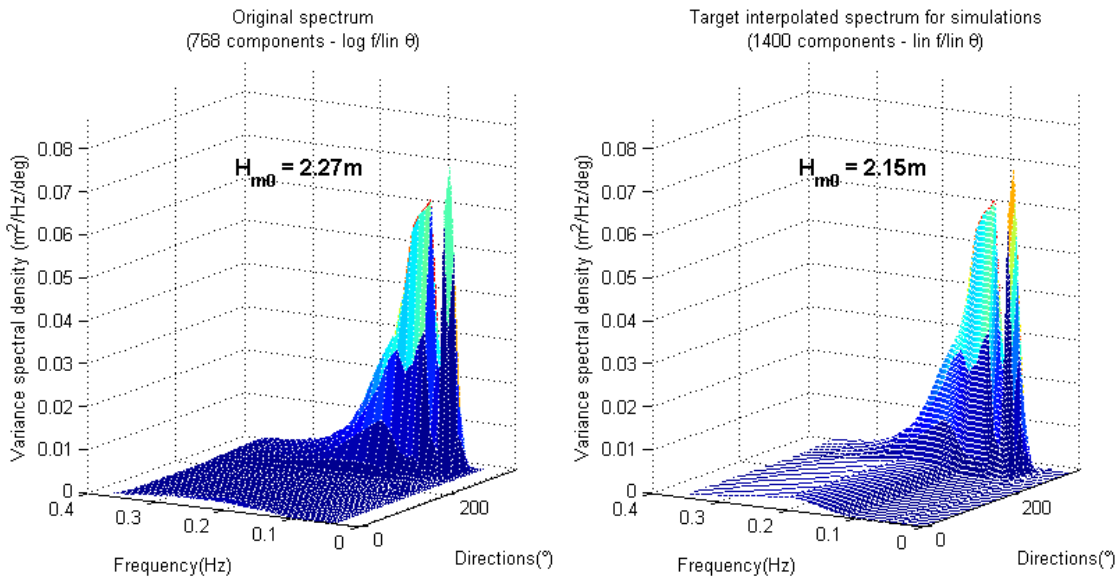

Figure 8.3: Re-sampling of the raw WWIII directionl spectrum at the Californian location NDBC 46063, on the 20th of January 2007, 3AM.

One single – even extended – simulation of the WEC in a given target sea-state is not sufficient to approach the expected mean extracted power value. That is why a few simulations of the same target wave spectrum are often required to derive a better estimation, as the power estimators' mean. According to the conclusions exposed in Section 3.5 as well as in Saulnier et al. (2009), the simulations are carried out in frequency and directions ($f_0 = \Delta f = 1/500 = 0.002Hz$, $\Delta\theta = 15\,°$) by selecting random phases only (*method b*) and taking wave amplitudes $A(f_i, \theta_j)$ equal to

$$A(f_i, \theta_j) = \sqrt{2S(f_i, \theta_j)\Delta f \Delta\theta}$$

For the case of a heaving axi-symmetrical device – moreover equipped with a non-linear PTO mechanism – indeed, it has been shown that *method b* was not inducing biased mean power estimations compared with *method a* (random amplitudes and phases). Furthermore, *method b* permits to approach the expected value of the process faster than *method a*. It is thus assumed that these conclusions are valid for the case of the SEAREV numerical simulator in three dimensions. This allows to reduce the number

of simulations to be run – to around 20 for each simulated sea-state –, which is highly desirable when one knows that each single $500s$-simulation is extremely time consuming[1]. The automatic simulation processing is performed on the CAPARMOR Phase II server (at IFREMER Centre of Brest) which allows for running numerous simulations simultaneously (sixteen jobs per user in a row).

Figures 8.4(a-f) present the mean power extracted by the SEAREV in monochromatic waves against excitation wave period (and frequency) for three wave incidence cases already described previously. The mean power value is provided by considering or not the transient regime from rest position (100 first seconds in each simulation). These figures lead to the following observations:

1. the mean power estimation with or without transient phase does not seem very different, except for very high power values for which it may appear more significant (around $50kW$ for $T_{exc} = 9s$, that is, less than 10%-error against the permanent regime estimation);

2. the wave incidence from 0 to 30 does not induce large variations in terms of performance since the WEC extracts around $10kW$ less for 30 than in front waves (over a bit less of $600kW$);

3. whatever the wave incidence within the condidered angular sector, the system essentially extracts energy from waves in the excitation period range $[6s; 10s]$; in terms of excitation frequency, the system appears particularly sensitive between $0.10Hz$ and $0.17Hz$, and then less and less up to $0.30Hz$.

The simulated WEC therefore is very little sensitive to wave directionality as soon as it is aligned with the main wave direction – at least within an angular sector of moreless 30 for incoming waves. Moreover, the WEC is mostly sensitive to a frequency interval corresponding to wind-seas and old swells (end of swell wavetrains): during the active systems selection, low-frequency swells as well as very young wind-seas (i.e. whose peak frequency is superior to $0.20Hz$) shall be discarded.

[1]From two to three hours required on average per simulation (∼1000 wave components) for an AMD Athlon 64 of $2.40GHz$ with $2Go$ of RAM; some sea-states involving about 2000 wave components even require up to six hours.

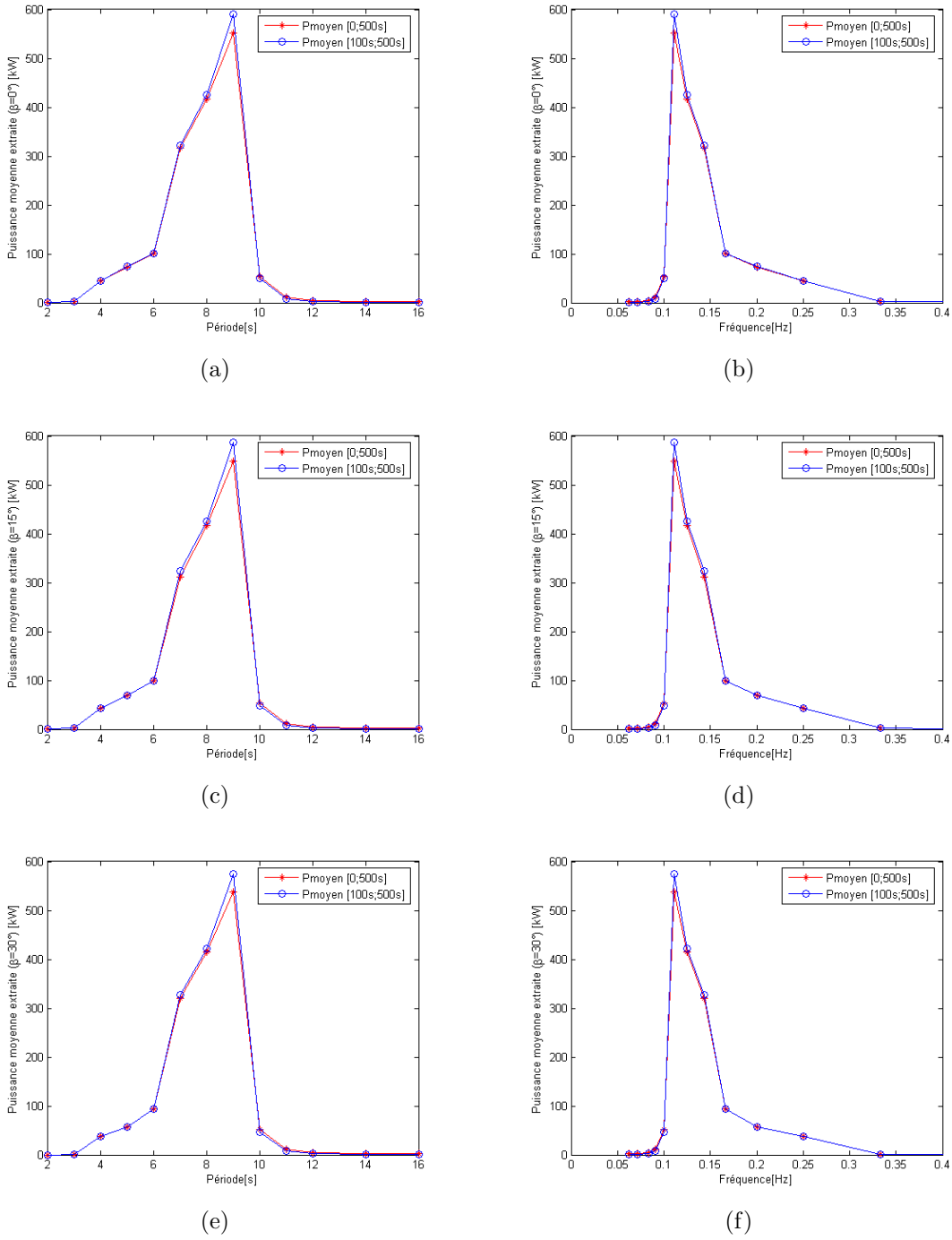

Figure 8.4: Mean power (kW) extracted by the SEAREV in monochromatic waves against wave period (left hand figures) and wave frequency (right hand figures) for three wave incidence cases: $\beta = 0$(a,b), 15(c,d), and 30(e,f); the mean power value is calculated over the whole simulation signal (500s from rest position, red line) as well as over the permanent regime only (400 last seconds of the simulations, blue line).

8.3 Californian wave climate

The WEC must be simulated in wave conditions such that its sensitivity to wave groupiness may be easily assessed. An appropriate wave climate (or weather window, here) should therefore present the following conditions:

- the direction of the most frequent wave systems (swells and wind-seas) should very little vary: this enables to look for a constant float's heading throughout the simulations (fixed slack moorings);
- the directional spreading of the most frequent systems must remain quite restrained: thus, the WEC may be even less sensitive to crest directionality;
- the active systems are clearly separated from the passive ones (i.e. swells with $f_p < 0.1Hz$ and wind-seas with $f_p > 0.2Hz$) without pronounced frequency and direction overlapping and whose number of occurrences is sufficiently important to avoid working on particular cases only;
- there is a great variability in terms of wave power (P_w) among the active systems to ensure a diversified overview of the local sea-states.

Such a wave climate – whose spectral data are available – has been found, which corresponds to the Californian NDBC measurement buoy n°46063 located off the coast of Santa Barbara (34 °16'21"N, 120 °41'55"W, Fig. 8.5) and named *Point Conception*. The NDBC has been collecting wave spectral data in that location thanks to a directional buoy, among which the spectral estimates of the ocean's water elevation as well as the four first Fourier coefficients of the directional function. Here however, the used data are output from the WWIII wind-wave model implemented by the SHOM (whose input wind fields are provided by the ECMWF). The local water depth is about $632m$ but the location remains close from the shoreline for the continental shelf is quite abrupt along the Californian coasts. Eventhough it may constitute a tricky engineering issue for the installation of submarine cables linking the plant zone to the grid onshore, the bathymetry is optimal to allow for assuming deep water conditions. The WWIII wave spectra are calculated every $3h$ and the selected weather window refer to the month of January 2007, which yields about 240 successive wave spectra (up to the 30th).

The extraction of wave systems is carried out with SPOP and the spatiotemporal tracking algorithm (with [0.6,0.3,0.1]-linear co-variogram model, see Chapter 6) is then run for the two NDBC sea points 46063 and 46069 (33 °39'0"N, 120 °12'0"W, *South Santa Rosa Island*, see Fig. 8.5) where the extraction has been also performed from SHOM WWIII spectral data. The tracking results related to parameters f_p, θ_p and H_{m0} are provided in figures 8.6(a-c).

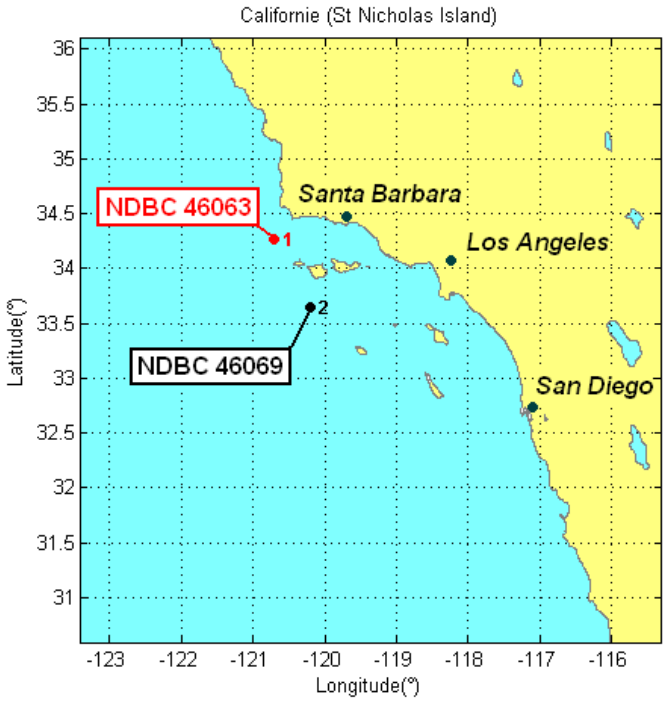

Figure 8.5: California zone: buoy locations NDBC 46063 and 46069, off Santa Barbara and Los Angeles (Califorina, U.S.A.).

These results highlight the nearly monodirectional trend followed by the wave systems around $\sim 300\,^{\circ}$ (Fig. 8.6(b)), as either swells or wind-seas. There are numerous occurrences of coexisting swells and wind-seas, where these latter sometimes reach significant energy levels (up to $4m$ wave heights). Wind-sea 'CUHI' is divided in two successive events: in the first one, a wind-sea is formed, whose peak frequency is not going below $0.15Hz$; then, a stronger second wind blow lets peak frequency drop down to $0.08Hz$ without merging with the close swell system 'OEBI' though. There is no observable fusion either between wind-sea 'QOWO' and 'OEBI', which is very persistent (tracked over 11–12 days). However, the local maximum noticed in the peak frequency history of swell 'MAUA' – contemporaneous of a sequence of successive low-energetic wind-seas 'FEMO' and 'AEWU' ($H_{m0} < 1m$) – let think that a swell/wind-sea fusion occurred, which is confirmed herebelow.

From the systems extracted at Point Conception, the active systems (or partitions, here) such that $0.1Hz < f_p < 0.2Hz$ and which do not notably overlap with neighbouring passive systems – as described in the hereabove listed requirements (see Fig. 8.7) – are retained for our study. The raw partitions are drawn from the SPOP algorithm before fitting with parametric shapes.

From these partitions (indexed by "sa"), which are integrated over directions, the following spectral parameters are calculated (see Appendix A):

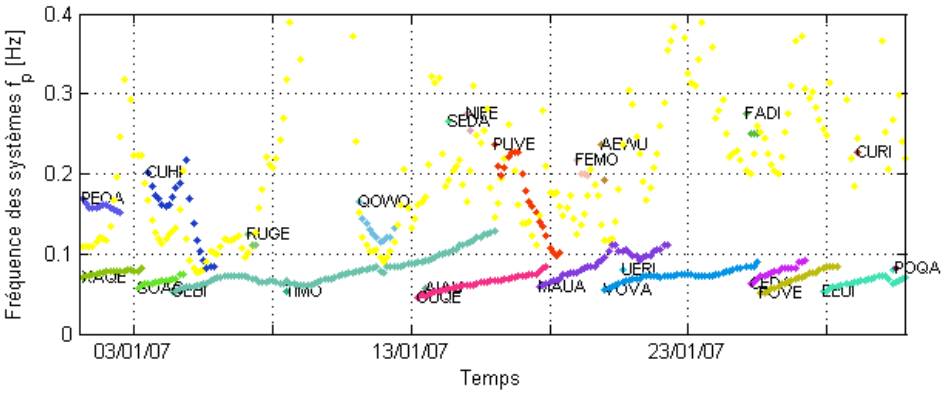

(a)

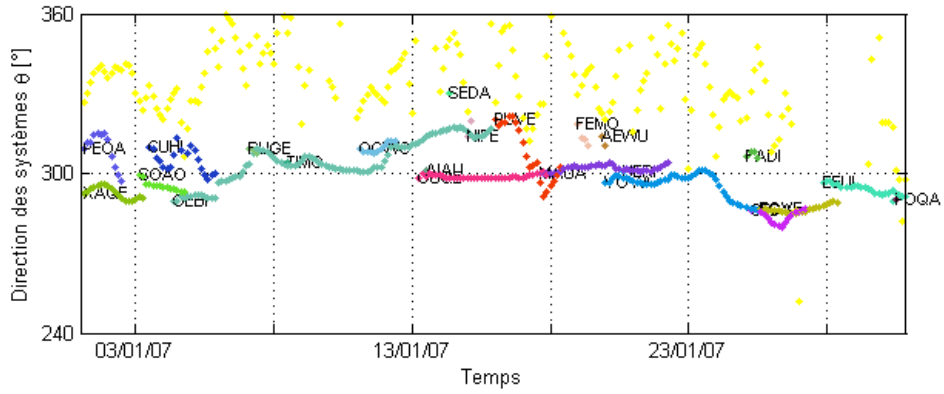

(b)

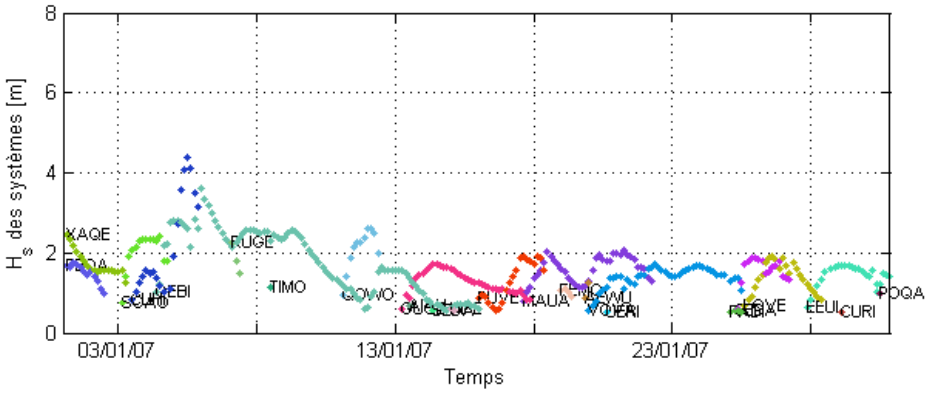

(c)

Figure 8.6: Time tracking of peak frequency (a), peak direction (b), and significant wave height (c) of wave systems extracted in January 2007 at the NDBC 46063 location, derived from the spatiotemporal coherence analysis lead on two points with linear co-variogram model ([0.6,0.3,0.1]); yellow plots stand for local wind data (separation frequency – Eq. (5.6) – in (a) and mean direction in (b)).

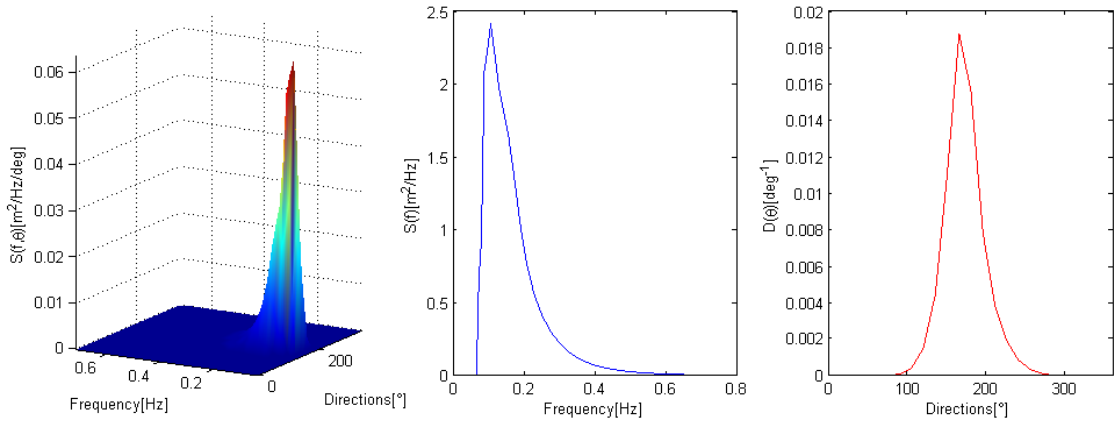

Figure 8.7: Active partition as extracted from the wave spectrum on the 20th of January 2007 at Point Conception (to be related to Fig. 8.3), corresponding frequency spectral density and directional distribution (beware, in this latter directions do not match with the actual ones due to some definition vector changings operated in the SPOP algorithm).

$$\{H_{m0,sa}, T_{-10,sa}, T_{p,sa}, T_{01,sa}, P_{w,sa}, \varepsilon_{2,sa}, \varepsilon_{0,sa}, \sigma_{f,sa}, \sigma_{T,sa}, Q_{p,sa}, Q_{e,sa}, \kappa_{sa}, \Lambda_{sa}, B_{w,sa}\} \tag{8.2}$$

As stressed before, the wave systems mostly arise from a narrow angular sector centred on $\sim 300\,^{\circ}$ (north-western waves). The systems extraction showed indeed that the spreading parameter s obtained after directional fitting was in majority included in the range [15;36], which corresponds to a maximal angular disperion of about $40\,^{\circ}$ around the mean wave direction. Similarly, the parameters in (8.2) are also calculated for the global spectrum (as not-indexed symbols). Let us remark in addition that in the parameter calculation, the cut-off frequencies are only defined as the own partitions' frequency limits, as extracted on the directional spectrum (parameter ε_2, for instance, may be extremely sensitive in this respect, as demonstrated in Appendix A).

Nevertheless, such active wave systems do not occur at each sea-state. That is why it is necessary to focus our work on a set of wave sequences, where well-behaved active systems are easily identified: it generally deals with wind-seas, but ends of long swells may also match the same requirements. Each sequence describe a whole (or a portion of) wave event; for wind-seas namely, the event is kept as entire as possible, eventhough the first or last instants of observation stand outside the frequency interval $[0.1Hz;0.2Hz]$. This permits to consider the parameters' variability throughout their time evolution. Thus, nine sequences are isolated, each of them corresponding to a particular wave event. Figures8.8(a-c), 8.9(a-c), 8.10(a&b), 8.11(a&b) and 8.12(a&b) depict the time evolution of parameters in (8.2) applied to both the active partition and the corresponding global wave spectrum. Accordingly, these sequences follow the wave systems (listed by apparition order): 'PEOA' (n°1), 'CUHI' (n°1&2), 'RUGE' (n°4), 'QOWO' (n°5), 'OEBI' (n°6), 'PUVE' (n°7), 'FEMO' (n°8) and 'MAUA' (n°9).

The time tracking of the active partitions' (bandwidth) parameters may exhibit some discontinuities that are probably due to the wave system extraction (catchment area technique) and grouping procedures realised within SPOP. While both peak frequency and energy of the partitions remain time-coherent, cut-off frequencies and partition groupings have a noticeable influence on the bandwidth parameters. This is namely observable for dimensional parameters such as Λ_{sa} (which is much surprinsingly correlated to $f_{p,sa}$) in sequence n°5. The values calculated between 9AM to 6PM seem to be underestimated with respect to the global time evolution of the parameter. Similarly, an important discontinuity is visible in all figures at the beginning of sequence n°6: from 3AM to 6AM, it is clear that the system suddenly moves from narrow- to quite broad-banded. This is accounted for by the fact the system – an old swell – may have been merged with a close wind-sea during either the extraction or grouping step (this is confirmed when looking at the evolution of significant wave height). When considering the evolution of parameters like Λ_{sa}, $\sigma_{f,sa}$ and $\sigma_{T,sa}$, it seems evident that the spectral bandwidth of a growing wind-sea mainly decreases as time goes by (see Section 5.2.1) unless an old swell in high-frequency, whose bandwidth is expected to increase against time (see namely Gjevik et al., 1988). Now, event n°6 is identified as a swell according to the time tracking of parameter $f_{p,sa}$ (Fig. 8.8(a)); yet, its bandwidth exhibits a non-negligible decrease, characteristic of a wind-sea. Therefore, sequence n°6 is much likely to result from the fusion of an old swell with a close wind-sea (in both frequency and direction). These remaks also hold for sequence n°9.

More generally, it may be said here that the active partition – very often – corresponds to the secundary wave system. Indeed, the main peak often appears in low-frequency so that the sea-states mostly are bimodal (swell + wind-sea) throughout the considered sequences. Sequence n°5 is an exception though, for the sea-states become unimodal (as wind-sea dominated, see Fig. 8.8(a&b)). According to the observed wave characteristics, the float's heading is definitely set to direction 305 $^\circ$ in the numerical simulations.

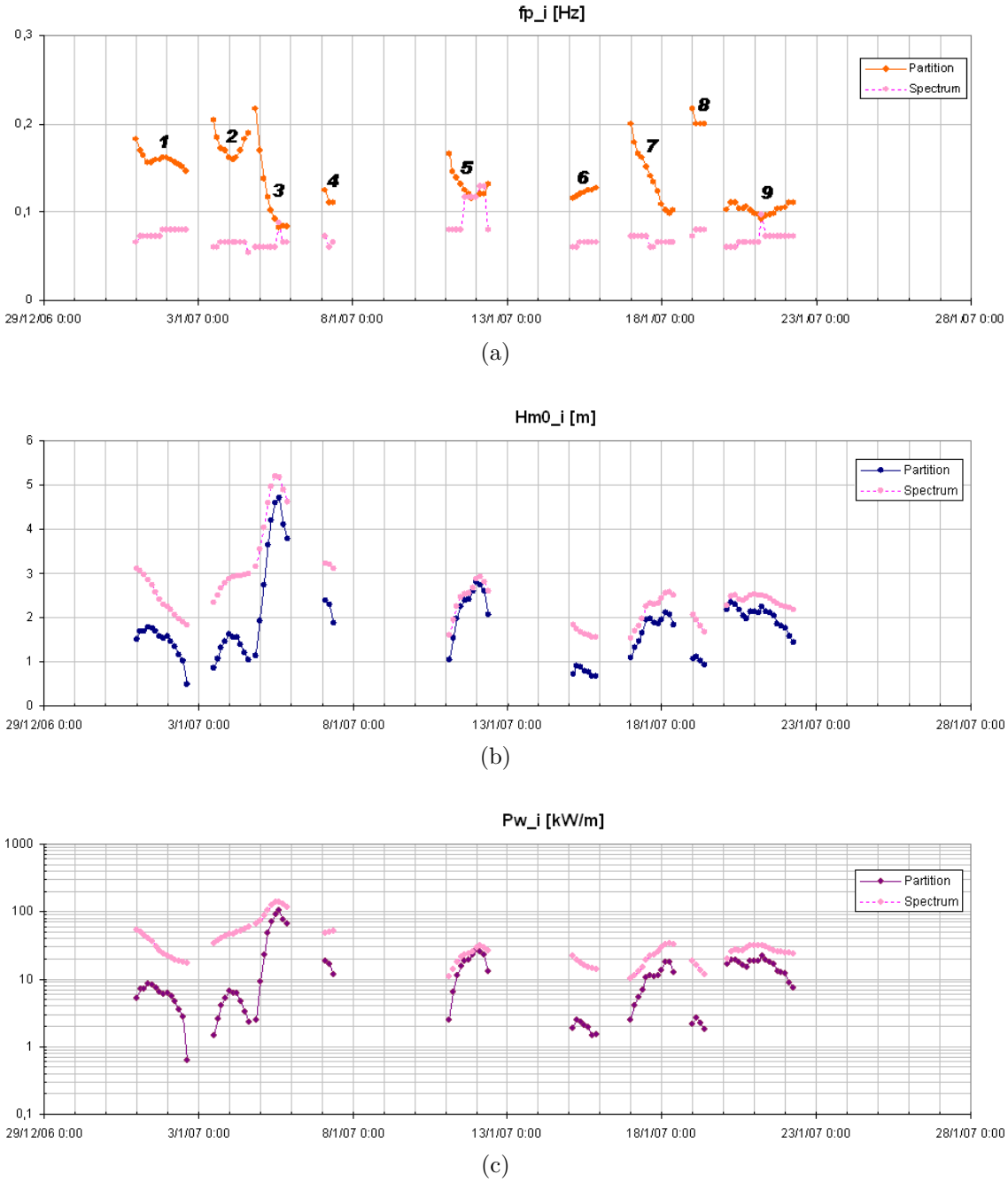

Figure 8.8: Time tracking of parameters $f_{p,sa}$ and f_p (a), $H_{m0,sa}$ and H_{m0} (b), and $P_{w,sa}$ and P_w in log. scale (c) in the nine active partitions sequences during the month of January 2007 at sea point NDBC 46063.

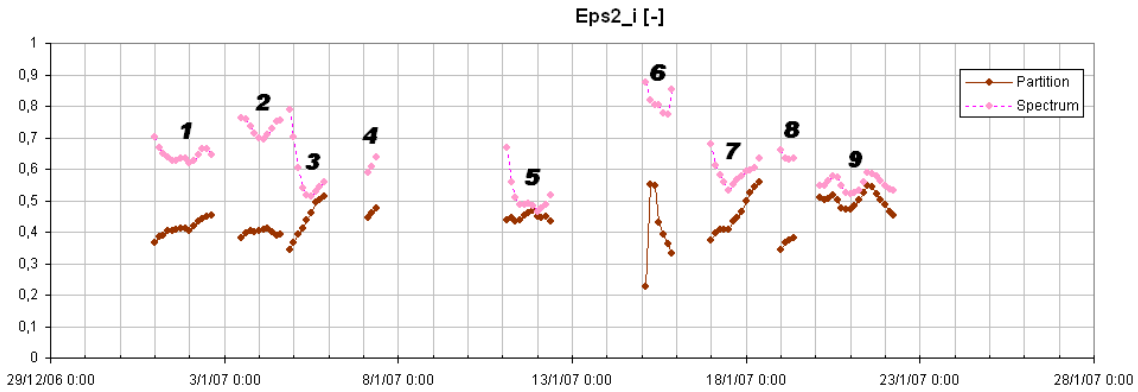

(a)

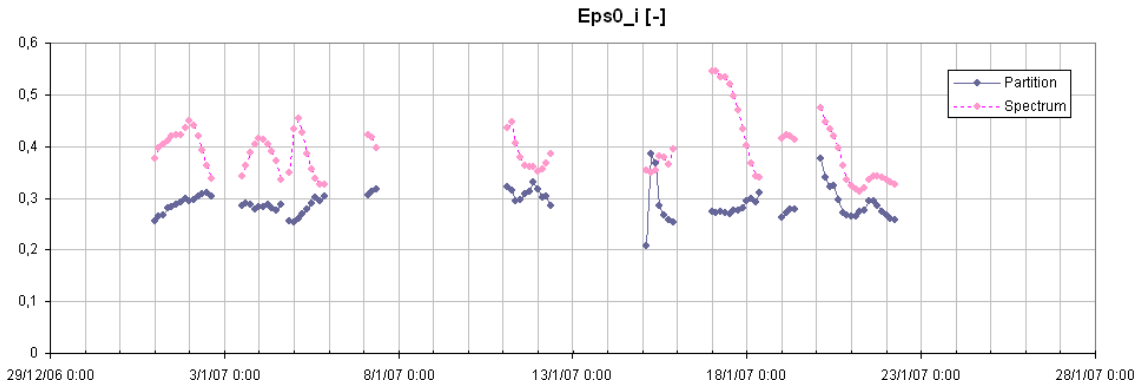

(b)

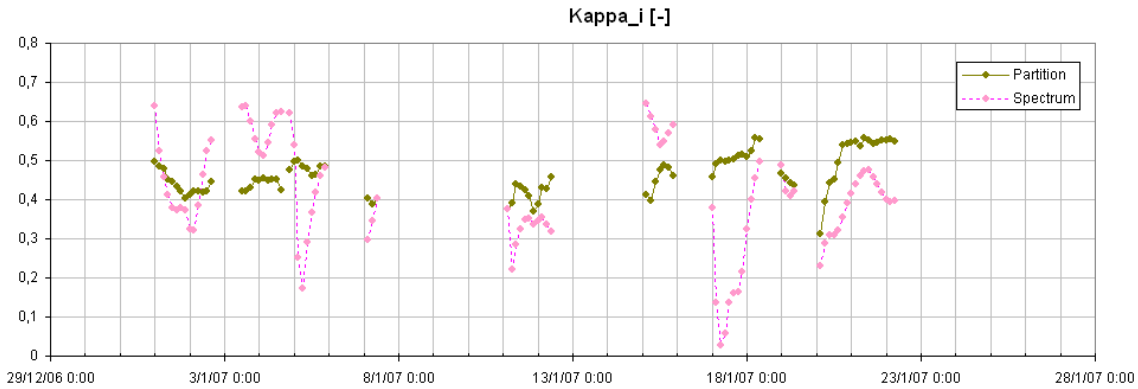

(c)

Figure 8.9: Id. Fig. 8.8 for parameters $\varepsilon_{2,sa}$ and ε_2 (a), $\varepsilon_{0,sa}$ and ε_0 (b), and κ_{sa} and κ (c).

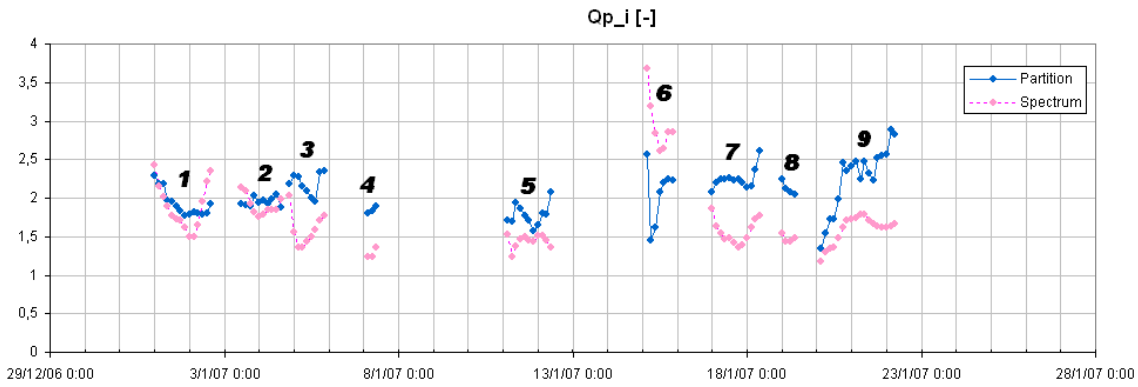

(a)

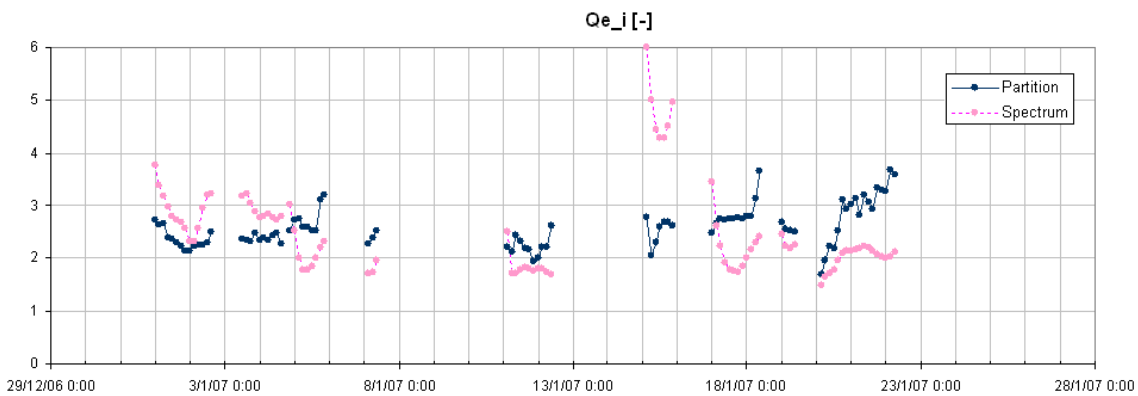

(b)

Figure 8.10: Id. Fig. 8.8 for parameters $Q_{p,sa}$ and Q_p (a), and $Q_{e,sa}$ and Q_e (b).

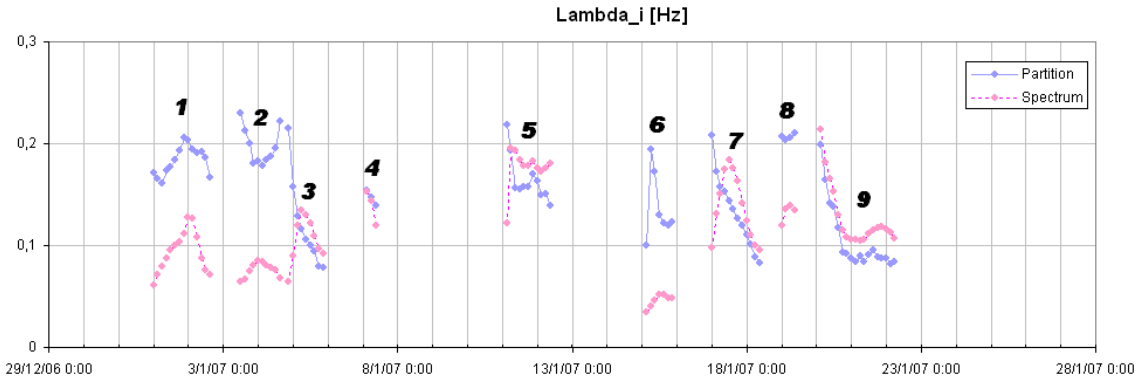

(a)

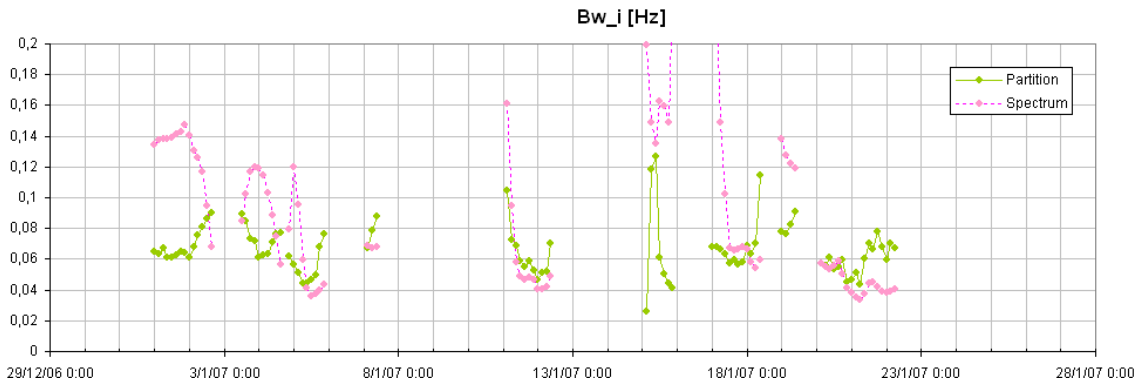

(b)

Figure 8.11: Id. Fig. 8.8 for parameters Λ_{sa} and Λ (a), and $B_{w,sa}$ and B_w (b).

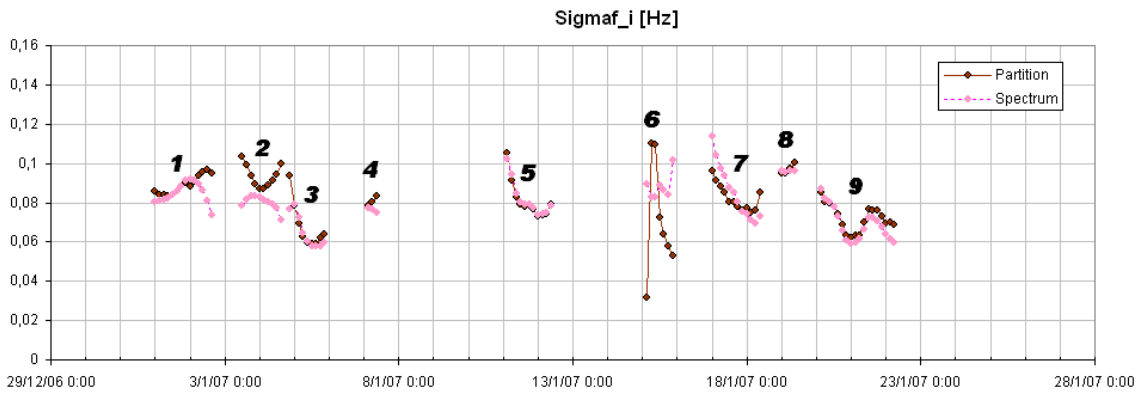

(a)

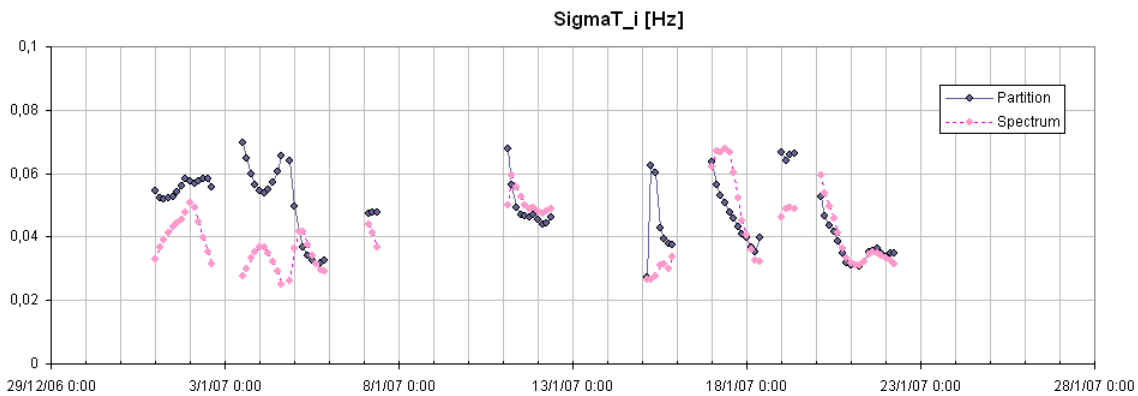

(b)

Figure 8.12: Id. Fig. 8.8 for parameters $\sigma_{f,sa}$ and σ_f (a), and $\sigma_{T,sa}$ and σ_T (b).

8.4 Simulation results

In each isolated sequence, the simulator is used to figure out an estimation of the mean converted power (in kW) at each time step. Thus, for each target wave spectrum, the mean power figure (denoted by $\overline{P_{PTO}}$ by commodity) is estimated as the average of the deterministic power estimators $\hat{P}_{PTO}$, whose number ranges from 17 to 40 at each time step (20–24 on average). The 10th and 90th percentiles are also calculated for a better description of the estimator dispersion.

Figures 8.13(a&b) yield the mean power estimation resulting from the simulations (in linear and logarithmic scale), as well as the associated 80% confidence interval. Figure 8.13(c) also depicts the joint time evolution of capture width parameters $\chi_{P,sa}$ (Eq. (8.1)) and χ_P (Eq. (3.28)) in m.

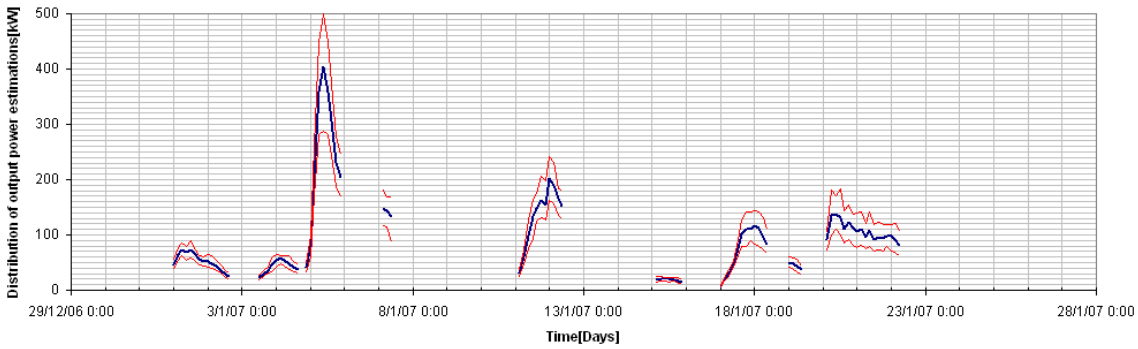

(a)

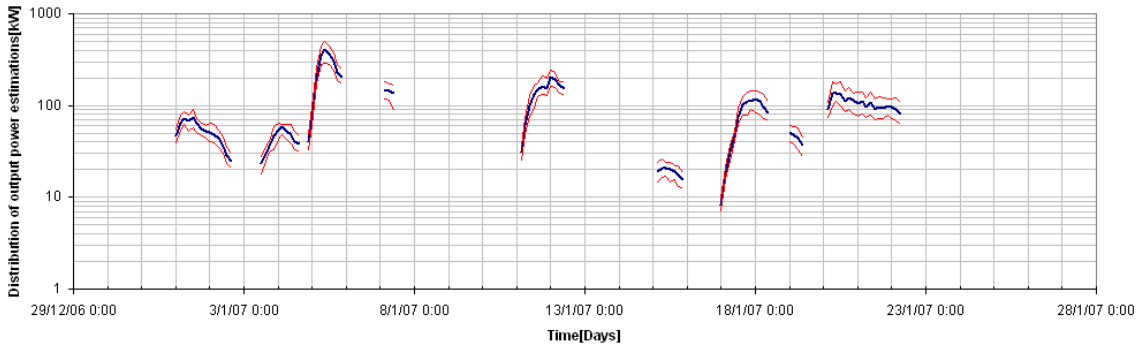

(b)

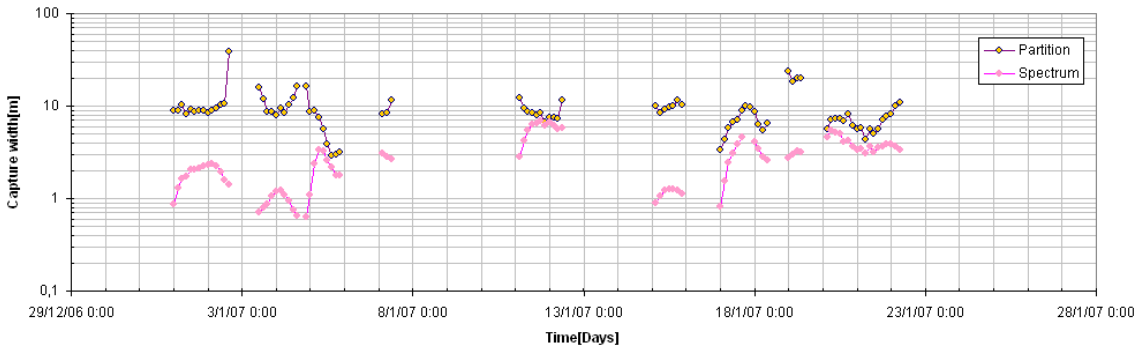

(c)

Figure 8.13: Mean power extracted by the SEAREV WEC estimated in nine wave sequences during the month of january 2007 at Point Conception (NDBC 46063) in linear (a) and logarithmic scale (b); capture width related to the global spectrum (χ_P, Eq. (3.28)) and active partition ($\chi_{P,sa}$, Eq. (8.1)) in logarithmic scale (c).

8.4.1 Simulation results in relation to the global spectrum

This first subsection aims at analysing the simulation results in relation to the global spectrum's characteristics and parameters. Contrary to the study lead in Section 3.3, this work is not dealing with particular restrained period bins – the sea-state sample should have been much bigger – but rather considers the results ($\overline{P_{PTO}}$ and χ_P) of the nine sequences all together as one single sample. However, each sequence will be duly marked in the following graphical results in order to visualise each event more easily and therefore allow an event-focussed analysis.

Correlation of $\overline{P_{PTO}}$ to P_w

By looking at the results of figures 8.13(a) and 8.8(c) linking the estimated mean power to global omnidirectional wave power P_w, a very rough correlation is observed. By examining this correlation more closely (Fig. 8.14(a&b)) it appears that the correlation is not uniform for all sequences since the wave power parameter is not sufficient to account for the WEC's performance. Each event taken separately exhibits a certain coherence indeed, but the global correlation is too poor to characterise properly the mean converted power.

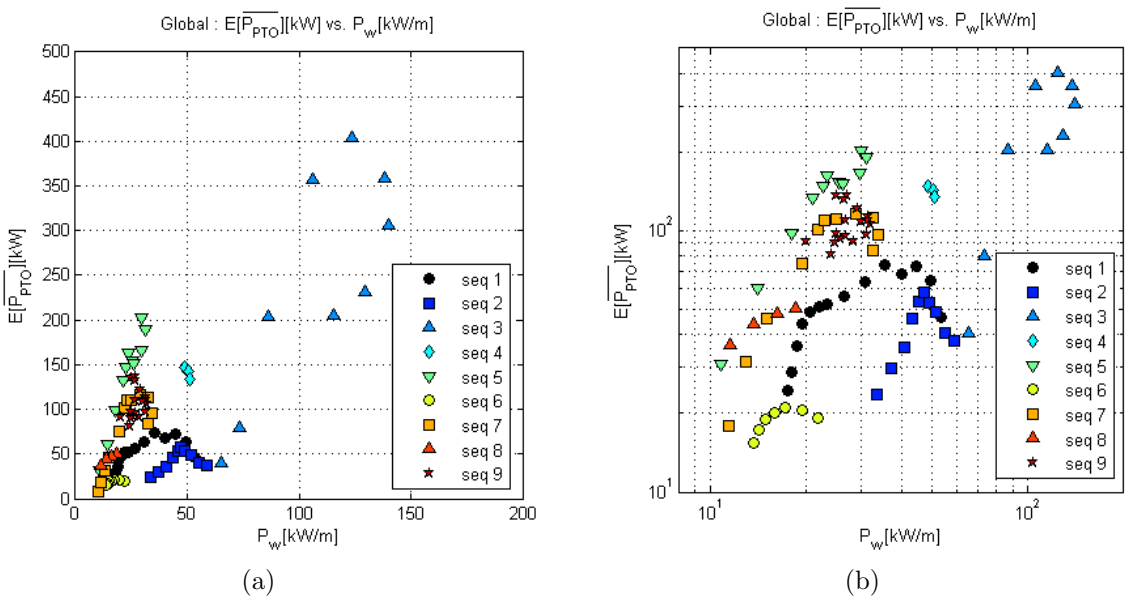

Figure 8.14: Mean estimated power (kW) against global omnidirectional wave power P_w (kW/m) in linear (a) and logarithmic (b) scale in the nine sequences over January 2007 at sea point NDBC 46063.

Correlation of χ_P to spectral bandwidth and wave groupiness parameters

Let us inspect now the sensitivity of capture width χ_P to the spectral bandwidth and wave groupiness parameters listed in last section. Figures 8.15, 8.16, 8.17 and 8.18 compare χ_P to parameters Λ and B_w, Q_p and Q_e, ε_2 and ε_0, and σ_f, σ_T and κ respectively. Most of these figures exhibit a clear correlation between both capture width and specral bandwidth figures, namely in relation to parameters Λ, Q_p-Q_e, ε_2, σ_T and κ – the most spectacular cases being for Q_p and Q_e (very distinct uniform $1/x$-decrease for all observed sequences). In all cases, the correlation is essentially noticed for narrow-banded sea-states: the case of κ, Λ and σ_T is a good illustration. The dispersion increases for sea-states of larger bandwidth corresponding to sequences n°5, 7, 8 et 9. As this analysis is based on the admissibility of comparing results obtained in far different sea-states all together, the WEC sensitivity is naturally subject to the wave field's energy localisation in frequency. Accordingly, as the wind-sea event n°7 moves from $0.2Hz$ to $0.1Hz$ it is expected that only the intermediary sea-states will match the resonance interval of the device. This is well observed for parameters κ, Λ et σ_T, for which the system's time continuity is perfectly suggested. Once again, sequence n°5 is an exception of the rule: even if it remains close to the response interval of the WEC throughout its evolution, it does not seem to induce the same kind of results as other similar sequences. Let us stress however that sequence n°5 is probably the only one in the sample showing unimodal sea-states, the rest of the sea-states being mostly bimodal (coexisting with energetic swells).

Parameter B_w does not seem relevant for this kind of study: no clear correlation with the global capture width has been found in the related figures. Parameter σ_f is not suitable either, probably because of its extreme sensitivity to cut-off frequencies, just as narrowness parameter ε_2. This latter – very surprisingly – seems much influent on the global capture width, so that it is tough to draw conlusions on this parameter. Indeed, its sensitivity to high frequencies (up to $\sim 0.7Hz$ here) is clearly emphasized for it changes its own nature: it is now decreasing against spectral bandwidth when it should be the contrary in reality, like ε_0. As far as this latter is concerned, besides, let us remind it represents basically – like ε_2 – a relative bandwidth parameter, which has to be multiplied to some well-chosen frequency yields a bandwidth measure in Hz (see Appendix A). Thus, such a parameter is more indicated for characterising spectral shape variations in sea-states of same mean frequency (or mean period), as it was the case in previous studies.

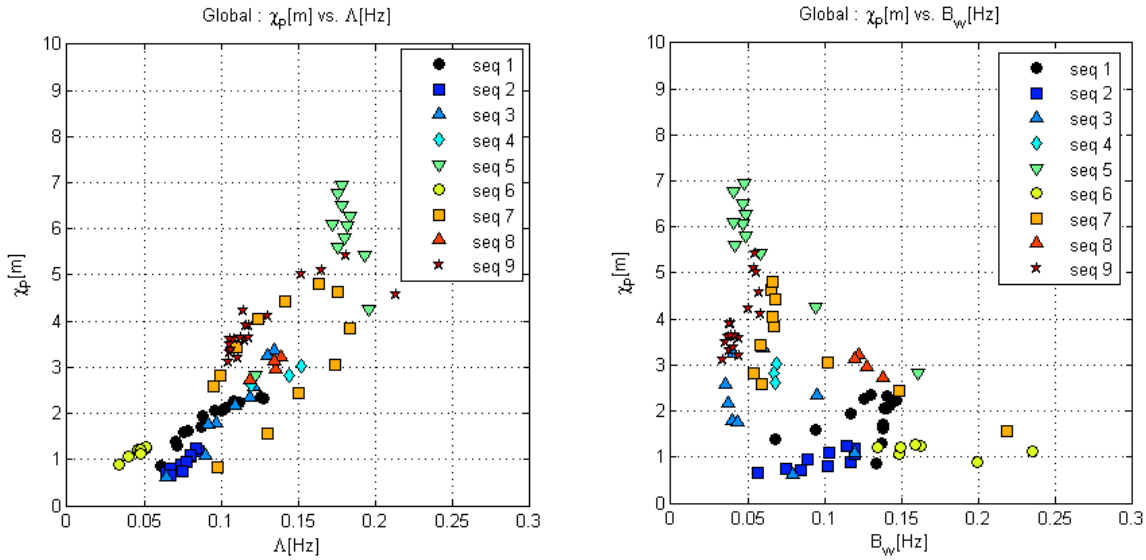

(a) (b)

Figure 8.15: Capture-width χ_P against parameters Λ(a) and B_w(b).

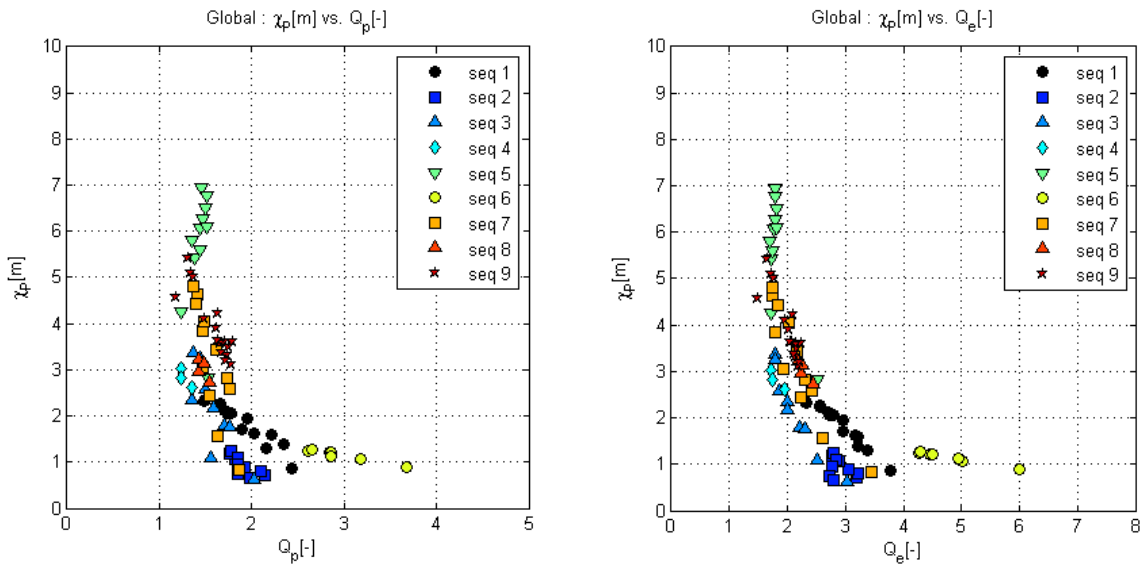

(a) (b)

Figure 8.16: Id. Fig. 8.15 against parameters Q_p(a) and Q_e(b).

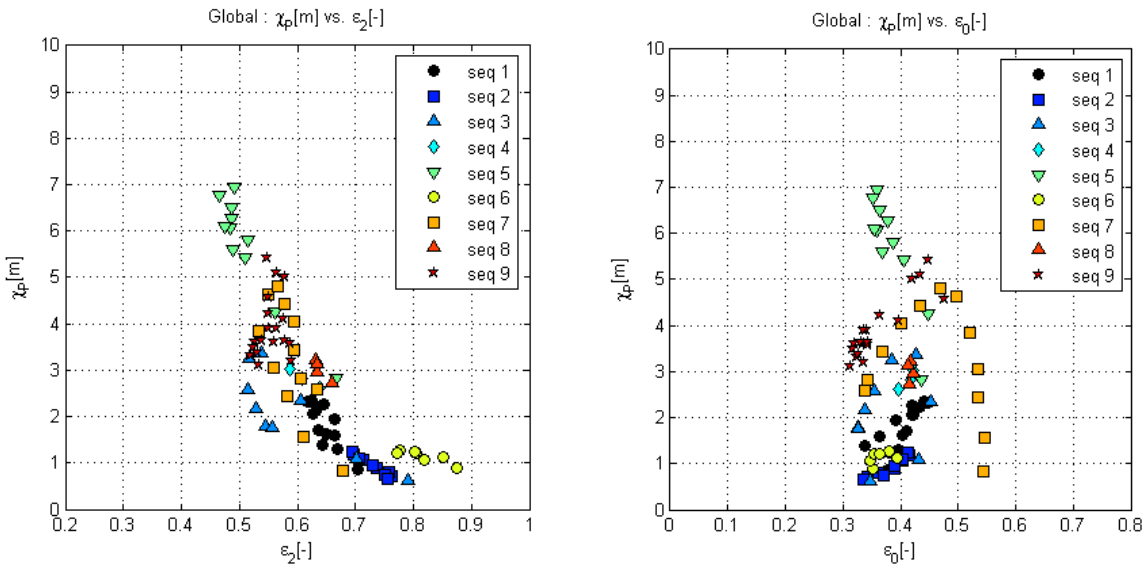

(a) (b)

Figure 8.17: Id. Fig. 8.15 against parameters ε_2(a) and ε_0(b).

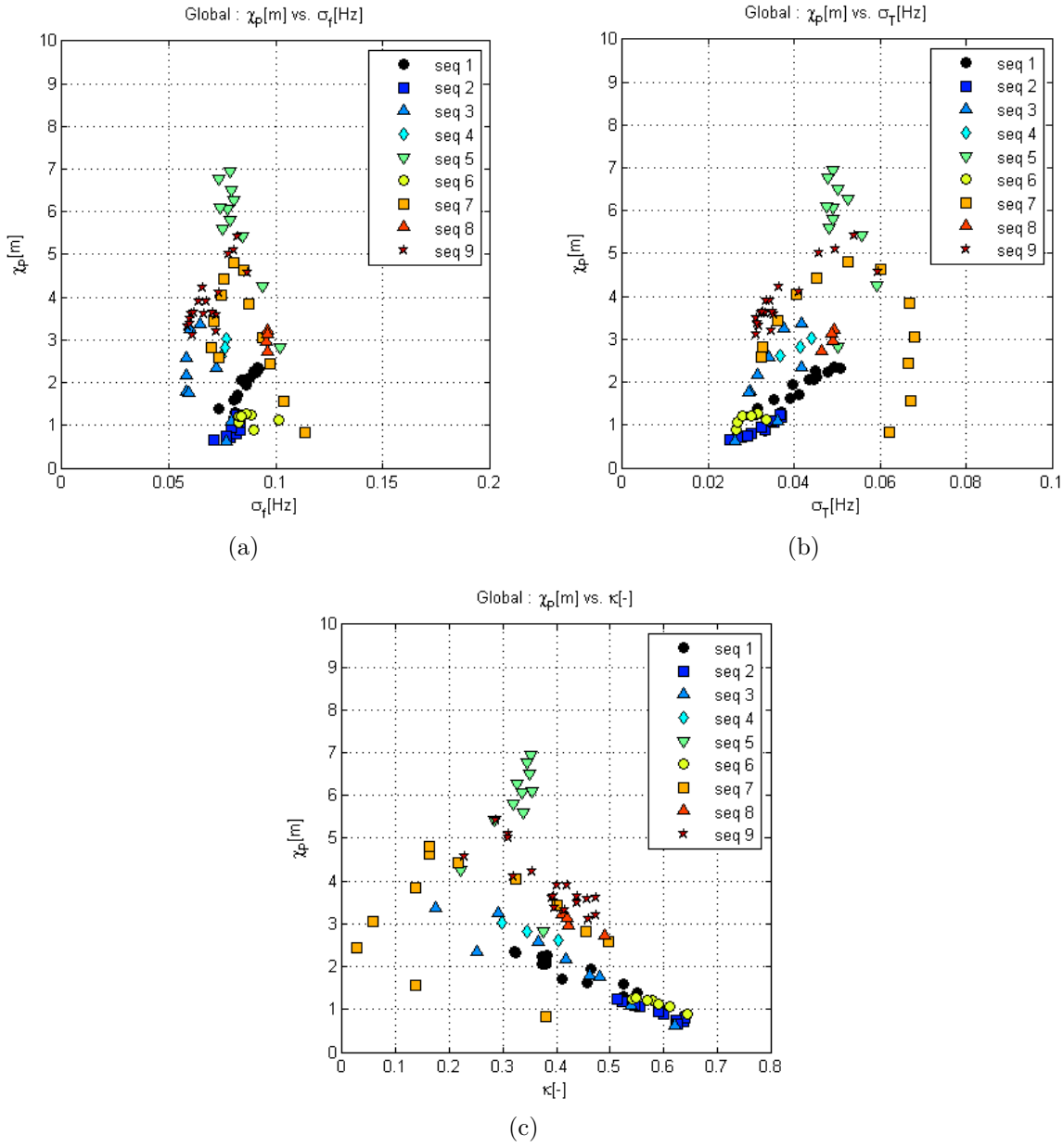

Figure 8.18: Id. Fig. 8.15 against parameters σ_f(a), σ_T(b) and κ(c).

8.4.2 Simulation results in relation to the active wave system

Correlation of $\chi_{P,sa}$ to spectral bandwidth and wave groupiness parameters

By the same manner, the sensitivity of $\chi_{P,sa}$ (Eq. (8.1)) is observed in relation to the same spectral parameters indexed by "sa". Contrary to global parameters (computed on the whole wave spectrum), these parameters are not exhibiting a great variability and this is why the corresponding figures – not represented here – do not bring any information on the sensitivity of the performance figure to the active systems' bandwidth. On is then lead to conclude that the bandwidth of the active partition is not a sufficient – and perhaps not relevant – characteristic to account for the variability of capture width $\chi_{P,sa}$. As an example though, the results related to parameters $Q_{e,sa}$ and Λ_{sa} are plotted in figures 8.19(a&b).

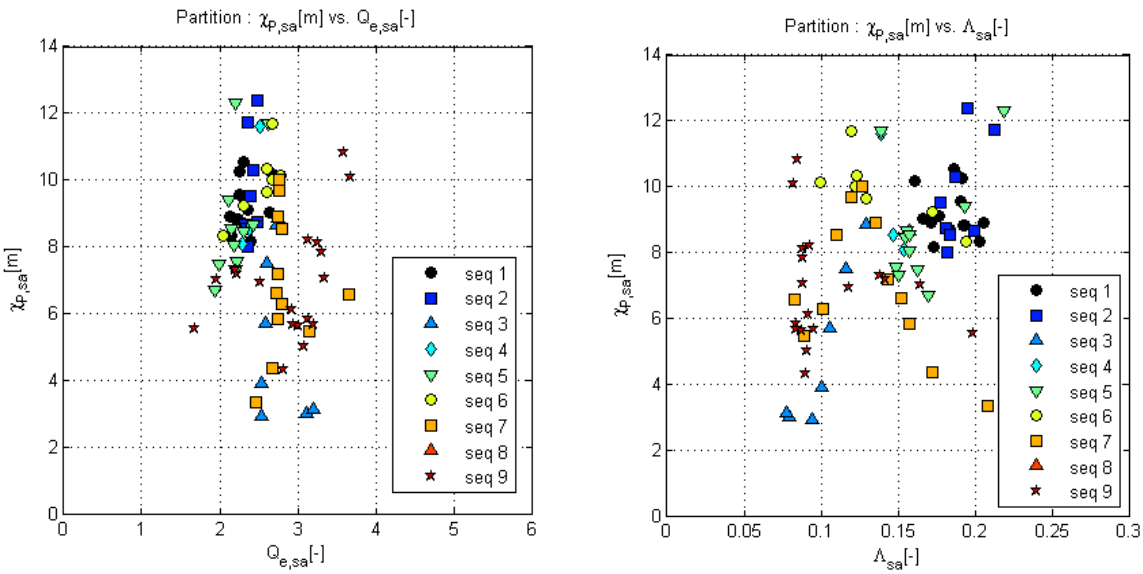

(a) (b)

Figure 8.19: Capture width $\chi_{P,sa}$ against parameters $Q_{e,sa}$(a) and Λ_{sa}(b).

Correlation of $\overline{P_{PTO}}$ to $P_{w,sa}$

Thanks to the multi-system description, it is possible to isolate the active wave system so that the energy that is effectively harnessed by the WEC should be that of the partition. To verify this assertion, let us observe how estimated power $\overline{P_{PTO}}$ and "active" omnidirectional wave power $P_{w,sa}$ are fundamentally linked to each other, in figures 8.20(a&b). These figures tend to confirm this last intuition, by exhibiting an almost linear correlation between both parameters. Besides, the logarithmic scale representation permits to indentify the sequences which are not exactly following this trend:

it essentially deals with sequences n°3, 7 and 8. Two of them are wind-seas whose peak frequency suddenly drops down from $0.2Hz$ to $0.1Hz$. It is therefore not surprising to obtain poor results in some cases where the "activeness" of the partitions is far from good, as already stressed before. Similarly, sequence n°8 even shows peak frequency superior to $0.2Hz$. Then the resulting distribution is absolutely consistent according to physics of the modelled WEC. As a conclusion, the multi-system description owns a major advantage on any other description, for it permits to focus on the energy really available to the WEC.

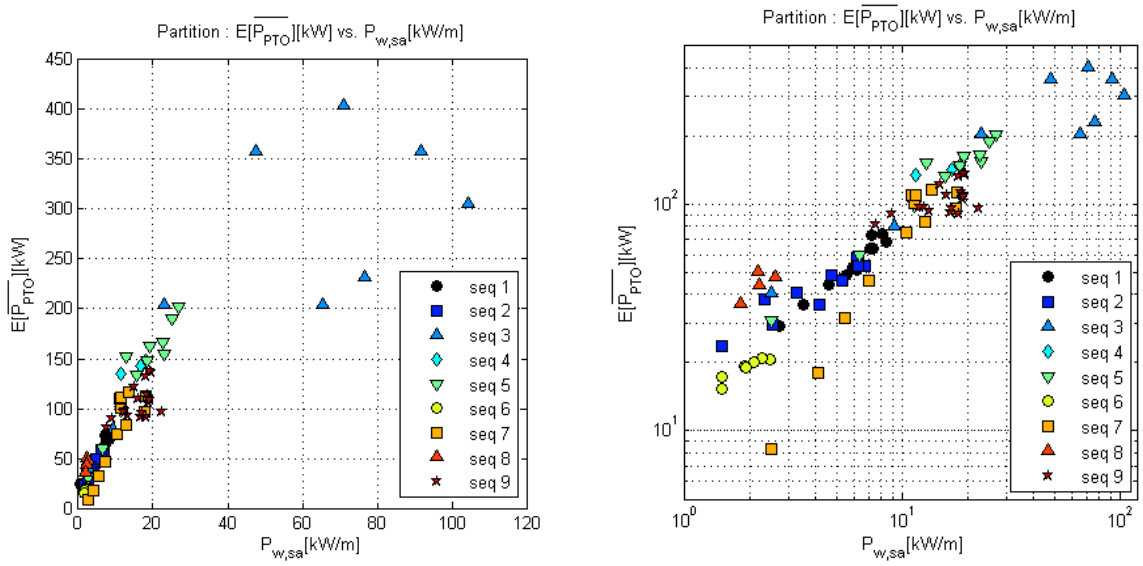

(a) (b)

Figure 8.20: Mean estimated power (kW) against active (partition) omnidirectional wave power $P_{w,sa}$ (kW/m) in linear (a) and logarithmic (b) scale in the nine sequences over January 2007 at sea point NDBC 46063.

8.4.3 Dispersion of the numerical power estimators

Before closing this last chapter, let us quickly come back on the precision of mean power figure estimation during the SEAREV WEC simulations. For each simulated sea-state (with *method b*), the standard deviation of power estimator $\hat{P}_{PTO}$ distribution is calculated. Now, by representing the power deviation $\sigma\left[\hat{P}_{PTO}\right]$ against the estimated mean power $\mathrm{E}\left[\hat{P}_{PTO}\right]$ (or more simply $\overline{P_{PTO}}$), the scatter plot in figure 8.21 is obtained. Both parameters are manifestly linked by a linear law, whose regression by least squares method fitting yields quite a high R^2 coefficient ($\sim$0.95). Eventhough those results do not refer to simulations performed with *method a*, it is tempting to link it to equation (3.48) which enables to derive a measure of the – linear equivalent – WEC's

response bandwidth $\Lambda_{\dot{\alpha}}$ (the converted DOF here is the pendulum's pitch indeed) from both the regression's slope and simulation length $T = 400s$ (in permanent regime), which is equal to

$$\Lambda_{\dot{\alpha}} = \frac{1}{T} \cdot \left(\frac{\mathrm{E}\left[\hat{P}_{PTO}\right]}{\sigma\left[\hat{P}_{PTO}\right]} \right)^2 \approx 0.074\ Hz \tag{8.3}$$

and can be identified in figures 8.4(b,d,f). This empirical linear law may be used to derive the power estimation precision in further time-domain simulations of same duration.

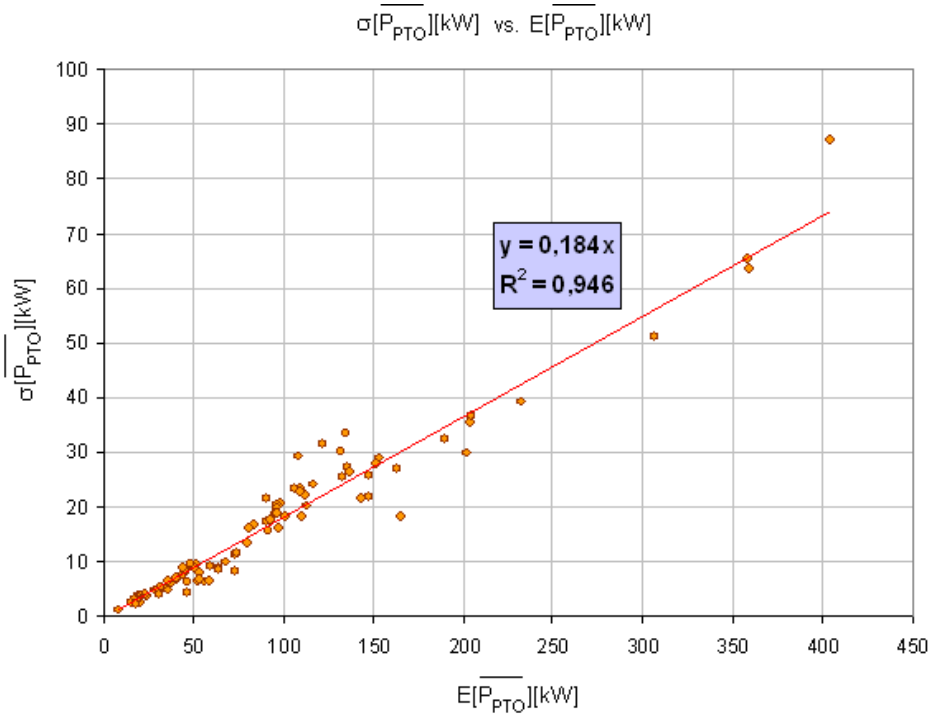

Figure 8.21: Standard deviation against mean of power estimator $\hat{P}_{PTO}$ in the SEAREV 3D-simulation sample obtained at the Californian site, and linear regression.

8.5 Conclusion about the performance study of a non-linear WEC

This chapter has presented the simulation of a WEC in the time domain by taking into account both the hydrodynamic non-linearities of the SEAREV WEC in three dimensions as well as the multimodal nature of the encountered sea states (multimodal decomposition and isolation of the so-called "active" partitions). It has been shown that, for this particular case, the performance of the WEC was still highly sensitive to

the overall spectral bandwidth (though e.g. parameters Q_e, Q_p, Λ and κ), the WEC being very little sensitive to wave directionality (the observed sea states are mostly mono-directional). This was observed in very different sea states, exhibiting very different characteristics (as wind-sea or end-of-swell active partitions). It was not the case, though, against the active systems' bandwidths characteristics, according to the results. Nevertheless, a very strong and almost linear relation has been found when plotting the estimated mean converted power against the active partition's omnidirectional wave power, which highlights the relevance of the multimodal decomposition for this kind of study. Furthermore, a linear relation has been found between the standard deviation of the mean power estimator (obtained from the time-domain simulations) and the mean power value when using *method b* in the wave simulations (deterministic modulus and random and uniformly distributed wave phases). This constitutes a precious information to keep in mind when running future simulations of the same device in the time domain.

Chapter 9

Conclusions

This work explored the possible refinements of sea-state description for the development of offshore WECs. Out of common global data as significant wave height H_s, peak period T_p (or mean energy period T_e) and mean wave direction $\overline{\theta}$, it is aimed at proposing a new characterisation of the sea conditions, adapted to the study of WECs behaviour, either by introducing new global spectral parameters – such as spectral bandwidth and wave groupiness – or by performing a precise metocean description, which separaties and tracks the wave systems composing the sea-state (*multi-system analysis*).

In a first part, it has been considered that the set of descriptive wave parameters could be extended with the characterisation of the spectral bandwidth, which is directly related to the wave groupiness phenomenon. Some descriptive spectral methods have been reviewed to this aim, as well as some deterministic methods lead in time domain, whose groupiness factors have shown to be nicely correlated with the spectral parameters obtained by spectral analysis of wave records. These methods are mostly based on the classical linear representation of the water elevation process (as Fourier series of independent harmonic components) assumed as Gaussian, centred, stationary, homogeneous and ergodic, which have shown to reproduce fairly well the natural groupiness of waves observed at sea. This review permitted to determine a set of spectral parameters that are computed on the whole energy spectral densities $E(f)$, such as ε_2, ε_1, ε_0, Q_p, Q_e, κ, Λ, B_w, as well as groupiness factors obtained in instantaneous wave energy histories such as GF_{SIWEH}, among others (Chapter 2).

Once these new parameters have been identified, the sensitivity of WEC models has been assessed against the global bandwidth of ongoing sea-states (Chapter 3). This sensitivity was first of all formulated for simple linear models in the frequency domain, which permitted to highlight that the system's mechanical transfer function (or *impedance*) – linking input waves to the DOF responsible for energy conversion – conditions the influence of wave groupiness on the mean production. Therefore, as soon as the WEC is *tuned* to the incident waves' frequency interval, its behaviour is expected to be significantly correlated with the bandwidth of the corresponding wave spectrum. Parameters like ε_0, for instance, are relevant to account for this dependence, namely within samples

of wave spectra of similar energy periods.

After, one of the wave groupiness method reviewed beforehand (Hilbert envelope) has been applied to the motions and velocity of a linear heaving 1-DOF WEC model: some statistics related to groups of successive power peaks have been formulated and successfully validated against long numerical simulations of the model. This formulation therefore constitutes an interesting theoretical basis for the dimensioning of PTO mechanisms.

When WEC models are refined and require time-domain simulations – due to the introduction of modelling non-linearities –, the mean power figure has to be deterministically estimated in each sea-state in order to approach the probabilistic value, which is not directly computable since the frequency domain is not practicable anymore. Here again, the spectral bandwidth of the wave process plays a capital role; the estimation precision of wave parameters indeed is directly influenced by both bandwidth parameter $\Lambda(Hz)$ and simulation length T: the more Λ and T increase, the more the simulation is representative of the process, and hence, the better the estimation. Similarly for the mean power figure estimation in a given sea-state, whose precision is related to the bandwidth of the WEC's response, itself dependent on that of the waves if both are tuned to each other. Two wave simulation methods have been considered separately: the first one (*method a*) selects both random amplitudes and phases in the Fourier series, while the second (*method b*) – widely adopted in ocean engineering, eventhough the simulated process is not Gaussian anymore – selects random phases only. *Method a* permits to derive estimation results which are consistent with the theoretical dispersions, whereas *method b* reduces the dispersion without inducing any bias in the mean power figure estimations. This has been verified for various models of WECs – linear as well as non-linear – in both theoretical and realistic sea-states (estimated by buoy-measurements). As a consequence, even if *method b* is not consistent with the Gaussian wave-theory, it may be used on purpose to obtain quicker performance estimations such as the mean extracted power in numerical WEC simulations.

Last, two types of capacitive PTO mechanisms have been simulated in time domain, both coupled to the linear heaving WEC-model: the one as a flywheel system that filters the peaks of instantaneous extracted power, and the second as a short-term energy storage reservoir with nominal output power. The inertia induced by the capacitive system indeed modifies the correlation of the output power to encountered wave energy groups, which was namely observed in the case of flywheel PTO against the SIWEH wave energy history (among others). Accordingly, these signals seem relevant to identify wave groups in time domain simulations or wave records of finite duration. The second PTO model leads by definition to a binary and intermittent power output, which allows to define a quality factor as the ratio of the cumulated production time over the total simulation length. Such a parameter – naturally subject to wave groupiness influence – has shown to be quite sensitive to the wave simulation method, although it did not appear to be correlated with deterministic groupiness factors such as GF_{SIWEH} when simulating with *method b* (random phases). It then resulted that such deterministic parameters – introduced to characterise wave groupiness – are not relevant for this kind of studies.

In the second part, both the uni- and multimodal sea-state representations were presented in order to emphasize the refinements brought by the multi-system description of the sea conditions. First, the relevance of the unimodal representation, which is commonly adopted in many offshore engineering and naval architecture design purposes, was questionned by comparing the long-term energy production of a linear directional WEC obtained from both the exact directional wave spectra $E(f, \theta)$ (possibly multipeaked) and their unimodal representation $S(f, \theta)$ (one single shape-fixed spectral peak). This study – among others – has shown that the approximation induced by the unimodal sea-state modelling is too significant to go ahead in WEC design without improving the representation (Chapter 4).

A brief review of wave systems extraction methods in both directional and omnidirectional wave spectra has been made, along with the main methods aiming at identifying and tracking the time coherent systems, after reduction to a state matrix containing the wave system's descriptive parameters – which in turn enables to reconstruct the original spectrum. These methods were illustrated thanks to the Matlab application SPOP, developped at IFREMER Brest centre, which allows for automatically executing these successive tasks on directional spectra time histories, up to the building of refined wave climatologies including joint swell and wind-sea occurrences (Chapter 5).

As it is unavoidable to loose information when tracking wave systems in time at punctual locations, an attempt of extending the correlation analysis to time and space has been made. To this aim, basic geostatistical tools (namely variographic analysis, through the use of co-variograms) were implemented to deal with the space and time coherence of homogeneous swell and wind-sea sea-state components. The proposed algorithm was applied to sets of wave systems extracted by SPOP from WWIII directional wave spectra in a few neighbouring sea points in the Bay of Biscay and near Yeu Island in France (Chapter 6).

The third part of this thesis illustrated the proposed refinements for the sea-state description in various long-term WEC performance studies applied to some particular devices. The annual mean power output by several linear WEC configurations in two locations (Portugal and North Sea) was figured out, from three-entries joint occurrence tables (wave height/period/spectral bandwidth) convoluted with corresponding power matrices, which were obtained by modelling the representative sea-states in each cell as a unimodal shape-variable spectrum (with the aid of Q_p-spectra). The results showed that clear estimation improvements could be obtained in both wave climates when taking the spectral bandwidth characteristic into account, namely through parameters ε_0 or ε_1 (Chapter 7).

Last, the SEAREV WEC (ECN) has been simulated in time domain (non-linear 3D simulator) in nine climatic sequences – exhibiting wave systems to which the device is particularly sensitive – during one month in a Californian location. The performance

results (mean output power and related capture width) were compared to spectral bandwidth parameters calculated on both the whole spectral density and the *active* wave partition. It has been observed that: first, the WEC's capture width is in general highly correlated to global spectral bandwidth parameters such as Q_e and Q_p, Λ, κ, among others, and even more when the active partition matches the response frequency interval of the device: in such cases, the multi-system description is therefore not necessarily required; second, it has been found that the correlation was poor when comparing the performance figures to the active partitions' spectral bandwidth characteristics; however, a nice agreement has been found between the mean power output and the partition's wave power in each sea-state, which suggests that the multi-system analysis brings a precious information from this point of view (Chapter 8).

As a conclusion, it seems evident that characterising the spectral shape of sea-states – as spectral bandwidth and wave groupiness – is capital for wave-energy purposes. The sensitivity of WECs to that characteristic has been clearly emphasized throughout this work. Accordingly, when no finer wave data are available, it may be sufficient to consider main global wave parameters like significant wave height (energy), mean period (frequency localisation), spectral bandwidth (wave groupiness), and possibly mean wave direction, in short and long-term WEC performance studies, as soon as the main wave frequencies match the device's response and the WEC is not too sensitive to wave directionality.

However, it seems also manifest that, as well as the sea-states are governed by an underlying spatiotemporal coherence through mutual wave systems interactions, these are expected to equally induce some time coherence in the mean production of WECs (deployed as single units or arrays). From this point of view, it is lively encouraged to develop and promote the multi-system analysis in wave-energy studies, for it brings a very fine metocean information on the most likely wave events occurring locally: such a knowledge may be of a major interest in the future, namely for WECs performance and survivability purposes.

In the end of this thesis, several axes of further work may be envisioned, among which:

- applying the multi-system approach in WEC design studies, especially for devices extremely sensitive to wave directionality, and more particularly for wave farms, whose both configuration and orientation optimisation represent a crucial challenge for developpers;
- applying the method of spatiotemporal analysis presented in this work to real spectral data (*in situ* buoys networks), and observing the spatial variations of each identified wave structure;
- thanks to the previously acquired knowledge, improving the prevision of WEC performance at short-term through a better statistical prevision of local sea states from the available surrounding spatial information (transfer functions offshore/nearshore, etc.).

Part IV

Appendices

Appendix A

Spectral bandwidth parameters

This appendix presents some spectral parameters found in the literature related to the spectral bandwidth of sea-states. Each parameter is reviewed, starting with a brief historical introduction, and followed by the mathematical formulation along with the theoretical limits of application.

A.1 The spectral bandwidth of literature

Spectral width parameter ε_4 (Cartwright and Longuet-Higgins)

This parameter – also known as "ε" – was introduced by Cartwright and Longuet-Higgins (Cartwright and Longuet-Higgins, 1956). It is probably one of the very first parameters that were proposed in offshore engineering, and is expressed as

$$\varepsilon_4 = \varepsilon = \sqrt{1 - \left(\frac{N_v}{N_{max}}\right)^2} \tag{A.1}$$

where N_v denotes the number of upcrossing waves and N_{max} the number of local maxima in a wave record $\eta(t)$. For a very narrow-banded wave signal (almost monochromatic wavetrain), both numbers tend to be equal so that ε_4 tends to zero. On the contrary, for a very broad-banded signal, the number of maxima is likely to be much higher than the number of waves, so that ε_4 tends to 1. Assuming $\eta(t)$ is Gaussian, one can show (Ochi, 1988) that – from the joint probability density of its first and second derivatives – this parameter is approached by

$$\varepsilon_4 = \sqrt{1 - \frac{m_2^2}{m_0 m_4}} \tag{A.2}$$

As one can see, one of the major drawbacks of such a parameter is its dependency to high-order spectral moments ($2^{nd}$and 4th), which makes it very sensitive to the high-frequency contents of the wave spectrum. For this reason, it is little used in practice.

Narrowness parameter ε_2 or ν (Longuet-Higgins)

This parameter was proposed by Longuet-Higgins (Longuet-Higgins, 1984) to derive wave group statistics in narrow-banded sea-states. Its formulation is very similar to parameter ε_4, yet involving spectral moments up to 2nd-order only. It is indeed expressed as

$$\varepsilon_2 = \nu = \sqrt{\frac{m_0 m_2}{m_1^2} - 1} \tag{A.3}$$

Longuet-Higgins recommends to filter the spectrum in $[0.5f_p; 1.5f_p]$ before computing the parameter in order to obtain statistics related to the most energetic part of the process – not distorted by low- and high-frequency components. Let us add that a straighforward spectral interpretation can be provided about ε_2, which is basically linked to the spectral density's standard deviation calculated as followed. The mean frequency of the density is

$$\begin{aligned} \bar{f} = f_{01} = T_{01}^{-1} &= \mathrm{E}\left[f\right] \\ &= \frac{1}{m_0}\int_0^\infty fE(f)df \\ &= \frac{m_1}{m_0} \end{aligned} \tag{A.4}$$

Then, its variance may be written

$$\begin{aligned} \sigma_f^2 = \mathrm{E}\left[(f-\bar{f})^2\right] &= \mathrm{E}\left[f^2\right] - \bar{f}^2 \\ &= \frac{m_2}{m_0} - \left(\frac{m_1}{m_0}\right)^2 \\ &= \left(\frac{m_1}{m_0}\right)^2 \cdot \left(\frac{m_0 m_2}{m_1^2} - 1\right) \\ &= \bar{f}^2 \varepsilon_2^2 \end{aligned} \tag{A.5}$$

hence

$$\varepsilon_2 = \frac{\sigma_f}{\bar{f}} \tag{A.6}$$

Parameter ε_0 (Mollison)

In the same way, the relative standard deviation of period spectral density $E(T)$ ($T = 1/f$) may be derived from the equality

$$E(T) = E(f) \cdot \left| \frac{\mathrm{d}f}{\mathrm{d}T} \right| = \frac{E(f = 1/T)}{T^2} \tag{A.7}$$

The advantage of representing the wave spectral density against period instead of frequency is that the high-frequency cut-off issue may be disregarded, for it becomes a low-bound cut-off period. Furthermore, the period density generally looks more symmetrical than the frequency density, so that calculating the standard deviation seems more meaningful is that case. The influence of high-frequencies may then reappear in low-frequency (or high periods); most of the time yet, the density $E(T)$ tends to zero faster as T increases than $E(f)$ does as f increases, as depicted in figures A.1(a&b) (Bretschneider spectrum). The bandwidth parameter referred to here is expressed as

$$\varepsilon_0 = \sqrt{\frac{m_0 m_{-2}}{m_{-1}^2} - 1} \tag{A.8}$$

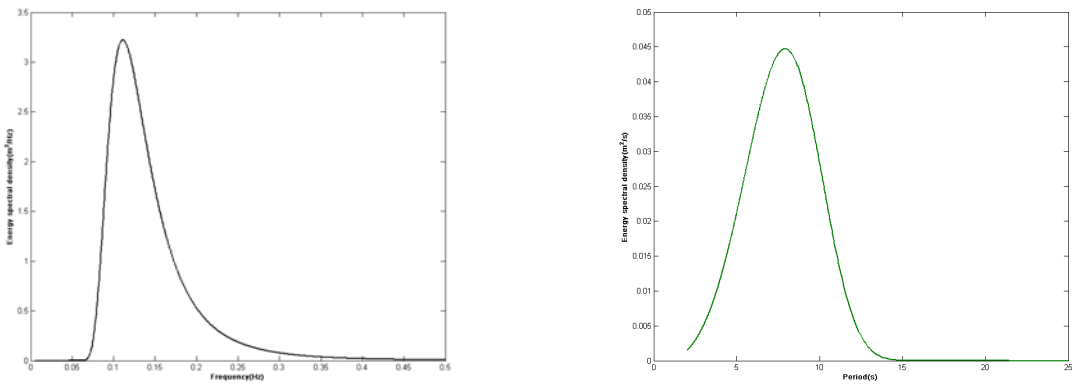

(a) (b)

Figure A.1: Energy spectral density of water elevation (Bretschneider spectrum) against frequency (a) and period (b).

Indeed, the spectrum's mean period is

$$\bar{T} = \frac{m_{-1}}{m_0} = T_{-10} = T_e \tag{A.9}$$

which yields for the density's variance

$$\begin{aligned}\sigma_T^2 &= \left(\frac{m_{-1}}{m_0}\right)^2 \cdot \left(\frac{m_0 m_{-2}}{m_{-1}^2} - 1\right) \\ &= T_e^2 \varepsilon_0^2 \end{aligned} \tag{A.10}$$

that is

$$\begin{aligned}\varepsilon_0 &= \frac{\sigma_T}{\overline{T}} \\ &= \frac{\sigma_T}{T_e} \end{aligned} \tag{A.11}$$

This parameter – much more stable that ε_2 – was proposed by Mollison (1985) in the aim of describing the bandwidth properties of sea-states for wave energy resource purposes. The same author also recommended the standard use of energy period parameter T_e $(= T_{-10})$ for wave climatology. This parameter – widely adopted now in wave-energy studies – is therefore equally referred to with both notations in this report. From the period standard deviation σ_T, an equivalent frequency figure may be obtained as

$$\sigma_T\,[Hz] = \frac{\sigma_T\,[s]}{T_e^2} = \frac{\varepsilon_0 T_e}{T_e^2} = \frac{\varepsilon_0}{T_e} \tag{A.12}$$

From there on, it is immediate that any bandwidth parameter with spectral formulation of type $\sqrt{\frac{m_{n1}m_{n2}}{m_{n1+n2/2}^2} - 1}$ or $\sqrt{1 - \frac{m_{n1+n2/2}^2}{m_{n1}m_{n2}}}$ are potentially expected to characterise the spectrum's bandwidth adequately, at least for those which involve low-order moments (i.e. such as $|n| \leq 2$). For instance, a new parameter – denoted here by ε_1 – is introduced in Smith et al. (2006) for characterising the wave energy resource, defined as

$$\varepsilon_1 = \sqrt{\frac{m_1 m_{-1}}{m_0^2} - 1} \tag{A.13}$$

Peakedness factor Q_p (Goda)

This factor has been proposed by Goda (1970) to characterise the sharpness (or *peakedness*) of the spectrum's main peak, and consequently, the spectral width and wave groupiness somehow. Wave groups become indeed more pronounced as the spectrum's peakedness increases. The mathematical formulation of this factor is

$$Q_p = \frac{2}{m_0} \int_0^\infty f E^2(f)\,\mathrm{d}f \tag{A.14}$$

Obviously, such a parameter only makes sense when calculated on unimodal spectra (one peak); otherwise, its physical meaning is invaluable. Ewing (1973) and Goda (1976) observed from both wave numerical simulations and measured wave records that peakedness factor Q_p was directly proportional to the mean group length of successive wave heights. A fully developped sea spectrum (Pierson-Moskowitz/Bretschneider) corresponds to a Q_p around 2, whereas swell peaks typically exhibit much higher values of Q_p.

Peakedness factor Q_e (Medina et Hudspeth)

This new peakedness factor – very similar to Q_p – was used by Medina and Hudspeth (Medina and Hudspeth, 1987) to control the variance variability of numerically simulated wave processes. Its expression is

$$Q_e = \frac{2m_1}{m_0^3} \int_0^\infty E^2(f)\,\mathrm{d}f \tag{A.15}$$

Equivalent spectral bandwidth Λ (Blackman and Tukey)

Medina and Hudspeth (1987) indicate their factor Q_e (Eq. (A.15)) is linked to the inverse of the equivalent spectral bandwidth (Hz) introduced long before by Blackman and Tukey (1959) and here denoted by Λ

$$\Lambda = \frac{m_0^2}{\int_0^\infty E^2(f)\,\mathrm{d}f} = \frac{2m_1}{m_0} \cdot \frac{1}{Q_e} = \frac{2\bar{f}}{Q_e} = \frac{2\left(\varepsilon_1^2+1\right)}{T_{-10}Q_e} \tag{A.16}$$

The sharper the peak, the higher Q_e and the less spectral bandwidth Λ.

Correlation parameter κ (Battjes and Van Vledder)

In view of computing the correlation coefficient of successive wave heights in a signal without requiring wave-by-wave analysis – namely when implementing Kimura's method (Kimura, 1980) to draw wave group statistics –, Battjes and Van Vledder (Battjes and van Vledder, 1984) proposed a spectral parameter derived from previous works of Arhan and Ezraty (Arhan and Ezraty, 1978) (among others), which depends on a mean wave lag τ (in s, thus, a mean wave period) and arbitrarily taken equal to *zuc* mean wave period $T_{02} = \sqrt{m_0/m_2}$, as

$$\kappa = \kappa(\tau) = \frac{1}{m_0} \left| \int_0^\infty E(f) e^{2i\pi f\tau}\,\mathrm{d}f \right| \tag{A.17}$$

This parameter comes as close to its experimental value (i.e. measured in the wave record) as the wave process is narrow-banded, which means that the waves are more correlated to each other.

Bandwidth parameter B_w (Prevosto)

For studying the influence of wave groupiness and low-frequency excitations of floating structures, Prevosto (Prevosto, 1988) introduces a spectral bandwidth parameter B_w (Hz) whose expression is

$$\begin{aligned} B_w &= \frac{4}{m_0^2} \int_0^\infty E^2(f) \left(f - \bar{f}\right)^2 \mathrm{d}f \\ &= \frac{4}{m_0^2} \int_0^\infty E^2(f) \left(f - \frac{m_1}{m_0}\right)^2 \mathrm{d}f \end{aligned} \tag{A.18}$$

which is related to the shape of the wave signal's envelope spectrum. Out of the fact it is a dimensional parameter (Hz) as Λ, this parameter differ from all others by its independence to the frequency location of the peak. Thus, its value remains almost unchanged by translating the spectrum along the frequency axis.

A.2 Influence of spectral density smoothing on the numerical value of spectral parameters

The energy spectral density of water elevation requires the computation of a Fourier transform, either that of elevation signal $\eta(t)$, or that of autocorrelation function $R(\tau)$. The spectral estimates therefore are discretised in the frequency vector $(f_i)_{1 \leq i \leq N_f}$ as $(E_i)_{1 \leq i \leq N_f}$, where N_f denotes the total number of frequencies (and whose highest component must be inferior to the Nyquist frequency). The gross estimation mostly exhibit important noise, so that a smoothing procedure is often required to obtain a better visualisation of the measured process. Several smoothing methods exist, which are essentially the block spectral analysis (or "periodogram" method) and moving-average spectral smoothing (see Tucker et al., 1984). This latter – much easier to carry out – smoothes the spectral estimates by averaging them with neighbouring values, so that the resulting smoothed shape may slightly differ from the original process. The block spectral analysis – more complex to implement – consists in dividing the original wave record into K possibly overlapping blocks $\eta_i(t)$ $(1 \leq i \leq K)$, whose number of sampling points is a power of 2, and estimating the spectrum by averaging the computed

spectra thanks to Fast Fourier Transforms (FFT) of each one of the K blocks. Both methods are based on the stationarity assumption (in time) of signal $\eta(t)$. In the end, each spectral estimate E_i at frequency f_i represents a mean of raw estimations. Either by applying a m-points moving-average smoothing on the raw spectrum, or performing a K-blocs spectral anaysis, the resulting spectrum's number of degrees of freedom will be $\nu = 2m = 2K$. According to linear theory indeed, a Gaussian wave random signal is characterised by normally-distributed Fourier coefficients $(a_i)_{1\leq i\leq N_f}$ and $(b_i)_{1\leq i\leq N_f}$. The raw spectral estimation E_i is proportional to $a_i^2 + b_i^2$ and hence is χ^2-distributed with 2 degrees of freedom. The smoothed density therefore is χ^2-distributed with a number of degree of freedom equal to twice the number of estimations required for the smoothing. The more the degrees of freedom, the better and the more accurate the final spectral estimation. When using moving-average smoothing, it is assumed yet that the frequency bins are sufficiently small – that is, the signal is sufficiently long – to allow for a large number of degrees; simulatenously, m must be chosen in accordance with the width of the smoothing window. Similarly for the block spectral analysis, if the number of blocks K is too large, each portion of signal – not representative of the process – results in very inaccurate spectral estimations. Last, the signal cannot be too long (several hours), for the stationarity assumptions might not hold anymore.

According to the accuracy of the spectral estimates (degrees of freedom), the numerical estimation of spectral parameters may be biased (see Elgar et al., 1985). This can be shown by decomposing the gaussian signal $\eta(t)$ into the Fourier series

$$\eta(t) = \sum_{i=1}^{N_f} a_i cos(2\pi f_n t) + b_i sin(2\pi f_n t) \tag{A.19}$$

Amplitudes a_i and b_i are two independent random variables with zero-mean and same variance $S_i \Delta f_i$, where S_i denotes the exact value of the spectrum at frequency f_i, and Δf_i the corresponding frequency bin. From a signal measured on a finite duration, only an estimation $E(f)$ of $S(f)$ can be derived, that is, estimators $(\tilde{a}_i)_{1\leq i\leq N_f}$ and $(\tilde{b}_i)_{1\leq i\leq N_f}$ of target amplitudes $(a_i)_{1\leq i\leq N_f}$ and $(b_i)_{1\leq i\leq N_f}$ respectively. Then, the random variable

$$\tilde{Z}_i^2 = \frac{\tilde{a}_i^2 + \tilde{b}_i^2}{S_i \Delta f_i} \tag{A.20}$$

is found to be χ^2-distributed with 2 degrees of freedom, whose probability density is such that $\forall x \in \mathbb{R}_+^*$,

$$f_{\chi^2}(x) = \frac{1}{2^{\nu/2}\Gamma(\nu/2)} \cdot x^{\nu/2-1} e^{-x/2} \tag{A.21}$$

where $\nu = 2$, and whose mean value is ν. Since the spectral estimator may be written (Parseval's theorem)

$$E_i = \frac{\tilde{a}_i^2 + \tilde{b}_i^2}{2\Delta f_i} \tag{A.22}$$

it is straightforward to show that the expectation of the spectral moment estimator $\tilde{m}_n$ is

$$\begin{aligned} E\left[\tilde{m}_n\right] &= E\left[\sum_{i=1}^{N_f} f_i^n \cdot \frac{\tilde{a}_i^2 + \tilde{b}_i^2}{2\Delta f_i} \cdot \Delta f_i\right] = E\left[\sum_{i=1}^{N_f} f_i^n \cdot \frac{\tilde{Z}_i^2 S_i \Delta f_i}{2\Delta f_i} \cdot \Delta f_i\right] \\ &= \frac{1}{2} \cdot \sum_{i=1}^{N_f} f_i^n \cdot E\left[\tilde{Z}_i^2\right] \cdot S_i \Delta f_i \\ &= \frac{\nu}{2} \cdot \sum_{i=1}^{N_f} f_i^n \cdot S_i \Delta f_i \equiv \frac{\nu}{2} \cdot \int_0^\infty f^n S(f)\,\mathrm{d}f \\ &= \frac{\nu}{2} \cdot m_n = m_n \end{aligned} \tag{A.23}$$

This mean value, obtained from the raw estimated spectral density $E(f)$ (with 2 degrees of freedom) of target spectrum $S(f)$ therefore is unbiased. This is still true for smoothed densities, for which $\nu = 2k$ $(k > 1)$, since

$$E_i = \frac{1}{k} \cdot \sum_{j=1}^{k} \frac{\tilde{a}_i^2 + \tilde{b}_i^2}{2\Delta f_i} \tag{A.24}$$

Then, the random variable

$$\tilde{Z}_i^2 = \sum_{j=1}^{k} \frac{\tilde{a}_{ij}^2 + \tilde{b}_{ij}^2}{S_i \Delta f_i} \tag{A.25}$$

is logically χ^2-distributed with $\nu = 2k$ degrees of freedom and mean equal to $2k$. This yields for the spectral moment estimator

$$\begin{aligned} E\left[\tilde{m}_n\right] &= E\left[\sum_{i=1}^{N_f} f_i^n \cdot \frac{1}{k} \cdot \sum_{j=1}^{k} \frac{\tilde{a}_{ij}^2 + \tilde{b}_{ij}^2}{2\Delta f_i} \cdot \Delta f_i\right] = E\left[\sum_{i=1}^{N_f} f_i^n \cdot \frac{\tilde{Z}_i^2 S_i \Delta f_i}{2k\Delta f_i} \cdot \Delta f_i\right] \\ &= \frac{1}{2k} \cdot \sum_{i=1}^{N_f} f_i^n \cdot E\left[\tilde{Z}_i^2\right] \cdot S_i \Delta f_i \\ &= \frac{\nu}{2k} \cdot \sum_{i=1}^{N_f} f_i^n \cdot S_i \Delta f_i \equiv \frac{\nu}{2k} \cdot \int_0^\infty f^n S(f)\,\mathrm{d}f \\ &= \frac{\nu}{2k} \cdot m_n = m_n \end{aligned} \tag{A.26}$$

Accordingly, any spectral parameter calculated with estimated spectral moments (i.e. computed on estimated wave spectra) exclusively is unbiased with respect to the real value of the process, whatever the level of smoothing. This is namely the case for

wave parameters H_{m0}, T_{02}, T_{-10}, T_{01}, ε_0, ε_1, ε_2, $\varepsilon_4 \ldots$

Now, let us investigate the case of other spectral parameters, and more particularly those based on the square of the spectrum, like e.g. Q_p. First, let us notice the expectation of the square of a random χ^2-distributed variable with ν degrees of freedom is $\nu^2 + 2\nu$ (Elgar et al., 1985). If one considers an estimated spectral density with $\nu = 2k$ degrees of freedom, the expectation of estimator $\tilde{Q}_p$ is

$$\begin{aligned} E\left[\tilde{Q}_p\right] &= E\left[\frac{2}{m_0^2} \cdot \sum_{i=1}^{N_f} f_i \cdot \left(\frac{1}{k} \cdot \sum_{j=1}^{k} \frac{\tilde{a}_{ij}^2 + \tilde{b}_{ij}^2}{2\Delta f_i}\right)^2 \cdot \Delta f_i\right] \\ &= E\left[\frac{2}{m_0^2} \cdot \sum_{i=1}^{N_f} f_i \cdot \frac{S_i^2}{4k^2} \cdot \left(\frac{\tilde{a}_{ij}^2 + \tilde{b}_{ij}^2}{S_i \Delta f_i}\right)^2 \cdot \Delta f_i\right] \\ &= \frac{2}{m_0^2} \cdot \sum_{i=1}^{N_f} f_i \cdot \frac{S_i}{4k^2} \cdot \left((2k)^2 + 4k\right) \cdot \Delta f_i \equiv \frac{4k^2 + 4k}{4k^2} \cdot Q_p \\ &= \left(1 + \frac{1}{k}\right) \cdot Q_p = \left(1 + \frac{2}{\nu}\right) \cdot Q_p \end{aligned} \tag{A.27}$$

If no smoothing is carried out on the raw spectral density (i.e., if $\nu = 2$), the mean value of estimator $\tilde{Q}_p$ is equal to twice the exact value of parameter Q_p. In other terms, when estimating Q_p, the numerical value is always biased (and overestimated). Now, if the smoothing is sufficient (typically $\nu > 20$ to ensure less than a 10% error), the estimator will tend to the real value of the process. The same holds for parameters Q_e, Λ^{-1} and B_w. As far as parameter κ is concerned, its estimation might not be biased a priori for the integral in equation (A.17) does not involve squared spectra.

A.3 Influence of high-frequency cut-off on the numerical value of spectral parameters

When comparing several spectral parameters with each other, the stability against the cut-off high-frequency may be a crucial argument for retaining or discarding them. Some of them may be particularly sensitive to the high-frequency contents, namely those that are based on high-order spectral moments. The low-frequency cut-off may be less problematic because the wave spectral densities generally decrease rapidly as frequency goes to zero. Rye (1977) presented a stability study involving several parameters, like H_{m0}, T_{02}, T_{10}, ε_4, and ε_2, which were computed on JONSWAP-like spectral shapes of various peakednesses. From Hasselmann et al. (1973), these spectra are formulated as

$$S(f) = \frac{\alpha_P g^2}{(2\pi)^4 f^5} \cdot e^{-\frac{5}{4}\left(\frac{f}{f_p}\right)^{-4}} \cdot \gamma^{e^{\frac{(f-f_p)^2}{2\sigma^2 f_p^2}}} \tag{A.28}$$

where α_P is the Phillip's constant, f_p the peak frequency, γ the peak enhancement factor (1 to 7), and σ a bandwidth parameter such that $\sigma = \sigma_a$ for $f < f_p$ and $\sigma = \sigma_b$ for $f > f_p$. When $\gamma = 1$, the JONSWAP spectrum becomes equivalent to a Pierson-Moskowitz spectrum (Pierson and Moskowitz, 1964) which characterise a fully developped wind-sea. Higher enhancement values like 3.3 and 7 respectively correspond to the mean and maximal values observed during the campaign in the North Sea, which characterise different levels of sea growth. The three spectral shapes used by Rye are depicted in figure A.2 against dimensionless frequency $f^* = f/f_p$

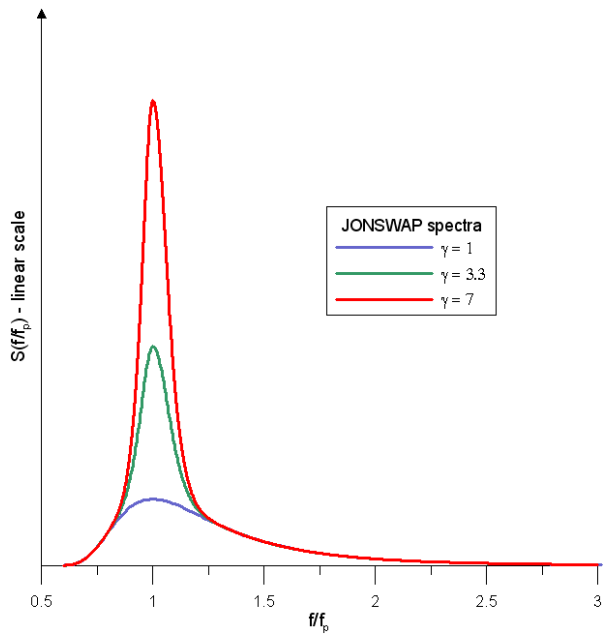

Figure A.2: JONSWAP spectra used by Rye (1977).

The same approach is lead here – with identical spectra – and applied to the bandwidth parameters listed previously in this appendix. The dimensioning parameters of the three JONSWAP shapes are given in Table A.1.

The stability results are plotted in figures A.3(a-e) for parameters ε_4, ε_2, ε_1, ε_0 and κ respectively on the one hand, and in figures A.4(a-d) for parameters Q_p, Q_e, B_w and Λ respectively on the other hand.

Among the "ε"-like parameters, it clearly appears that ε_0 is the most stable and the most able to characterise the three different bandwidths. On the contrary, ε_4 hardly converges to its asymptotic value and seems totally unable to reproduce the nuances of bandwidth. Intermediary parameters ε_2 and ε_1 logically lie in between. Then, correlation parameter κ is found to be extremely stable: the convergence is indeed almost

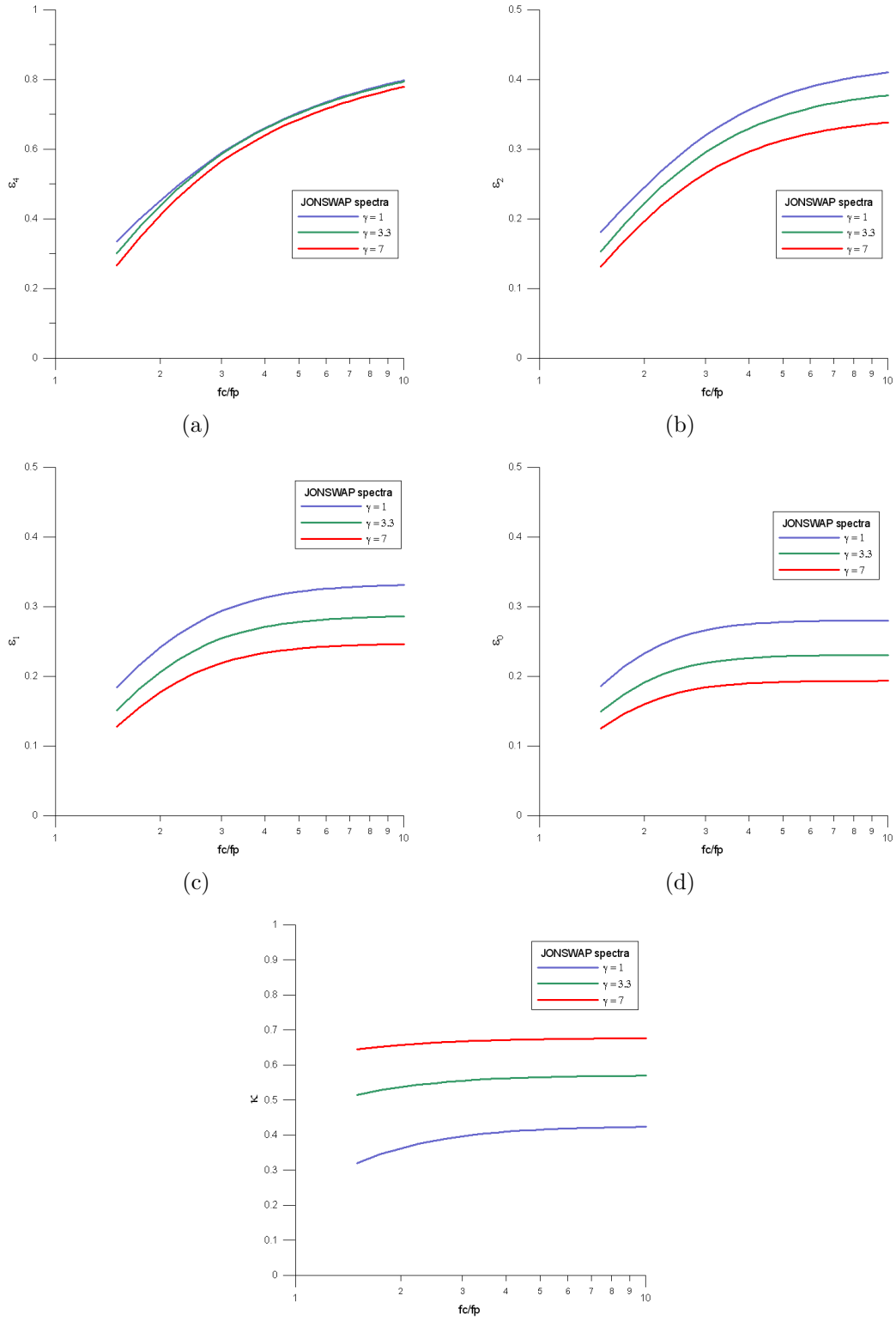

Figure A.3: Stability of parameters ε_4(a), ε_2(b), ε_1(c), ε_0(d) and κ(e) to cut-off high-frequency (non-dimensionalised by peak frequency, in logarithmic scale) calculated on the JONSWAP spectra depicted in figure A.2.

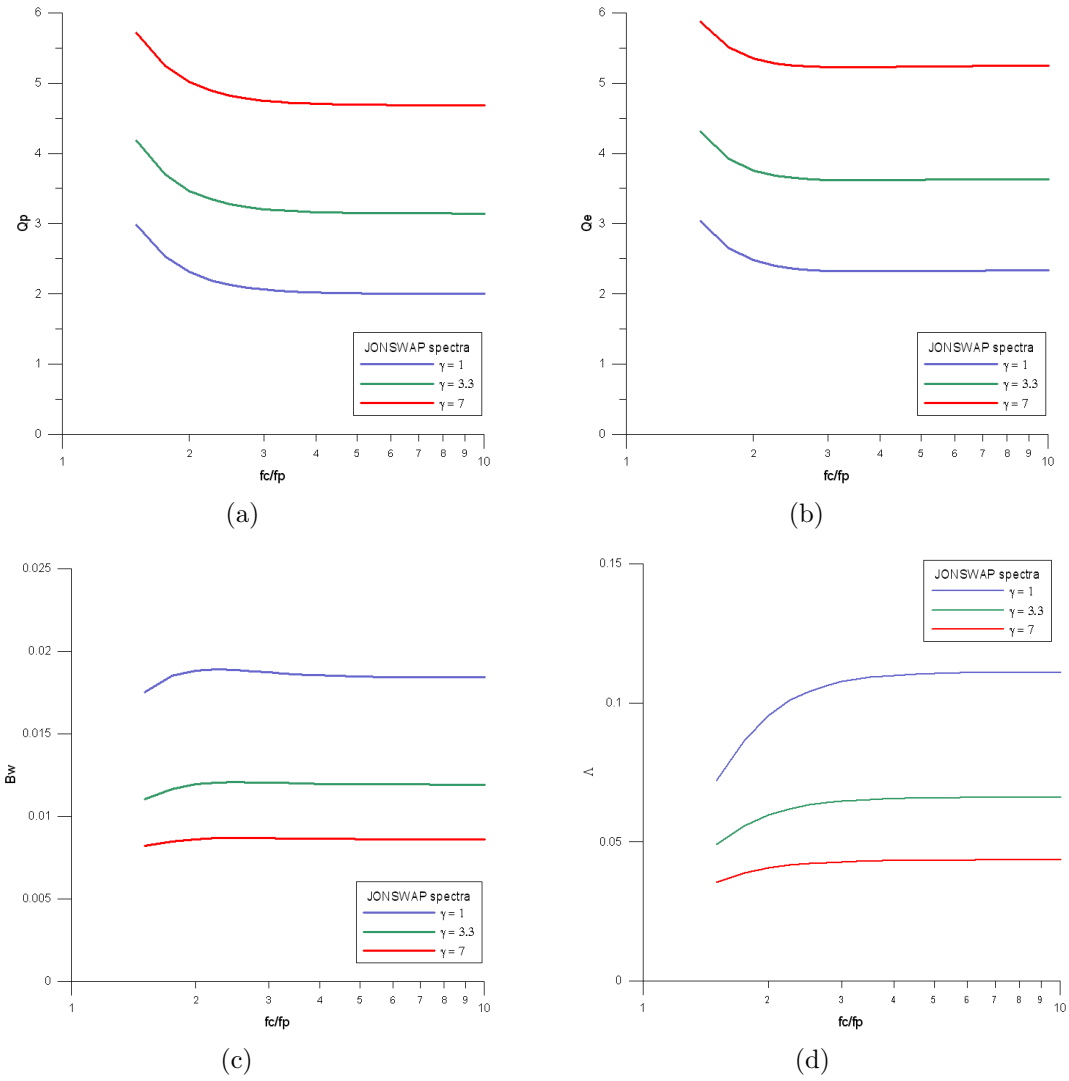

Figure A.4: Id. Fig. A.3 for parameters Q_p(a), Q_e(b), B_w(c, in Hz) and Λ(d, in Hz).

Table A.1: Characteristics of the JONSWAP spectra depicted in figure A.2.

Parameter	**Value**
α_P	0.0081
f_p	0.10 Hz
γ	1, 3.3 et 7
σ_a	0.07
σ_b	0.09

instantaneously reached for the narrowest spectrum ($\gamma = 7$, red line). The four last parameters Q_p, Q_e, B_w and Λ are also stable according to these plots, and the asymptotic value is reached for $f_c/f_p < 3-4$. Yet, let us notice the particularity of parameter B_w, whose trends are not absolutely monotonic and exhibit a slight maximum before convergence. Last, it is of interest to remark that the decreases observed for peakedness parameters Q_p and Q_e seems independent of the spectral shape, contrary to all other spectral width parameter so far.

Appendix B

Note on the Fourier series decomposition of the water elevation signal

B.1 Fourier series of the water elevation signal

Let $\eta(t)$ be a real zero-mean signal defined and integrable over $[0;T]$. Assuming its Fourier transform exist, it is noted (see Eq. (2.2))

$$\begin{aligned}\mathcal{F}\{\eta(t)\}(\omega) &= \int_0^T \eta(t)e^{-i\omega t}\,\mathrm{d}t \\ &= \int_0^T \eta(t)\left[cos\left(\omega t\right) + isin\left(\omega t\right)\right]\,\mathrm{d}t\end{aligned}$$

This signal may be decomposed into a Fourier series, as

$$\eta(t) = A_0 + \sum_{p=1}^{\infty} A_p cos\left(\omega_p t\right) + B_p sin\left(\omega_p t\right) \tag{B.1}$$

where A_p and B_p are the real Fourier coefficients associated to circular frequency $\omega_p = p * \omega_0 = \frac{2\pi}{T}$, and calculated as

$$A_p = \frac{2}{T}\int_0^T \eta(t)cos\left(\omega_p t\right)\,\mathrm{d}t \quad ,\forall p \in \mathbb{N}_+ \tag{B.2}$$

$$B_p = \frac{2}{T}\int_0^T \eta(t)sin\left(\omega_p t\right)\,\mathrm{d}t \quad ,\forall p \in \mathbb{N}_+^* \tag{B.3}$$

As the signal is defined as zero-mean, this immediately yields $A_0 = 0$. The signal may alternatively be decomposed into a series involving complex coefficients, as

$$\eta(t) = \sum_{p=-\infty}^{\infty} C_p e^{i\omega_p t} \tag{B.4}$$

where coefficients $C_p \in \mathbb{C}$ are calculated as

$$C_p = \frac{1}{T}\int_0^T \eta(t) e^{-i\omega_p t}\,\mathrm{d}t \tag{B.5}$$

with $C_0 = A_0/2 = 0$, and where the negative circular frequencies are such that $\omega_{-p} = -\omega_p$. Hence $C_{-p} = C_p^*$, which denotes the complex conjugate of C_p, the signal being real. After some algebra from expression (B.4), it yields

$$\begin{aligned}\eta(t) &= C_0 + \sum_{p=1}^{\infty} C_p e^{i\omega_p t} + C_{-p} e^{-i\omega_p t} \\ &= 0 + \sum_{p=1}^{\infty} 2Re\left[C_p e^{i\omega_p t}\right] \\ &= \sum_{p=1}^{\infty} 2\left|C_p\right| cos\left(\omega_p t + arg\left(C_p\right)\right)\end{aligned}$$

Remarking that $C_p = \frac{1}{2}\left(A_p - iB_p\right)$ and letting $\eta_p = 2\left|C_p\right| = 2\sqrt{A_p^2 + B_p^2}$ and $\varphi_p = arg\left(C_p\right) = -atan2\left(A_p, B_p\right)$ (Fortran90 command), the simplified and well-known formulation of the signal is found, as

$$\eta(t) = \sum_{p=1}^{\infty} \eta_p cos\left(\omega_p t + \varphi_p\right) \tag{B.6}$$

Expressed in function of the signal's Fourier transform, these coefficients may be written

$$A_p = \frac{1}{T}\cdot\left[\mathcal{F}\{\eta(t)\}(\omega_p) + \mathcal{F}^*\{\eta(t)\}(\omega_p)\right] \tag{B.7}$$

$$B_p = -\frac{i}{T}\cdot\left[\mathcal{F}\{\eta(t)\}(\omega_p) - \mathcal{F}^*\{\eta(t)\}(\omega_p)\right] \tag{B.8}$$

$$C_p = \frac{1}{T}\cdot\mathcal{F}\{\eta(t)\}(\omega_p) \tag{B.9}$$

$$\eta_p = \left|A_p - iB_p\right| = 2\left|C_p\right| = \frac{2}{T}\cdot\left|\mathcal{F}\{\eta(t)\}(\omega_p)\right| \tag{B.10}$$

The Parseval's theorem applied to signal $\eta(t)$ in $[0;T]$ is expressed as

$$\int_0^\infty \eta^2(t)\,\mathrm{d}t = \frac{1}{2\pi}\int_{-\infty}^{\infty} \left|\mathcal{F}\{\eta(t)\}(\omega)\right|^2 \mathrm{d}\omega \tag{B.11}$$

or, after discretisation,

$$\int_0^\infty \eta^2(t)\,\mathrm{d}t \equiv \frac{1}{2\pi}\sum_{p=-\infty}^{\infty} \left|\mathcal{F}\{\eta(t)\}(\omega_p)\right|^2 \Delta\omega_p \tag{B.12}$$

where $\omega_p = 2\pi\Delta f = 2\pi/T$. Since $|\mathcal{F}\{\eta(t)\}(\omega_p)| = T\,|C_p|$, $|C_{-p}| = \left|C_p^*\right| = |C_p|$, and $C_0 = 0$, this equality leads after some algebra to

$$\int_0^\infty \eta^2(t)\,\mathrm{d}t \equiv T\sum_{p=1}^{\infty}\frac{\eta_p^2}{2}$$

that is,

$$\frac{1}{T}\int_0^\infty \eta^2(t)\,\mathrm{d}t = \overline{\eta^2(t)} = var\left[\eta(t)\right] \equiv \sum_{p=1}^{\infty}\frac{\eta_p^2}{2} \tag{B.13}$$

$$\equiv \sum_{p=1}^{\infty} S(\omega_p)\Delta\omega_p \tag{B.14}$$

where spectral density $S(\omega_p)$ corresponding to harmonic p is defined such as

$$S(\omega_p)\Delta\omega_p = \frac{\eta_p^2}{2} \tag{B.15}$$

Hence

$$S(\omega_p) = \frac{2}{T}\left|\mathcal{F}\{\eta(t)\}(\omega_p)\right|^2 \tag{B.16}$$

B.2 Gaussian signal simulation from spectral data

It is possible to simulate a random Gaussian signal $\eta(t)$ from a discretised spectrum $S(f)$ (or $E(f)$ if the spectrum is estimated), which governs the process followed by this

signal. This only requires the calculation of amplitudes A_p and B_p (Eq. (B.1)) or modulus η_p (Eq. (B.6)) and phases φ_p for each frequency component ω_p (or $f_p = 2\pi\omega_p$).

According to linear theory, the wave amplitudes – and, a fortiori, the modulus – have to be randomly selected following certain distributions, in order to reproduce a Gaussian process. This point is namely addressed thoroughly by Tucker et al. (1984). Indeed, the amplitudes are normally distributed with zero-mean and variance equal to $S(\omega_p)\Delta\omega_p$, whereas modulus must be Rayleigh-distributed with the same variance $S(\omega_p)\Delta\omega_p$ while phases are uniformly distributed over $[0; 2\pi]$. In offshore engineering however, the synthesis of wave signals using modulus and phases is simplified to

$$\eta_p = \sqrt{2S(\omega_p)\Delta\omega_p} = \sqrt{2S(f_p)\Delta f_p} \tag{B.17}$$

– which is asymptotically correct as signal length $T \to +\infty$ – while phases still are randomly selected as uniformly distributed variables. Yet, Tucker et al. (1984) recall that such a simplification has some consequences on the simulated process, namely on the wave statistics calculated on the resulting signals. Indeed, the likelihood space is necessarily restrained: for instance, all signals simulated this way will turn out to have the same variance (that of the spectrum, see Parseval's theorem, Eq. (B.14)). This contradicts – or at least limits – the Gaussian nature of the process under consideration. Then, Tucker et al. observe that the distributions of successive wave heights derived from wave records are particularly sensitive to such a simplification. Accordingly, they underline the fact a number of wave groups studies, either lead on numerical simulations or in wave tank experiments, may have resulted in erroneous conclusions by the authors, who did not simulate the wave field properly. Section 3.5 addresses this issue, where both methods – respectively denoted by *method a* (random amplitudes or modulus and phases) and *method b* (random phases only) – are compared to each other when estimating the mean power extracted by WECs. For such studies (see also Olagnon et al., 1990), *method b* is shown to yield unbiased results, so that its use is admissible in some such cases: the power estimator's dispersion is reduced and a precise estimation of the mean power figure is obtained faster.

Practically, the sum in equations (B.1) and (B.6) is truncated at the Nyquist frequency $f_{Nyq} = 1/(2\Delta t)$, which corresponds to a number of terms equal to half of the simulation points (if that number is even). The numerical synthesis of water elevation signals may be carried out very quickly by means of Inverse Fast Fourier Transform ($IFFT$), when the number of frequency components (equal to the number of simulated points) is a power of 2. It is also simple to numerically compute the sum in equation (B.6) up to a certain frequency, above which the energy is assumed to be zero (typically above $0.6Hz$ for wave signals). However, the numerical run time is longer – increasing as T increases – and the resulting signals may not satisfy the Parseval's equality anymore, due to the frequency truncature.

Appendix C

Note on the Q_p-spectra

The "Q_p"-spectra are a generalisation of the Bretschneider spectrum (Bretschneider, 1959), which models a fully developped wind-seas in the frequency domain just as the Pierson-Moskowitz spectrum (the difference lies in the fact the Bretschneider formulation dimensions the spectrum from wave parameters, as H_s and T_p, whereas the Pierson-Moskowitz one is only based on the local wind data, see Pierson and Moskowitz, 1964). As for *JONSWAP* (Hasselmann et al., 1973), the Q_p-spectra are based on three wave parameters which characterise: 1/ the *energy* (spectral significant wave height H_{m0}), 2/ the *frequency localisation* (peak period T_p), and 3/ the spectrum's *peakedness*, which accounts for the frequency spreading (peakedness factor Q_p, see Goda, 1970). The original Bretschneider shape does not include this third degree of freedom and that is why this new formulation is proposed herebelow, as an alternative to JONSWAP spectra (whose peakedness is governed by peak enhancement factor γ), which mainly describes growing wind-seas up to energetic balance ($\gamma = 1$).

In the following, the analytic formulation along with the mathematical expression of the most commonly used wave parameters related to this spectrum are provided. Then, an extension to multimodal sea-states is formulated as the superimposition of individual swells and wind-sea. This is exemplified with the bimodal case, which can be used as an alternative to other well-known analytic models (Ochi and Hubble, 1976; Torsethaugen and Haver, 2004, among others).

C.1 The unimodal Q_p-spectrum

From given spectral significant wave height H_{m0} (in m), peakperiod T_p (in s) and peakedness factor Q_p, the corresponding Q_p spectrum is defined as

$$S_{Q_p}(f) = \frac{H_{m0}^2}{16} T_p (1 + 2Q_p) \frac{e^{-\alpha (f T_p)^{-2Q_p}}}{(f T_p)^{1+2Q_p}} \tag{C.1}$$

where $\alpha = 1 + 1/(2Q_p) = 1 + \delta/2$ and f is wave frequency (in Hz). The particular case $Q_p = 2$ refers to the original Bretschneider shape, that is, a fully developped wind-sea. Swells are mostly characterised by sharp peaks, whose Q_p is greater than 2[1]. Let us now introduce the *Gamma* function, defined as

$$\Gamma : \mathbb{R}_+^* \longrightarrow \mathbb{R} \tag{C.2}$$

$$x \longmapsto \int_0^\infty u^{x-1} e^{-u} \, \mathrm{d}u \tag{C.3}$$

which owns the following properties:

$$\forall n \in \mathbb{N}^*, \Gamma(n) = (n-1)! \tag{C.4}$$

$$\forall x \in \mathbb{R}_+^*, \Gamma(x+1) = x\Gamma(x) \tag{C.5}$$

$$\Gamma(1/2) = \sqrt{\pi} \tag{C.6}$$

Thanks to this function, it becomes straightforward to derive the analytical formulation of the spectral moments

$$m_n = \int_0^\infty f^n S_{Q_p}(f) \, \mathrm{d}f \tag{C.7}$$

$$= \frac{H_{m0}^2}{16} T_p^{-n} \alpha^{\frac{n\delta}{2}} \Gamma\left(1 - \frac{n\delta}{2}\right) \tag{C.8}$$

$$= m_0 T_p^{-n} \alpha^{\frac{n\delta}{2}} \Gamma\left(1 - \frac{n\delta}{2}\right), Q_p > \frac{n}{2} \tag{C.9}$$

since by definition $H_{m0} = 4\sqrt{m_0}$. This therefore yields the various mean wave periods

$$T_{01} = \frac{m_0}{m_1} = \frac{T_p}{\alpha^{\alpha-1}\Gamma\left(1 - \delta/2\right)}, Q_p > \frac{1}{2} \tag{C.10}$$

$$T_{02} = \sqrt{\frac{m_0}{m_2}} = \frac{T_p}{\sqrt{\alpha^\delta \Gamma\left(1 - \delta\right)}}, Q_p > 1 \tag{C.11}$$

$$T_{-10} = \frac{m_{-1}}{m_0} = T_p \frac{\Gamma\left(\alpha\right)}{\alpha^{\alpha-1}} \tag{C.12}$$

[1]Let us stress, however, that this model, unlike other ones proposed in the literature, is not consistent with a f^{-4} or f^{-5} high-frequency tail, which is commonly admitted by oceanographers. Thus, such a model may not always be relevant for physical oceanography applications.

In case $Q_p = 2$ (Bretschneider), this yields

$$T_{01} = 0.7718 \cdot T_p \tag{C.13}$$

$$T_{02} = 0.7104 \cdot T_p \tag{C.14}$$

$$T_{-10} = 0.8572 \cdot T_p \tag{C.15}$$

The peakedness factor Q_p is obviously retrieved when calculating (see Eq. (2.18))

$$Q_p = \frac{2}{m_0^2} \int_0^\infty f S_{Q_p}^2(f)\,\mathrm{d}f \tag{C.16}$$

as well as bandwidth parameters (see Eq. (A.3),(A.8)&(A.13))

$$\varepsilon_0 = \sqrt{\frac{m_0 m_{-2}}{m_{-1}^2} - 1} = \sqrt{\frac{\Gamma\left(1+\delta\right)}{\Gamma^2(\alpha)} - 1} \tag{C.17}$$

$$\varepsilon_1 = \sqrt{\frac{m_{-1} m_1}{m_0^2} - 1} = \sqrt{\Gamma(\alpha)\Gamma\left(1 - \frac{\delta}{2}\right) - 1}, Q_p > \frac{1}{2} \tag{C.18}$$

$$\varepsilon_2 = \sqrt{\frac{m_0 m_2}{m_1^2} - 1} = \sqrt{\frac{\Gamma(1-\delta)}{\Gamma^2\left(1-\delta/2\right)} - 1}, Q_p > 1 \tag{C.19}$$

The "squared" moments at nth-order are calculated as

$$m_{2,n} = \int_0^\infty f^n S_{Q_p}^2(f)\,\mathrm{d}f = \frac{m_0^2 Q_p}{2T_p^{n-1}} \cdot \frac{\Gamma\left(2 + \frac{(1-n)\delta}{2}\right)}{(2\alpha)^{(1-n)\frac{\delta}{2}}} \tag{C.20}$$

In particular, it yields

$$m_{2,0} = \frac{m_0^2 Q_p}{2} T_p \cdot \frac{\Gamma\left(2 + \frac{\delta}{2}\right)}{(2\alpha)^{\frac{\delta}{2}}} \tag{C.21}$$

Hence, the equivalent spectral bandwidth parameter of Blackman and Tuckey (Blackman and Tukey, 1959, Eq. (A.16))

$$\Lambda = \frac{m_0^2}{m_{2,0}} = \frac{2}{Q_p T_p} \cdot \frac{(2\alpha)^{\frac{\delta}{2}}}{\Gamma\left(2 + \frac{\delta}{2}\right)} \tag{C.22}$$

as well as Prevosto's parameter (Prevosto, 1988, Eq. (A.18))

$$B_w = \frac{4}{m_0^2}\int_0^\infty \left(f - \frac{m_1}{m_0}\right)^2 S_{Q_p}^2(f)\,\mathrm{d}f \tag{C.23}$$
$$= \frac{Q_p}{T_p}\left\{\frac{2\Gamma\left(2-\frac{\delta}{2}\right)}{(2\alpha)^{-\frac{\delta}{2}}} - 4\frac{T_p}{T_{01}} + 2\left(\frac{T_p}{T_{01}}\right)^2 \cdot \frac{\Gamma\left(2+\frac{\delta}{2}\right)}{(2\alpha)^{\frac{\delta}{2}}}\right\}, Q_p > \frac{1}{4}$$

which represents – together with Λ – a measure (in Hz) of the spectral bandwidth, and does not depend on the frequency location of the spectrum.

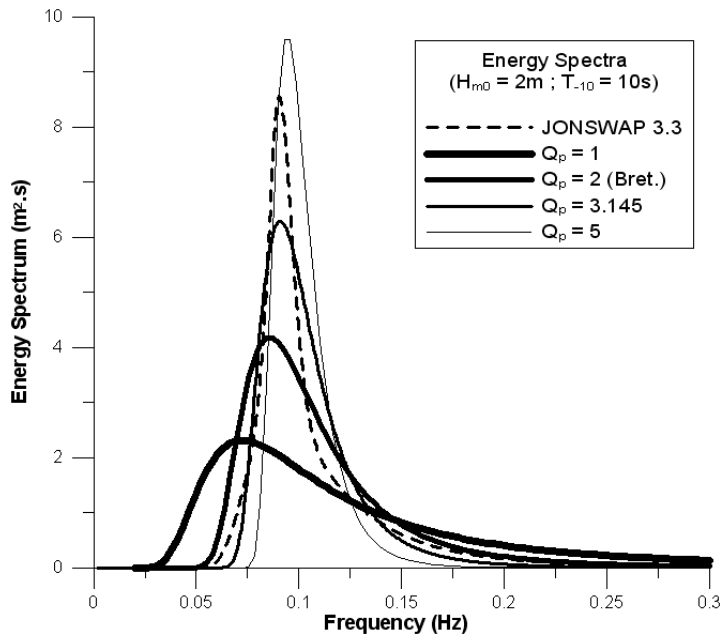

Figure C.1: Examples of Q_p-spectra ($Q_p = 1, 2, 3.145, 5$) and JONSWAP ($\gamma = 3.3$) spectrum, all with $H_{m0} = 2m$ and $T_{-10} = 10s$.

In figure C.1, a few examples of Q_p-spectra obtained with various values of peakedness factor ($Q_p = 1, 2, 3.145$ and 5) are depicted along with a JONSWAP spectrum with peak enhancement factor $\gamma = 3.3$ (see Eq. (A.28)). For each spectrum, $H_{m0} = 2m$ and $T_{-10} = 10s$. The corresponding factor Q_p of the JONSWAP3.3 spectrum is 3.145, and it is added to the figure for comparison.

C.2 Generalisation to n systems: multimodal formulation

A multimodal sea-state containing n systems is simply obtained as the linear combination of Q_p-spectra $\left(S_{Q_p i}(f)\right)_{1\leq i\leq n}$. For each system i, let us denote by η_{m0i} its relative

energy such that $\eta_{m0i} = m_{0i}/m_0$ (where global m_0 is equal to $H_{m0}^2/16$), by T_{pi} its peak period, and by Q_{pi} its peakedness factor (which in turn yields α_i and δ_i). The resulting spectrum may be written as

$$S(f) = \sum_{i=1}^{n} S_{Qpi}(f) = \frac{H_{m0}^2}{16} \cdot \sum_{i=1}^{n} \eta_{m0i} T_{pi}(1+2Q_{pi}) \frac{e^{-\alpha_i (fT_{pi})^{-2Q_{pi}}}}{(fT_{pi})^{1+2Q_{pi}}} \tag{C.24}$$

By linearity, the spectral moments are computed as

$$\begin{aligned} m_n &= \int_0^\infty f^n S(f)\,\mathrm{d}f = \int_0^\infty f^n \left[\sum_{i=1}^{n} S_{Q_{pi}}(f)\right] \mathrm{d}f = \sum_{i=1}^{n} \int_0^\infty f^n S_{Q_{pi}}(f)\,\mathrm{d}f \\ &= \sum_{i=1}^{n} m_{ni} \\ &= \frac{H_{m0}^2}{16} \cdot \sum_{i=1}^{n} \eta_{m0i} T_{pi}^{-n} \alpha_i^{\frac{n\delta_i}{2}} \Gamma\left(1 - \frac{n\delta_i}{2}\right) \end{aligned} \tag{C.25}$$

An example of such a multimodal spectrum is depicted in figure C.2: the sea-state is composed of four independents wave systems, eventhough the global frequency spectrum only exhibits two main peaks. This latter does not enable to identify the original systems, except if the underlying directional spectrum is known (Fig. C.3).

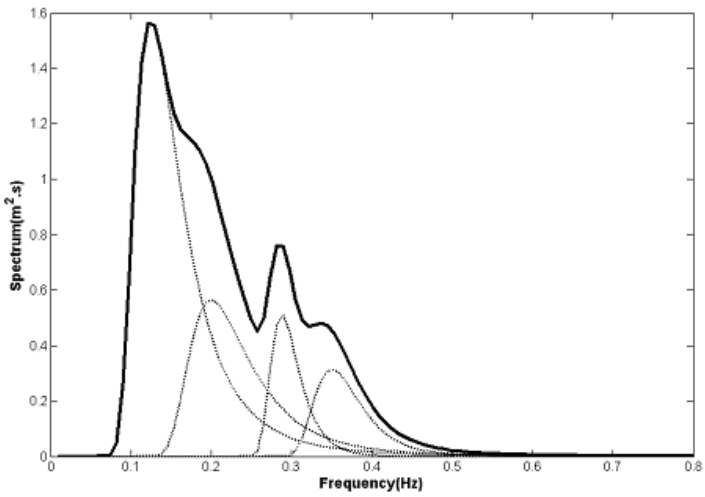

Figure C.2: Example of multimodal spectrum resulting from the superposition of four Q_p-spectra ($H_{m0} = 2m$ and $T_p \approx 8s$).

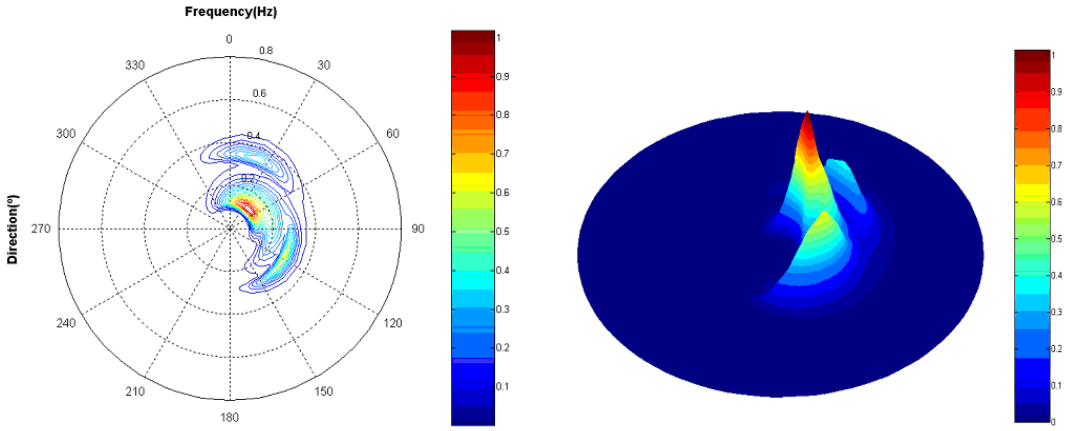

(a) (b)

Figure C.3: Underlying directional spectrum (a&b) corresponding to frequency spectrum of figure C.2.

C.3 Bimodal formulation

Let us illustrate the previous formulation to the particular case of bimodal sea-states ($n = 2$). Both systems are indexed as 1 and 2 respectively such that $f_{p1} < f_{p2}$, and η denotes the first system's relative energy, i.e. $\eta_{m01} = \eta$ and $\eta_{m02} = 1 - \eta$. The following ratios are then formed

$$\varphi = \frac{f_{p1}}{f_{p2}} \tag{C.26}$$

et

$$\tau = \frac{1}{f_{p1} T_{-10}} \tag{C.27}$$

where T_{-10} is the energy period of the bimodal sea-state. Expression (C.24) becomes

$$S(f) = \frac{H_{m0}^2}{16} T_{-10} \cdot \left\{ \eta\tau(1+2Q_{p1}) \frac{e^{-\alpha_1 (fT_{-10}\tau)^{-2Q_{p1}}}}{(fT_{-10}\tau)^{1+2Q_{p1}}} + (1-\eta)\varphi\tau(1+2Q_{p2}) \frac{e^{-\alpha_2 (fT_{-10}\tau\varphi)^{-2Q_{p2}}}}{(fT_{-10}\tau\varphi)^{1+2Q_{p2}}} \right\} \tag{C.28}$$

Therefore,

$$T_{-10} = \frac{m_{-1}}{m_0} = T_{-10} \cdot \left\{ \eta\tau\alpha_1^{-\frac{\delta_1}{2}} \Gamma(\alpha_1) + (1-\eta)\varphi\tau\alpha_2^{-\frac{\delta_2}{2}} \Gamma(\alpha_2) \right\} \tag{C.29}$$

Hence, the equality

$$\eta\tau\alpha_1^{-\frac{\delta_1}{2}}\Gamma(\alpha_1) + (1-\eta)\varphi\tau\alpha_2^{-\frac{\delta_2}{2}}\Gamma(\alpha_2) = 1 \tag{C.30}$$

that is,

$$\varphi = \frac{1 - \left(\eta\tau\alpha_1^{-\frac{\delta_1}{2}}\Gamma(\alpha_1)\right)}{(1-\eta)\tau\alpha_2^{-\frac{\delta_2}{2}}\Gamma(\alpha_2)} \tag{C.31}$$

or also

$$\tau = \left(\eta\alpha_1^{-\frac{\delta_1}{2}}\Gamma(\alpha_1) + (1-\eta)\varphi\alpha_2^{-\frac{\delta_2}{2}}\Gamma(\alpha_2)\right)^{-1} \tag{C.32}$$

Accordingly, by fixing indifferently either φ or τ, it is possible to fully define the bimodal spectrum thanks to the set of parameters: $\{H_{m0}, T_{-10}, \eta, Q_{p1}, Q_{p2}, \varphi \text{ or } \tau\}$. Examples of shapes obtained with both parametrisations are depicted in figures C.4(a&b), where $H_{m0} = 2m$, $T_{-10} = 10s$, $\eta = 0.6$, $Q_{p1} = 1, 1.5 \ldots 4$, $Q_{p2} = 2$ (developed wind-sea); the parameterisation in figure C.4(a) is based on definition $\tau = 1.5$, while in figure C.4(b) it is $\varphi = 0.4$. The only varying parameter here therefore is the first system's (swell) peakedness factor.

This formulation may be used as well as other well-known ones like Ochi et Hubble (Ochi and Hubble, 1976) or even Torsethaugen et Haver (Torsethaugen and Haver, 2004). The most typical configurations are: $\eta = 1$ (pure swell or wind-sea), $\eta = 0.8$ (swell dominated sea-state), $\eta = 0.5$ (mixed sea) and $\eta = 0.3$ (wind-sea dominated sea-state).

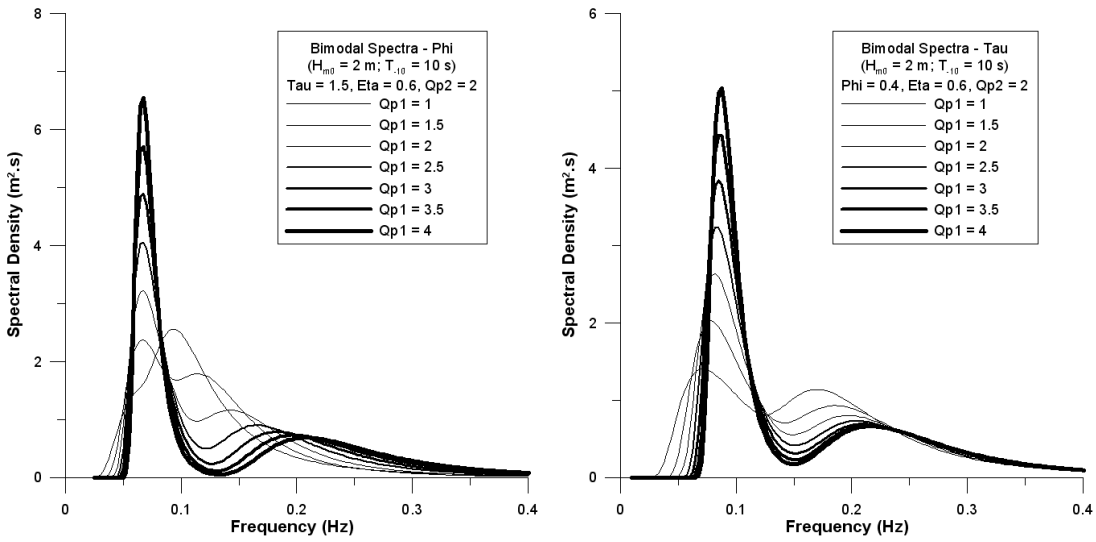

(a) (b)

Figure C.4: Example of bimodal spectra resulting from the superimposition of two Q_p-spectra such that $H_{m0} = 2m$, $T_{-10} = 10s$, $\eta = 0.6$, $Q_{p1} = 1, 1.5 \ldots 4$, $Q_{p2} = 2$ and $\tau = 1.5$(a) and $\varphi = 0.4$(b).

Appendix D

Stochastic modelling of a 1-DOF linear heaving WEC

This appendix addresses the stochastic modelling of a 1-DOF heaving WEC, which is linear in the frequency domain (linear hydrodynamics and PTO). This system is similar to that presented in Section 3.2 (Fig. 3.1), for which the same equations hold for describing the hydrodynamics of the axi-symmetrical buoy depicted in figure D.1.

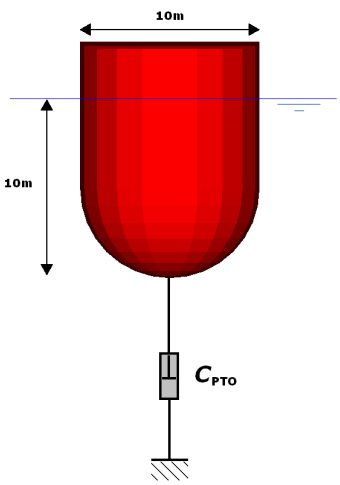

Figure D.1: Panelized heaving buoy (hull).

The radius of the float is $5m$, the draft $10m$, and the bottom part of the float is hemispherical in order to limit the vorticity effects and eddy-making along the hull when heaving. The cross-sectional area S near the free surface (or waterplane area) is not varying whatever the buoy's heave (provided heave motions remain within reasonable amplitudes, of course). These characteristics allow to rewrite the equation of dynamics applied to the buoy along its vertical symmetry axis (Oz) in the frequency domain using equation (3.1), that is

$$(m + A_{33}(\omega))\,\underline{\ddot{z}}(\omega) + (B_{33}(\omega) + C_{PTO})\,\underline{\dot{z}}(\omega) + (\rho g S + K_{33add})\,\underline{z}(\omega) = \underline{\Phi_{33}}(\omega)\underline{\eta}(\omega) \quad \text{(D.1)}$$

where K_{33add} denotes the additional stiffness that can be used to model moorings or modify the PTO characteristics. Here, the hydrodynamic coefficients of radiation (added mass $A_{33}(\omega)$ and damping $B_{33}(\omega)$) and excitation forces (impulse response $\underline{\Phi_{33}}(\omega)$) are computed in time domain thanks to the numerical codes ACHIL3D and DFHIL3D respectively, both developped at *Ecole Centrale de Nantes*. The additional stiffness is taken equal to zero (no moorings and no PTO modification).

As the model is linear by construction, and since wave excitation signal $\eta(t)$ is centred and Gaussian, the buoy's motions should be centred and Gaussian too. The time response of the buoy – heave velocity $\dot{z}(t) = \mathrm{d}z/\,\mathrm{d}t$ for instance – therefore may be formulated as

$$\begin{aligned}\dot{z}(t) &= \Re\{\sum_{p=1}^{\infty} \underline{\dot{z}}(\omega_p)e^{i\omega_p t}\} \\ &= \sum_{p=1}^{\infty} |\underline{H_{\dot{z}\eta}}(\omega_p)|\eta_p cos(\omega_p t + \varphi_p + \Psi_p)\end{aligned} \tag{D.2}$$

where amplitudes η_p and phases φ_p of the water elevation signal are defined as in Appendix B (Eq. (B.6)), and phase lag Ψ_p denotes the delay induced by the linear transfer function for harmonic p, which is equal to the argument of complex impedance $H_{\dot{z}\eta}(\omega)$ defined in equation (3.6).

Thus, it is possible to reproduce the time signals (heave velocity here in particular) related to the buoy motions from the stochastic modelling of the whole system, without requiring the resolution of dynamic equation in the time domain (*Cummins' equation*, Cummins, 1962). After, an inertial energy converter device as those presented in Section 3.6 may be coupled to the buoy's output to model a more realistic WEC (inertial flywheel, high-pressure gas accumulator with hydraulic mototr and generator...). The resolution of a simple differential equation as equation (3.50) is then only required to figure out the instantaneous power output from the converter.

Appendix E

Matrix determination of indirect associations

This appendix briefly exposes how to numerically identify the indirect associations of elements belonging to the same ensemble, when these are not directly associated according to some criteria while compared with each other. The final aim is to partition the initial ensemble into a finite number of disjointed sub-ensembles.

To illustrate the resolution of this problem, let us consider three elements a, b, and c which are compared to each other through their respective inter-distance (criterion), as depicted in the figure herebelow.

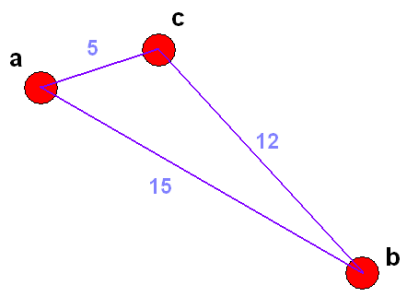

First case: two elements are associated (1) if and only if their inter-distance is inferior to $l^* = 10$; otherwise, they are not (0). According to the figure, a is directly associated with c whereas b cannot be associated with either a or c. The governing association (binary) matrix defined on the base (a, b, c) is therefore

$$\begin{pmatrix} 1 & 0 & 1 \\ 0 & 1 & 0 \\ 1 & 0 & 1 \end{pmatrix} \tag{E.1}$$

The resulting associations $\{a, c\}$ and $\{b\}$ are perfectly disjointed.

Second case: the criterion is now $l^* = 13$. Thus, b is associated with c since their inter-distance is $12 < l^*$. However, b cannot be associated with a. The association matrix is therefore

$$\begin{pmatrix} 1 & 0 & 1 \\ 0 & 1 & 1 \\ 1 & 1 & 1 \end{pmatrix}$$

In this case, the identified associations are not disjointed. Indirectly indeed, b is associated with a through c. The final association matrix is then equal to the unit matrix

$$\begin{pmatrix} 1 & 1 & 1 \\ 1 & 1 & 1 \\ 1 & 1 & 1 \end{pmatrix} \tag{E.2}$$

which characterises the original ensemble $\{a, b, c\}$.

This resolution seems straightforward when dealing with three-elements configurations. Now, when considering tens, hundreds or even thousands of elements to be compared with each other, the task appears much more complex while the partitioning of the ensemble into disjointed parts is still needed. Then, it is possible to work on the "raw" association matrix and transform it in order to end up with a stable one which defines disjointed ensembles as in cases (E.1)&(E.2) (block diagonalisable matrices). A default iterative algorithm is proposed herebelow.

1. **Initial state:** it is checked that the initial matrix M is squared and symmetrical; the current matrix M_{ref} is then defined as a nil matrix of same dimensions as M;
2. *[Loop]* While $M_{ref} \neq M$:
   - $M \leftarrow M_{ref}$
   - the sum of the terms in each row i of M is computed: if it is ≤ 1, skip to next row; otherwise, the ensemble $\mathscr{J}$ of column indices (j) for which $M_{ij} = 1$ is formed, and the substitutions $M_{kl} = 1$, $\forall (l, k) \in \mathscr{J}^2$, $l \neq k$ are made.
3. **Final state:** matrix M has converged to a matrix defining disjointed association sub-ensembles by construction. If one proceeds to a permutation of elements within the initial matrix base by gathering the elements according to the final associations, the resulting matrix should be block diagonal.

Bibliography

Aarnes, J. E. and Krogstad, J. E. (2001). Partitioning sequences for the dissection of directional ocean wave spectra: a review. Technical report, E.U. EnviWave (EVG-2001-00017) Wp4 Res. Prog.

Ardhuin, F., Collard, F., Chapron, B., Queffeulou, P., Filipot, J.-F., and Hamon, M. (2008). Spectral wave dissipation based on observations: a global validation. In *Proc. Chinese-German joint Symposium, Darmstad, Germany.*

Arhan, M. and Ezraty, R. (1978). Statistical relations between successive wave heights. *Oceanologica Acta*, 1(2):151–158.

Babarit, A. (2005). *Optimisation hydrodynamique et contrôle optimal d'un récupérateur d'énergie des vagues.* PhD thesis, Ecole Centrale de Nantes, France.

Baillargeon, S. (2005). *Le krigeage: revue de la théorie et application à l'interpolation spatiale de données de précipitations.* PhD thesis, Faculté des Sciences et de Génie, Laval University, Québec, Canada.

Battjes, J. A. and van Vledder, G. P. (1984). Verification of Kimura's theory for wave group statistics. In *Proc. I.C.C.E.'84, Houston, Texas, U.S.A.*, volume 1, pages 642–648.

Bendat, J. S. and Piersol, A. G. (1986). *Random data. Analysis and measurements procedures*, pages 484–516. 2^{nd}ed. J. Wiley & Sons Inc., New-York, U.S.A.

Benoit, M., Frigaard, P., and Schäffer, A. (1997). Analysing multidirectional wave spectra: a tentative classification of available methods. In *Proc. I.A.H.R.'97, Seminar on Multidirectional Waves and their Interaction with Structures, San Francisco, U.S.A.*, pages 131–158.

Blackman, R. B. and Tukey, J. M. (1959). *The measurement of power spectra*, pages 19–20. Dover Publications Inc., New-York, U.S.A.

Bretschneider, C. L. (1959). Wave variability and wave spectra for wind-generated gravity waves. Technical Report 118, Beach Erosion Board, U.S. Army Corps of Engineers, Washington D.C., U.S.A.

Cartwright, D. E. and Longuet-Higgins, M. S. (1956). Statistical distribution of the maxima of a random function. *Phil. Trans. R. Soc. Lond., A*, 237:212–232.

Cartwright, D. E. and Smith, N. D. (1964). Buoy techniques for obtaining directional wave spectra. In *Proc. Buoy Technology Symposium, Mar. Tech. Soc.*, pages 173–182.

Cressie, N. A. C. (1993). *Statistics for spatial data*. Wiley Series in Probability and mathematical Statistics. Revised ed. J. Wiley & Sons Inc., New-York, U.S.A.

Cummins, W. E. (1962). The impulse response function and ship motions. *Schiffstechnik*, 9(1661):101–109.

Elgar, S., Guza, R. T., and Seymour, R. J. (1984). Groups of waves in shallow water. *Jour. of Geophys. Research*, 89(C3):3623–3634.

Elgar, S., Guza, R. T., and Seymour, R. J. (1985). Wave group statistics from numerical simulations of a random sea. *Applied Ocean Research*, 7(2):93–96.

Evans, D. V. (1976). A theory for wave-power absorption by oscillating bodies. *Jour. of Fluid Mechanics*, 77:1–25.

Ewing, J. A. (1973). Mean length of runs of high waves. *Jour. of Geophys. Research*, 78(12):1933–1936.

Falcão, A. F. O. (2002). Control of an oscillating-water-column wave power plant for maximum energy production. *Applied Ocean Research*, 24:73–82.

Falcão, A. F. O. (2005). Modelling and control of oscillating-body wave energy converters with hydraulic power take-off and gas accumulator. In *Proc. E.W.T.E.C.'05, Glasgow, U.K.*

Falcão, A. F. O. (2007). Modelling and control of oscillating-body wave energy converters with hydraulic power take-off and gas accumulator. *Ocean Engineering*, 34(14-15):2021–2032.

Falnes, J. (2002). *Ocean waves and oscillating systems*. Cambridge University Press, Cambridge, U.K.

Funke, E. R. and Mansard, E. P. D. (1980). On the synthesis of realistic sea states. In *Proc. I.C.C.E.'80*, pages 2974–2991.

Gerling, T. W. (1992). Partitioning sequences and arrays of directional ocean wave spectra into component wave systems. *Jour. of Atmospheric and Oceanic Technology*, 9:444–458.

Gjevik, B., Krogstad, H. E., Lygre, A., and Rygg, O. (1988). Long period swell wave events on the Norwegian shelf. *Jour. of Phys. Oceanogr.*, 18:724–737.

Goda, Y. (1970). Numerical experiments on wave statistics with spectral simulation. *Rep. Port Harbour Res. Inst.*, 9:3–75.

Goda, Y. (1976). On wave groups. In *Proc. Behaviour of Offshore Structures Conf.'76*. The Norwegian Institute of Technology.

Guedes-Soares, C. (1984). Representation of double-peaked sea wave spectra. *Ocean Engineering*, 11(2):185–207.

Hanson, J. L. and Phillips, O. M. (2001). Automated analysis of ocean surface directional wave spectra. *Jour. of Atmospheric and Oceanic Technology*, 18:277–293.

Hasselmann, K., Barnett, T. P., Bouws, E., Carlson, H., Cartwright, D. E., Enke, K., Ewing, J. A., Gienapp, H., Hasselmann, D. E., Kruseman, P., Meerburg, A., Müller, P., Olbers, D. J., Richter, K., Sell, W., and Walden, H. (1973). Measurements of wind-wave growth and swell decay during the Joint North Sea Wave Project (JONSWAP). *Deutsche Hydr. Zeit. (8°)*, A12:1–95.

Hasselmann, S., Brüning, C., Hasselmann, K., and Heimbach, P. (1996). An improved algorithm for retrieval of ocean wave spectra from synthetic aperture radar image spectra. *Jour. of Geophys. Research*, 101:16615–16629.

Henderson, R. (2006). Design, simulation, and testing of a novel hydraulic power take-off system for the pelamis wave energy converter. *Renewable Energy*, 31:271–283.

Hogben, N. and Lumb, F. E. (1967). *Ocean waves - Statistics*. H.M.S.O., Londres, U.K.

Huang, N. E., Long, S. R., Tung, C.-C., Yuen, Y., and Bliven, L. F. (1981). A unified two-parameter wave spectral model for a general sea-state. *Jour. of Fluid Mechanics*, 112:203–224.

Huang, N. E., Shen, Z., Long, S. R., Wu, M. C., Shih, H. H., Zheng, Q., Yen, N.-C., Tung, C. C., and Liu, H. H. (1998). The empirical mode decomposition and the Hilbert spectrum for nonlinear and non-stationary time series analysis. *Proc. R. Soc. Lond.*, 454:903–995.

Hudspeth, R. T. and Medina, J. R. (1988). Wave group analysis by the Hilbert transform. In *Proc. I.C.C.E.'88 CERC/ASCE, chap. 66*, pages 884–898.

Josset, C., Babarit, A., and Clément, A. H. (2007). A wave-to-wire model of the SEAREV wave energy converter. In *Inst. of Mech. Engineers, Part M: Jour. of Engineering for the Maritime Environment*, volume 221, pages 91–93.

Kahma, K., Hauser, D., Krogstad, H. E., Lehner, S., Monbaliu, J. A. J., and Wyatt, L. R. (2005). Measuring and analysing the directional spectra of ocean waves. E.U. C.O.S.T. Action 714, EUR 21367, ISBN 92-898-0003-8.

Kerbiriou, M.-A. (2007). Energie des vagues: méthodologie d'estimation du potentiel d'énergie récupérable par un dispositif d'extraction d'énergie des vagues au regard du potentiel naturel du site. Final post-doctoral report, ref.: Ifremer/ERT/HO: R05 HO 07, conv. ADEME n°05 05 C0156, IFREMER/ADEME.

Kerbiriou, M.-A., Maisondieu, C., Prevosto, M., Babarit, A., and Clément, A. H. (2007). Influence of an improved sea-state description on a wave energy converter production. In *Proc. Int. Conf. on O.M.A.E.'07, San Diego, U.S.A.*

Kimura, A. (1980). Statistical properties of random wave groups. In *Proc. I.C.C.E.'80, Sydney, Australia*, pages 2955–2973.

Kofoed, J.-P. (2002). *Wave overtopping of marine structures – utilization of wave energy.* PhD thesis, Aalborg University, Denmark.

Komen, G. J., Cavaleri, L., Donelan, M., Hasselmann, K., Hasselmann, S., and Janssen, P. A. E. M. (1994). *Dynamics and modelling of ocean waves.* Cambridge University Press, Cambridge, U.K.

Krogstad, H. E., Barstow, S. F., Haug, O., and Peters, D. J. H. (1997). Directional distributions in wave spectra. In *Proc. 3rdConf. Ocean Wave Measurement and Analysis, Virginia Beach, Virginia, U.S.A.*, volume 2, pages 883–895.

List, J. H. (1991). Wave groupiness in the nearshore. *Coastal Engineering*, 5:475–496.

Liu, P. C. (2000). Wave grouping characteristics in nearshore Great Lakes. *Ocean Engineering*, 15:1221–1230.

Liu, Z., Elgar, S., and Guza, R. T. (1993). Groups of ocean waves: linear theory, approximations to linear theory, and observations. *Jour. of Waterway, Port, Coastal and Ocean Engineering*, 119(2):144–159.

Long, R. B. (1980). The statistical evaluation of directional spectrum estimates derived from pitch/roll buoy data. *Jour. of Phys. Oceanogr.*, 10(6):944–952.

Longuet-Higgins, M. S. (1957). The statistical analysis of a random moving surface. *Phil. Trans. R. Soc. Lond., A*, 249:321–387.

Longuet-Higgins, M. S. (1984). Statistical properties of wave groups in a random sea state. *Phil. Trans. R. Soc. Lond., A*, 312:219–250.

Masson, D. and Chandler, P. (1993). Wave groups: a closer look at spectral methods. *Coastal Engineering*, 20:249–275.

Max, J. (2004). *Méthodes et techniques de traitement du signal.* Dunod, coll. Sciences Sup, 5thed.

Medina, J. R. and Hudspeth, R. T. (1987). Sea states defined by wave height/period functions. In *Proc. 22thI.A.H.R. Congress: Seminar on wave analysis and generation in laboratory basins, Lausanne, Switzerland*, pages 249–259.

Medina, J. R. and Hudspeth, R. T. (1990). A review of the analyses of ocean wave groups. *Coastal Engineering*, 14:515–542.

Middleton, D. (1960). *Statistical communication theory.* McGraw-Hill, New-York, U.S.A.

Mitsuyasu, H., Tasai, F., Suhara, T., Mizuno, S., Ohkuso, M., Honda, T., and Rikishi, K. (1975). Observations of the directional spectrum of ocean waves using a cloverleaf buoy. *Jour. of Phys. Oceanogr.*, 5(2):750–760.

Mollison, D. (1985). Wave climate and the wave power resource. In Evans, D. and Falcão, A. F. O., editors, *Proc. IUTAM Symposium, Hydrodyamics of Ocean-Wave Energy Utilization, Lisbonne, Portugal*, pages 133–156.

Nolte, K. G. and Hsu, F. H. (1972). Statistics of ocean wave groups. In *Proc. 4th Offshore Tech. Conf., Dallas, E.U.A.*, number 1688, pages 139–146.

Ochi, M. K. (1988). *Ocean waves - The stochastic approach.* Cambridge Ocean Technology Series 6. Cambridge University Press, U.K.

Ochi, M. K. and Hubble, E. N. (1976). On six-parameters wave spectra. In *Proc. 15th Coastal Engineering Conf.*, volume 1, pages 301–328.

Olagnon, M., Robin, A., Legras, J. I., and Chaloin, B. (1990). Numerical simulation of actual irregular wave properties. In *Proc. Int. Conf. on O.M.A.E.'90, Houston, U.S.A.*, volume 1A, pages 9–16.

Oliveira-Pires, H., Aguiar, R., and Pontes, M. T. (1999). Directional statistics and the characterisation of the wave energy resource. In *Proc. Int. Conf. on O.M.A.E.'99, St John's, Newfoundland, Canada.*

Papoulis, A. (1991). *Probability, random variables and stochastic processes.* Series in Electrical Engineering. Ed. McGraw-Hill.

Pierson, W. J. and Moskowitz, L. (1964). A proposed spectral form for fully developped wind seas based on the similarity theory of S. A. Kitaigorodskii. *Jour. of Geophys. Research*, 69:5181–5190.

Polinder, H., Mecrow, B. C., Jack, A. G., Dickinson, P. G., and Mueller, M. A. (2005). Conventional and TFPM linear generators for direct-drive wave energy conversion. *I.E.E.E. Transactions on Energy Conversion*, 20(2):260–267.

Pontes, M. T. (1998). Assessing the european wave energy resource. *Jour. of Offshore Mechanics and Arctic Engineering*, 120:226–231.

Pontes, M. T., Barstow, S., Bertotti, L., Cavaleri, L., and Oliveira-Pires, H. (1997). Use of numerical wind-wave models for assessment of the offshore wave energy resource. *Jour. of Offshore Mechanics and Arctic Engineering*, 119:184–190.

Portilla, J., Ocampo-Torres, F. J., and Monbaliu, J. (2009). Spectral partitioning and identification of wind sea and swell. *Jour. of Atmospheric and Oceanic Technology*, 26(1):107–122.

Prevosto, M. (1988). Groupage de vagues et excitation basse fréquence - Etude ARAE. Technical report, IFREMER, Plouzané, France.

Price, W. G. and Bishop, R. E. D. (1974). *Probabilistic theory of ship dynamics*. Chapman et Hall, Londres, U.K.

Ricci, P., Saulnier, J.-B., Falcão, A. F. O., and Pontes, T. (2008). Time-domain models and wave energy converters performance assessment. In *Proc. Int. Conf. on O.M.A.E.'08, Estoril, Portugal*.

Rice, S. O. (1944). The mathematical analysis of random noise. *Bell Syst. Tech. Jour.*, 23:282–332.

Rice, S. O. (1945). The mathematical analysis of random noise. *Bell Syst. Tech. Jour.*, 24:46–156.

Rodríguez, G. and Guedes-Soares, C. (1999). A criterion for the automatic identification of multimodal sea wave spectra. *Applied Ocean Research*, 21:329–333.

Rye, H. (1974). Wave groups formation among storm waves. In *Proc. I.C.C.E.'74*, pages 164–183.

Rye, H. (1977). The stability of some currently used wave parameters. *Coastal Engineering*, 1:17–30.

Salter, S. (1980). Recent progress on ducks. *I.E.E.*, 127(5):308–319.

Saulnier, J.-B. and Pontes, M. T. (2006). Wavetrain deliverable n°5: Representative sea states. Technical report, E.C. WAVETRAIN R.T.N., Contract MRTN-CT-2004-505167.

Saulnier, J.-B., Ricci, P., Clément, A. H., and Falcão, A. F. O. (2009). Mean power estimation of WECs in simulated sea. In *Proc. E.W.T.E.C.'09, Uppsala, Sweden*.

Saulnier, J.-B., Ricci, P., Falcão, A. F. O., and Pontes, M. T. (2007a). Sensitivity of an axisymmetrical wave energy converter to spectral bandwidth. In *Proc. I.S.O.P.E.'07, Lisbon, Portugal*.

Saulnier, J.-B., Ricci, P., Falcão, A. F. O., and Pontes, M. T. (2007b). Spectral bandwidth and WEC performance assessment. In *Proc. E.W.T.E.C.'07, Oporto, Portugal*.

Sawnhey, M. D. (1963). A study of ocean wave amplitudes in terms of the theory of runs and a markov chain process. Technical report, Dept. Meteorology and Oceanography, New-York University, U.S.A.

Schlurmann, T., Schimmels, S., and Dose, T. (2002). Spectral analysis of freak waves using wavelet spectra (Morlet) and Hilbert spectra (EMD). *Jour. of Offshore Mechanics and Arctic Engineering*, 124(1):22–27.

Smith, G. H., Venugopal, V., and Fasham, J. (2006). Wave spectral bandwidth as a measure of available wave power. In *Proc. Int. Conf. on O.M.A.E.'06, Hamburg, Germany*.

Stansell, P., Wolfram, J., and Linfoot, B. (2004). Improved joint probability distribution for ocean wave heights and periods. *Jour. of Fluid Mechanics*, 503:273–297.

Tayfun, A. and Lo, J.-M. (1989). Wave envelope and related spectra. *Jour. of Waterway, Port, Coastal and Ocean Engineering*, 155(4):515–533.

The WAMDI Group (1988). The WAM model - A third generation ocean wave prediction model. *Jour. of Phys. Oceanogr.*, 18:1775–1810.

Thompson, E. F. and Seelig, W. N. (1984). High wave grouping in shallow water. *Jour. of Waterway, Port, Coastal and Ocean Engineering*, 110(2):139–157.

Tolman, H. L. (2002). User manual and system documentation of WAVEWATCH-III version 2.22. Technical Report 222, NOAA/NWS/NCEP/MMAB.

Torsethaugen, K. and Haver, S. (2004). Simplified double peak spectral model for ocean waves. In *Proc. I.S.O.P.E.'04, Toulon, France*, volume 3, pages 76–84.

Tucker, M. J., Challenor, P. G., and Carter, D. J. T. (1984). Numerical simulation of a random sea: a common error and its effect upon wave group statistics. *Applied Ocean Research*, 6(2):118–122.

Uhlenbeck, G. E. (1943). Theory of random process. Technical Report 454, MIT Radiation Lab., E.U.A.

Veltcheva, A. D. (2002). Wave and group transformation by a Hilbert spectrum. *Coastal Engineering*, 44(4):283–300.

Voorrips, A. C., Makin, V. K., and Hasselmann, S. (1997). Assimilation of wave spectra from pitch-and-roll buoys in a North Sea wave model. *Jour. of Geophys. Research*, 102:5829–5849.

Wang, D. W. and Hwang, P. A. (2001). An operational method for separating wind sea and swell from ocean wave spectra. *Jour. of Atmospheric and Oceanic Technology*, 18(12):2052–2062.